2007

Multivariable robust control of a simulated hybrid solid oxide fuel cell gas turbine plant

Alex Tsai
West Virginia University

Multivariable Robust Control of a Simulated Hybrid Solid Oxide Fuel Cell Gas Turbine Plant

Alex Tsai

Dissertation Submitted to the College of
Engineering and Mineral Resources at
West Virginia University
In partial fulfillment of the requirements for the degree of

Doctor of Philosophy
In
Mechanical Engineering

Larry Banta, PhD Chair
Muhammad Choudhry, PhD
Mario Perhinschi, PhD
Natalia Schmid, PhD
David Tucker, PhD

Department of Mechanical Engineering
2007

Abstract

Multivariable Robust Control of a Simulated Hybrid Solid Oxide Fuel Cell Gas Turbine Plant

Alex Tsai

This work presents a systematic approach to the multivariable robust control of a hybrid fuel cell gas turbine plant. The hybrid configuration under investigation built by the National Energy Technology Laboratory comprises a physical simulation of a 300kW fuel cell coupled to a 120kW auxiliary power unit single spool gas turbine. The public facility provides for the testing and simulation of different fuel cell models that in turn help identify the key difficulties encountered in the transient operation of such systems. An empirical model of the built facility comprising a simulated fuel cell cathode volume and balance of plant components is derived via frequency response data. Through the modulation of various airflow bypass valves within the hybrid configuration, Bode plots are used to derive key input/output interactions in transfer function format. A multivariate system is then built from individual transfer functions, creating a matrix that serves as the nominal plant in an H_∞ robust control algorithm. The controller's main objective is to track and maintain hybrid operational constraints in the fuel cell's cathode airflow, and the turbo machinery states of temperature and speed, under transient disturbances. This algorithm is then tested on a Simulink/MatLab platform for various perturbations of load and fuel cell heat effluence.

As a complementary tool to the aforementioned empirical plant, a nonlinear analytical model faithful to the existing process and instrumentation arrangement is evaluated and designed in the Simulink environment. This parallel task intends to serve as a building block to scalable hybrid configurations that might require a more detailed nonlinear representation for a wide variety of controller schemes and hardware implementations.

Pray, hope, and don't worry. Do not worry over things that generate anxiety. Only one thing is necessary, to lift up your spirit and love God.

Padre Pio of Pietrelcina
1917

To my parents, Robert and Nellie Tsai, for the many blessings bestowed on me through them.

Acknowledgements

This work is possible, thanks to the many combined prayers of family and friends, in particular those of my beloved mother, who probably hasn't slept in months. I am eternally grateful to my brother Scott for his constant intercession, my father for his patience and support, my baby girl for being my baby, and my wife Diana, for her care, love, and cooking that has kept me fat and healthy all these years. Without them, I would still be watching television going nowhere fast.

I would also like to thank my advisor Dr. Larry Banta, and the NETL team of Dr. David Tucker, Dr. John VanOsdol, Eric Liese, Larry Lawson, Susan Shoemaker, and David Rhuel. Special thanks go to my good friend Francesco Nicolo for his invaluable help and friendship. Funding for this research was provided by the National Energy Technology Laboratory.

Table of Contents

List of Figures

Nomenclature

A	Area
AFR	Air to Fuel Ratio
APU	Auxiliary Power Unit
ATR	Advanced Transport Reactor
BA	Bleed Air Valve
C	Capacitance
CA	Cold Air Valve
COE	Cost of Electricity
d	Diameter
e	Intensive Energy
EGT	Exhaust Gas Temperature
EL	Electrical Load
f	Friction Factor
FRR	Fuel Reformate Ratio
FU	Fuel Utilization
g	Constant of Gravity
GAP	Graphical
GAP	Graphical Application Programmer
GT	Gas Turbine
H	Angular Momentum
h	Enthalpy
H_∞	Hardy Space Infinity Norm
HA	Hot Air Valve
HAT	Humid Air Turbine
HHV	Higher Heating Value
HP,LP	High and Low Pressure
HX	Heat Exchanger
HyPer	Hybrid Performance
k	Conduction Coefficient
K	Loss Coefficient
k	PID Gain
Le	Equivalent Length
LHV	Lower Heating Value
LQG	Linear Quadratic Gaussian
LQR	Linear Quadratic Regulator
LTI	Linear Time Invariant
MIMO	Multiple Input Multiple Output
N	Rotational Shaft Speed
NETL	National Energy Technology Laboratory
NFCRC	National Fuel Cell Research Center
NTU	Number of Transfer Units
P	Pressure

PEM	Proton Exchange Membrane
PID	Proportional Integral Derivative
PR	Pressure Ratio
R	Universal Gas Constant
Re	Reynolds Number
RGA	Relative Gain Array
RHP	Right Hand Plane
Rt	Thermal Resistance
SISO	Single Input Single Output
SOFC	Solid Oxide Fuel Cell
STCR	Steam to Carbon Ratio
SVD	Singular Value Decomposition
T	Temperature
TF	Transfer Function
TIT	Turbine Inlet Temperature
u	Internal Energy
U	Overall Heat Transfer Coefficient
v	Velocity
V	Volume
W	Weight Matrix
YSZ	Yttria-Stabilized Zirconia
τ	Time Constant

Subscripts

amb	Ambient
BW	Bandwidth
comp	Compressor
CS	Control Surface
CV	Control Volume
d	Delay
l	Major Pressure Loss
lm	Minor Pressure Loss
n	Noise Bound
p	Plant
P	Pressure
ss	Steady State
st	Stored
surf	Surface

Symbols

ε	Effectiveness
ε	Relative Roughness
η	Efficiency
κ	Condition Number

μ	Dynamic Viscosity
ν	Kinematic Viscosity
ρ	Density
ω	Frequency

1 Introduction

Fuel cell technology has fast advanced in the field of power generation, and is currently sought as one viable alternative for the replacement of conventional power systems, as an efficient and clean source of electricity. As the research in this field progresses, it is more evident that existing technologies must be incorporated in the design of these systems in order to achieve the highest possible efficiency without sacrificing performance or cost. It is therefore convenient to utilize the synergy of current power producing methods with power generating fuel cells. However, the resulting coupling difficulties of fuel cells and gas turbines are yet to be successfully mastered.

One of the most promising technologies for hybrid power generation systems is the coupling between Solid Oxide Fuel Cells and gas turbines. Siemens-Westinghouse and the National Fuel Cell Research Center or NFCRC for example, have recently built and tested one such system, capable of producing 220kW of power with more than 50% electrical efficiency based on the LHV of natural gas fuel. It is estimated that enhanced configurations of similar types of hybrid systems can deliver more than 70% efficiencies. This is far greater than systems running on coal or natural gas alone, for equivalent sized plants. In addition, fuel cells may offer advantages over conventional power plants in the area of carbon sequestration.

Despite the success of the NFCRC in proving the practical implementation of the conceptual hybrid design, the resulting system was meant to serve only as a test bed for future designs. There are still many issues to address, before a fully integrated and functional configuration is ready for commercialization. One such concern is the ability to safely control the plant in the presence of disturbances, as defined by sudden load demands. An inherent difficulty of the fuel cell – gas turbine assembly, is that interactions between the high-pressure gas turbine flow and the fragile fuel cell material can lead to severe equipment damage, and malfunction. This constitutes the essential control problem of hybrid systems, to successfully regulate and follow load demands in a

system that exhibits a wide mismatch between component time constants, and large differences between their structural strengths.

Researchers have sought to find the solution to these problems mostly with the use of analytical models that are subsequently incorporated into various control methodologies. To date, hundreds of models have been based on the first principles of energy and mass conservation, and presented in various degrees of complexity, ranging from lumped parameter, to one and two-dimensional models. This limited form of characterization can be primarily attributed to the lack of any test facility large enough to faithfully duplicate the effects of a real hybrid plant. An experimental facility robust enough to test the operational limits was simply not available, and for most, cost prohibitive. Without an alternate way in which to physically model the system, the analytical models could not be validated, nor their accuracy measured.

In face of these challenges, the National Energy Technology Laboratory, or NETL has designed and constructed a test facility that allows for the simulation of a hybrid system, under a particular hybrid configuration. The facility simulates with hardware a 300kW Solid Oxide Fuel Cell coupled to a gas turbine. Hardware control of this system has been partially achieved for quasi-steady state scenarios. However, centralized control has yet to be implemented for transient occurrences and other quasi-steady state conditions.

The main objectives of this research are:

- To make use of the existing NETL hybrid facility for the generation and subsequent analysis of frequency response data useful for control development
- To derive a set of mathematical equations stemming from the aforementioned frequency response tests that more realistically predict the hybrid component interactions
- To develop and implement a control methodology based on the derived empirical multivariate model that can robustly regulate fuel cell and turbo-machinery critical parameters

A successful completion of these tasks will result in the following original contributions of this work, primarily:

- The availability of real frequency response data of a hybrid system as given in magnitude and phase Bode plots
- The derivation of empirical Transfer Functions never before obtained for a hardware hybrid configuration
- The design of a centralized state space robust controller for a hybrid system based entirely on an experimental model
- The validation of existing analytical multivariate models with the use of the empirical Transfer Function matrix

The scope of this work thus lays in the development of a centralized robust controller that can manage flow to maintain fuel cell operational constraints under multivariate transient disturbances. A robust controller is necessary for the safe and stable implementation of such a hybrid system. This is especially the case when detailed models are unattainable due to the complexity of the system itself, like that of a coupled gas turbine compressor assembly, or a system having combustion dynamics as it is in the present case. Robustness, as defined by the ability to sustain control in the presence of model uncertainty, is also preferred in a system required to dismiss low frequency perturbations. Random loss of electrical load is, for the most part, a real life low frequency occurrence. Such events could impose the possible destructive forces on a fuel cell, when they are not dealt with accordingly, because of the inevitable rise in turbine speed, and hence mass flow that accompanies a loss of electrical load. Thus, a controller that can mitigate both, high and low frequency phenomena is desired for the early stages of the hybrid design. Frequency domain loop shaping techniques are suitable to achieve these goals. System identification can provide empirical transfer functions for the linear window of fuel cell operation, while more insight into system coupling effects can be gained by examination of Bode plots. These transfer functions are in turn used in the design of an H_∞ controller, which can be tested offline with a high fidelity model of the hybrid configuration.

Online testing of the resultant controller design will provide a means of quantifying the applicability of the abovementioned control methodology to new assemblies of the hybrid configuration. With the use of every available input, including electrical load, bypass valves and fuel, such a design can be accomplished with maximum thermal management capability under a stable envelope of operation for any system disturbance.

An analytical nonlinear model of the hardware facility at NETL has also been developed in the MatLab/Simulink environment. This model serves as a complementary tool to the aforementioned empirical analysis. Although originally intended to predict steady state behavior, ongoing work aims at incorporating full system dynamics to more accurately predict transient system behavior. Adjustment and tuning of the model is necessary if controller performance is to be evaluated prior to its real time implementation on the physical facility.

2 Literature Review

Hybrid power generating systems of the fuel cell type are mainly categorized according to the energy management strategy used. Whether the process is a recuperated heat process, a heat of compression configuration or a steam turbine bottoming cycle, the performance is generally based on the power produced per unit fuel consumed with respect to the lower heating value LHV of the fuel utilized. Following is a description of the existing and suggested hybrid configurations in literature as well as the different types of controllers being adapted to each assembly.

2.1 Solid Oxide Fuel Cell

Fuel cells have been described as replenishable batteries that operate continuously under a constant fuel supply. These electrochemical devices are able to produce power as a result of the ionic interaction between hydrogen and oxygen. A fuel cell thus has cathode and anode electrodes, an electrolyte, and conductive interconnections that allow for the transport of electrons through a resistive load from cathode to anode sides. In principle, hydrogen is supplied at the anode side and oxygen at the cathode side. The overall reaction in the fuel cell can be summarized as that of Eq.2.1.1, where electrons and heat are released as a consequence of the exothermic reaction.

$$H_2 + \frac{1}{2}O_2 \rightarrow H_2O \qquad \text{Eq.2.1.1}$$

Power electronics coupled to a resistive load can then convert this generated DC voltage to AC, when the fuel cell is used in stationary power generating applications.

For the most part, fuel cells are distinguished by the type of electrolyte used. The solid oxide fuel cell electrolyte has a Yttria-Stabilized Zirconia YSZ ceramic solid structure that allows ionic transport while remaining impermeable to electrons. The cathode and anode sides are composed of a mixture of ceramic and metals, mainly a Zirconia cermet that allows high temperatures and high electronic conductivity. The interconnects between cathode and anode sides are made of Lanthanum Chromite, a ceramic that can

increase conductivity when mixed with compatible alkaline materials (Larminie et al. 2003). These components combined together can withstand temperatures of up to 1000°C, and produce as much as 250MW of power, when assembled in compounding stacks (Carlson et al. 2004). It is because of these characteristics that the solid oxide fuel cell SOFC is the favorable candidate for large power applications.

A simplified schematic of the SOFC is shown in Figure 2.1. As noted earlier, electrons are expelled from the hydrogen molecules when the H_2 reacts with two oxygen anions to produce water and heat. The anode and cathode half reactions are accordingly:

$$2H_2 + 2O^{=} \rightarrow 2H_2O + 4e^{-} \qquad \text{Eq.2.1.2}$$

$$O_2 + 4e^{-} \rightarrow 2O^{=} \qquad \text{Eq.2.1.3}$$

A graph showing cell performance based on voltage/current density data is shown in Appendix A.

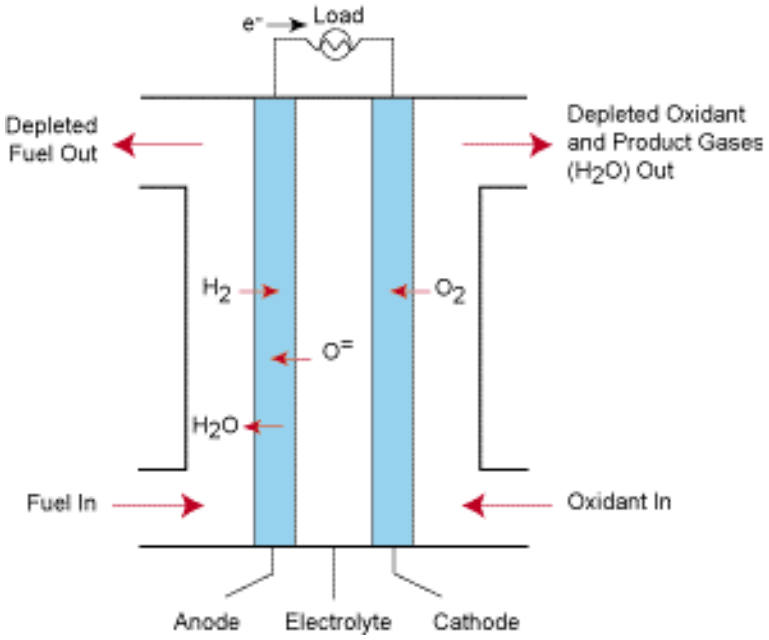

Figure 2.1 SOFC Operation

For this and any other fuel cell, the voltage produced is a function of the Gibbs free energy ΔG_f and thus of the reactant concentrations within the cell. The Gibbs free energy

is a measure of the amount of useable work that can be extracted from a chemical reaction. This energy is defined as the change in the enthalpy of formation minus the heat released as expressed in Eq.2.1.4. The fuel cell voltage can then be related to this available amount of work as that given by Eq.2.1.5.

$$\Delta g_f = \Delta h_f - T\Delta s \qquad \text{Eq.2.1.4}$$

$$E_{OC} = -\frac{\Delta g_f}{z \cdot F} \qquad \text{Eq.2.1.5}$$

where E_{OC} is the open circuit voltage, z is the number of electrons and F, Faraday's constant. In the presence of irreversibilities, the actual voltage per cell is given by the reversible Nernst potential cell voltage minus all irreversibilities, as shown in Eq.2.1.6,

$$E = E^0 + \frac{R \cdot T}{z \cdot F} \cdot \ln\left(\frac{\frac{P_{H_2}}{P^0} \cdot \left(\frac{P_{O_2}}{P^0} \right)^{\frac{1}{2}}}{\frac{P_{H_2O}}{P^0}} \right) - \eta_A - \eta_{FC} - \eta_O - \eta_C \qquad \text{Eq.2.1.6}$$

$$E^0 = -\frac{\Delta h_f}{z \cdot F} \qquad \text{Eq.2.1.7}$$

where the main irreversibilities η's are those of activation, fuel crossover, ohmic, and concentration losses (Larminie et al. 2004). Equation 2.1.6 assumes that the oxidation process produces pure hydrogen to the cell. Activation losses are attributed to the voltage loss due to the driving force required to kick start the ionic exchange of the overall chemical reaction. Fuel crossover losses are those voltage drops observed when the electrolyte permits some electrons and fuel to permeate its membrane and mix with the cathode side stream. Ohmic losses are those relevant to the resistance of current flow, whereas concentration losses are those due to fluctuations in the stoichiometric quantities of the reactants. Ways in which to minimize these overpotentials are described in more detail in (Larminie et al. 2004). It can be seen from Eq.2.1.6 that the cell voltage is dependent on the partial pressures of the reactants, as well as the temperature of the cell.

Appendix A also shows how these irreversibilities affect the current voltage relationship in the cell.

So far it has been stated that fuel cells produce power by the electrochemical reaction of H_2 and O_2, once the latter is broken into anions. Hydrogen however, must be produced in pure form for the reaction to take place. With the use of pure H_2, power generation can result in zero pollutant emissions, having only water as a byproduct. Various methods to produce hydrogen exist, such as the use of primary fossil fuels like natural gas or coal. If coal is used, a gasification process combines high temperatures with water vapor and oxygen, while a natural gas fuel would require reforming and hydrogen shift reactions to to produce H_2. Equations 2.1.8 and 2.1.9 detail the chemistry for the reforming, and shift reaction respectively of methane fuel (Karvountzi et al. 2004). Typical combustion NO_X and SO_X pollutants are thus eliminated in a fuel cell, having only the carbon dioxide capture logistics to handle.

$$CH_4 + H_2O \leftrightarrow CO + 3H_2 \qquad \text{Eq.2.1.8}$$

$$CO + H_2O \leftrightarrow CO_2 + H_2 \qquad \text{Eq.2.1.9}$$

Solid Oxide Fuel Cells are most suited to stationary hybrid power generation applications because they can operate at high enough temperatures to directly oxidize CO and CH_4. Proton Exchange Membrane fuel cells for example cannot withstand CO as a fuel or byproduct, because carbon monoxide poisons the electrolyte membrane. Since large realistic hybrid plants would require the production of massive amounts of hydrogen either by reforming a hydrocarbon or from coal syngas, it is likely that hydrocarbon byproducts appear at the anode along with hydrogen. The versatility of being able to withstand a wide variety of fuels, is a highly desirable feature of SOFC that becomes especially important if coal based systems are to be mandated.

In order for the fuel cell to maintain performance and operability, the cell's temperature, anode fuel flow, cathode airflow, and reactant partial pressure constraints must be met. Each of these parameters plays a major role in the thermal efficiency and the net power output of the fuel cell. Research on ways to optimize the cell's power production via the

synergistic use of its thermal characteristics has led to the successful coupling of existing gas turbine technology. In the following sections it will be seen that simple gas turbine cycles for stationary power generation benefit from exhausted fuel cell heat, while fuel cells increase in efficiency from recuperation and pressurized air, both byproducts of expanders and compressor assemblies.

2.2 The Brayton Cycle

A simple gas turbine cycle using air as the working fluid is illustrated in Fig.2.2. Ambient air enters point "1" and is adiabatically compressed to a higher temperature and pressure at point "2". Heat through a combustor further increases the temperature of the compressed air at point "3", where it is then expanded in a turbine to generate electrical power through a generator at point "4". The ideal cycle for this configuration is known as the Brayton Cycle, and the closed loop version is shown to the right in Fig.2.2.

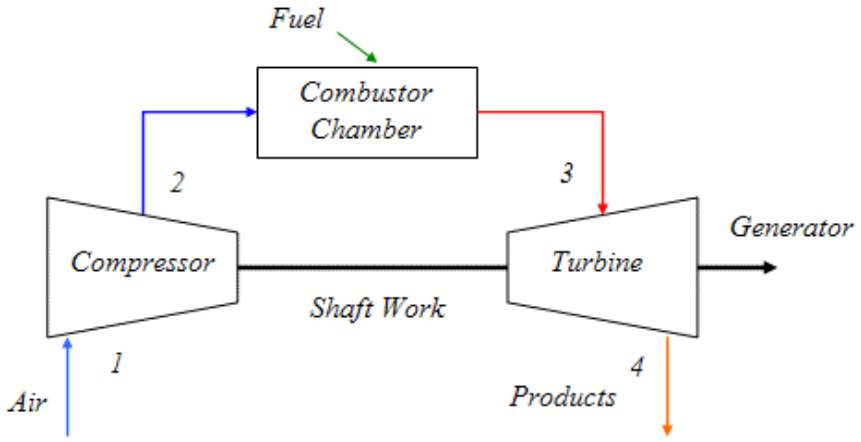

Figure 2.1 Brayton Cycle Schematic (Saad 1997)

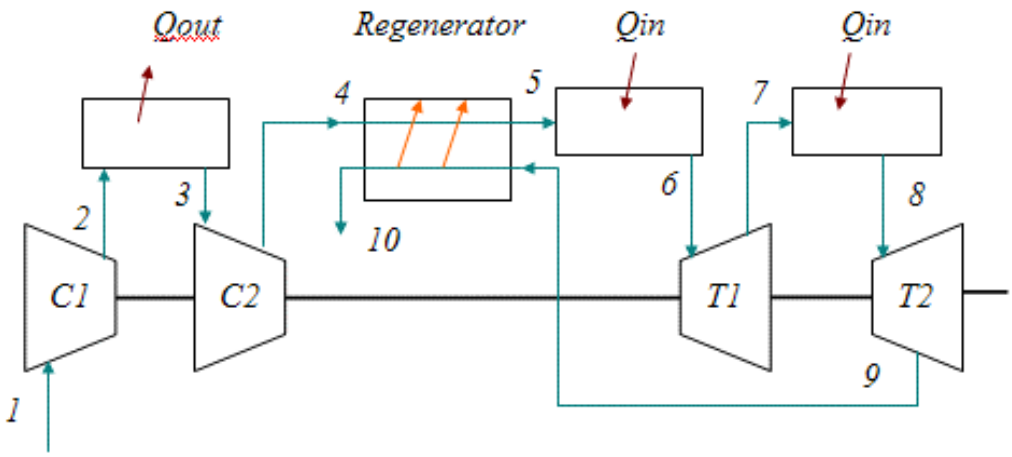

Figure.2.3. Regenerative Brayton Cycle with Stage Compression (Saad 1997)

A single shaft connects the compressor to the turbine, and the latter provides the compressor work required to pressurize the working fluid. In order to improve cycle efficiency by means of energy transfer, various configurations, including compressor stage intercooling and expander stage reheat have been studied and proven to work (Saad 1997), as shown in Fig.2.3. The higher the difference between the turbine inlet temperature TIT and the exhaust gas temperature EGT is, the more power the turbo machinery can generate. If an external source of heat can be freely extracted and supplied to the turbine inlet, then less fuel would be required in the combustor to produce the same amount of power, increasing thus the efficiency of the cycle. A SOFC can provide this complementary source of heat, and at the same time utilize the pressurized oxygen in the air to produce electricity. However, there are significant difficulties in combining these technologies, with the most noticeable in the interaction between the fragile ceramic fuel cell components and a high-pressure dynamic system. Large differences in fuel cell and gas turbine time constants add to the complexity and challenge of designing a successful control strategy for the hybrid system.

As will be noted in subsequent sections, fuel cell mass flow rate is a critical parameter that greatly affects the performance of the overall hybrid system. The synergistic advantage of SOFC and gas turbines is clear, when taking into account the parasitic losses that would otherwise be incurred when running a blower to provide airflow in the

stand-alone fuel cell configuration. Since the turbine runs the compressor that supplies the oxidant and cooling flow to the fuel cell cathode side, there is no loss in efficiency due to the required energy to run the blower.

The equations derived in this work, governing the energy and mass interactions between system components of the compressor-turbine assembly will be discussed in detail throughout Chapter 4. However, models for the dynamic behavior of compressors presented below have yielded valuable information in preventing the unwanted phenomena known as stall and surge.

2.3 Compressor Stall and Surge

Greitzer developed a compressor system model in order to predict the instances in which the stall and surge phenomena would occur in axial flow compressors (Greitzer 1976a). Rotational stall is defined as the sudden loss of positive airflow through a compressor blade, which leads to a sharp decrease in effectiveness, with efficiency values measured at 20%. During stall, flow around the circumference of an axial compressor blade is non-uniform, with high flows on one side, and low flows on the other. Long periods of time in rotational stall can cause combustor and engine damage, due to the excessive temperatures induced by the low mass flows that are not being "pushed" through the compressor. Also, because of the unsteady flow field that is caused in the compressor blades, stresses can develop, affecting blade life. Once the stall limit is reached, the only way in which to return to the un-stalled condition is to reduce the shaft rotational speed. However, this in turn results in a reduction of the compressor pressure ratio. Because of the compressor hysteresis effects, opening the throttle valve is an ineffective means of stall recovery.

A surge on the other hand, is defined as large amplitude sustained oscillation of averaged airflow that can only occur after the stall limit is reached. Surge is only observed to happen at high rotational speeds. For the most part, compressors do not surge at small downstream volumes, but their occurrence is dependent on how large the downstream volume is. Large damaging inlet over-pressures within a compressor can

result from a surge, while the stall condition can occur several times before a surge manifests. In fact, the frequency of stalls is orders of magnitude higher than that of surge oscillations, which occur at low frequencies. It is because of this that the model developed by Greitzer assumes incompressible flow, with densities taken at ambient values. Greitzer's work aims at determining if a slight change in throttle opening during compressor steady state operation would result in a stall or surge condition, from the mass and pressure response output of a nonlinear time dependent model. To validate the model in part II of his work, Greitzer models the compressor pressure rise as an actuator disk connected to a plenum of moderate volume via a constant area duct. The continuity and momentum equations for the compressor, plenum and throttle are all non-dimensioinalized, and the variation of one particular parameter, B, is examined. The four main equations that comprise the compressor system are:

$$\left(P - P_b\right) + P_r = \rho \cdot L_c \cdot \frac{dv}{dt} \qquad \text{Eq.2.3.1}$$

$$\Delta P - P_{th} = \frac{L_{th}}{A_{th}} \cdot \frac{d\dot{m}_{th}}{dt} \qquad \text{Eq.2.3.2}$$

$$\frac{d\rho_p}{dt} = \frac{\rho_p}{k \cdot P_p} \cdot \frac{dP_p}{dt} \qquad \text{Eq.2.3.3}$$

$$\dot{m}_c - \dot{m}_{th} = \frac{\rho \cdot V_p}{\gamma \cdot P} \cdot \frac{dP}{dt} \qquad \text{Eq.2.3.4}$$

Equation 2.3.1 is the momentum equation for the compressor, Eq.2.3.2 is that for the throttle, and Equations 2.3.3 and 2.3.4 are for the plenum

Greitzer concludes that in practice, stall and surge cannot be predicted from compressor or throttle static maps since the transient compressor behavior is determined by the dynamic considerations of pressure and mass flow rate in the compressor and throttle assembly. These elements give the energy input and dissipation of the system. The net amount of energy the compressor inputs to sustain oscillations is greater than that at steady state, thus the cycle oscillations of the surge phenomena are sustained when the

energy input of the compressor balances the energy dissipation of the throttle. In other words, static instability does not create surge cycles.

Part II of Greitzer's work tests the validity of a previous nonlinear compressor model for a three stage axial compressor (Greitzer 1976b). The setup consisted of a compressor that drove ambient air into a large plenum vessel that has two throttle valve openings, one of 1.5m and the other of 1.53m at its exhaust. The plenum volumes under study ranged from $2.8m^3$ to $34.9m^3$.

The tests concluded that during stall, pressure fluctuations inside the plenums were negligible even though the mass flow rates through the compressor were unsteady. Also, during the surge cycles induced, the data showed that the compressor's operating condition moved in and out of stall. In short, just as was predicted in the model, the system's dynamic response was greatly dependent on the normalized parameter B, defined as the resonant frequency. The dynamic response was rather set by the time history of the compressor operating point, and not the rotational speed or throttle valve position.

The work of Greitzer was extended to centrifugal single stage compressors in Hansen's study of deep surge for a plenum volume of $0.025m^3$ (Hansen et al. 1981). The inputs to Greitzer's model are system geometry, measured steady state positive and negative characteristic branches, estimated unstable branch, throttle valve characteristic, and a compressor flow relaxation time. In order to predict deep surge, Hansen inserted a negative flow branch into the compressor characteristic from surge data by injecting plant air at the compressor exhaust, and measuring the reverse flow. In order to initiate stall and surge, the throttle was slowly closed to allow for flow reversal in the compressor at speeds as low as 7,000rpm, from the nominal operating speed of 65,000rpm. The work concluded that Greitzer's model can be used to model centrifugal compressors, with slight modifications to the relaxation time variable N, assumed to be constant by Greitzer. Greitzer's compressor model has been extensively used in the modeling of fuel cell – gas turbine hybrid systems, as described most recently by Hahn (2004).

With regard to the control of surge, Blanchini outlines the positive and negative aspects of designing high gain linear controllers capable of stabilizing compressor surge in the face of measurement noise and high frequency disturbances for multistage centrifugal compressors (Blanchini et al. 2002). If a throttle valve serves as the actuator, and a differential pressure transducer as the feedback signal, to suppress surge a large value of gain is required. This however, implies that system noise is amplified, and saturation of the actuator can occur due to this noise fluctuation. A trade off between speed and stability is therefore warranted. The noise is thus filtered at a cutoff frequency that is not too large to affect attenuation properties, and not too low to introduce phase lags that might be detrimental to system stability. Based on Greitzer's model, Blanchini's control law is highly dependent on the steady state value of the throttle valve position and the non-dimensional parameter B, which can be interpreted as the ratio between pressure forces and inertia forces acting in the compressor duct. This parameter strongly affects system stability. B increases with increasing speed and plenum volume, and decreases with increasing compressor pipe length. To avoid noise disturbances, a second order low pass filter was designed with the inclusion of a notch filter to attenuate a dominant frequency observed in the noise spectrum. To improve the controller's speed, the throttle valve was replaced by one having a smaller inertia to allow fast throttle fluctuations during control, while the notch filter reduced the stall noise disturbances. The stability range for operation was not however concluded, this being attributed to the intrinsic nature of the stability limit of the compression system, dependent in great measure on the B parameter.

The next sections compare different types of hybrid SOFC / Gas Turbine configurations in terms of electrical and thermal efficiencies, performance, cost of electricity, and net power output.

2.4 Hybrid Configurations

The first prove-of-concept hybrid system was built by Siemens-Westinghouse in conjunction with the National Fuel Cell Research Center (NFCRC 2007). It consisted of

a 220kW Solid Oxide Fuel Cell Gas Turbine facility that utilized a tubular seal-less stack design within the SOFC. Figures 2.4 and 2.5 illustrate the physical arrangement of the hybrid system that produced efficiencies of 53%, based on the LHV of the fuel (Smith 2006). Figure 2.4 compares observed and predicted results of a dynamic model of the hardware configuration developed by the NFCRC. Testing consequently showed that the cathode airflow was the dominant factor in the overall performance of the hybrid system. Ambient pressure, temperature, and humidity were also found to affect turbo machinery performance (Smith 2006). The pressure ratio for this system was 3:1.

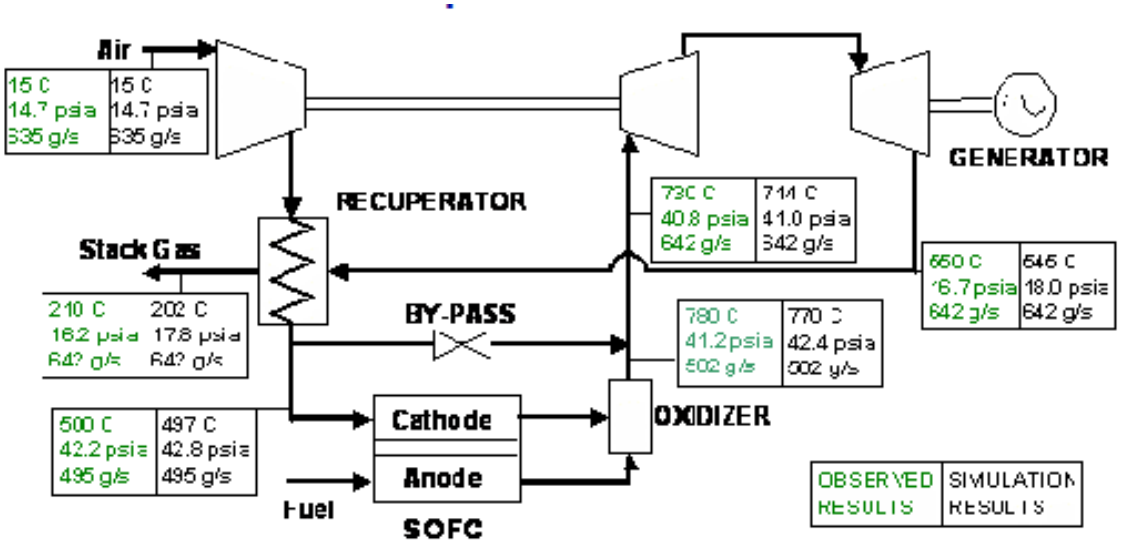

Figure.2.4. Simulated and Observed Results for the 220kW System [NFCRC]

Figure.2.5. Siemens-Westinghouse 220kW Hybrid System [NFCRC]

Veyo makes a figure of merit comparison between four SOFC/GT hybrid system configurations in terms of cost, efficiency, relative system complexity, net power output, number of cells, and overall performance (Veyo et al. 2003). The four configurations under study are: 1) an atmospheric pressure system, 2) a pressurized system, 3) a turbocharged SOFC, and 4) a pressurized recuperated SOFC with intercooling and micro gas turbine reheat. Each of these configurations, as they appear in the paper, is shown below.

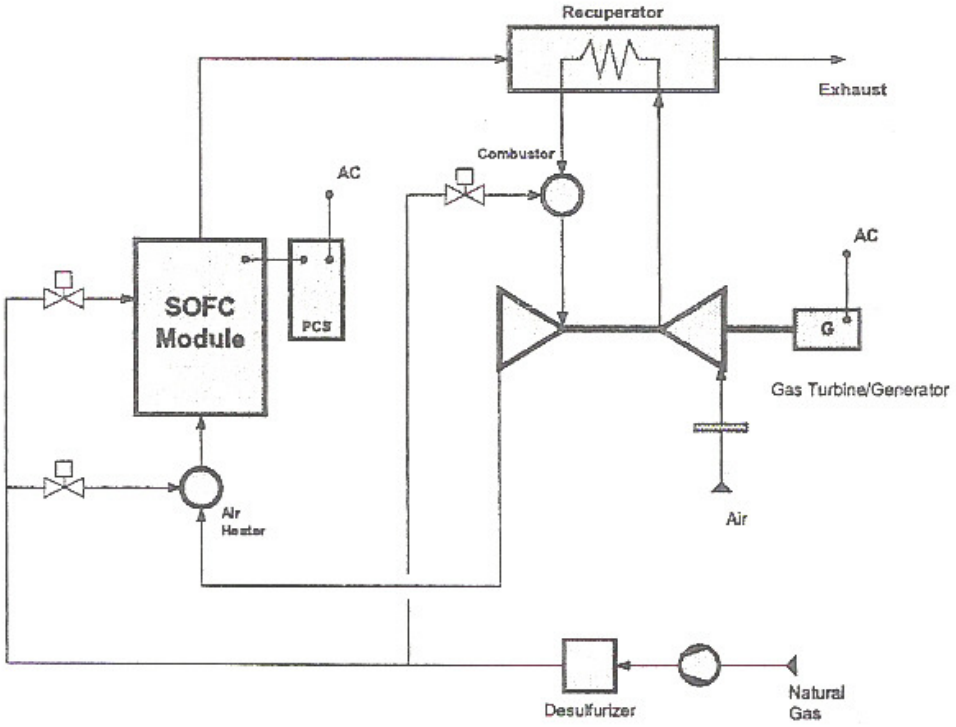

Figure.2.6. Atmospheric Hybrid [Veyo]

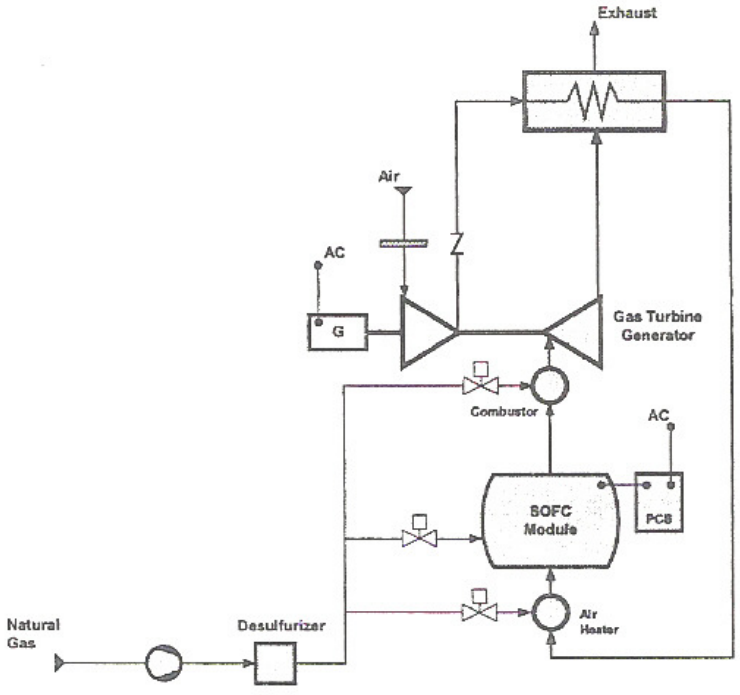

Figure.2.7. Pressurized Hybrid [Veyo]

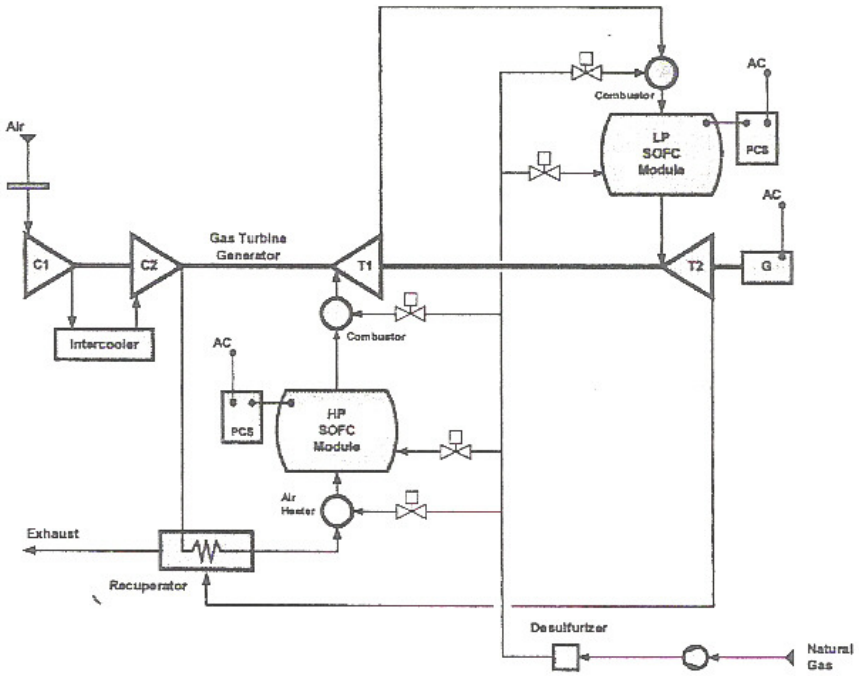

Figure.2.8. Pressurized Intercooled Hybrid [Veyo]

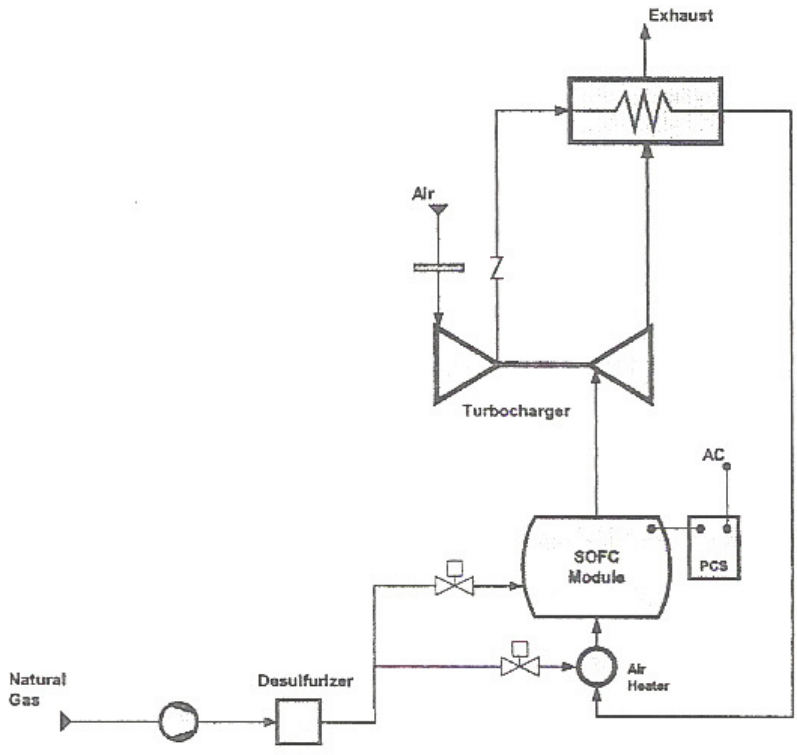

Figure.2.9. Turbo-Charged Hybrid [Veyo]

Test results show that even though the ambient pressure hybrid system is more efficient than the stand alone SOFC, it is less efficient than a pressurized system. The latter has a net system electrical efficiency of 59%, and the former 52% efficiency for 300kW plants. The reason the ambient hybrid excels over the SOFC, is that the exhaust stack heat is used by the turbine to generate additional electrical power. For the atmospheric hybrid, the SOFC cathode side receives airflow from the turbine exhaust. The turbine in turn recuperates exhaust heat from the fuel cell by the use of a heat exchanger. In order to reach maximum peak efficiency under this configuration, the recuperator effectiveness, TIT, and gas side inlet temperature must conform to design specifications, and are the key control parameters to monitor. For a very effective recuperator, an optimal TIT can be obtained without firing the combustor, with temperatures of 950°C.

In pressurized hybrids there is a reduction in NO_X and CO_2 emissions, a higher fuel cell stack voltage, and a higher cell operating efficiency for a set stack current. This configuration exhibits efficiencies in the order of 60% for a SOFC, but is also more costly due to pressurization constraints. The turbocharged hybrid system in contrast, pressurizes the fuel cell but does not generate electrical power. The cell exhaust heat is only used to drive the compressor through the turbine. The turbocharged hybrid has the lowest system efficiency, with only 47%.

Lastly, the pressurized intercooled with reheat hybrid cycle demonstrates a 64% efficiency for 2 turbines and compressors, and 2 SOFC modules both for the high and low-pressure sides. The high pressure SOFC operates at 7atm, and the lower at 3atm for a fuel cell exhaust temperature of 850°C. This configuration shows the lowest emission levels, and the best fuel economy due to the low pressure SOFC operating at a low current density.

Rao compares the thermal efficiencies, exergy destruction, and specific power produced by analytical models for three pressurized tubular SOFC hybrid configurations: an intercooled preheated SOFC recuperated gas turbine cycle, a single SOFC humid air

turbine HAT cycle, and a dual SOFC-HAT cycle that incorporates a second low pressure SOFC (Rao et al. 2003). Exergy calculations are meant to define the thermal efficiency of each cycle, since Carnot efficiencies are not suitable for power cycles incorporating electrochemical reactions. The three configurations are shown below.

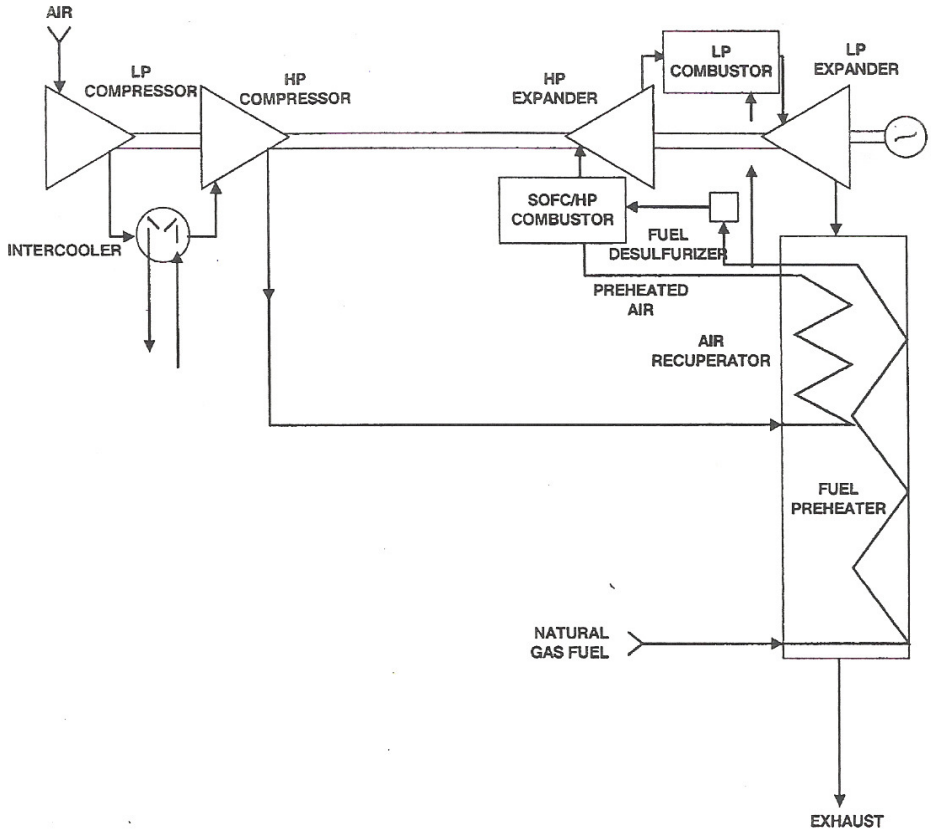

Figure.2.10. Base Cycle Configuration [Rao]

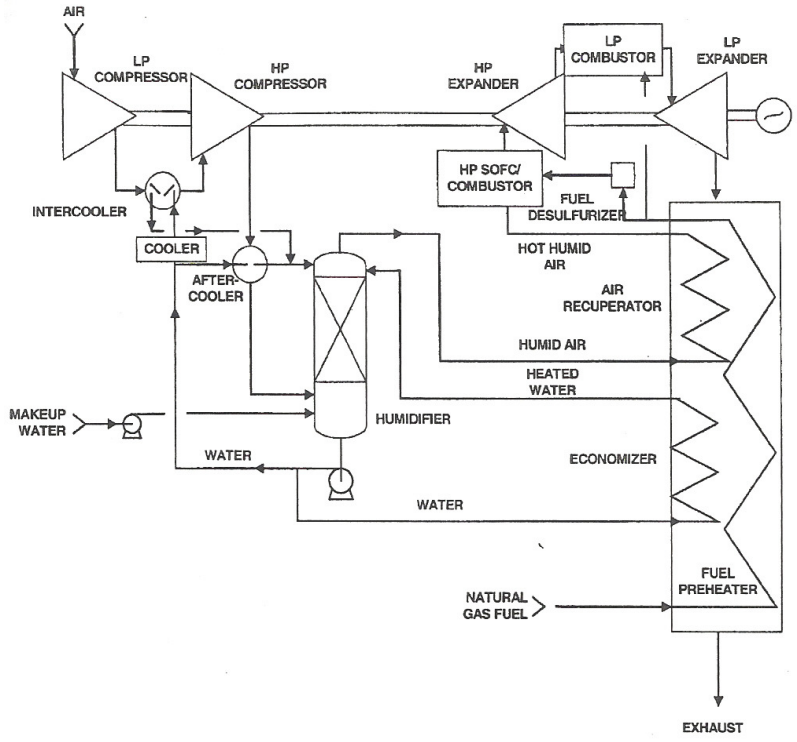

Figure.2.11. Single SOFC-HAT Cycle [Rao]

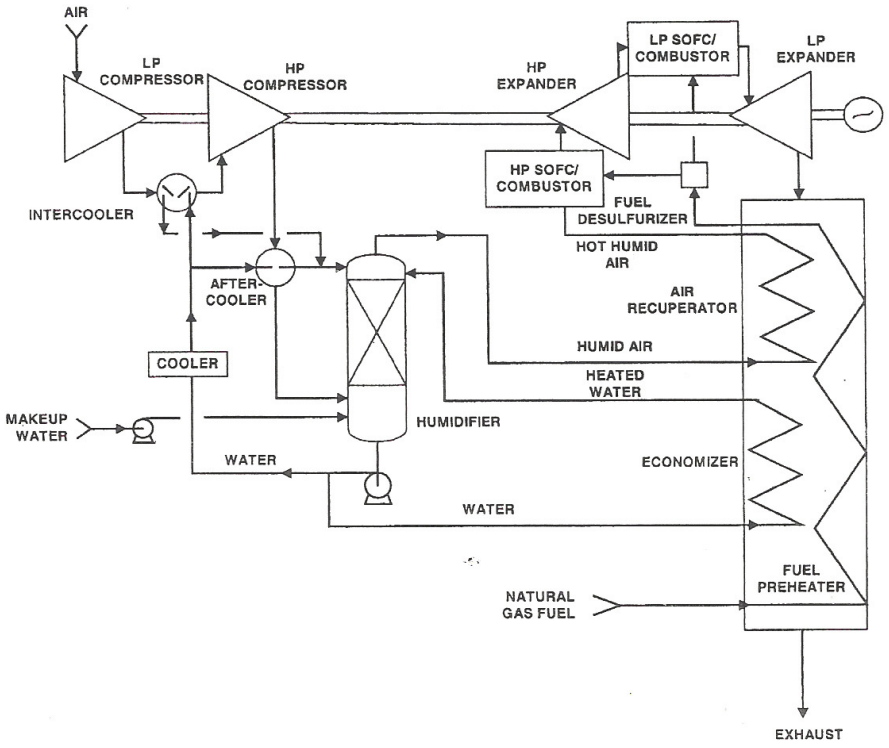

Figure.2.12. Dual SOFC-HAT cycle [Rao]

The intercooled preheated cycle efficiency i.e. that of the base case, is found to be weakly related to the pressure ratio PR. This is due to the increase in the low-pressure turbine exhaust temperature, which in turn increases the preheated air entering the fuel cell stack. Irreversibilities in the LP combustor are reduced with a lower PR, and the exergy loss by the intercooler is also reduced as PR goes down, because less heat is being rejected. The second configuration generates steam through a humidifier that is in direct contact with the pressurized system air, in the single HAT cycle. Compressed air is humidified prior to being reheated in the recuperator before reaching the fuel cell stack. Heat for hot water is recovered from the intercooler and low-pressure expander rejected energy, reducing exergy destruction during the heat transfer. The downside to this is that the partial pressure of O_2 is reduced in the cathode stream, increasing activation and concentration losses in the cell. However, the cycle allows for an increase in the PR, offsetting the oxygen partial pressure reduction. Based on the LHV of the fuel, the highest efficiency for this cycle is 69.05% at a PR of 15. The SOFC-HAT system has less exergy destruction than the base case, but the fuel consumption per unit of inlet air is higher because of the high water vapor concentration in the combustion air.

In the dual SOFC-HAT configuration, a low-pressure combustor and fuel cell are added between the HP and LP expanders, resulting in an efficiency of 75.98% at a PR of 15. Due to an increase in the concentration of water vapor and CO_2, the current density in the lower operating pressure cell for this cycle is lower than the previous two cycles. Rao concludes that by adding another SOFC in the dual HAT cycle, the specific power, defined as the net power cycle output per unit air entering the system, is more than doubled from that of the base case, with no humidification.

Diverting flow from the cathode side of the fuel cell has been a control strategy aimed at managing thermal transients of a hybrid SOFC gas turbine assembly (Tucker et al. 2005). With the use of the three main bypass valves of the recuperated cycle configuration, shown in Fig.2.13, the effect of bypass flow is studied in terms of system efficiency and performance. Tucker demonstrates that among the three valves, the CA bypass valve is

the most effective in increasing the stall/surge margin by providing a decrease in system pressure drop. The data correspond to the assumption that fuel cell operation remains constant, despite changes in cathode airflow. This valve has also proven to divert cathode airflow by almost 50% with a slight penalty on system efficiency.

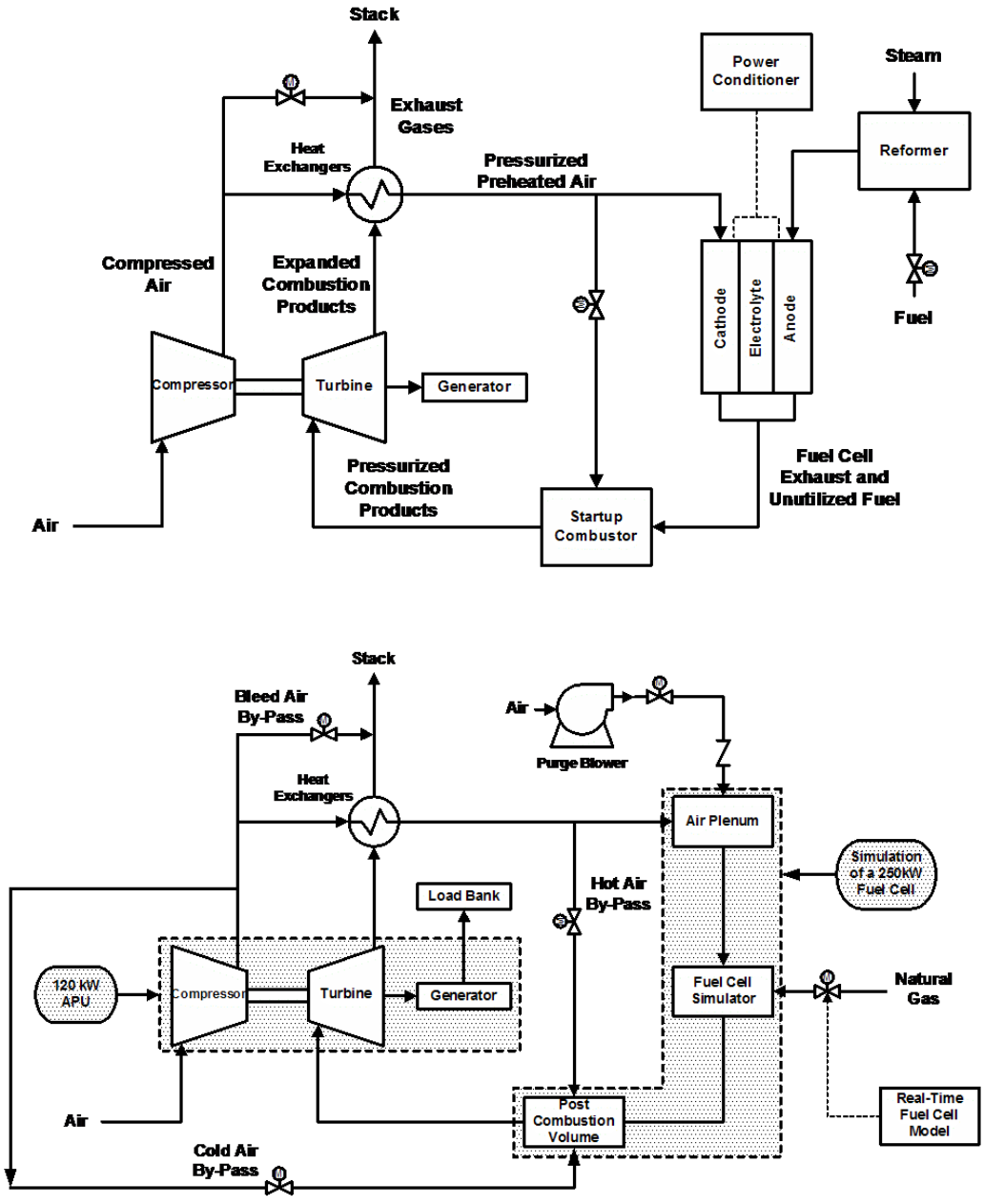

Figure.2.13. Above: Recuperated SOFC Hybrid Cycle. Below: Hardware Simulation

In contrast with the CA bypass valve, the bleed air BA valve has shown to be very effective in absorbing thermal transients. When the BA was used over its full range of operation, there was a 40% increase in fuel flow utilization. This means that the valve can be used as a sink to counteract the effect of load loss in a fuel cell. The hypothesis is that whenever there is a sudden fuel cell load loss, un-utilized amounts of fuel passes the cell, only to be combusted prior to reaching the turbine. This rise in wasted energy causes an increase in shaft speed to the turbine that would in turn increase airflow to the cathode side. An increase in cathode flow would overcool the fuel cell ceramic material, thus creating thermal stresses and possible cell destruction. The BA thus allows for management of a substantial increase in energy, while contributing also to an increased stall/surge margin by increasing compressor inlet flow and reducing compressor discharge pressure. This stall margin is however largely restricted by the exhaust gas temperature or EGT limit. Thus through hardware simulation, operational constraints and control capabilities for the HyPer bypass configuration were set as a means of control and performance.

Tucker's work on valve characterization extends to cases where there is turbine loading in coal based fuel cell models (Tucker et al. 2006c). Thermal management for this hybrid configuration was achieved solely through the use of bypass valves, allowing for uninterrupted synchronous operation of the turbine's generator. This approach benefits large-scale coal based plants in stationary power generation, where variable generator loads are not used to manipulate shaft speed, and hence cathode airflow. In Tucker's tests, compressor bleed air, cold air, and hot air bypass valves were varied over their operating range to examine their effect in system efficiency, pressure loss, turbine inlet temperature, cathode inlet pressure, and cathode inlet mass flow rate, while the turbine was loaded to 45kW. Results show that bleed air (BA) has a negligible effect on cathode inlet flow, increases the compressor discharge pressure, has no effect on system pressure drop, adds an additional load to the turbine shaft, and can be used to absorb thermal transients as well as to increase stall margins.

Hot air (HA) on the other hand was observed to effectively decrease the cathode inlet airflow by close to 50%. It can also lower system pressure drop by 10%, has the least cost in terms of required fuel per bypass compressor flow, decreases the cathode inlet temperature, has no change in the TIT for a constant fuel cell effluent, and has no effect on compressor inlet flow. The HA bypass valve is thus useful mostly for cathode air flow management.

The cold air (CA) valve was shown to be the most influential in altering the cathode airflow, increasing cathode pressure, decreasing cathode temperature, decreasing TIT, and increasing the compressor surge margin. This valve can also be used to manage thermal transients due to the high-energy utilization at wide valve openings.

Hardware-Based simulation has been successfully implemented in the HyPer facility, and is the subject of study in Smith's work (Smith et al. 2006). In the hardware-in-the-loop simulation, electrical load transients are induced in the fuel cell model in order to analyze the hybrid system's response to the heat effluence of the SOFC under the natural gas configuration. The model comprises 1500 planar fuel cell stacks connected in series, which generate 350kW of electrical power. The stack's power rating was chosen to match the thermal input required by the turbine at a 45kW electrical load set point. As in similar tests conducted in the HyPer facility, parallel loop bypass valves are used to manage flow into the cathode fuel cell side. To simulate the transients, a 5% fuel cell current increment was first applied, followed by a 5% current shed. Results show that for the current drop, the fuel cell voltage increased at first causing a thermal effluent rise due to the lower percent of fuel utilization. This caused an increase in the TIT, as well as the turbine speed, increasing hence the mass flow rate. After the transient, the fuel cell began to cool down relative to the lower current demand, and lower heat effluence. It is noted that the opposite occurs when the current demand is increased for the 5% case.

The effect of ambient pressure on system performance was also studied at the NETL facilities. Tucker presents a study of how compressor inlet pressure affects system pressure drops, flows and temperatures via the introduction of concentric orifice plates

(Tucker et al. 2006b). These plates restricted the inlet of the compressor in order to simulate changes in ambient pressures. Testing demonstrated that system pressures varied linearly with changes in inlet pressure, while temperatures had a nonlinear dependency. The pressure ratio is unaffected by changes in ambient pressure, but the reduction in airflow due to the orifice plate obstruction reduces the stall margin with increasing ambient pressure. Discrepancies between actual and derived values are attributed to model assumptions, such as constant turbine backpressure and compressor map error.

In his work, Lundberg studied the performance and cost of a high efficiency 20MWe SOFC hybrid power system that utilizes an advanced turbine system, operating at a pressure ratio of 9.5:1 (Lundberg et al. 2003). The proposed system configuration is a recuperated cycle similar to the 220kWe hybrid first built by Siemens-Westinghouse. In Lundberg's design, the Mercury 50 single shaft turbine supplies pressurized preheated air to four fuel cell generator modules, each comprising 20 sub-stacks of 576 tubular SOFC. The operating nominal conditions for the hybrid require a combustor exit temperature of 1150°C, and a SOFC exhaust temperature of 870°C. In order to optimize the system in terms of the cost of electricity (COE) parameter, the effect of cell sub-stack variation was shown in plots of efficiency and relative cost as a function of net AC power. It was shown that the optimal number of stacks that would balance the COE and efficiency was 72. With this number of stacks, one power block of 4 cell generator modules produces 12.5MWe at 60% efficiency. In designing the turbine, intercooling and recuperation improvements allowed for a range of generated output voltages of 13,800V.

Two bottoming cycles were studied in conjunction with the proposed hybrid configuration. One integrated a heat recovery steam generator and turbine, and the other an ammonia/water absorption power cycle. Results show that adding a bottoming cycle to the proposed hybrid system would increase the efficiency to 64%.

Ferrari studied the influence of anodic side fuel transients on hybrid system performance for a simulated 300kW SOFC plant (Ferrari et al. 2005). The work concentrates on

modeling and validation of a single stage ejector that recycles anode fuel flow for reforming, and on sustaining acceptable steam-to-carbon ratios in the cell stack. Ferrari outlines the critical parameters affecting hybrid operability, mainly: high cell temperature, high pressure difference between cathode and anode sides, low STCR in the reformer, high rotational turbine speed, low surge/stall margin, and excessive temperature gradients in the heat exchangers. The dynamic ejector model is based on 1-D Euler fluid dynamic equations, having adiabatic flow and semi-ideal gas behavior with variable specific heats. The code calculates mass flow rate, momentum, and total enthalpy at the ejector's primary nozzle from isentropic and normal wave equations.

Validation tests with a 0.686m long ejector show that a 10% reduction in the ejector's primary nozzle total pressure with an 85% constant fuel utilization results in the anodic side having 3 different time scale interactions, namely fuel flow time delay, depressurization time delay, and a thermal time delay. The time constants are respectively 1s, 100s, and 300s. Also, it was shown that the differential pressure between anode and cathode sides was within range, that of 20mbar during the transient. A greater fuel variation however can result in greater oscillations exceeding the operational range. The compressor surge/stall the margin is increased because a reduction in the average fuel cell temperature causes an increase of mass flow on the cathode side, and a subsequent decrease in PR. This hybrid system efficiency was found to be 64% for a recirculation mass flow ratio of 7.2, with a primary fuel flow of 0.009kg/s.

The Department of Energy evaluated several different system configurations for thermal management in coal based hybrid plants through numerical simulation (Ford et al. 2006). The steady state analysis was done with the comparison of a lumped parameter model in ASPEN Plus, and a 1-D high fidelity model in which the cell is subdivided, each module having a mass and energy balance calculation. System efficiencies were also compared for natural gas and coal based plants. Ford presents 3 configurations: heat of compression, a cathode recycle, and a recuperation combined cycle. In the heat of compression configuration, the turbo-machinery preheats air to the cathode, and its flow

steadies the temperature difference between the inlet and outlet cathode stream. The cathode recycle configuration comprises two methods for recycling air to the cathode, through a high temperature blower and an ejector that uses compressor discharge flow as the primary recycle flow. In the recuperation cycle, two more methods are analyzed: an upstream combustor to the fuel cell that preheats compressed air, and the addition of fuel to the post combustor firing the turbine. The data showed that heat recuperation is only possible for PR of 10 or greater for a TIT of 1500K.

Calculations of the three configurations give efficiencies of: 57%, 54%, and 64% based on syngas, for heat of compression, cathode ejector recycle, and recuperation upstream preheat systems respectively. The efficiencies based on coal were: 49%, 46%, and 56% for the same methods. This shows that recuperated cycles are the most efficient, by increasing the power contribution of the turbine, and thus the power density of the cell. It is also noted that for coal based systems, thermal management and power generation are more dependent on the turbine's work for the high cathode flows required, as compared to natural gas systems. On the other hand, cathode recycle configurations show promising efficiencies that are harder to control due to flow limitations on blowers and ejectors. As a point in case, the ejector's pressure drop plays a key role in system performance and stability, since there is a decrease in surge/stall margin with increasing pressure differential.

As part of the Department of Energy's FutureGen program aimed at reducing power plant emissions, Samuelsen presents a sensitivity analysis for a coal based zero emission hybrid configuration (Samuelsen et al. 2006). Plant optimization is based on an advanced transport reactor (ATR) for coal, which receives preheated humidified oxygen and gasifies partially dried coal and limestone into a syngas fuel for use in SOFC gas turbine combined cycle. This configuration provides for the removal of CO_2 and the separation of H_2 for anodic recycling. With the use of design of experiments (DOEx), Samuelsen is able to identify the major factors affecting plant performance, in terms of net system efficiency and net SOFC power output. The design factors chosen were SOFC pressure,

voltage, fuel utilization and ATR carbon conversion, while the outputs of interest were net system efficiency, and net SOFC power output.

There are two factor interactions for the SOFC power output response, namely SOFC pressure and voltage. These two factor interactions of pressure and voltage mean that both these parameters combined result in a net power increase, which is greater than their individual power increase contributions. The order of influence on the net system efficiency output was: SOFC pressure, fuel utilization, ATR carbon conversion, and SOFC voltage. Therefore it is concluded that pressure is the most significant factor affecting system performance. In order to increase system efficiency, the original plant configuration was modified to add heat exchangers upstream of the cell stack to preheat cathode inlet air, and to remove the downstream combustor.

2.5 Fuel Cell Models

Wächter has represented a tubular SOFC/GT hybrid system dynamic linear and nonlinear model in state space format for the development of modern control algorithms (Wächter et al. 2006). The nonlinear model has 19 dynamic states, for a system comprised of a compressor, turbine, recuperator, ejector, reformer, and load. This model divides the plant into 6 separate lumped volumes that represent the fluid dynamics, into 17 dynamic states, these being: 6 fluid and 3 solid temperatures, 6 pressures, 1 mass flow, 1 shaft speed, and 2 current densities. The equations for mass, energy, and momentum conservation are described below, and are employed in each of the 6 separate volumes, mainly: compressor-recuperator, cathodic side, ejector-diffusor, reformer, anodic side, and combustion zone with turbine-recuperator volumes.

$$\frac{\partial p}{\partial t} = \frac{\kappa \cdot R \cdot T}{V} \cdot \left[\sum_{in} \dot{m} - \sum_{out} \dot{m} \right] \qquad \text{Eq.2.5.1}$$

$$\frac{\partial \dot{m}}{\partial t} = \frac{1}{L} \cdot \left[\sum_{in} \dot{m} \cdot v - \sum_{out} \dot{m} \cdot v + A \cdot \left(p_{in} - p_{out} \right) \right] \qquad \text{Eq.2.5.2}$$

$$\frac{\partial T}{\partial t} = \frac{R \cdot T}{V \cdot p \cdot c_v} \cdot \left[\sum_{in} \dot{m} \cdot h_T - \sum_{out} \dot{m} \cdot h_T + \dot{Q} \right] \qquad \text{Eq.2.5.3}$$

$$\frac{dn}{dt} = \frac{1}{4 \cdot \pi \cdot n \cdot J} \cdot \left[\sum_{in} P - \sum_{out} P \right] \qquad \text{Eq.2.5.4}$$

$$\frac{dT}{dt} = \frac{1}{c \cdot m} \cdot \left[\sum_{in} \dot{Q} - \sum_{out} \dot{Q} \right] \qquad \text{Eq.2.5.5}$$

The electrochemical reaction rate, gas composition, and the heat and mass flows between volumes are calculated via algebraic equations, whereas current-voltage relationships are modeled thru the use of an electrical network having passive elements, to simulate cell voltage losses and Nernst potentials, as described by Eq.2.5.6.

$$\frac{di_{H_2}}{dt} = \frac{1}{L} \cdot \left[V_{Nerst\_H_2} - \sum V_{losses\_H_2} - \sum V_{losses\_cathode} - V_{Load} \right] \qquad \text{Eq.2.5.6}$$

In order to numerically solve the system of equations, analytical time constants are found for each of the hybrid components. The results are grouped into three categories: system performance in terms of current density, power, cell voltage, and efficiency, gas turbine behavior as shown for mass flow, pressure, power, and TIT, and lastly additional parameters such as STCR, electrolyte pressure differential, FU ratio, and ejector mass flow. For the system performance criteria, all the outputs showed a strong dependency on current. This same trend is seen for the efficiency.

Linearization of the model for state space representation in the Simulink platform required the inclusion of time delays in order to avoid algebraic loops. State space matrices were obtained for each individual subsystem, from a Simulink command having 3 inputs and 78 outputs. The final matrix had 18 states with the exclusion of a variable shaft speed parameter. Simulations were performed for disturbances of 0.1% and 0.5% from nominal operating values, and these showed a discrepancy between the response of the linear and nonlinear models. Wächter attributes this difference to linearization errors, the time delay inclusions, and the lack of accuracy from the ever-changing numerical convergence that is dependent on the perturbation form and magnitude. The linear model however, decreases computational time from 21 hours to less than two minutes.

The experimental facilities of the HyPer project were modeled by Shelton for the purposes of aiding in the design of test plans, understanding system dynamics, and as a prelude to testing a control algorithm for future hardware implementation (Shelton et al.

2005). The model is a lumped parameter model done in the Simulink platform that only simulates the hardware facility, without the fuel cell electrochemistry. In order to validate the model, two test runs were conducted, one for a resistive load shed and another for a speed set point change. The model follows previous modeling logistics that incorporate the couplings between flow and pressure calculation modules. These modules account for the plenum vessel, post combustor, combustor, heat exchangers, compressor, turbine, and generator. The model is aided by empirical data, such as the use of compressor and turbine maps, measured friction factors, and experimental turbine inertia parameters.

The results show that the model accurately tracks system oscillations for each of the two perturbations, but fails to match maximum magnitude values for speed and fuel. Shelton explains that this is due to the model under-prediction of the required fuel, stemming from a possible sensor error in the airflow measurement.

The lumped parameter model incorporates look-up tables and empirical curve fitting for the compressor and turbine that pose simulation difficulties. Because of the iterative nature of the look-up table, and the closeness of data in compressor and turbine maps, the model is only able to run at half the nominal speed of 40,500rpm i.e. 20,000rpm. It is thus desirable to develop a model that can simulate startup tests, in order to fully replicate a hybrid's system dynamics from startup to shutdown.

The dynamic bulk model of a pressurized SOFC was also incorporated and tested in the HyPer facility at NETL, by Smith (2006). The model was intended to run in real-time, and its performance was to be compared to a previous 1-D model of the fuel cell electrochemistry. For this and the previous 1-D model, the hardware measured states received as inputs to the model were the flow, temperature and pressure of the inlet to the air plenum, as described in the HyPer configuration, since this is the plenum that represents the fuel cell stack volume. The model receives hypothetical input values of current flow demand, fuel flow utilization, and anode recycle percentage. Because this is a model based on natural gas, there is an inclusion of an external reformer that recycles

exhaust cathode air to reform methane into H_2 and CO. The exiting gases from the cathode and un-utilized fuel from the anode side are then oxidized together in a combustor prior to reaching the turbine inlet. Present models tested on the HyPer facility have no reformers since they are based on coal syngas fuel. This model, as with the coal syngas based model, predicts the heat effluence of the fuel cell as a function of cathode inlet flow and temperature. Smith's model calculates Nernrst voltage and overpotentials, disregarding the dynamic effects on temperature inside the cell stack. Because this model is directly coupled to the turbine, the effect of pressure is of the most importance.

For the test, the methane flow and current density were adjusted until 80% fuel utilization and 0.7V were reached for the atmospheric case. Once these values were reached, the pressure was increased to 360kPaa, simulating the hardware's system pressure. In comparison to the 1-D model, this bulk model showed that the cathode exit temperature was affected at a higher degree. The model also demonstrated to work well in controlling turbine speed as a function of fuel cell heat exhaust for the three transient cases under study: cathode airflow increase, inlet cathode temperature increase, and load current demand decrease.

2.6 Control Strategies and Designed Controllers

Rancruel's work concentrates on studying the effect of different control strategies on the transient behavior of hybrid systems for startups and shutdowns (Rancruel et al. 2004). This 5kW net power SOFC based APU configuration comprises a fuel reformer, a fuel cell stack having air, water and thermal management, power electronics, power conditioning, and energy buffering mechanisms for electricity, fuel, and air. Energy buffering by means of auxiliary fuel and air tanks is intended to aid the BOP control outputs during transient disturbances, as an alternative to delayed load following, which would allow sufficient BOP recovery times. Rancruel examines fuel consumption and startup response times for two startup approaches: one with steam re-circulation and system component preheating, and the other without.

The control variables are the steam-to-methane ratio (STMR), fuel utilization (FU), air-to-fuel ratio (AFR), and fuel reformate ratio (FRR). The STMR controls the chemical reaction within the steam reformer, while the FU affects the heat and work recovery as well as the fuel cell reaction rates. The AFR is related to the parasitic power requirements, mass flow and temperature of combustion gases, and the FRR controls the exhaust temperature of the methane reformer. The multi level control approach consists of a controller aiming at keeping the air and fuel tank pressures fixed under transient conditions, an actuator valve that regulates cathode and anode flow from the respective pressure tanks, and a battery activated by fuel cell current demand rate of change. RGA analysis pairs the corresponding inputs and outputs in this multiple model based PID controller. Open loop tests show that the reformer thermal response is heavily dependent on the fuel utilization, having the fastest response to a power increase. Rancruel concludes that as the fuel utilization increases, so does the internal losses in the fuel cell stack, and thus the fuel reformer is the most critical component of the BOP.

Traverso present an analytical model of a 300kW SOFC hybrid system whose configuration includes the use of recuperated heat, and anode recycle via the use of a single stage ejector, in the Simulink/MatLab platform (Traverso et al. 2005). All modeled components use the lump volume technique, with fluid dynamic delays, and they all take into account heat exchange and variations in the chemical composition of the fuel. The system is set to distribute net hybrid power demand to the fuel cell stack and the micro turbine with the use of multiple parallel PID controllers. The bypass of a fractional flow valve that redirects compressed air to regulate fuel cell temperature, accomplishes the distribution of power demand and speed control. PID controllers tuned at different response rates in separate loops determine the fuel cell current, anode side recycle flow, turbine speed, and power distribution values between fuel cell stack and turbine. The simulation aims at controlling the critical parameters of excessive stack temperature gradient, low steam-to-carbon ratio in the reformer and the cell, stack and heat exchanger thermal stress, micro turbine rotational speed, pressure differential between anode and cathode sides, and surge/stall margin, all within operational constraints.

The simulation results show that there are initial difficulties in achieving stability due to the large discrepancies between system time constants i.e. that of the fast turbine, in contrast with the slow cell thermal response. Overall, the 10% power decrease did not cause the aforementioned critical parameters to exceed operational limits during the transient. For the power decrease, turbine rotational speed momentarily increased, to steady out at the lower value of 64krpm. Initial fuel cell temperature decreases after the transient, but steadies out to the design point of 1230K. The surge/stall margin was actually increased and there is also an increase in net power distribution to the cell. After the transient, the net plant efficiency, which is primarily determined by the cell temperature, settles to 63%. This same control scheme was implemented in a MCFC hybrid.

Mueller describes the design of a centralized linear quadratic regulator (LQR) with state estimation for a 250kW bottoming SOFC indirectly heated gas turbine hybrid cycle (Mueller et al. 2006). The control objective is to maintain a set point power output, fuel cell temperature, and fuel utilization target under ambient temperature and fuel composition variations, for 40°C fluctuations, and 5% reduction in the methane mole fraction. This controller scheme is then compared to the performance of a previously designed decentralized controller derived from a nonlinear dynamic model. The LQR approach stems from a Relative Gain Array RGA analysis that shows strong coupling between independent control loops for time scales greater than one second. This fact limits the performance of cascaded decentralized controllers that make use of one feedback signal at a time, and fail to incorporate the interaction and effects between states. The linear quadratic guassian (LQG) uses all the multiple input/output signals for disturbance rejection by first linearizing the model, reducing the model's order, designing the optimal state feedback, estimating the states via the use of a Kalman filter, and introducing an integral power feedback based on fuel cell current demand. The linearized model sustains 70 states, for which model reduction improves to a minimal realization of 58, once the uncontrollable and unobservable states are removed. Further reduction

based on the magnitude of the Hankel singular values of each state, results in a total of 27 states, the remaining having singular values greater than $1x10^{-3}$.

The LQR integrated system response showed that neither the combustor temperature nor the fuel cell temperature were adequately controlled by the estimated states. Mueller attributes this to the fuel mole fraction disturbance not being utilized in the estimation. Power could be controlled to zero steady state error, with the use of the integral feedback action. However, when the LQR was tested in the nonlinear model, the controller exhibited a slow response, in spite of the fact that it was able to reject a 20% reduction in fuel composition, and a 40°C ambient variation with minor offsets.

Control simulations of other types of fuel cell hybrid systems have also given insight into the cathode side dynamic issues that are similarly encountered in SOFC systems (Pukrushpan et al. 2004). As an example, Pukrushpan suggests a control methodology for a proton exchange membrane PEM fuel cell hybrid system that takes into account fuel cell voltage and partial reactant pressure of the cathode side as the feedback signals. In contrast with the SOFC, PEM fuel cells operate at a much lower temperature of 50-100°C, enabling fast starts while maintaining a high power density of $0.6W/cm^2$. According to Pukrushpan, airflow, pressure regulation, heat transfer, and water management all limit fuel cell power. It is thus necessary to manage cathode side airflow in order to regulate the critical excess oxygen ratio λ, and the partial pressure of the reactants. It is this lumped parameter value λ, that is the measure in which the airflow controller prevents oxygen starvation, as opposed to the immediate fuel cell shutdown by the removal of current demand.

In his work, Pukrushpan concludes that in order to overcome the trade-off of increasing power, by decreasing compressor voltage to decrease parasitic losses, and therefore affecting λ, it is necessary to filter the current drawn from the stack, use an additional energy source for the compressor, and have available oxygen that would fire upon recognition of a transient event.

Another proposed multi loop control methodology for a SOFC/GT hybrid configuration similar to the 220kW Siemens-Westinghouse system is given by the Norwegian University of Science and Technology (Stiller et al. 2005). PI and PID decentralized control loops of various time scales regulate SOFC power, fuel utilization, airflow, and temperature, using fuel cell current, fuel flow, and generator power as the manipulated variables. This control strategy allows the turbine's shaft speed to vary, resulting in greater degrees of freedom for regulating air and fuel utilization to the fuel cell. In this work, Stiller uses inferential control in an analytical model to maintain fuel cell inlet temperature, by readjusting cathode airflow set-points from measurements of fuel cell exhaust temperature. The result is a stable plant under a strict linear region of operation. In particular, this configuration is very sensitive to fuel flow overestimation, and thus not robust to degradation or malfunction of fuel flow measurement equipment.

The modeling of an industrial twin shaft gas turbine in state space format has been recently presented for a 11.2MW turbine. Weibel shows how the linearization of a 15^{th} order nonlinear model composed mainly of time delays allows for the design of modern state space controllers (Weibel et al. 2005). The time delays for the most part, represent the heat transfer dynamics within the turbine system. According to Weibel, it is possible to obtain satisfactory results in the speed control of the shaft turbine for load sheds of 2MW in magnitude. The paper combines three algorithms combined with the derived state space plant matrices: a pole placement, an optimal linear quadratic regulator, and a PI pole placement controller.

The MIMO system is reduced to a SISO system in its present version. Huge setbacks are attributed to the large magnitude difference between elements in the system matrix A. These differences gave way to simulation problems in the numerical solution of these.

Of the three controllers, the extended PI pole placement algorithm gave the best results. On the other hand, the objectives imposed on the optimal controller of being fast acting, non-oscillating, and energy minimizing on the control effort, were not satisfactorily met.

The paper thus however, shows that gas turbines can, with the proper set of constraints and assumptions, be controlled via the use of modern state space algorithms.

System performance of a decentralized control scheme combined with an input/output decoupling strategy has been tested on a MIMO system comprising an axle automotive durability test rig. Vaes argues that modeling of multivariate systems is prone to inaccuracies due to the coupling complexities between signals, and that the resulting controllers suffer in performance because of the tuning difficulties encountered in MIMO systems (Vaes et al. 2004). The work thus focuses on deriving a decoupled transformation of the plant in which a number of independent control loops can be designed using SISO H_∞ robust techniques from the diagonal components of the new transformed plant matrices.

Tests on the rig show that the strategy is able to guarantee robustness for all frequencies. One caveat however, is that the scheme is only applicable to square MIMO systems having a certain degree of symmetry. Also, the decoupling strongly depends on the choice of frequencies, if the system is not dyadic. Decentralized controllers that are decoupled in this manner can share the same sensitivity and complementary sensitivity singular values, and lack robustness, whereas robust decentralized controllers can violate the performance bounds and still be robust. This ambiguity, together with the absence of a generalized approach for the decoupling of unsymmetrical system matrices, makes the scheme impractical for varying hybrid configurations. The paper also acknowledges that it is current industry practice to implement high performance MIMO controllers that reduce the number of numerical iterations. It is thus not viable to use a decentralized control scheme on a hybrid application, because of the unsymmetrical nature of the system matrices, and the high degree of coupling between states.

Iwasaki developed a state space controller that meets multiple frequency domain specifications for semi-infinite frequency ranges without the introduction of weighting matrices (Iwasaki et al. 2004). For the most part, weighting matrices are introduced as adaptors to the robust algorithm in order to fit the small sensitivity at low frequencies and

the control roll-off at high frequencies requirements into the control law. The form and order of these weights can however, increase the complexity of the controller, and the iterative effort to realize them can become tedious and time consuming. The design specifications are met in the frequency domain by the use of transfer function loop shaping techniques, similar to the ones used in H_∞ control. Iwasaki proves the utility of the algorithm via the benchmark cart spring system plant application, where a stabilizing state feedback controller forces the closed loop transfer function frequency response to be within performance bounds.

Model based control has been successfully implemented in combustion rigs for the purpose of stabilizing flame instabilities. Morgans presents the study of how an empirically derived transfer function of a combustion system has greater applicability in designing a controller, than an analytically derived model would have (Morgans et al. 2005). Morgans is able to design three separate controllers and prove their effectiveness by the use of an experimental transfer function measured via the oscillation of a fuel valve input signal. The rig consists of a scaled down version of a combustor setup that represents one of the nine combustor chambers in the Rolls-Royce RB211-DLE industrial gas turbine. Among the controllers derived are a Nyquist designed phase-lag compensator, a notch filter, and an H_∞ robust controller. These are compared to a time delay controller that is also derived experimentally. The actuator control signal is that of a fuel valve, whereas the feedback signal of the SISO system is that of a pressure transducer.

For three different equivalence ratios, the controllers, based solely on the empirical plant, show a satisfactory response in the face of the flame instabilities. The system plant is obtained by dividing the Fourier transform of the input valve voltage and output pressure transducer voltage and plotting the frequency response on Bode Plots for a range of 75Hz to 350Hz. The frequency sweep includes the system dynamics seen in the open loop power spectra of the pressure signal. From the Bode Plots for the three different equivalence ratios, the gain spikes were assumed to pertain to second order systems. The transfer function is then derived by hand-fitting mode coefficients into the generic second

order polynomials. Once the empirical TF was obtained, the controllers were designed to stabilize the 200Hz instability. Out of the three, the notch filter demonstrated the greatest capability to reduce noise, be robust, and avoid fuel valve saturation.

This paper aims at proposing a methodology by which any hybrid configuration can achieve a stable appropriate control using solely experimental data. One beneficial consequence to this approach is the avoidance of high fidelity models that are inherently time consuming to develop and computationally difficult to implement. If a robust controller can be designed with an estimated empirical plant via the use of simple tests, then further state space algorithms can be built upon this safety benchmark. Thus the following sections outline a straightforward procedure of deriving the plant dynamics from experimental observations, leading to a dynamic MIMO controller.

3 Method of Analysis

The present chapter discusses the development and subsequent analysis of a multivariate empirical model of the Hybrid Performance facility at NETL, obtained via a set of frequency response tests pertaining to all input signals of the built hybrid configuration. With the use of experimental Bode plots, a set of Transfer Function equations are derived that can in turn result in a state space representation of the system. By the use of singular value decomposition, a multivariable Bode plot can be drawn to show overall MIMO system behavior that accounts for the interaction between all inputs and outputs for the given hybrid configuration.

This approach makes it feasible to outline a methodology for the control implementation of other hybrid configurations having different geometric scales and BOP arrangements. A robust multivariate state space controller is then designed for the empirical plant that meets sensitivity and co-sensitivity frequency domain criteria. The control law is intended to serve as a benchmark that gives both robust stability and performance, by regulating the cathode inlet states in the face of sudden perturbations to the thermal system representing the fuel cell stack.

In addition to the aforementioned empirical Transfer Function Matrix, a nonlinear lumped parameter analytical model of the facility is constructed in parallel to the experimental plant. The model includes balance of plant components, such as heat exchangers, air plenums, and turbo machinery, as well as fuel cell hardware element representations i.e. cathode volume and heat exhaust, with energy, continuity and momentum equations for each element. The model is intended to faithfully describe the entire system, and can be used as a test tool for future control law implementations. In subsequent chapters, the analytical model is validated for disturbances and startup tests, by comparing its response to relevant experimental data.

3.1 Hybrid Performance Facility Description

As described in Chapter 2, the HyPer hardware configuration makes use of a combustor and air plenums to simulate the heat effluence and stack volume of a 300kW solid oxide fuel cell. Heat exchangers recuperate exhaust heat from a turbine to increase the compressed inlet air to the fuel cell stack, closing the loop on an efficient bottoming and recuperated cycle. Figure 3.1 shows the HyPer facility and Figure 3.2 a rendering of the hardware in AutoCAD. Appendix H provides a Process and Instrumentation Diagram detailing piping arrangement, component material, and sensor/actuator specifications. Operation envelope, startup sequence, and bypass valve characterizations of the hybrid system are described by the earlier works of Tucker and Liese (Tucker et al. 2005, 2006b,c).

Figure 3.1 NETL HyPer Facility

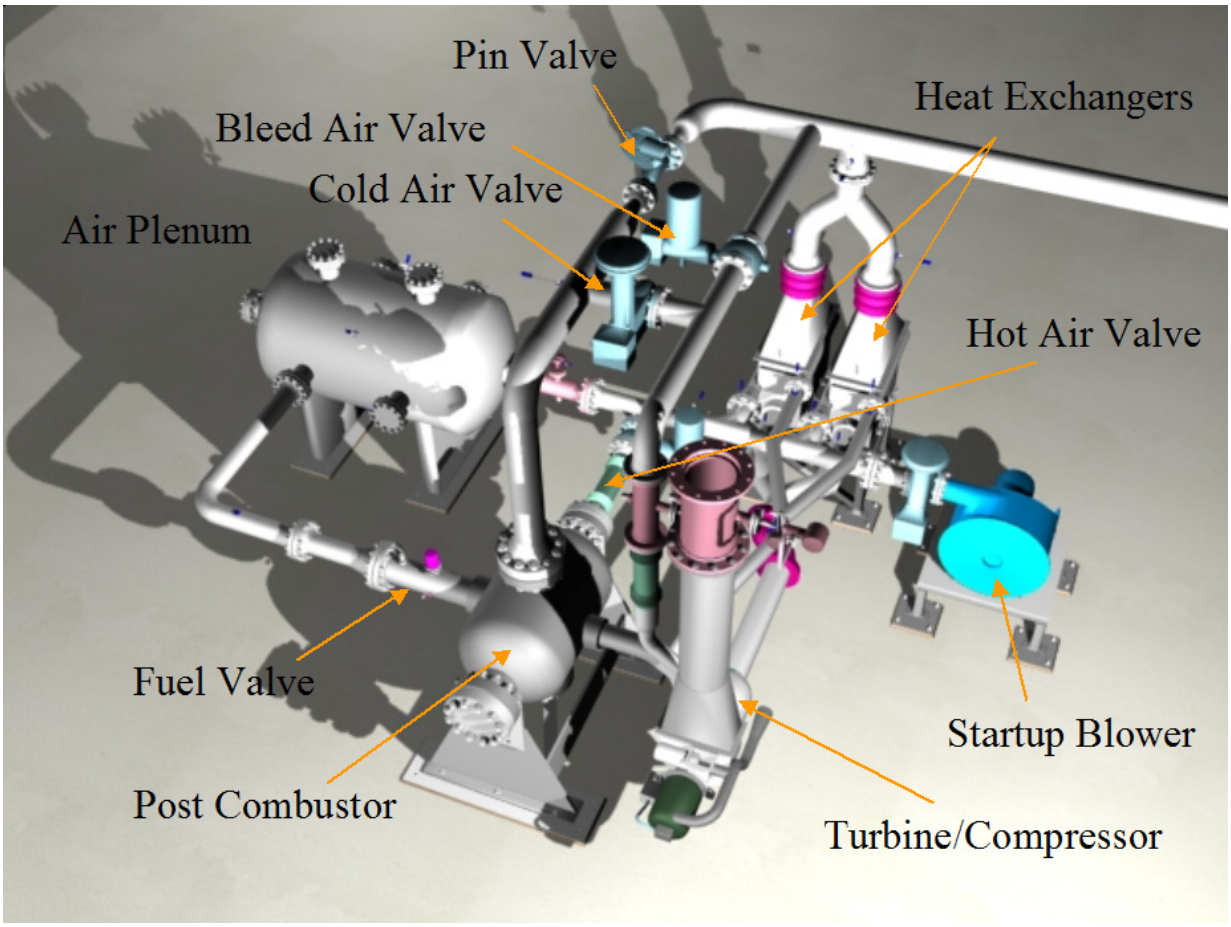

Figure 3.2 AutoCAD Rendering of HyPer Hardware Facility, courtesy of NETL

3.1.1 Auxiliary Power Unit

The gas turbine used in the HyPer configuration is a 120kW Garret Series 85 Auxiliary Power Unit (APU). The single shaft compressor/turbine assembly was designed to produce 400Hz of synchronous power, at a nominal speed of 40,500rpm. The turbine drives a double stage centrifugal compressor, producing approximately 2kg/s of compressed air at a pressure ratio of 4. The turbine is encased inside the compressor scroll. Compressed air exits the scroll around an insert shown in Figure 3.4, where the blue arrows indicate compressor airflow, and the orange arrow high temperature turbine inlet flow. This insert provides concentric cooling flow to the inlet of the turbine. The partially disassembled turbo machinery is shown in Figure 3.3.

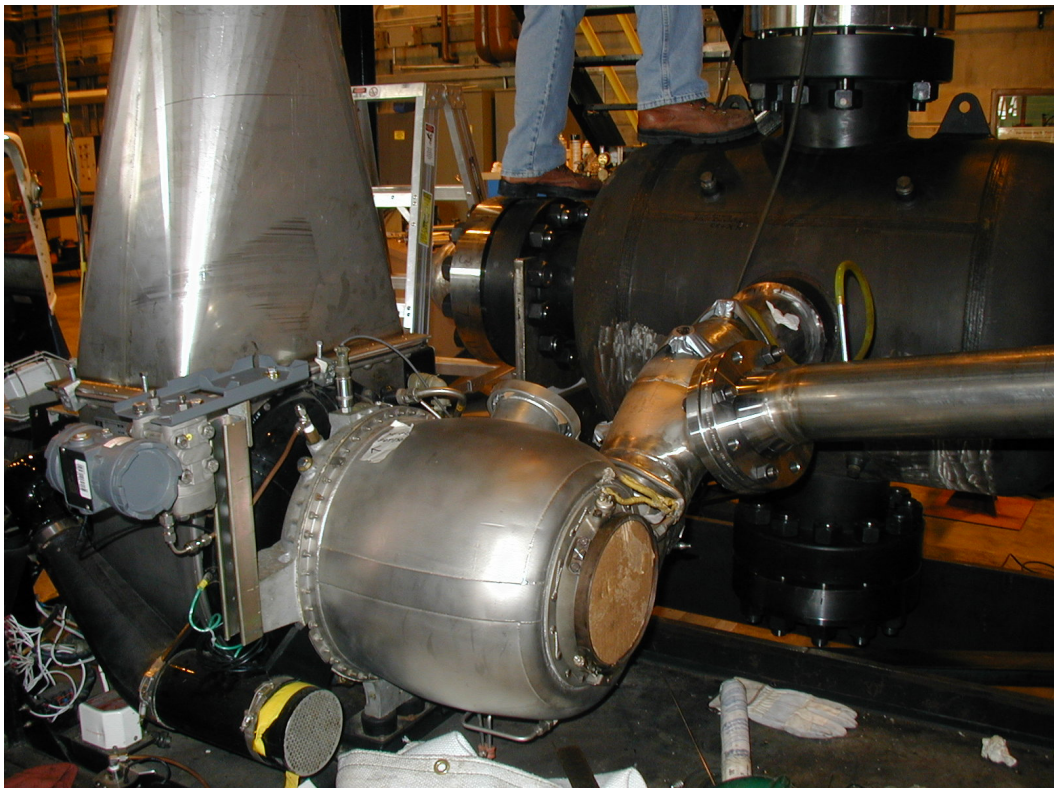

Figure 3.3 Turbine/Compressor Assembly

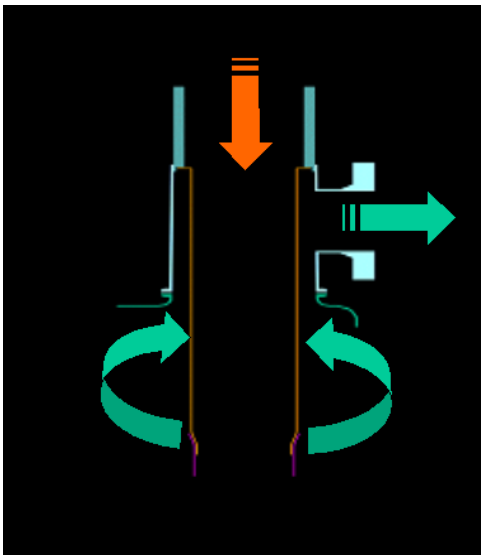

Figure 3.4 AutoCAD Drawing of Turbine Scroll Insert

3.1.2 Primary Surface Recuperators

The hybrid configuration utilizes two parallel counter flow heat exchangers from Solar Turbines. These primary surface recuperators transfer heat from the turbine exhaust to the compressed air preceding the FC cathode. In doing so, the air temperature entering the plenum is increased efficiently, reducing combustor fuel usage. The effectiveness of the recuperation is 89%, with hot side and cold side pressure loss of 3% and 2.5% respectively. The maximum design temperature conditions for cold side and hot side are: 1000F, and 1150F, for a maximum flow of 3.9lb/s, and 4.03lbs/s respectively. Test data for the HyPer facility give an inlet temperature of 395F for the cold side, and an inlet temperature of 1085F for the hot side. An uneven flow has been observed through the heat exchangers, one sustaining 90% of the total flow. Figure 3.5 shows the heat exchanger setup.

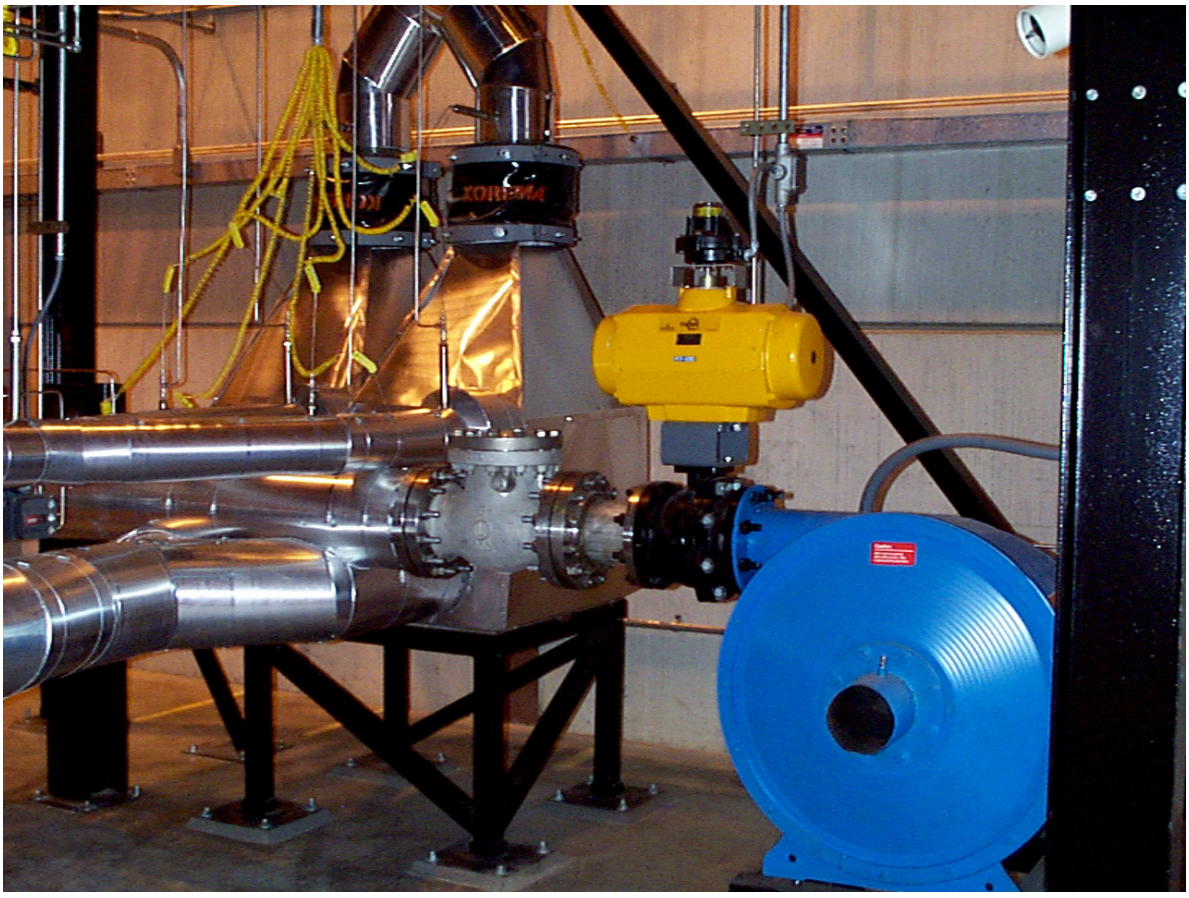

Figure 3.5 Heat Exchangers and Blower

3.1.3 Combustor and Swift Valve

The combustor canister simulates FC thermal effluence and it is located within an Incaloy pipe prior to the entrance of the post combustor plenum PC. The PC plenum serves as a vessel in which to burn unutilized fuel exiting the FC. Figure 3.6 is an AutoCAD rendering of the pierced canister, whose perforations allow for the adequate mixture of air/fuel ratio. A plasma igniter receives regulated fuel flow from a Woodward Industrial Controls Swift valve, fueling the combustion process by burning natural gas. This Swift valve is activated by a fast acting stepper motor, controlled with a PID controller using as feedback turbine speed. The valve comprises a sonic needle and nozzle arrangement.

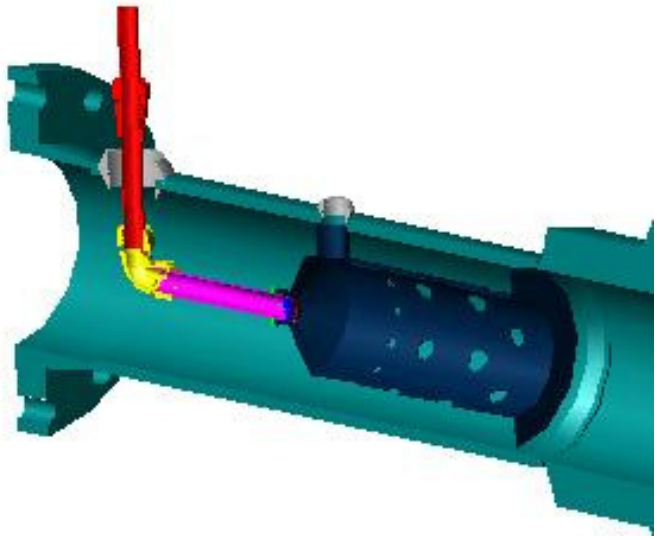

Figure 3.6 AutoCAD Rendering of the Combustor Canister

3.1.4 Air Plenum and Post Combustor

The air plenum is a $2m^3$ vessel that represents a SOFC cathode volume and associated piping manifolds. Its purpose is to simulate the flow impedance a 300kW fuel cell would impart if it were coupled to a hybrid configuration as the one in HyPer. The volume of the module can be increased or decreased with the use of extractable apertures, or by the insertion of metallic floats, to allow for a variety of fuel cell sizes to be tested. The post combustor is a $0.78m^3$ vessel that precedes the turbine/compressor unit. This vessel receives airflow from three possible paths, those of the mainstream, and bypass routes.

The volume thus allows for uniform temperature distribution of the airflows before reaching the turbine. The post combustor is fabricated from 1" Incaloy 800AT, capable of sustaining a design temperature of 1700F. Figure 3.7 and 3.8 show the plenum and post combustor before insulation was placed, and Figure 3.9 an AutoCAD rendering.

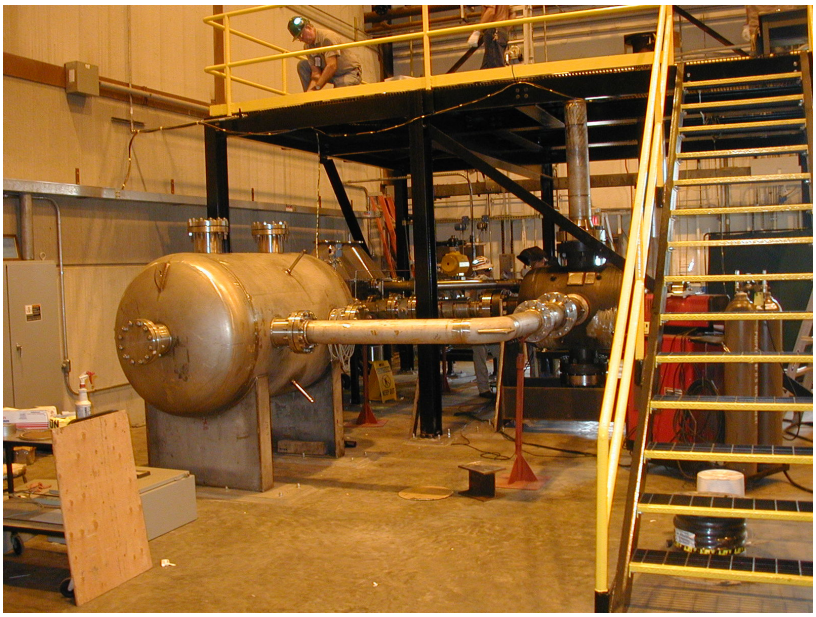

Figure 3.7 FC Cathode Simulator Without Insulation

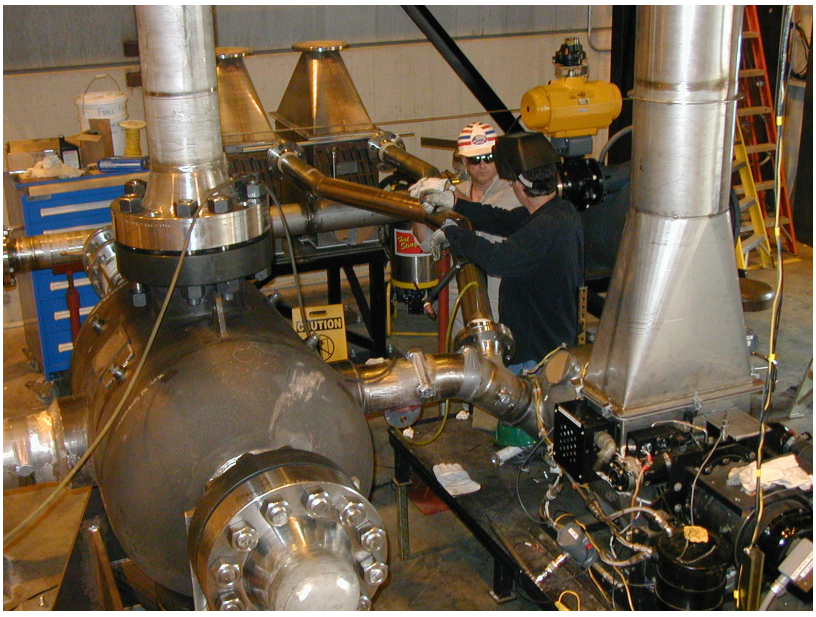

Figure 3.8 Post Combustor Without Insulation

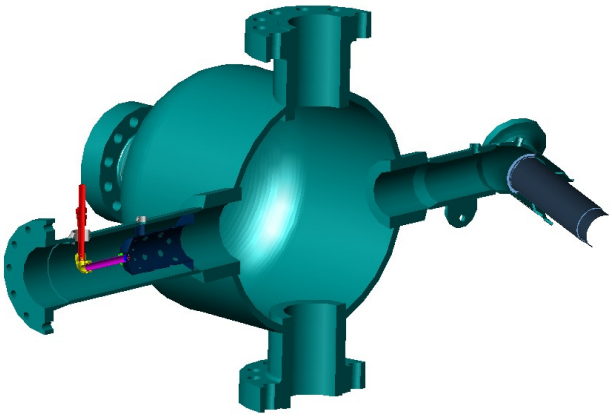

Figure 3.9 AutoCAD Rendering of the Midsection Post Combustor

3.1.5 Bypass Valves

The HyPer hardware configuration controls airflow to the air plenum via the use of bypass valves placed along flow loops parallel to the mainstream flow path. The three main valves, Cold Air CA, Hot Air HA, and Bleed Air BA each have particular attributes that affect system efficiency and performance. As discussed in Chapter 2, thermal management is possible with the use of these valves, when transient disturbances such as those occurring from compressor stall and surge, or sudden fuel cell load fluctuations threaten system stability. With the use of these valves, large system pressure drops are avoided in the mainstream path, which would otherwise lead to decreased stall/surge margin. In this manner airflow can be controlled at the fuel cell inlet. A detailed description of the effect each valve has on the hybrid plant is given by Tucker (2003). Figures 3.10 and 3.11 show the location of these valves, as well as the direction of airflow. All of the bypass valves are characterized according to their frequency response via Bode plots in Chapter 4. The HA and BA valves are Valteck MaxFlow and ShearStream eccentric plug rotary control valves, with full range slew rates of 2s and 1.5s respectively. The CA valve is a Fisher-Rosemont V-Ball with slew rate of 1.5s. All the valves are 15.4cm ID.

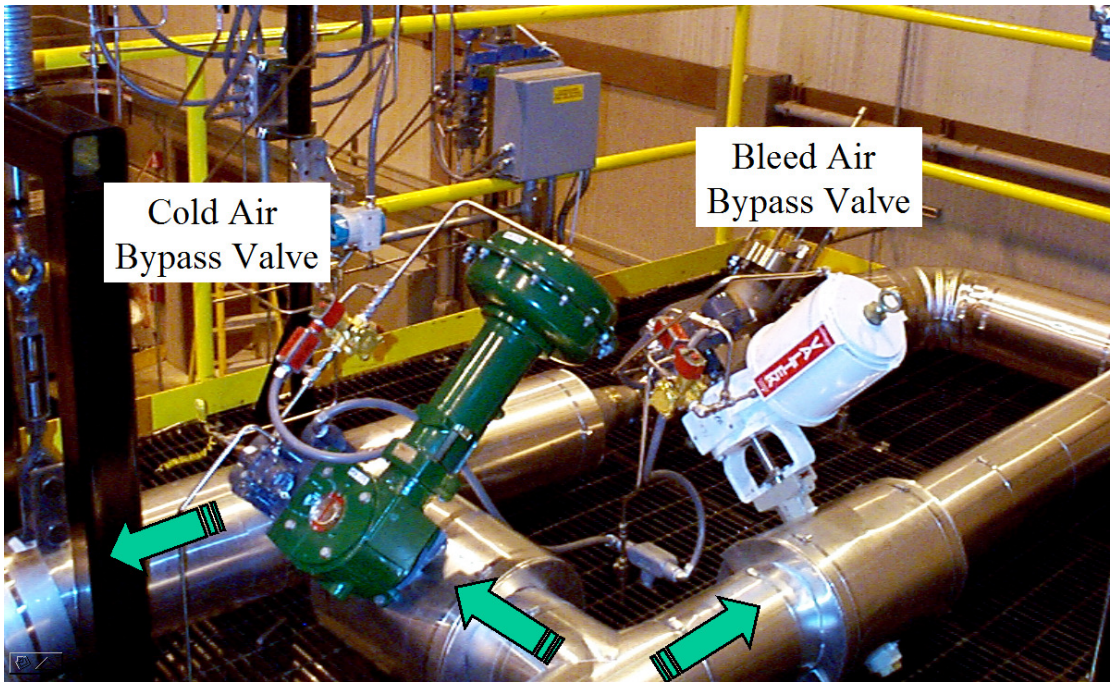

Figure 3.10 Cold Air and Bleed Air Bypass Valves

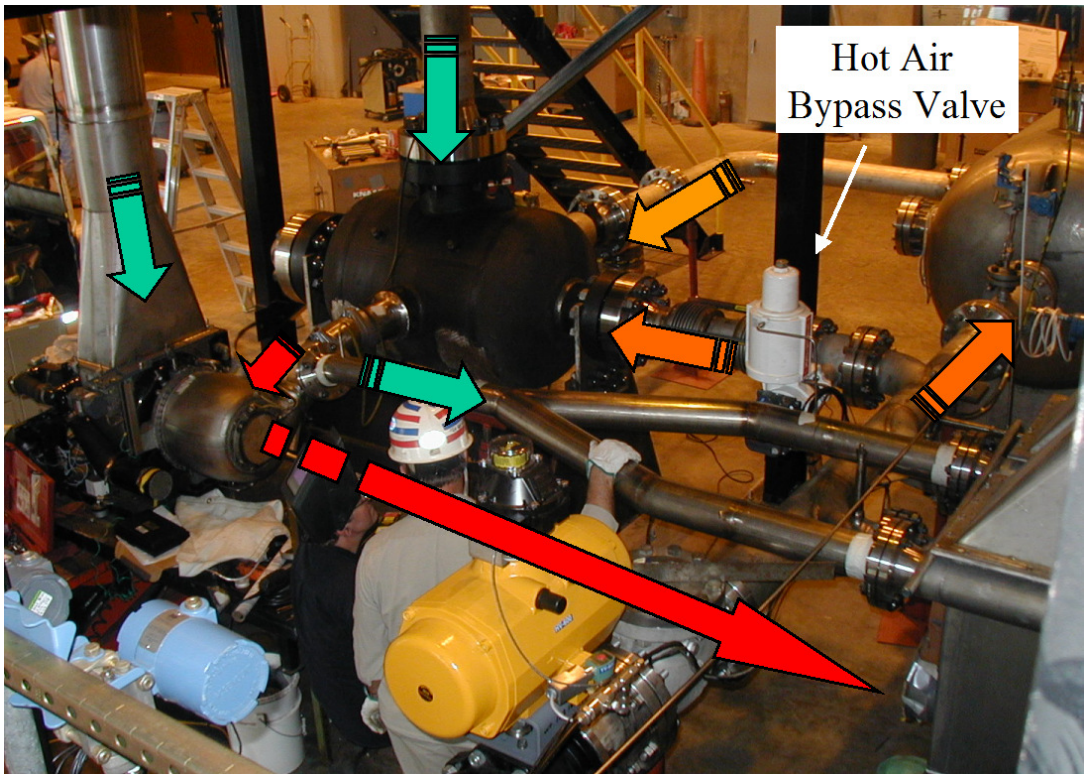

Figure 3.11 Hot Air Bypass Valve and Flow Paths

3.1.6 Instrumentation and Data Acquisition

Monitoring of 104 process variables is accomplished by three separate control systems. The Atlas control system is manufactured by Woodward Controls, and its main task is to control the Swift valve that regulates fuel flow to the combustor. This system can also acquire data at a sampling rate of 80ms. All the subsequent data presented in Chapter 4 is obtained from the Atlas system. The second control system is the APACS, manufactured by Moore Products. Its main objective is to protect the equipment through a series of operational interlocks. The sampling time of the APACS is 400ms. The third control system, QUADLOG, is also manufactured by Moore Products and it serves as the primary safety system by ensuring proper purge times and vent of gases (Tucker et al. 2003).

As stated above, speed control is achieved by the Atlas system, through a PI controller. The turbine speed is measured by an optical sensor placed at the end of the APU generator shaft, receiving a 1200Hz signal at the nominal rotational speed. Type K thermocouples and pressure transducers positioned throughout the piping comprise the bulk of the instrumentation, while annubar flow elements measure airflow. The relative errors and measurement precisions are given in previous works (Tucker et al. 2005).

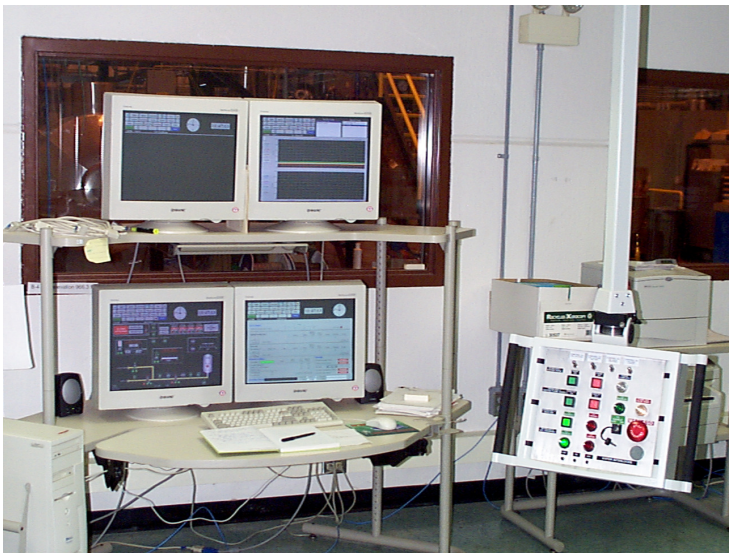

Figure 3.12 HyPer Control Panel

3.2 Experimental Procedure

The hybrid configuration under study manages thermal transients with the use of parallel piping routes having bypass valves, as explained in Chapter 2. There are five system inputs for the HyPer assembly: fuel flow, generator load, and the CA, HA, and BA bypass valves (Tucker et al. 2005). If each of these inputs is perturbed sinusoidally within the linear region of the nominal operating point, frequency response data in the form of magnitude and phase gains can be plotted for a characteristic range of system frequencies. These Bode Plots are used as a system identification tool to determine the Transfer Functions for outputs of interest. The aim of the controller is to maintain a prescribed mass flow at the inlet of the fuel cell within an acceptable window of operation, for disturbances in turbine shaft speed, fuel cell exhaust heat, and turbine generator load. Thus the plant Transfer Functions are derived for these outputs as a function of each of the abovementioned inputs independently.

3.2.1 GAP Programming Sequence

The control platform in use as described in earlier sections is the Graphical Application Programmer GAP, provided by Woodward Industrial Controls. The block oriented programming software can incorporate compiled code from a Simulink/MatLab source file and run it in real time, to the hardware-in-the-loop HyPer arrangement. Figure 3.13 and 3.14 show the command blocks that generate the sinusoids in each of the input channels, based on the Simulink sinusoid signal. Appendix G details the test plan for various tests, and the sequential use of these blocks during test operation.

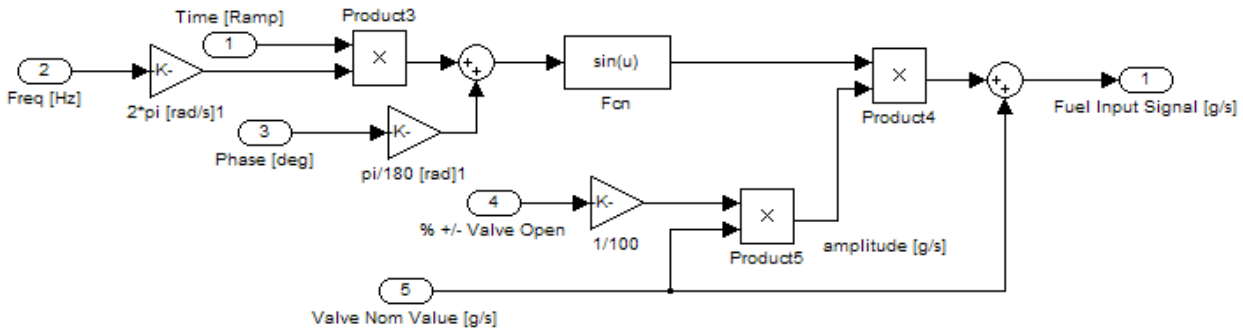

Figure 3.13 Simulink Sinusoid Subsystem

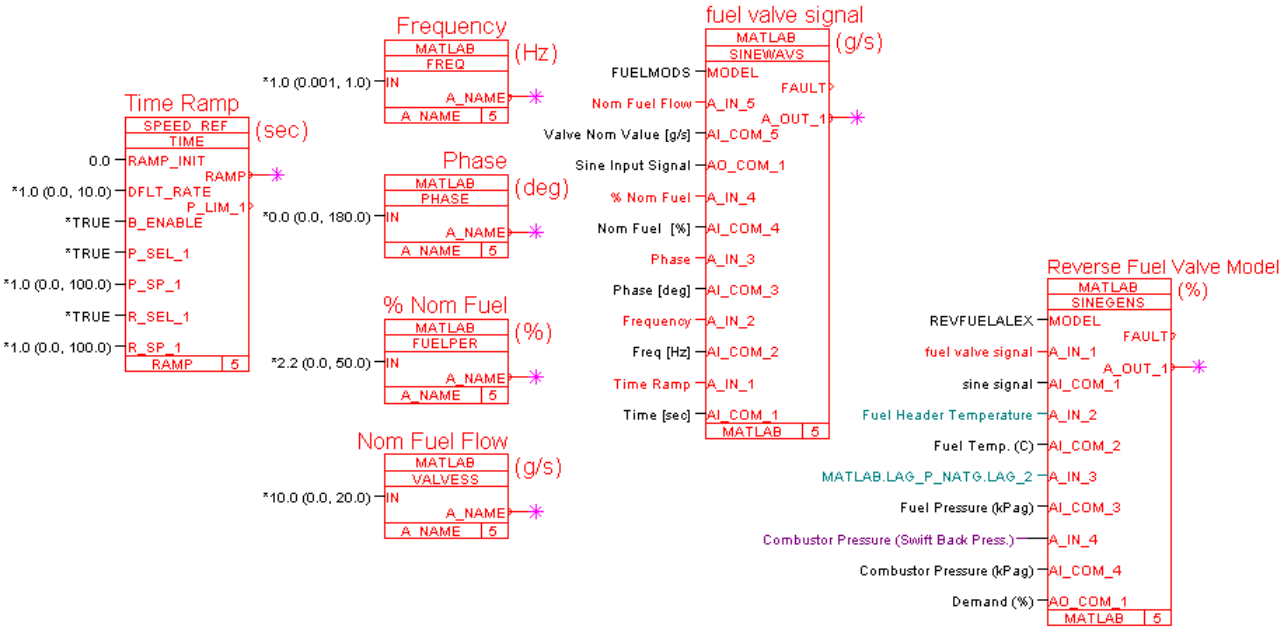

Figure 3.14 GAP MatLab Signal Blocks

3.2.2 Frequency Response Tests

Scoping tests were done to determine the allowable magnitude range of all the actuator inputs before a mechanical limit would hinder operation. The study was done in preparation for the frequency response tests that followed. Each input was fluctuated at given amplitude and frequency, for two separate chosen frequencies, specifically

0.017Hz~60s, and 1.67Hz~0.6s. The nominal value and initial range of fluctuation for the fuel valve, load bank, and BA, HA, CA bypass valves were respectively: 13.5g/s~39%+/-10%, 45kW+/-5kW, 14% +/-4% opened, 40%+/-10% opened, and 40%+/-10% opened. Each magnitude was then slowly increased at 1% steps, until a speed interlock was activated, or the EGT limit was reached. The speed limit interlock is set to avoid speeds below 38,475rpm to prevent circuit burn. For each case, the signal remained at a given frequency for up to 10 periods of oscillation, before the next frequency was tested. It is important to note that each individual input was excited with all the other inputs closed, except for the fuel valve, which remained opened at nominal value corresponding to 40,500rpm.

The purpose of the operational tests was to determine system structure by means of frequency response data. The excitation of each input covered a range of frequencies of three orders in magnitude, starting at 0.001Hz and ending at 1Hz, for a total of 28 frequency points having 10 samples per decade. The signal remained at a given frequency for up to 10 periods of oscillation for the first two decades, before dropping to 5 periods of oscillation for the last decade having the slowest frequency tested. The total test duration for each input was approximately 9.5 hours, including system startup time, system shutdown time, and elapsed time between frequency samples for the states to reach their steady state nominal values. Detailed test plans of the experimental procedure are shown in Appendix G. Appendix J shows the time series frequency response data for three frequencies under study, while Appendix F gives key programming sheets in Woodward's GAP software for turbine control.

3.3 Empirical Transfer Function Matrix

Transfer functions for states at the inlet of the air plenum, and turbo machinery are derived as a function of all system inputs of the HyPer plant. While these are obtained individually, they are tied into a matrix that aims at representing the entire coupled system. The proceeding subsections outline the steps by which the experimental model was generated.

3.3.1 Transfer Function Generation

In order to obtain the magnitude and phase Bode Plots, the input and output signals are transformed to the frequency domain with a FFT algorithm. The output is divided by the input signal, as defined by the Transfer Function relationship. For LTI systems, the output signal of a sinusoidal perturbed system has the same frequency component as the input signal. Hence the input frequency vector can serve as an index to extract the transformed output/input FFT element from the gain vector corresponding to a particular test frequency. This assumption holds valid if the fluctuations remain within the linear region of operation for each actuator. Chapter 4 shows the generated Bode Plot for the air plenum inlet pressure, temperature, and flow as a function of fuel flow fluctuation. The gain is converted to decibels dB, as a function of frequency Hz. The m-file that generates these graphs is included in Appendix E.

Equations 3.3.1-3.3.3 present various ways in which the pole zero rational polynomials can be written in classical Transfer Function format. These equations are derived from the open loop frequency response; in particular the rise and fall of the magnitude plot slopes, according to (Umez-Eronini 1999). On a semi log scale, a rise of 20dB/dec implies a zero in the vicinity of the inflection point, whereas –20dB/dec identifies a pole.

$$G_p(s) = K_{dc}\frac{(s+z_1)(s+z_2)\cdots}{(s+p_1)(s+p_2)\cdots} \qquad \text{Eq.3.3.1}$$

$$G_p(s) = \frac{(s+z_1)}{z_1}\cdot\frac{(s+z_2)}{z_2}\cdots\frac{(s+z_m)}{z_m}\frac{p_1}{(s+p_1)}\cdot\frac{p_2}{(s+p_2)}\cdots\frac{p_n}{(s+p_n)} \qquad \text{Eq.3.3.2}$$

$$G_p(s) = K_c\cdot\frac{p_1p_2\cdots p_n}{z_1z_2\cdots z_m}\cdot\frac{(s+z_1)\cdots(s+z_m)}{(s+p_1)\cdots(s+p_n)} \qquad \text{Eq.3.3.3}$$

Figure 3.14 shows how a particular Transfer Function was approximated from test data with the use of asymptotes at three corner frequencies from the magnitude plot. Note the presence of double zeros and poles with the rise and fall of the magnitude curve at +/-

40dB/dec in the corner frequencies. The Transfer Function of Figure 3.15 follows the format expressed in Eq.3.3.3. Once the corner frequencies and corresponding slope rates are identified in the magnitude plot, the phase plot is examined for nonminimum phase behavior (Franklin et al. 2006).

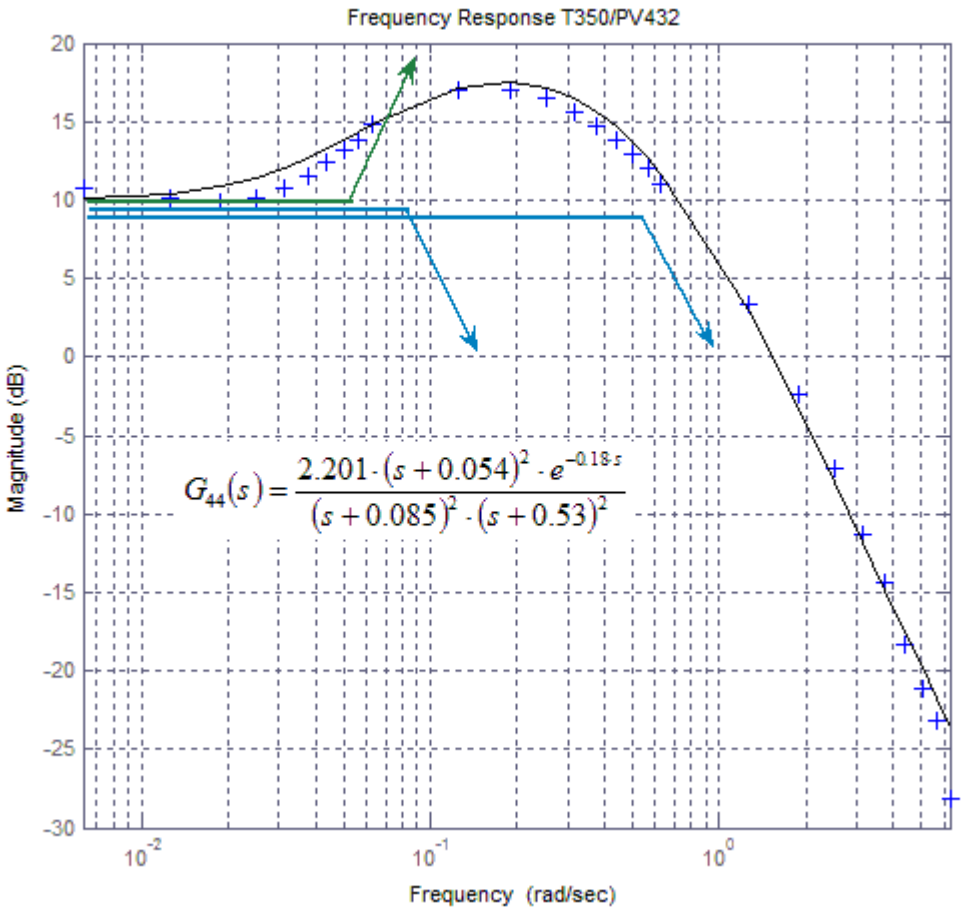

Figure 3.15 Graphical Generation of Transfer Function

For the most part, thermal systems have inherent time delays that perturb the phase plot in a decaying fashion. Pure phase lags can be expressed in Transfer Function format as $G_d(j\omega) = e^{-j\omega \cdot T_d}$, where T_d is the time delay. The phase lag can then be incorporated to the nominal plant as an exponential elevated to an integral or fractional power that is multiplied to the minimum phase Transfer Function as in Eq.3.3.4 (Katsuhiko 2002).

The addition of the exponential only affects the phase plot, as it is seen in Eqs.3.3.5-3.3.6, where the subscripts "non" and "min" stand for non-minimum and minimum Transfer Functions and phase angles. The delay time can then be obtained by reading the measured phase at a particular frequency ω_i as shown in Equation 5.

$$G_{pnon}(s) = G_{p\min} \cdot e^{-s \cdot T_d} \qquad \text{Eq.3.3.4}$$

$$\angle G_{non}(s) = \angle G_{\min}(s) + \angle G_d(s) \qquad \text{Eq.3.3.5}$$

$$T_d = \frac{\pi}{180} \cdot \frac{\phi_{non}(\omega_i) - \phi_{\min}(\omega_i)}{\omega_i} \qquad \text{Eq.3.3.6}$$

Hence from the experimental data, it will be seen that the derived Transfer Functions for mass flow, pressure, and temperature as a function of fuel flow excitation are respectively:

$$G_{11}(s) = 0.024 \cdot \frac{(s+0.021)\cdot(s+0.3)\cdot e^{-1.4\cdot s}}{(s+0.033)\cdot(s+0.061)} \qquad \text{Eq.3.3.7}$$

$$G_{21}(s) = 2.6597 \cdot \frac{(s+0.03)\cdot(s+1)\cdot e^{-0.8\cdot s}}{(s+0.04)\cdot(s+0.1)} \qquad \text{Eq.3.3.8}$$

$$G_{31}(s) = 0.0502 \cdot \frac{(s+0.01)\cdot(s+0.015)\cdot e^{-0.5\cdot s}}{(s+0.04)\cdot(s+0.05)\cdot(s+0.1)\cdot(s+0.15)} \qquad \text{Eq.3.3.9}$$

Chapter 4 shows the resulting plots of Eq.3.3.7-3.3.9 in [rad/s]. Repeating this procedure for all the other controllable inputs results in a MIMO Transfer Function Matrix for the measurable states, as shown in Eq.3.3.10.

$$\begin{bmatrix} \dot{m}_{FT380} \\ P_{PT305} \\ T_{TE326} \\ T_{T350} \\ \Omega_{S505} \end{bmatrix} = \begin{bmatrix} G_{11}(s) & G_{12}(s) & G_{13}(s) & G_{14}(s) & G_{15}(s) \\ G_{21}(s) & G_{22}(s) & G_{23}(s) & G_{24}(s) & G_{25}(s) \\ G_{31}(s) & G_{32}(s) & G_{33}(s) & G_{34}(s) & G_{35}(s) \\ G_{41}(s) & G_{42}(s) & G_{43}(s) & G_{44}(s) & G_{45}(s) \\ G_{51}(s) & G_{52}(s) & G_{53}(s) & G_{54}(s) & G_{55}(s) \end{bmatrix} \cdot \begin{bmatrix} BA_{PV162} \\ CA_{PV170} \\ HA_{PV380} \\ FV_{FT432} \\ LB_{kW} \end{bmatrix} \qquad \text{Eq.3.3.10}$$

$$Y_i(s) = G_{i,j}(s) \cdot U_j(s) \qquad \text{Eq.3.3.11}$$

The rows of the TF matrix in Eq.3.3.10 are defined by the outputs of interest, while the columns pertain to the available inputs for control. This matrix will be extended to include the speed of the turbine shaft and the exhaust gas temperature as a row outputs, and the generator load bank as a column input, augmenting the plant to a 5 x 5 MIMO system. The complete analysis also includes calculating the poles and zeroes of the TF matrix, by solving a pole polynomial from the least common denominator of all the minors of $G_p(s)$ (Glad et al. 2000). To find the zeroes, the maximal minor of the matrix is normalized with the pole polynomial, and the roots of $G_p(s)^{-1}$ determines the MIMO zeroes.

3.3.2 Multivariable Bode Plot and SVD

In order to account for the interaction of each individual input to a particular output in a graphical manner, a multivariable Bode Plot has been formulated to accommodate the gain and phase shift properties of a matrix Transfer Function, by use of the singular value decomposition SVD methodology (Lewis 1992). The singular values of a matrix give a measure of the size of the matrix, just as the norm gives a measure of the size of a vector. For any input signal, the magnitude of this matrix is bounded above and below by its maximum and minimum singular value respectively. This induced gain is the ratio of the 2-norm of two signals, as given in Eqs.3.3.12-3.3.13. Singular values are thus dependent on the direction of the input vector, which is most often normalized as shown in Eq.3.3.15 and Eq.3.3.16.

$$y = G \cdot d \qquad \text{Eq.3.3.12}$$

$$\frac{\| y \|_2}{\| d \|_2} = \frac{\| G \cdot d \|_2}{\| d \|_2} = \frac{\sqrt{{y_{10}}^2 + {y_{20}}^2 + \cdots}}{\sqrt{{d_{10}}^2 + {d_{20}}^2 + \cdots}} \qquad \text{Eq.3.3.13}$$

$$\underline{\sigma}(G) \le \frac{\| G \cdot d \|_2}{\| d \|_2} \le \overline{\sigma}(G) \qquad \text{Eq.3.3.14}$$

$$\| u_i \| = \sqrt{| u_{i1} |^2 + | u_{i2} |^2 + \cdots + | u_{il} |^2} = 1 \qquad \text{Eq.3.3.15}$$

$$\| v_i \| = \sqrt{| v_{i1} |^2 + | v_{i2} |^2 + \cdots + | v_{il} |^2} = 1 \qquad \text{Eq.3.3.16}$$

Equation 3.3.17 expresses the SVD notation for a square matrix G, with U and V being unitary square matrices, and Σ a diagonal matrix containing the singular values. In Eq.3.3.17, V^* denotes the complex conjugate of V .

$$G = U \cdot \sum \cdot V^* \qquad \text{Eq.3.3.17}$$

$$\sum = \begin{bmatrix} \sigma_1 & 0 & 0 & 0 \\ 0 & \sigma_2 & 0 & 0 \\ 0 & 0 & \ddots & 0 \\ 0 & 0 & 0 & \sigma_r \end{bmatrix} \qquad \text{Eq.3.3.18}$$

In Eq.3.3.18, the rank of the matrix G determines the number of singular values, which are ordered from highest to smallest $\sigma_1 > \sigma_2 > \ldots > \sigma_r$. For a complex valued matrix H(ω), the maximum and minimum singular values $\overline{\sigma}(H(j\omega))$, and $\underline{\sigma}(H(j\omega))$, are an induced matrix norm, having the following properties:

$$\overline{\sigma}(H(j\omega)) = \sqrt{\lambda_{\max}(H^* \cdot H)} \quad , \quad \underline{\sigma}(H(j\omega)) = \sqrt{\lambda_{\min}(H^* \cdot H)} \qquad \text{Eq.3.3.19}$$

$$\overline{\sigma}(H(j\omega)) = \frac{1}{\underline{\sigma}(H(j\omega)^{-1})} \qquad \text{Eq.3.3.20}$$

$$\overline{\sigma}(A \cdot B) \leq \overline{\sigma}(A) \cdot \overline{\sigma}(B) \qquad \text{Eq.3.3.21}$$

where $\lambda_{max,\ min}$ are the largest and smallest eigenvalues of H^*H , and H^* denotes the complex conjugate transpose of matrix H (Belanger 1995). Equation 3.3.21 is an important norm inequality useful in the derivation of optimal controllers, as will be seen in section 3.4. Figure 3.16 shows a sample SV plot of a generic MIMO system. Thus the gain of a multivariate system lies within its maximum and its minimum singular values.

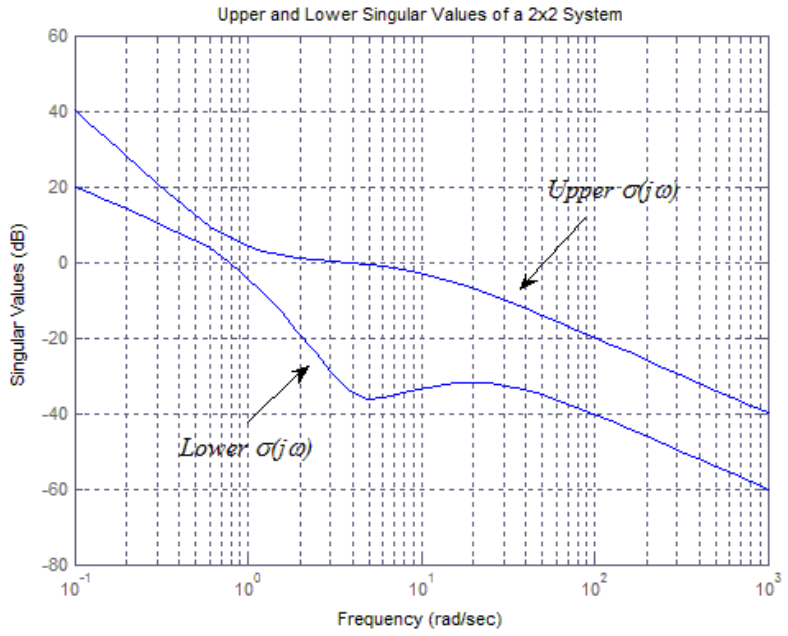

Figure 3.16 Singular Values of a Sample 2x2 TF matrix

It will later be shown that design specifications for MIMO systems in the frequency domain are stated in terms of singular values and their norm properties. Thus computing the singular values of a Transfer Function matrix allows for a multivariate Bode Plot that in turn can be utilized for control design by the use of loop shaping techniques. The singular values in this case are functions of frequency, and thus can provide classical frequency response information i.e. poles, zeroes of the overall MIMO system. Robust

control designs use algorithms that are based on limit bounds of a loop gain, following criteria from the open loop TF plot i.e. its singular values.

3.3.3 Relative Gain Array and MIMO Limitations

Another useful analysis that can be performed on a complex valued Transfer Function matrix is that of the measure of the degree of coupling between input and output signals. The Relative Gain Array RGA provides such a measure by observance of the deviation of its elements from a unitary matrix. Strong cross coupling is then associated with elements that deviate the most from 1 (Glad et al. 2000). For a square matrix A, RGA is defined as $RGA(A) = A. \cdot \left(A^{-1}\right)^T$, where A. implies element wise multiplication. The term 'Relative Gain' comes from the ratio of matrix terms when: all loops are left opened with only one input acting, and all loops are closed, with the rest of the inputs forcing all the other outputs to zero. The signs and magnitudes are interpreted in various ways in the literature, but they mostly agree in the avoidance of decentralized pairing when negative signs arise, and that the control difficulty rises when there is a deviation from the unitary matrix i.e. large RGA elements (Glad et al. 2000). A frequency dependent RGA plot can give insight on the time it takes for a system to fully develop coupling among all its input/output signals.

The open loop response of a MIMO system also provides valuable data concerning bandwidth limits for systems having time delays $\omega_{BW} < \frac{1}{t_d}$, unstable system poles $\omega_{BW} \geq 2p$, and nonminimum phase zeroes $\omega_{BW} \leq \frac{z}{2}$. It will be seen that the performance of the compensated system is always degraded in the presence of RHP transmission zeros that are too close to the origin. Even though there are alternatives to bypassing this detrimental effect to another output channel (Skogestad et al. 2005), it is unlikely to do so in a highly coupled system having orders of magnitude between component time constants. There will therefore be a compromise between speed and stability, whenever RHP transmission MIMO zeros arise.

One measure used to characterize the ease or difficulty of controlling a MIMO plant is given in terms of the condition number κ. It is defined as the ratio of maximum and minimum singular values at a given frequency: $\kappa = \frac{\bar{\sigma}(G)}{\underline{\sigma}(G)}$. Large condition numbers hint at ill-conditioned plants, and are problematic with respect to control implementation. The ability to suppress the magnitude of this criterion justifies any plant reduction and simplification, for control purposes.

3.4 Robust H_∞ Control Algorithm

Modern state space control algorithms are most commonly identified with the time domain for MIMO systems, whereas the well-known classical SISO control schemes pertained to the frequency domain. The elegance of the H_∞ control methodology becomes apparent when the two domains fuse, synthesizing a state space MIMO controller from data based on classical methods.

3.4.1 Closed Loop Transfer Function Descriptions

Controllers for MIMO systems designed in the frequency domain use loop shaping techniques in their algorithms, to guarantee closed loop stability in spite of plant variations and unmodeled dynamics. This is known as stability robustness. On the other hand, performance robustness accounts for exogenous disturbances and sensor noise (Lewis 1992). In particular, robustness is specified in terms of Transfer Function bounds and sensitivity correlations. In essence, sensitivity is defined as the ratio of the fractional change of the system TF to the change of a process TF for a small incremental difference, as expressed in Eq.3.4.1 (Dorf et al. 1998), (Nise 1995).

$$S = \frac{\partial T / T}{\partial G / G} = \frac{\partial T}{\partial G} \cdot \frac{G}{T} \qquad \text{Eq.3.4.1}$$

For a closed loop system depicted in Figure 3.17, the sensitivity, complementary sensitivity, closed loop, and input sensitivity functions are expressed in Eq.3.4.2-3.4.9, where r is the reference signal, w_u the controller disturbance, w the plant variations, and n the measurement noise (Glad et al. 2000). The subscripts r, p, and y refer to the reference, plant, and feedback signal respectively.

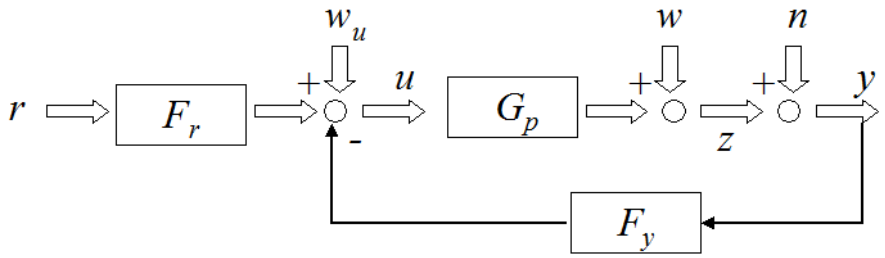

Figure 3.17 Closed Loop Control System [Glad]

$$z(t) = G(p)\cdot u(t) + w(t) \qquad \text{Eq.3.4.2}$$

$$y(t) = z(t) + n(t) \qquad \text{Eq.3.4.3}$$

$$\bar{u}(t) = F_r(p)\cdot r(t) - F_y(p)\cdot y(t) \qquad \text{Eq.3.4.4}$$

$$u(t) = \bar{u}(t) + w_u \qquad \text{Eq.3.4.5}$$

$$w(t) = G_d(p)\cdot d(t) \qquad \text{Eq.3.4.6}$$

$$z = \frac{G\cdot F_r}{(I + G\cdot F_y)}\cdot r + \frac{G}{(I + G\cdot F_y)}\cdot w_u + \frac{1}{(I + G\cdot F_y)}\cdot w - \frac{G\cdot F_y}{(I + G\cdot F_y)}\cdot n \qquad \text{Eq.3.4.7}$$

$$z = G_c\cdot r + G\cdot S_u\cdot w_u + S\cdot w - T\cdot n \qquad \text{Eq.3.4.8}$$

$$e = r - z = (I - G_c) \cdot r - G \cdot S_u \cdot w_u - S \cdot w + T \cdot n \qquad \text{Eq.3.4.9}$$

Equation 3.4.9 defines the error signal, while the sensitivity and complementary sensitivities are given by:

$$S = (I + G \cdot F_y)^{-1} \qquad \text{Eq.3.4.10}$$

$$T = I - S = G \cdot F_y \cdot (I + G \cdot F_y)^{-1} \qquad \text{Eq.3.4.11}$$

It is worth noting that for the case where F_y=F_r, T=G_c: the closed loop TF. It also can be seen that the TF between the plant disturbances w, and the control input u is given by:

$$G_{wu} = \frac{-F_y}{(I + F_y \cdot G)} = -F_y \cdot S \qquad \text{Eq.3.4.12}$$

3.4.2 Frequency Domain Specifications

For the case of MIMO systems, these TF's are matrices whose singular values define the system's closed loop response. System disturbances and reference inputs for example, are both low frequency phenomena, while measurement noise perturbations occur at high frequencies. It is thus desired to maintain the sensitivity function S small for the range of frequencies where the reference input and disturbances are large, and the complementary sensitivity function T small where noise effects dominate (Levine 1996). These restrictions cannot be met simultaneously, because of Eq.3.4.11. However, the magnitude of their singular values can be shaped by the use of weighting functions applied within the corresponding frequency range. Equations 3.4.13 and 3.4.14 express the S and T constraints, where K is the controller, and Figure 3.18 depicts the desired loop shapes.

$$\bar{\sigma}(S) = \bar{\sigma}\left[(I + G \cdot K)^{-1}\right] = \frac{1}{\underline{\sigma}(I + G \cdot K)} \approx \frac{1}{\underline{\sigma}(G \cdot K)} \qquad \text{Eq.3.4.13}$$

$$\bar{\sigma}(T) = \bar{\sigma}\left[\frac{G \cdot K}{I + G \cdot K}\right] \approx \bar{\sigma}(G \cdot K) \qquad \text{Eq.3.4.14}$$

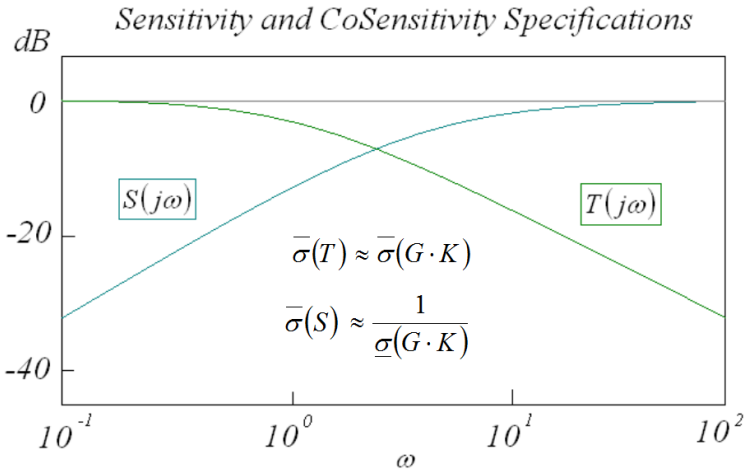

Figure 3.18 Sensitivity and Complementary Sensitivity Constraints [Lewis]

The low frequency specifications for robust performance requires that the minimum SV of the loop gain GK be $\underline{\sigma}(G \cdot K(j\omega)) >> 1$ for $\omega \le \omega_d$, and for good reference tracking and bounded steady state error that $\underline{\sigma}(G \cdot K(0)) > \frac{r}{\delta_\infty}$, where δ_∞ is the upper bound of the steady state error, and r is a step input. If the bandwidth is limited by high frequency noise considerations, it is required that the largest singular value, $\bar{\sigma}(G \cdot K(j\omega)) = 1$ at the cutoff frequency, ω_c. Disturbance rejection due to plant parameter variations is satisfied my making the minimum SV loop gain high on the low frequency range. This is because S is the Transfer Function between system disturbance and system output. The high frequency specifications require that $\bar{\sigma}(G \cdot K(j\omega)) << 1$ for $\omega \ge \omega_n$, and that the high

frequency multiplicative modeling uncertainty be bounded as shown in the following equations, were M is the unknown discrepancy (Lewis 1992).

$$G'(j\omega) = G(j\omega)\cdot[I + M(j\omega)] \qquad \text{Eq.3.4.15}$$

$$\bar{\sigma}(M(j\omega)) < m(\omega),\ \bar{\sigma}(G\cdot K(j\omega)) < \frac{1}{m(\omega)} \qquad \text{Eq.3.4.16}$$

The resultant desired frequency response in terms of singular values and their bounds are noted in Figure 3.19.

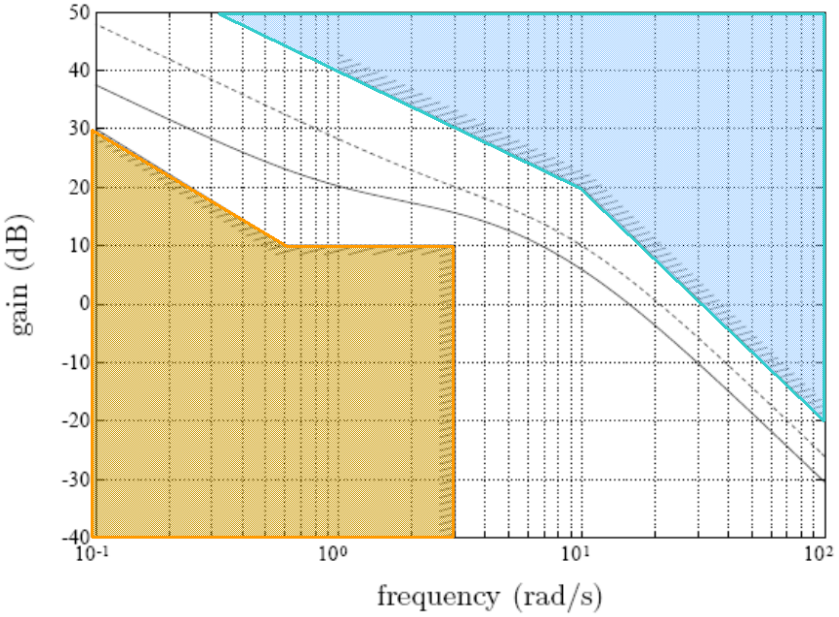

Figure 3.19 Low and High Frequency SV Bounds [Lewis]

3.4.3 H_∞ Control Formulation

In recent years, robust modern control theory has primarily focused its attention on the algorithms proposed by Glover and McFarlane (1992). These control schemes aim at minimizing the infinity norm of a series of closed loop transfer functions as defined in the following sections. In doing so, the detrimental effect of a disturbance signal can be

attenuated at the plant's outputs with guaranteed closed loop stability for all channels of the system. Although there have been a wide variety of modifications to these two methodologies, the mixed sensitivity and the robustification theory will be presented, together with their pro's and con's.

3.4.3.1 Mixed Sensitivity

As stated before, the sensitivity S, complementary sensitivity T, and the TF from system disturbance to control input G_{wu} cannot be made small simultaneously. Therefore, diagonal weighting matrices are chosen such that the aforementioned Transfer Functions are small for all frequencies. For "p" measured outputs and "m" control inputs, the TF sensitivity and co-sensitivity weights W_S, W_T have dimensions (p x p), while the weight of G_{wu} is an (m x m) matrix. In terms of norms, this result can be expressed as:

$$\left| W_S(j\omega) \cdot S(j\omega) \right| \leq \gamma \qquad \text{Eq.3.4.17}$$

$$\left| W_T(j\omega) \cdot T(j\omega) \right| \leq \gamma \qquad \text{Eq.3.4.18}$$

$$\left| W_u(j\omega) \cdot G_{wu}(j\omega) \right| \leq \gamma \qquad \text{Eq.3.4.19}$$

An extended closed loop system of Figure 3.17 is built so as to derive a combined Transfer Function matrix from inputs and disturbances "w" to the outputs "z", so that the requirements of Eq.3.4.17-3.4.19 are met with a single norm (Glad et al. 2000). Figures 3.20 and 3.21 precede the derivation of the norm.

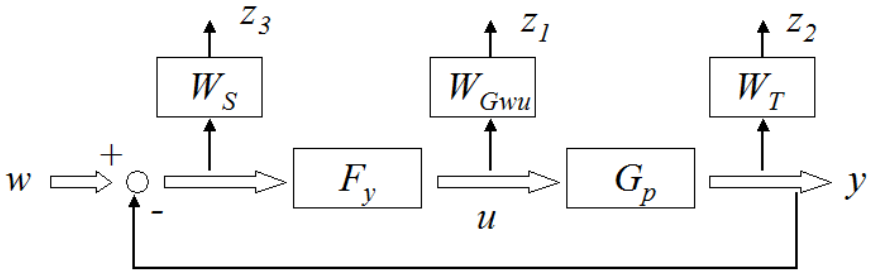

Figure 3.20 Generation of "z" variables from "u" and "w"

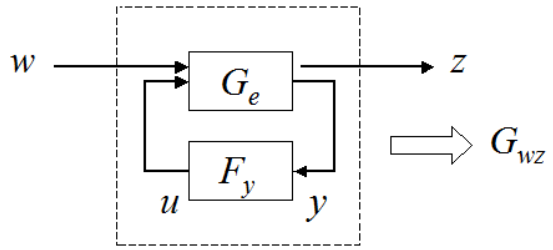

Figure 3.21 Closed Loop and Extended Transfer Functions [36]

To force the extended system G_e to be solely a function of the weighting matrices and the system plant G, the following relations are formulated: $z_1 = W_u \cdot u$, $z_2 = W_T \cdot G \cdot u$, $z_3 = W_S \cdot (G \cdot u + w)$, and $y = G \cdot u + w$. If $u = -F_y \cdot y$ is substituted in the output equations, then:

$$z = \begin{bmatrix} z_1 \\ z_2 \\ z_3 \end{bmatrix} = \begin{bmatrix} -W_u \cdot G_{wu} \\ -W_T \cdot T \\ W_S \cdot S \end{bmatrix} \cdot w = G_{ec} \cdot w \qquad \text{Eq.3.4.20}$$

The extended open loop plant G_e can then be transformed to state space by individually setting up states in controllable canonical form, with the resulting matrices:

$$\dot{x} = A \cdot x + B \cdot u + N \cdot w \qquad \text{Eq.3.4.21}$$

$$z = M \cdot x + D \cdot u \qquad \text{Eq.3.4.22}$$

$$y = C \cdot x + w \qquad \text{Eq.3.4.23}$$

From the previous state space realization, a controller can be derived following H_∞ algorithms, by solving a Ricatti equation that minimizes the infinity norm of the extended Transfer Function matrix G_{ec}. One such solution would proceed by obtaining the state space realization of the plant Transfer Function G, after incorporating the appropriate

weighting matrices W_u, W_S, and W_T. An upper bound γ would be chosen to solve the given Ricatti equation Eq.3.4.24 for a positive semidefinite solution $S=S_\gamma$ subject to $A - B \cdot B^T \cdot S_\gamma$ stable.

$$A^T \cdot S + S \cdot A + M^T \cdot M + S \cdot \left(\gamma^{-2} \cdot N \cdot N^T - B \cdot B^T\right) \cdot S = 0 \qquad \text{Eq.3.4.24}$$

$$\dot{\hat{x}} = A \cdot \hat{x} + B \cdot u + N \cdot \left(y - C \cdot \hat{x}\right) \qquad \text{Eq.3.4.25}$$

$$u = -B^T \cdot S_\gamma \cdot \hat{x} \qquad \text{Eq.3.4.26}$$

The controller is given by Eq.3.4.26, and the state estimator by Eq.3.4.25. If no solution exists, either the bound γ is chosen again through a number of iterations, or there simply isn't a linear controller that bounds the infinity norm of G_{ec}. Although this method has proven to be efficient in terms of robustness, problems could arise when attempting to satisfy the three different weight requirements simultaneously, since most often they have conflicting specifications, as is the case of the S and T functions. Also, the trial and error nature of the weight selection process makes it a tedious task to converge the iterative process. The proceeding sections discuss norm definitions and another more systematic approach to robust loop shaping i.e. maximally robust H_∞ controller.

3.4.3.2 Loop Gain Robustification

In deriving this particular algorithm, it has been noted that the gain of a Transfer Function matrix can be expressed as a norm $\|\cdot\|$ in its singular values, and as such, can be minimized accordingly. Minimization of this gain reduces the undesirable outputs subject to disturbance effects and noise interactions. The H_2 norm, and the H_∞ norms of the Transfer Function matrix between "w" and "z" are defined as follows (Boyd 1987)

$$\| H \|_2 \equiv \sqrt{\frac{1}{\pi} \int_{-\infty}^{\infty} tr\left(H(j\omega)^* H(j\omega)\right) d\omega} = \sqrt{\sum_{i,j} \frac{1}{\pi} \int_{-\infty}^{\infty} | H_{i,j}(j\omega) |^2 \, d\omega} \qquad \text{Eq.3.4.27}$$

$$\| H \|_{\infty} \equiv \sqrt{\max_{\omega} \lambda\left(H(j\omega)^{*} H(jw)\right)} = \max_{\omega} \sigma(H(j\omega)) \qquad \text{Eq.3.4.28}$$

where H(jω) is the previously defined closed loop TF G_{ec}. $\|H\|_2$ is defined as the total energy of the impulse response of a plant matrix. It is also the RMS value of the output "z" when the input "w" is driven by white noise. In contrast with the infinity norm of H, $\|H\|_2$ is not a gain. $\|H\|_{\infty}$ on the other hand, is the maximum singular value over the entire frequency spectrum and it is sometimes referred to as the worst case RMS value of the output for a given input of unknown spectrum (Boyd 1987). The minimization of the H_{∞} norm thus guarantees stability margins and robustness.

As a type of optimal control, this approach wishes to minimize a cost function given by Eq.3.4.29, such that Eq.3.4.30 holds for some small value ε (Green et al. 1995).

$$J = \int_0^{T_f} \left(z^T \cdot z - \gamma^2 \cdot w^T \cdot w\right) dt + x^T\left(T_f\right) \cdot \Delta \cdot x\left(T_f\right) \leq \varepsilon \cdot \| w \|^2_{2,[0,T_f]} \qquad \text{Eq.3.4.29}$$

$$\| z \|_2^2 - \gamma^2 \cdot \| w \|_2^2 \leq -\varepsilon \cdot \| w \|_2^2 \qquad \text{Eq.3.4.30}$$

Thus the H_{∞} solution satisfies two Hamiltonian matrices Eq.3.4.31 and Eq.3.4.32, for the state space plant partitioned as in Eq.3.4.33-3.4.35 (Belanger 1995).

$$H_c = \begin{bmatrix} A & \gamma^2 \cdot B_1 \cdot B_1^T - B_2 \cdot B_2^T \\ -C_1^T \cdot C_1 & -A^T \end{bmatrix} \qquad \text{Eq.3.4.31}$$

$$H_f = \begin{bmatrix} A & \gamma^2 \cdot C_1^T \cdot C_1 - C_2^T \cdot C_2 \\ -B_1 \cdot B_1^T & -A \end{bmatrix} \qquad \text{Eq.3.4.32}$$

$$\dot{x} = A \cdot x + B_1 \cdot w + B_2 \cdot u \qquad \text{Eq.3.4.33}$$

$$z = C_1 \cdot x + D_{11} \cdot w + D_{12} \cdot u \qquad \text{Eq.3.4.34}$$

$$y = C_2 \cdot x + D_{21} \cdot w + D_{22} \cdot u \qquad \text{Eq.3.4.35}$$

Glover and McFarlane derive an H_∞ algorithm that shapes the open loop singular values with one diagonal pre-compensator before realizing the loop gain in state space and forming the controller from two Ricatti equations that stem from the Hamiltonians of Eq.3.4.31-3.4.32 (Glad et al. 2000) for the state realization $\dot{x} = A \cdot x + B \cdot u$, $y = C \cdot x$.

$$A \cdot Z + Z \cdot A^T - Z \cdot C^T \cdot C \cdot Z + B \cdot B^T = 0 \qquad \text{Eq.3.4.36}$$

$$A^T \cdot X + X \cdot A - X \cdot B \cdot B^T \cdot X + C^T \cdot C = 0 \qquad \text{Eq.3.4.37}$$

The solution of Eq.3.4.36-3.4.37 requires that the matrices X and Z be positive definite. An algorithm that automatically adjusts the controller to achieve maximum degree of stability margin is given below:

$$\lambda_m = \underset{\max}{eigen}\left(X \cdot Z\right) \qquad \text{Eq.3.4.38}$$

$$\gamma = \alpha \cdot \sqrt{\left(1 + \lambda_m\right)} \qquad \text{Eq.3.4.39}$$

$$R = I - \frac{1}{\gamma^2} \cdot \left(I + Z \cdot X\right) \qquad \text{Eq.3.4.40}$$

$$L = B^T \cdot X \qquad \text{Eq.3.4.41}$$

$$K = R^{-1} \cdot Z \cdot C^T \qquad \text{Eq.3.4.42}$$

$$\dot{\hat{x}} = A \cdot \hat{x} + B \cdot u + K \cdot \left(y - C \cdot \hat{x} \right) \qquad \text{Eq.3.4.43}$$

$$u = -L \cdot \hat{x} \qquad \text{Eq.3.4.44}$$

where α is a scaling factor greater than 1. So in order to get the best stability margins, γ should be chosen as small as possible. The previous algorithm of Eq.3.4.36-3.4.44 will be applied to the empirical Transfer Function matrix obtained in section 3.2.1.

Figure 3.22 shows a desired loop shape of a robustly compensated system, with high lower singular values at the low frequencies for good performance, and low higher singular values in the high frequency range for robustness. Note the transition crossover slope of –20dB/dec. This slope rate ensures a safe stability margin, as seen in the phase plot.

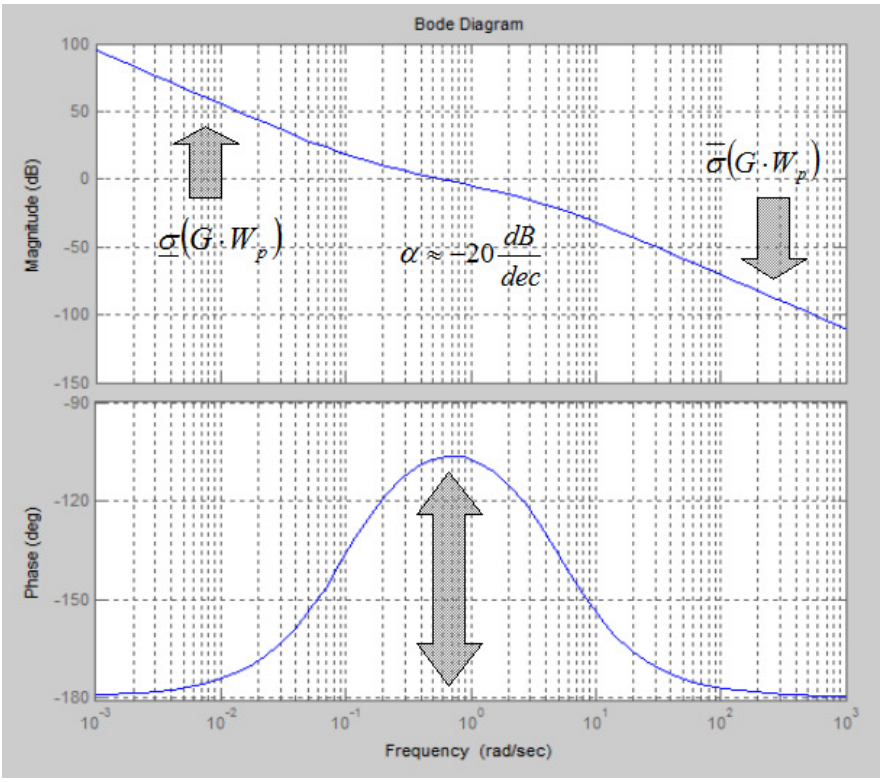

Figure 3.22 Simplified Desired Loop Gain Shape

For systems having multiple singular values, as is in the MIMO case, forcing the singular values to be close to each other around the crossover frequency is not a simple matter. Glad suggests a way to manipulate a particular singular value around a specified frequency to match the location of an adjacent singular value. Equation 3.4.45 successfully accomplishes this for a system having two singular values. This gain matrix consists of the input unitary matrix V and its transpose V^T evaluated at the crossover frequency, multiplied by a constant. The weight shown closes the gap between the first and third singular values at a given frequency. This weight is post multiplied to a scaled plant matrix as expressed in Eq.3.4.47.

$$W_1 = I + \frac{(\sigma_1 - \sigma_3)}{\sigma_3} \cdot V \cdot V^T \qquad \text{Eq.3.4.45}$$

A dynamic pre-compensator accomplishes the open loop gain shape, while the robust controller stemming from Eq.3.4.36-3.4.37 guarantees stability. The resulting diagonal compensator is pre-multiplied to the scaled plant. This pre-compensator is typically a first or second order Transfer Function that amplifies the gain at low frequency, and attenuates input signals at high frequency. One such example is given below, for a diagonal matrix,

$$W_p = \frac{A \cdot (s + \omega_c)}{s \cdot (s + \omega_{n1}) \cdot (s + \omega_{n2})} \cdot I \qquad \text{Eq.3.4.46}$$

where the zero is meant to smooth the SV transition at the crossover frequency, the integrator increase the dc gain at low frequencies, and the poles roll off SV prior to the noise and uncertainty levels. Before the algorithm outlined in Eqs.3.4.38-3.4.44 can be used, the Transfer Function Matrix must first be scaled. It is after scaling that the loop gain of Eq.3.4.50 can be utilized in state space format for the solution of Eq.3.4.36 and Eq.3.4.37. The pre-scaling matrix W_{pre} is a diagonal matrix of the maximum expected deviation in each of the controlled states, whereas the post-scaling matrix W_{post} includes the allowable changes of the actuator signals within their nominal operating point. These values are given in subsequent chapters.

$$G_{scaled}(s) = W_{pre}^{-1} \cdot G_p(s) \cdot W_{post} \quad \text{Eq.3.4.47}$$

$$W_{pre} = diag(\Delta\dot{m}_{FC}, \Delta P_{FC}, \Delta T_{FC}, \Delta T_{TIT}, \Delta\Omega) \quad \text{Eq.3.4.48}$$

$$W_{post} = diag(\Delta BA, \Delta CA, \Delta HA, \Delta PV, \Delta LB) \quad \text{Eq.3.4.49}$$

$$L_{loop} = W_2 \cdot G_{scaled} \cdot W_P(s) \cdot W_1 \quad \text{Eq.3.4.50}$$

The results of this algorithm will be analyzed for various uncertainty ranges in terms of parametric and unstructured uncertainty. The practicality of this approach can aid in the interpretation of underlying control complexities that can arise in the development of other control schemes.

4 Empirical Results

The results of the control methodology detailed in the preceding chapters are summarized presently for the empirical model. Analysis demonstrates the difficulty in controllability due to the strong coupling between system components, and a further need of model reduction in order to achieve good results that are applicable to the real system. The robust algorithm is then tested under various ranges of parametric and unstructured uncertainty, for regulation and reference tracking.

The following sections pertain to the analysis and further testing of an H_∞ controller derived from an experimental plant. First, frequency response plots of magnitude and phase are shown, followed by Bode plots of the generated Transfer Functions that fit test data. The scaled singular values are graphed before and after compensation of the chosen dynamic and scalar weights. Finally, the controller performance is tested for disturbance rejection and robustness in a Simulink/MatLab platform.

4.1 Frequency Response Plots

As stated in Chapter 3, the sinusoidal modulation of all input actuators to the HyPer plant was carried out individually, one valve at a time, around a nominal operating point. The fuel valve was excited at 45kW load with all the other bypass valves closed, and so were the rest of the bypass valves, one at a time. Figures 4.1-4.5 show the time series of the fuel valve modulation tests, from 0.001Hz to 1Hz. The signals graphed are those of the command signal PV432, fuel flow transmitter FT432, fuel flow signal auto-correlation function, plenum airflow FT380, turbine inlet temperature T350, and turbine speed S502A. Plots for the plenum temperature and pressure signals are not shown, for reasons discussed in subsequent sections. It is noted however, that the high frequency response trend is dominated by noise, for frequencies faster than 0.2Hz.

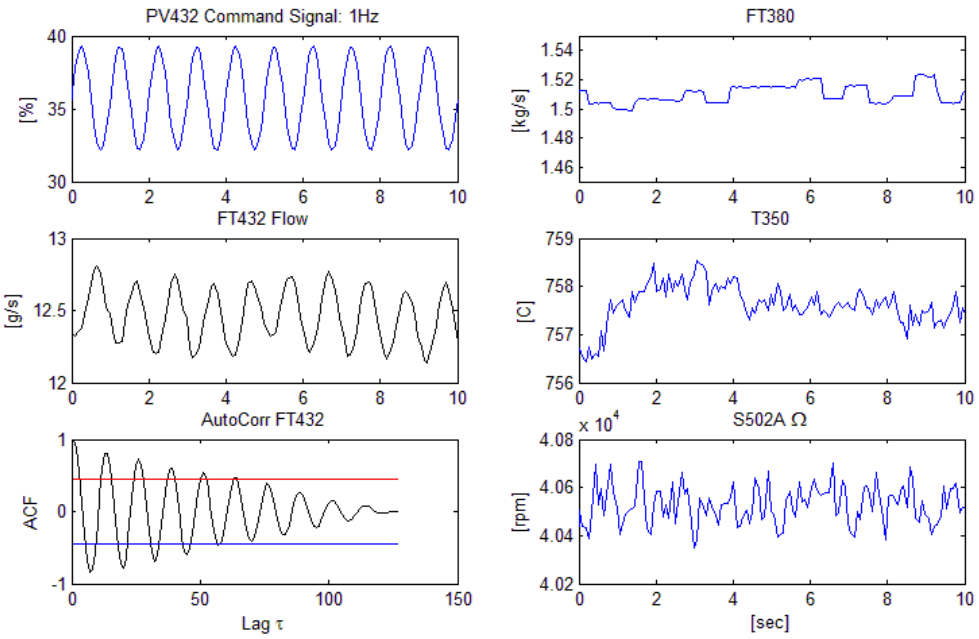

Figure 4.1 Time Series: Fuel Valve Modulation @ 1Hz

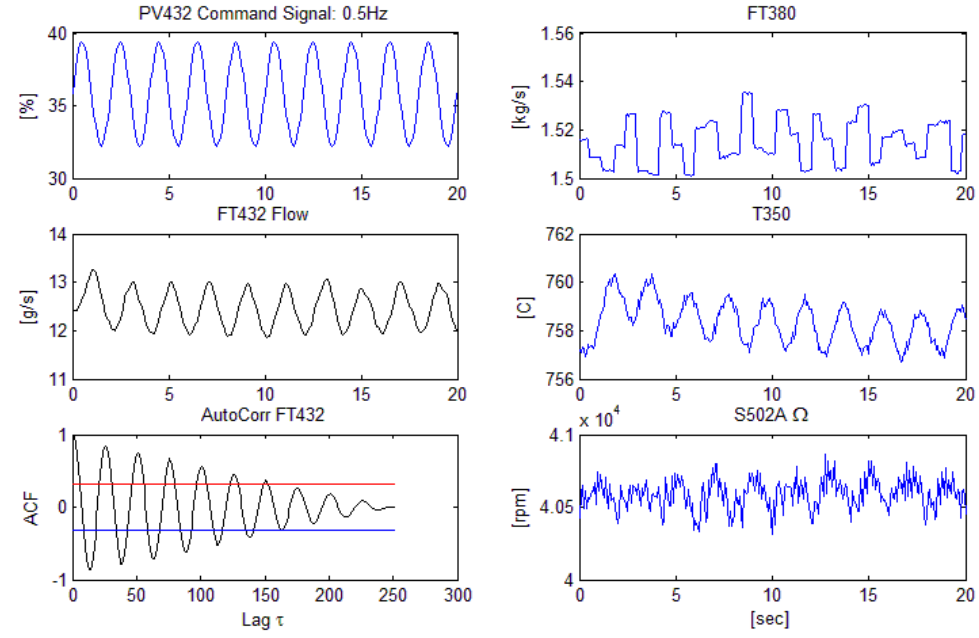

Figure 4.2 Time Series of Fuel Valve Modulation @ 0.5Hz

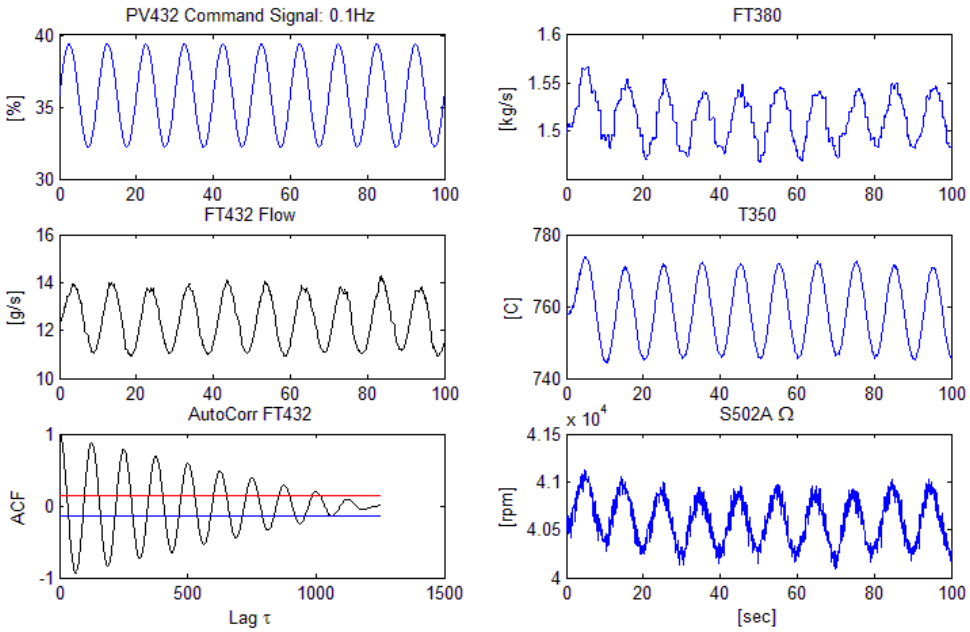

Figure 4.3 Time Series: Fuel Valve Modulation @ 0.1Hz

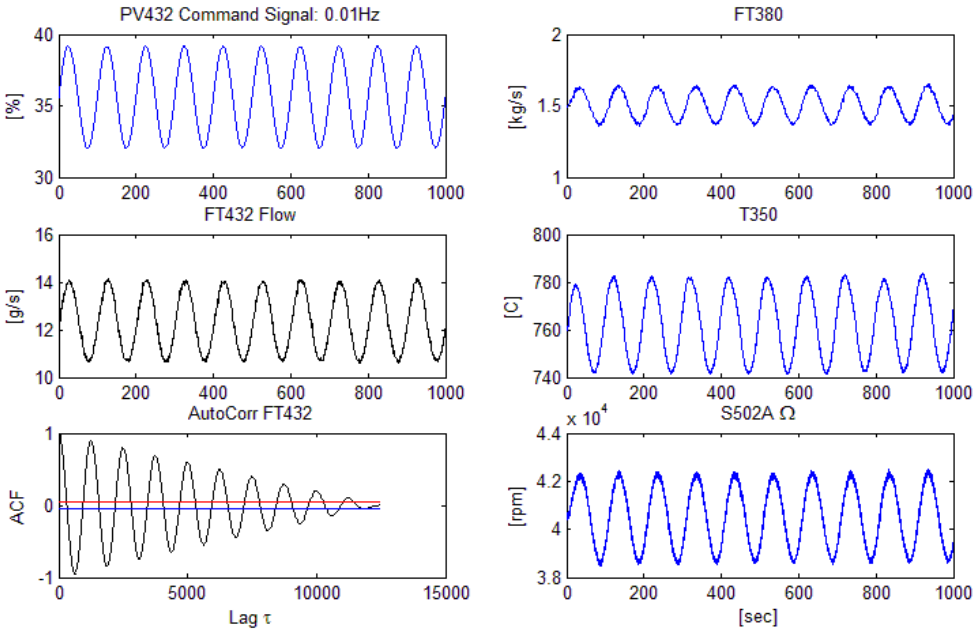

Figure 4.4 Time Series: Fuel Valve Modulation @ 0.01Hz

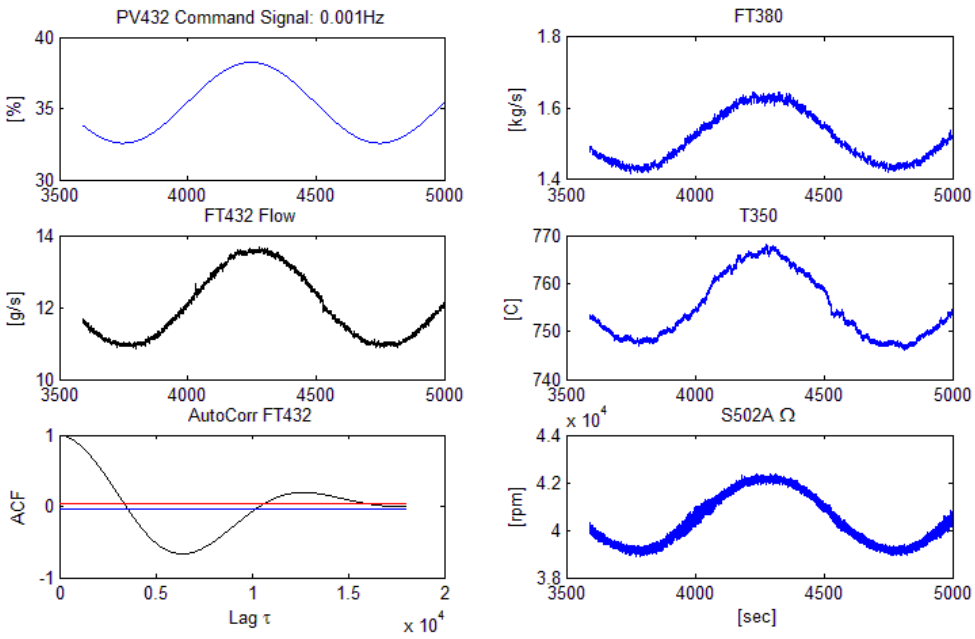

Figure 4.5 Time Series: Fuel Valve Modulation @ 0.001Hz

In the previous plots, the auto-correlation function for the fuel flow transmitter is used as an indicator of how well the driving signal form matches that of a sinusoid. The greater the red and blue uncertainty bounds, the more randomness the signal has, and the less confidence there is on the input signal being correlated in a sinusoidal fashion. As the number of data points increase, these bounds lessen, and the data becomes more reliable in terms of frequency response to a sine wave. Figures 4.6 and 4.7 show the magnitude and phase Bode plots for plenum airflow, pressure, and temperature, as well as turbine inlet temperature and speed. Each of the 28 data points covering three orders in magnitude are Fourier transformed ratios of the aforementioned outputs as a function of the command signal PV432. It is worth noting that discontinuities in the phase plots are a result of folding of the phase diagram about -180 degrees, meaning that a sample lag of -200° is instead shown as +160°. Thus all the phase graphs have default windows of +/-200 degrees. Figures 4.8 and 4.9 are the Bode plots of all the outputs of interest as a function of load bank fluctuation.

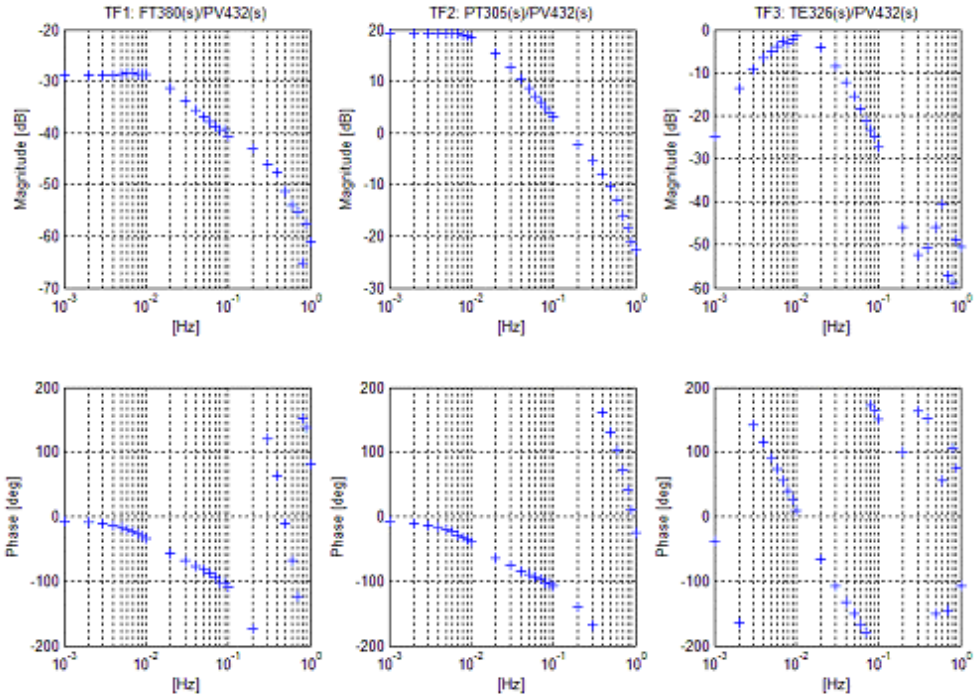

Figure 4.6 Fuel Valve Modulation Bode Plots: $\dot{m}$, P_{FC}, T_{FC}

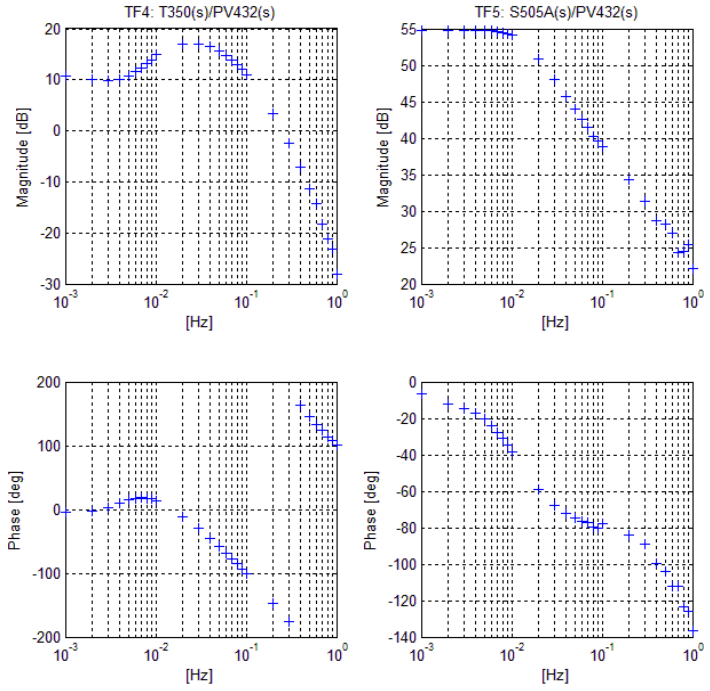

Figure 4.7 Fuel Valve Modulation Bode Plots: TIT, Ω

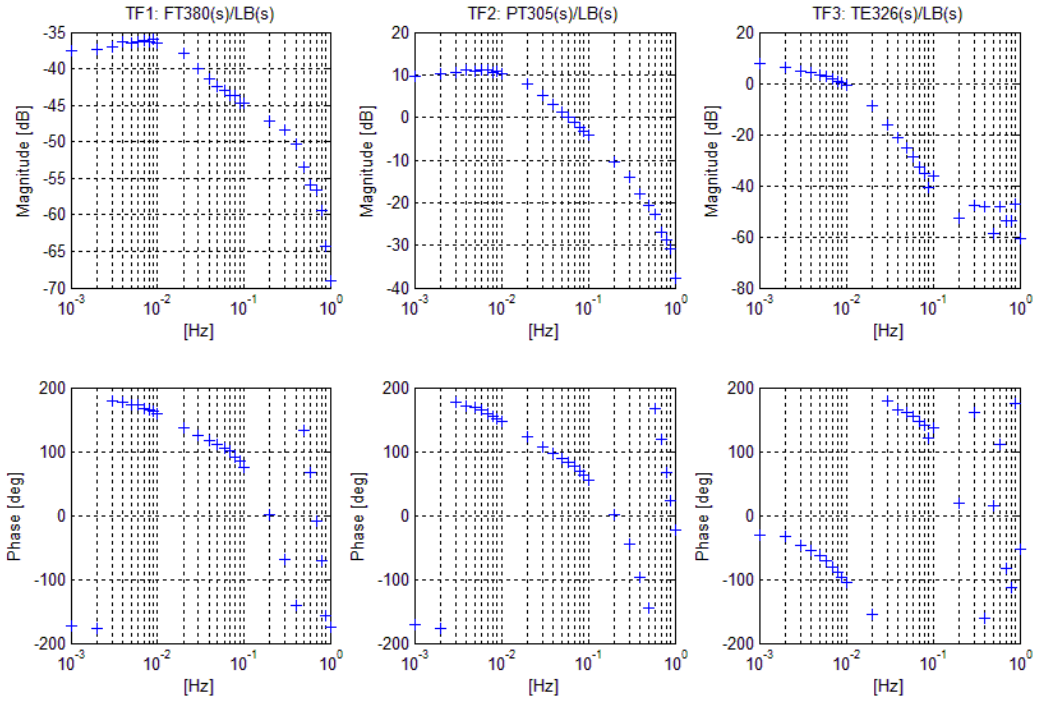

Figure 4.8 Load Bank Modulation Bode Plots: $\dot{m}$, P_{FC}, T_{FC}

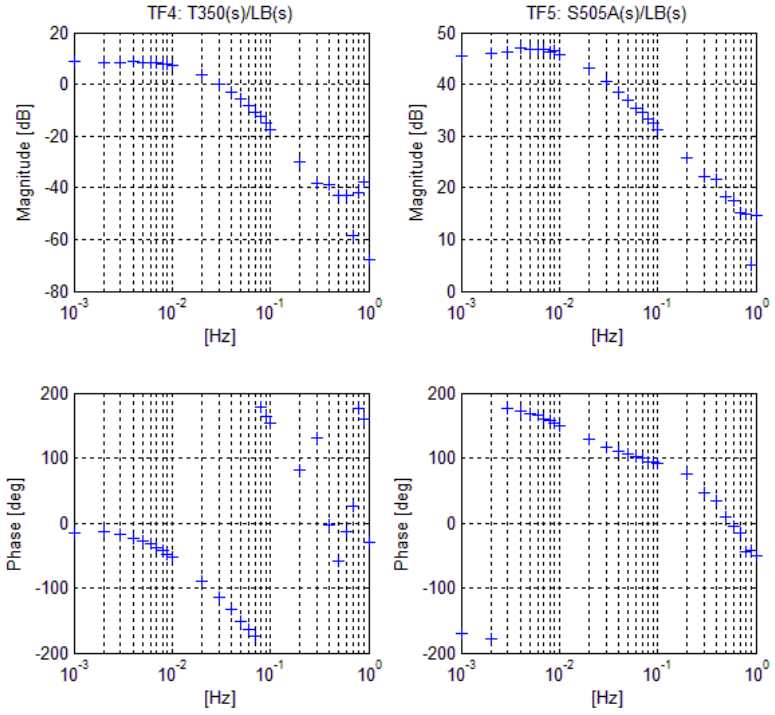

Figure 4.9 Load Bank Modulation Bode Plots: TIT, Ω

Figures 4.10-4.15 show the Bode plots of the BA, CA, and HA bypass valves. The response of the valves is characterized in an additional magnitude/phase plot. In this manner, the range of reliable data can thus be related to the bandwidth of each actuator, as determined experimentally. Blue crosshairs pertain to good data points, whereas red crosshairs, noisy data. This is seen in Figure 4.10 for the BA modulation of TF4. The red crosshairs commence at approximately 3dB below dc magnitude value. Table 4.1 displays the bandwidth, time constants, settling times, and range of operation of each of the bypass valves from the experimental data.

Inputs	Min	Ave	Max	Units	Bandwidth [Hz]	Bandwidth [rad/s]	τ [sec]	t_s~2% [sec]
BA	0	14	16	%	0.04	0.2513	3.98	15.92
CA	0	40	100	%	0.35	2.1991	0.45	1.82
HA	0	40	100	%	0.2	1.2566	0.80	3.18
FV	32	35	38	%	Specification	Specification	N/A	N/A
LB	0	45000	98000	kW	N/A	N/A	N/A	N/A

Table 4.1 Bypass Valve Characterization

Further discussion in upcoming sections will address the reasons behind the final selection of controlled variables and control signals. All of the outputs of interests are shown nonetheless, with the added variables of air plenum pressure PT305, and air plenum temperature TE326.

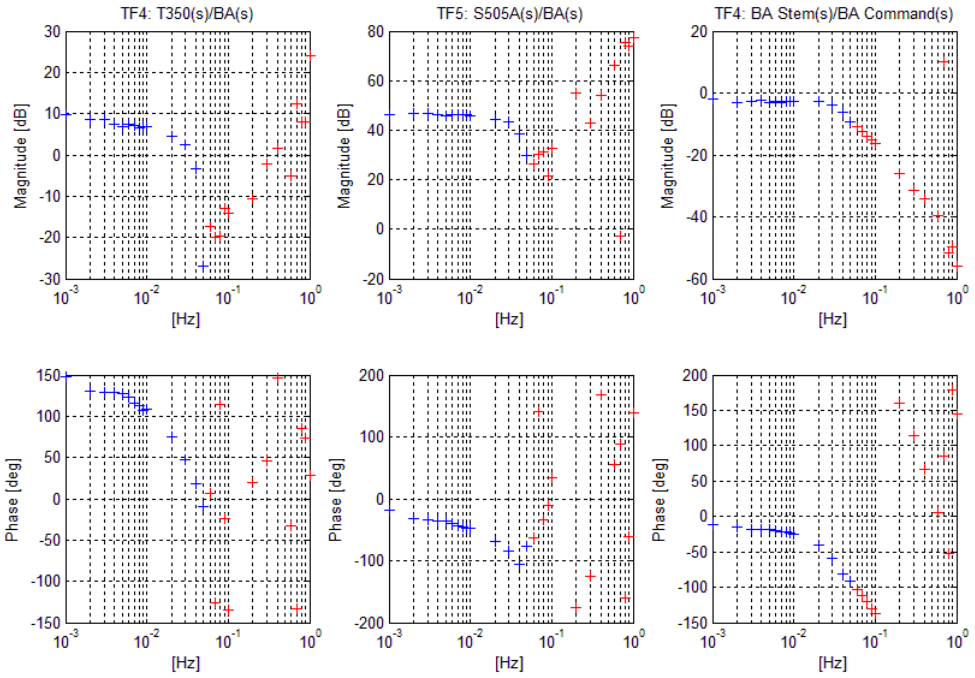

Figure 4.10 Bleed Air Modulation Bode Plots: TIT, Ω, Stem

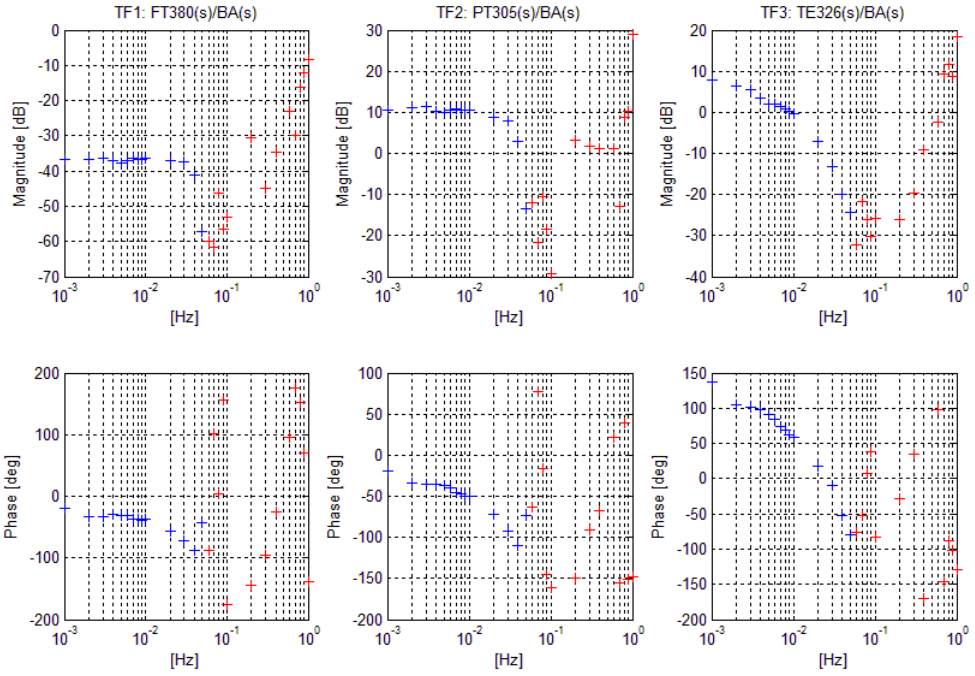

Figure 4.11 Bleed Air Modulation Bode Plots: $\dot{m}$, P_{FC}, T_{FC}

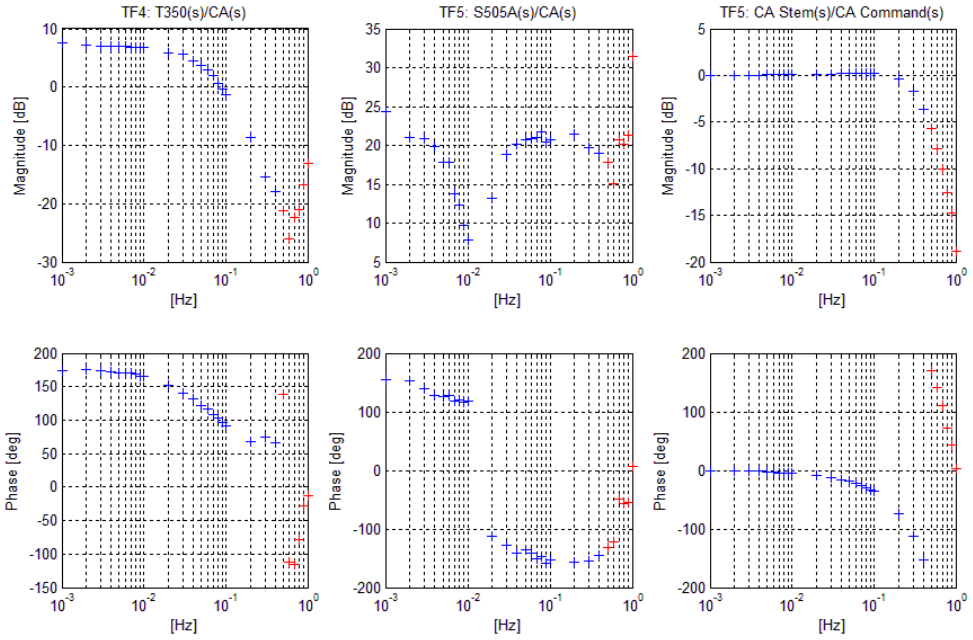

Figure 4.12 Cold Air Modulation Bode Plots: TIT, Ω, Stem

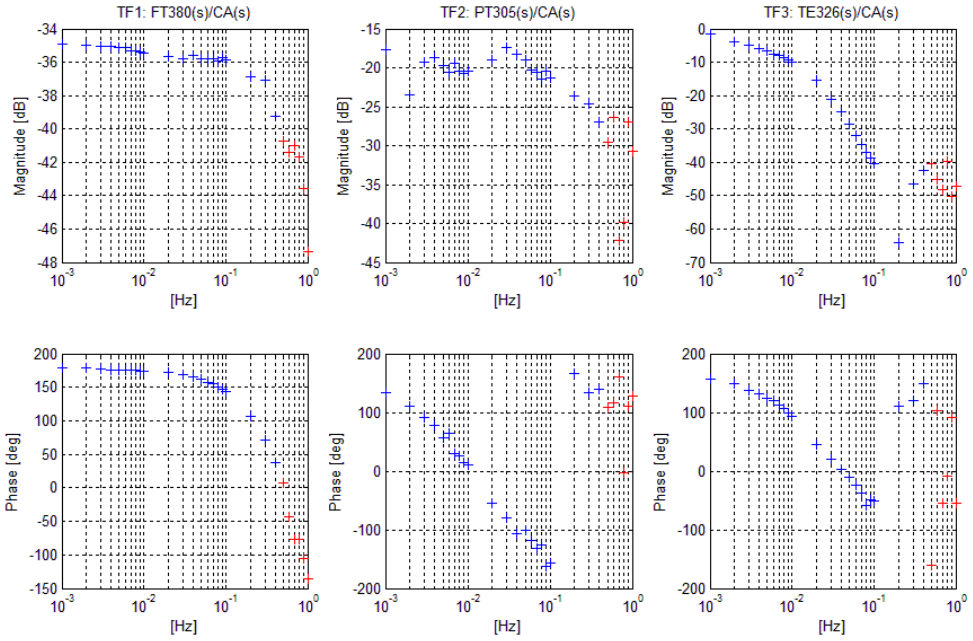

Figure 4.13 Cold Air Modulation Bode Plots: $\dot{m}$, P_{FC}, T_{FC}

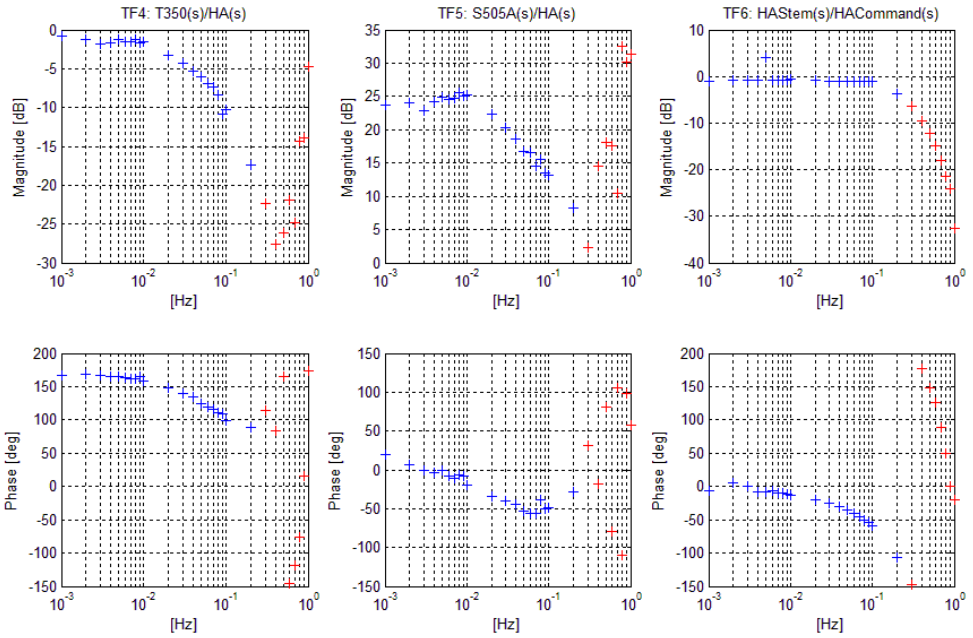

Figure 4.14 Hot Air Modulation Bode Plots: TIT, Ω, Stem

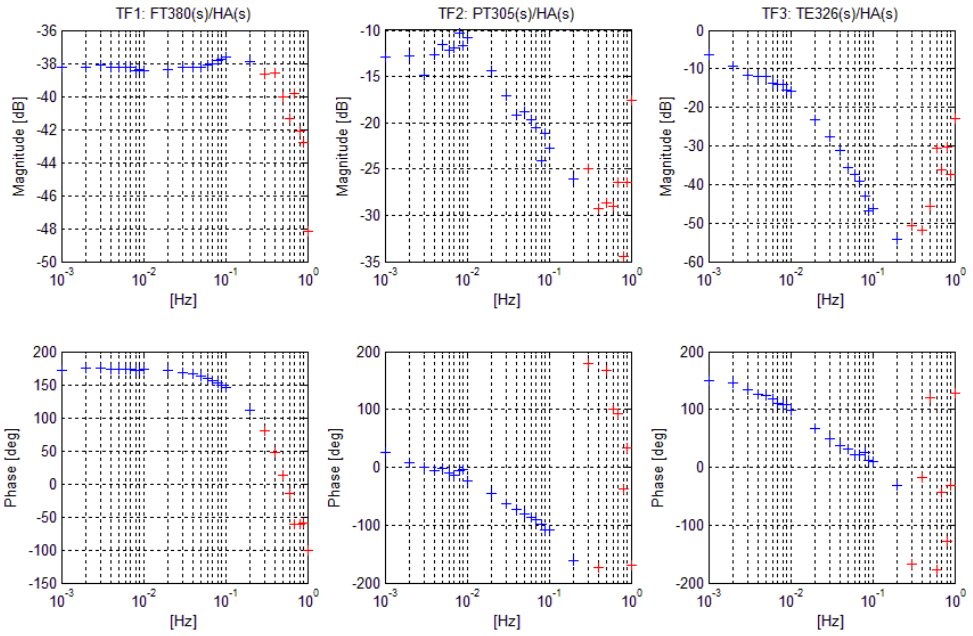

Figure 4.15 Hot Air Modulation Bode Plots: $\dot{m}$, P_{FC}, T_{FC}

4.2 Transfer Function Derivation

Following the methodology of Chapter 3, a Transfer Function equation is derived from all the plots of the previous section, for each of the fluctuated inputs. As stated previously, Transfer Functions for all 25 input/output combinations where obtained and inserted into the matrix of Eq.4.1.1. This matrix is further reduced to that of Eq.4.1.2, as explained later in the section. The individual Transfer Functions are listed below followed by their magnitude plot, which is compared to the experimental data. This superimposed Transfer Function Bode plot is graphed in Figures 4.16-4.20, where the blue crosshairs denote test data, and the solid line, the Transfer Function approximation.

$$\begin{bmatrix} \dot{m}_{FT380} \\ P_{PT305} \\ T_{TE326} \\ T_{T350} \\ \Omega_{S505} \end{bmatrix} = \begin{bmatrix} G_{11}(s) & G_{12}(s) & G_{13}(s) & G_{14}(s) & G_{15}(s) \\ G_{21}(s) & G_{22}(s) & G_{23}(s) & G_{24}(s) & G_{25}(s) \\ G_{31}(s) & G_{32}(s) & G_{33}(s) & G_{34}(s) & G_{35}(s) \\ G_{41}(s) & G_{42}(s) & G_{43}(s) & G_{44}(s) & G_{45}(s) \\ G_{51}(s) & G_{52}(s) & G_{53}(s) & G_{54}(s) & G_{55}(s) \end{bmatrix} \cdot \begin{bmatrix} BA_{PV162} \\ CA_{PV170} \\ HA_{PV380} \\ FV_{FT432} \\ LB_{kW} \end{bmatrix} \qquad \text{Eq.4.1.1}$$

$$\begin{bmatrix} \dot{m}_{FT380} \\ T_{T350} \\ \Omega_{S505} \end{bmatrix} = \begin{bmatrix} G_{12}(s) & G_{13}(s) & G_{14}(s) \\ G_{42}(s) & G_{43}(s) & G_{44}(s) \\ G_{52}(s) & G_{53}(s) & G_{54}(s) \end{bmatrix} \cdot \begin{bmatrix} CA_{PV170} \\ HA_{PV380} \\ FV_{PV432} \end{bmatrix} \qquad \text{Eq.4.1.2}$$

CA Bypass Valve Input Signal Transfer Functions:

$$G_{12}(s) = \frac{0.032 \cdot (s + 0.085) \cdot e^{-0.51 \cdot s}}{(s + .08) \cdot (s + 1.91)} \qquad \text{Eq.4.1.3}$$

$$G_{42}(s) = \frac{0.788 \cdot e^{-0.125 \cdot s}}{(s + 0.32) \cdot (s + 1.1)} \qquad \text{Eq.4.1.4}$$

$$G_{52}(s) = \frac{26.682 \cdot (s^2 + 0.0075 \cdot s + 0.0056) \cdot e^{-0.66 \cdot s}}{(s + 0.077) \cdot (s + 0.082) \cdot (s + 2)} \qquad \text{Eq.4.1.5}$$

$$G_{22}(s) = \frac{0.011 \cdot (s + 0.012) \cdot (s + 0.086) \cdot (s + 0.196) \cdot (s + 1.5) \cdot e^{-3.49 \cdot s}}{(s + 0.0095) \cdot (s + 0.198) \cdot (s + 0.235) \cdot (s + 0.264)} \qquad \text{Eq.4.1.6}$$

$$G_{32}(s) = \frac{7.01e-4 \cdot (s+2.4) \cdot (s+2.5) \cdot e^{-2.78 \cdot s}}{(s+0.025) \cdot (s+0.2)} \quad \text{Eq.4.1.7}$$

HA Bypass Valve Input Signal Transfer Functions:

$$G_{13}(s) = \frac{0.04 \cdot (s+0.7) \cdot e^{-0.77 \cdot s}}{(s+0.91) \cdot (s+2.5)} \quad \text{Eq.4.1.8}$$

$$G_{43}(s) = \frac{0.357 \cdot e^{-0.22 \cdot s}}{(s+0.2) \cdot (s+2)} \quad \text{Eq.4.1.9}$$

$$G_{53}(s) = \frac{2.543 \cdot (s+0.03) \cdot e^{-0.85 \cdot s}}{(s+0.06) \cdot (s+0.09)} \quad \text{Eq.4.1.10}$$

$$G_{23}(s) = \frac{0.176 \cdot (s+0.03) \cdot (s+0.9) \cdot (s+0.8) \cdot e^{-1.58 \cdot s}}{(s+0.045) \cdot (s+0.1) \cdot (s+4)} \quad \text{Eq.4.1.11}$$

$$G_{33}(s) = \frac{1.482e-4 \cdot (s+2.4) \cdot (s+2.5) \cdot e^{-1.08 \cdot s}}{(s+0.025) \cdot (s+0.2)} \quad \text{Eq.4.1.12}$$

Fuel Valve Input Signal Transfer Functions:

$$G_{14}(s) = \frac{0.041 \cdot (s+0.022) \cdot (s+0.3) \cdot e^{-1.38 \cdot s}}{(s+0.033) \cdot (s+0.061) \cdot (s+1) \cdot (s+4)} \quad \text{Eq.4.1.13}$$

$$G_{44}(s) = \frac{2.201 \cdot (s+0.054)^2 \cdot e^{-0.18 \cdot s}}{(s+0.085)^2 \cdot (s+0.53)^2} \quad \text{Eq.4.1.14}$$

$$G_{54}(s) = \frac{17.495 \cdot (s+0.03) \cdot e^{-0.2 \cdot s}}{(s+0.04) \cdot (s+0.07)} \quad \text{Eq.4.1.15}$$

$$G_{24}(s) = \frac{3.524 \cdot (s+0.03) \cdot e^{-0.43 \cdot s}}{(s+0.04) \cdot (s+0.07) \cdot (s+4)} \quad \text{Eq.4.1.16}$$

$$G_{34}(s) = \frac{0.024 \cdot (s+0.005) \cdot (s+0.015) \cdot e^{-3.40 \cdot s}}{(s+0.04) \cdot (s+0.05) \cdot (s+0.1) \cdot (s+0.15)} \quad \text{Eq.4.1.17}$$

Load Bank Signal Transfer Functions:

$$G_{15}(s) = \frac{0.048 \cdot (s+0.022) \cdot (s+0.3) \cdot (s+1.5) \cdot e^{-1.59 \cdot s}}{(s+0.043) \cdot (s+0.071) \cdot (s+1) \cdot (s+3.5)^2} \quad \text{Eq.4.1.18}$$

$$G_{45}(s) = \frac{0.071 \cdot e^{-5.9 \cdot s}}{(s+0.15)^2} \quad \text{Eq.4.1.19}$$

$$G_{55}(s) = \frac{21.339 \cdot (s+0.02) \cdot e^{-0.153 \cdot s}}{(s+0.04) \cdot (s+0.06)} \quad \text{Eq.4.1.20}$$

$$G_{25}(s) = \frac{1.476 \cdot (s+0.03) \cdot e^{-0.92 \cdot s}}{(s+0.05) \cdot (s+0.07) \cdot (s+4)} \quad \text{Eq.4.1.21}$$

$$G_{35}(s) = \frac{1e-3 \cdot (s+2.5)^2 \cdot e^{-2.71 \cdot s}}{(s+0.025) \cdot (s+0.1)} \quad \text{Eq.4.1.22}$$

BA Bypass Valve Input Signal Transfer Functions:

$$G_{11}(s) = \frac{5.34e-4 \cdot e^{-2.29 \cdot s}}{(s+0.12) \cdot (s+0.32) \cdot (s+0.8)} \quad \text{Eq.4.1.23}$$

$$G_{21}(s) = \frac{0.11 \cdot (s+0.042) \cdot e^{-0.19 \cdot s}}{(s+0.073) \cdot (s+0.1) \cdot (s+0.2)} \quad \text{Eq.4.1.24}$$

$$G_{31}(s) = \frac{3.99e-3 \cdot e^{-3.92 \cdot s}}{(s+0.025) \cdot (s+0.2) \cdot (s+0.3)} \quad \text{Eq.4.1.25}$$

$$G_{41}(s) = \frac{2.43e-3 \cdot e^{-1.03 \cdot s}}{(s+0.12) \cdot (s+0.2)^2 \cdot (s+0.9)} \quad \text{Eq.4.1.26}$$

$$G_{51}(s) = \frac{0.227 \cdot e^{-1.12 \cdot s}}{(s+0.046) \cdot (s+0.09) \cdot (s+1.1) \cdot (s+0.25)} \quad \text{Eq.4.1.27}$$

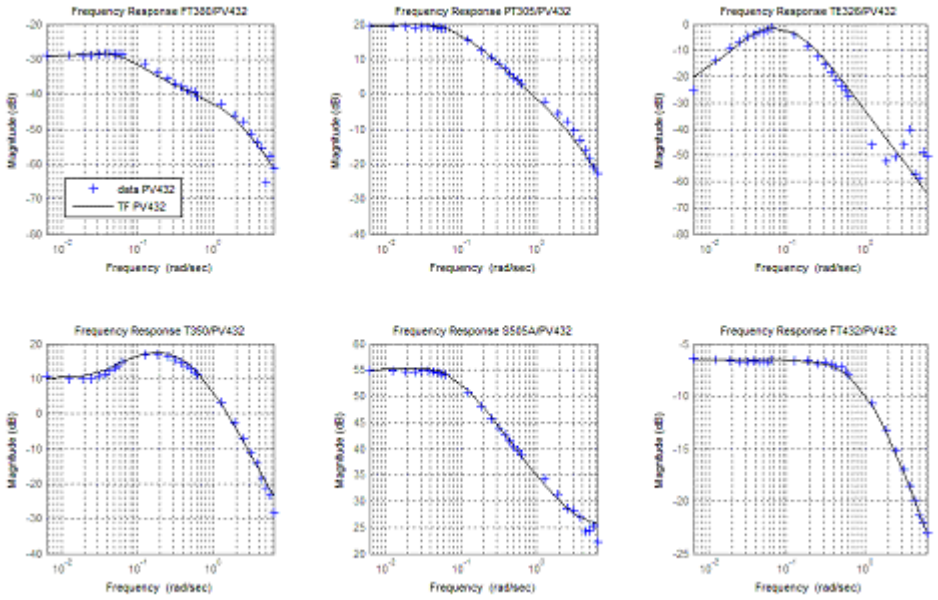

Figure 4.16 Generated and Test Data Bode Plots: Fuel Valve

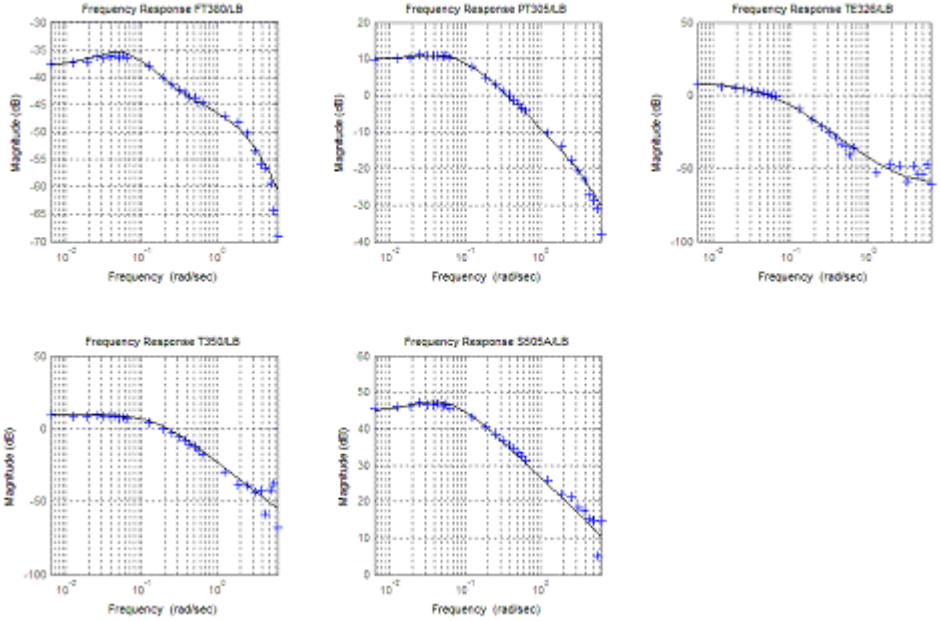

Figure 4.17 Generated and Test Data Bode Plots: Load Bank

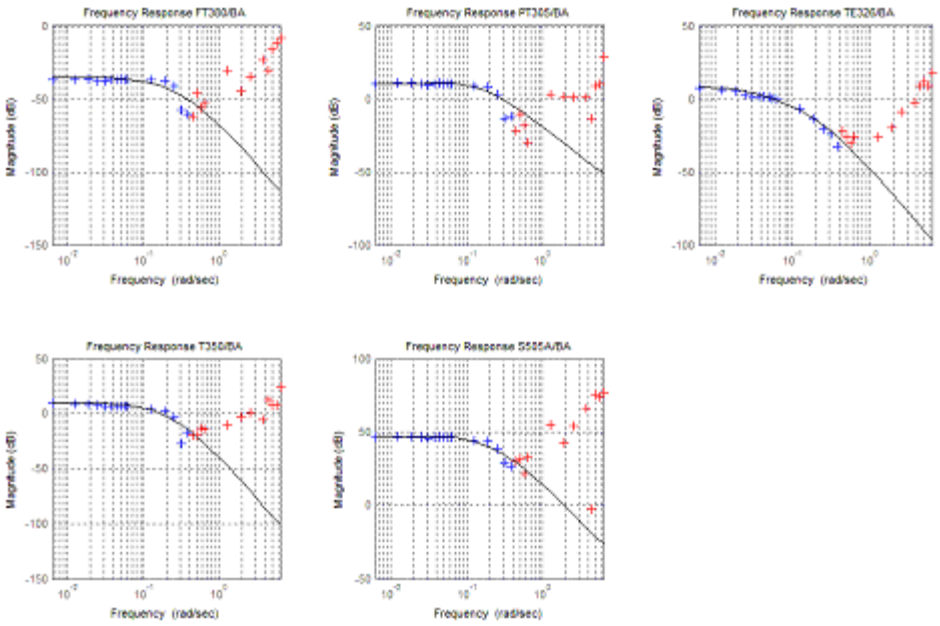

Figure 4.18 Generated and Test Data Bode Plots: Bleed Air Valve

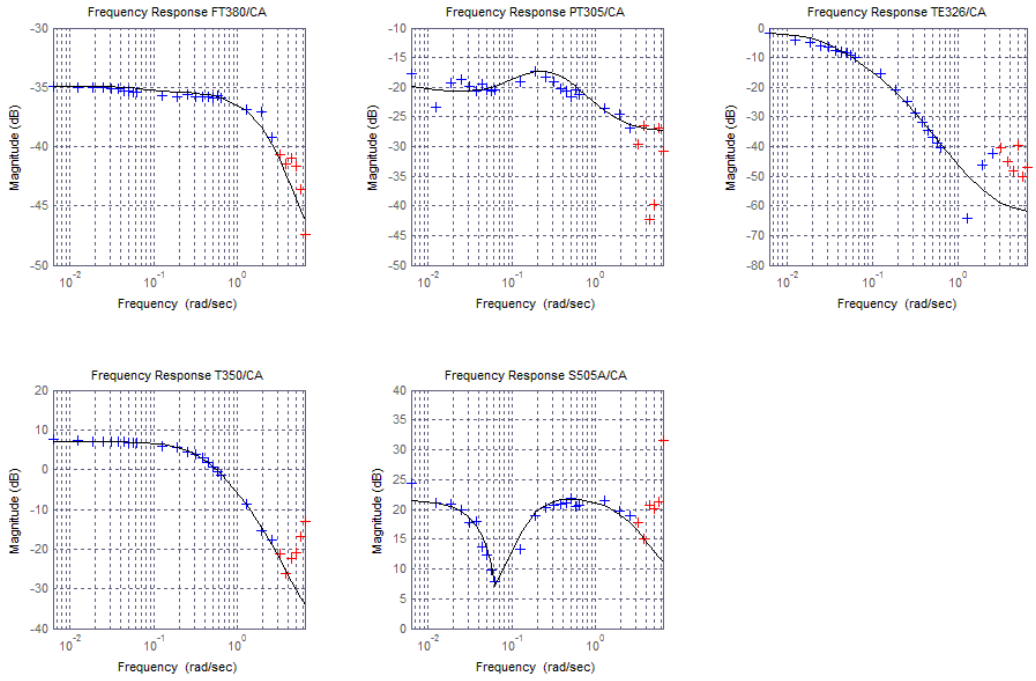

Figure 4.19 Generated and Test Data Bode Plots: Cold Air Valve

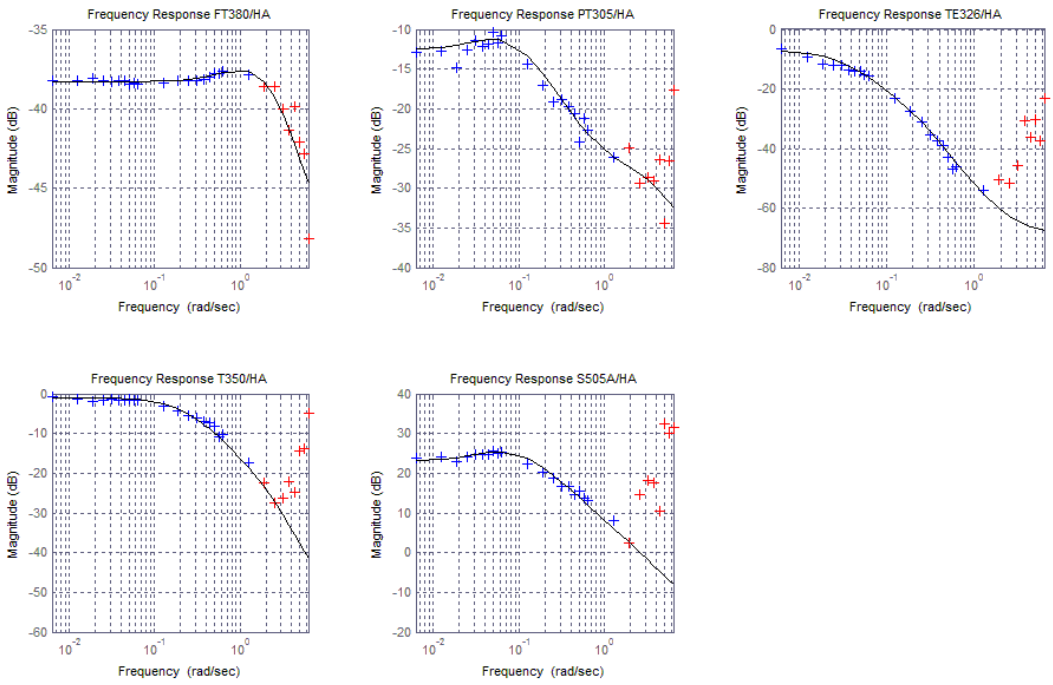

Figure 4.20 Generated and Test Data Bode Plots: Hot Air Valve

In order to incorporate the effect of the individual time delays, the exponential terms where replaced in MatLab by all pass first order Pade approximations, as given in Eq.4.1.28. This low order conversion is a possible source of error, but is required if the non-minimum phase behavior is to be modeled faithfully. The use of higher order Pade approximations is usually not warranted, for they add to the complexity of the model, and are most often the cause of detrimental effects in terms of computational time.

$$e^{-\tau_0 \cdot s} = \frac{2 - \tau_0 \cdot s}{2 + \tau_0 \cdot s} \qquad \text{Eq.4.1.28}$$

The system responses of the 3x3 matrix of Eq.4.1.2 for the CA, HA, and fuel valve step inputs are shown respectively in Figures 4.21-4.23. These are all open loop responses of the plenum airflow FT380, turbine inlet temperature TE350, and turbine speed S502A outputs of interest, as functions of CA valve Z170, HA valve ZC380, and fuel valve PV432. The solid blue line corresponds to the TF model response, while the noisy dark

plots are those of experimental data. The step values given to the manipulated variables are actual step percentages assigned during experimental tests. It is worth noting that the observed discrepancy between the model and data mass flow rates of Figure 4.23 are due to the fact that the open loop test data was conducted with the CA valve being opened at 34%. This would cause air that would otherwise route to the air plenum to be diverted. At no electrical load, the CA can divert as much as 20% of the airflow into the cathode, when opened at 35%. The model thus seems to overshoot the steady state value of the response by approximately 2.5%, at 45kW of electrical load.

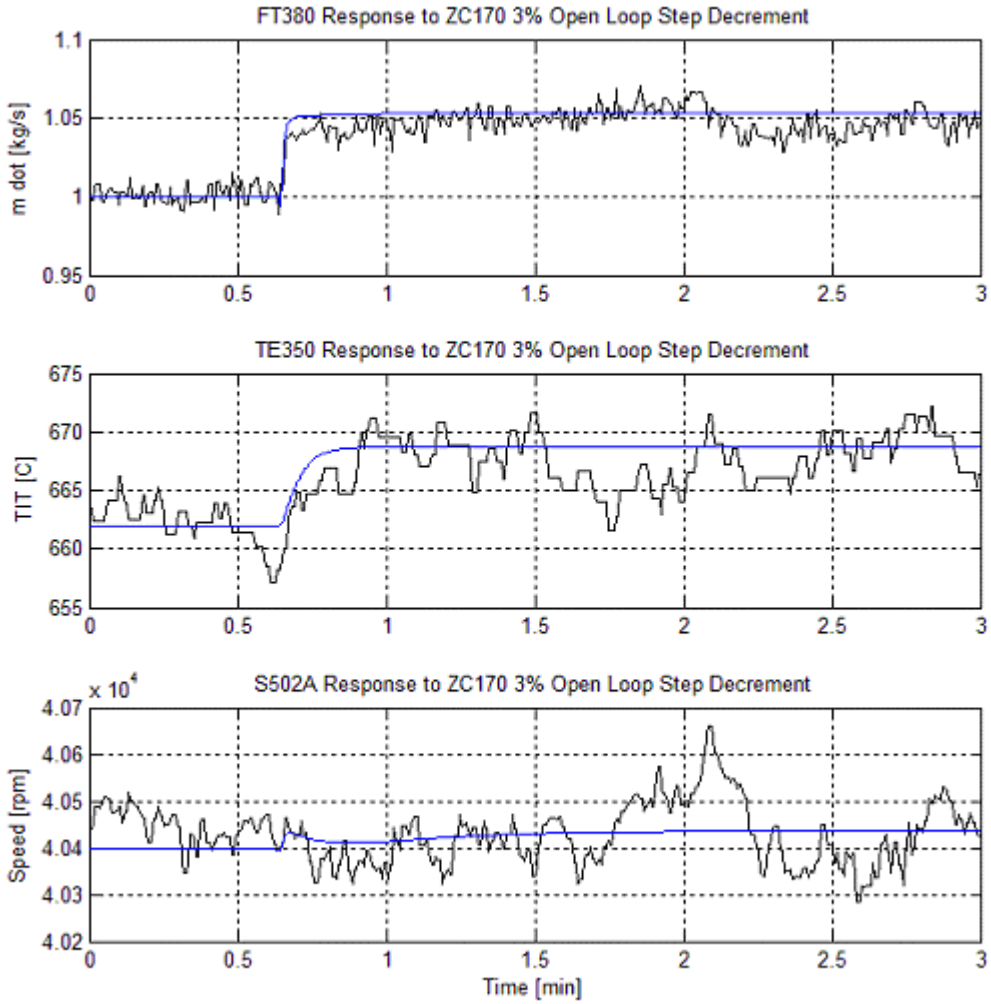

Figure 4.21 Cold Air Bypass Open Loop Step Response

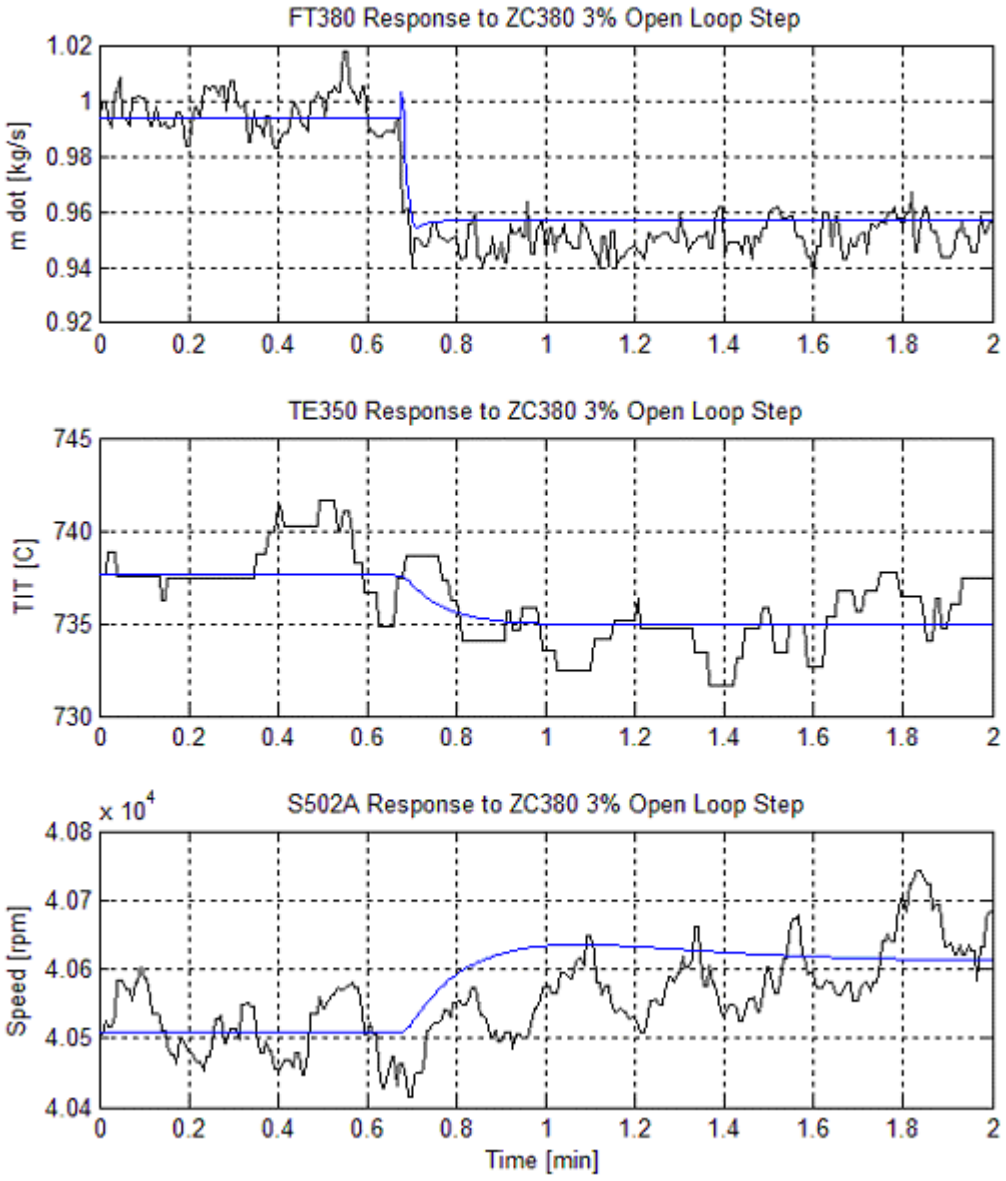

Figure 4.22 Hot Air Bypass Open Loop Step Response

These figures also show the measurement noise levels and quantization errors of the output signals, in particular that of the TIT. Due to the extensive use and hours of operation, most sheathed thermocouples of the HyPer facility required frequent replacement. This lead to sporadic instances of signal loss.

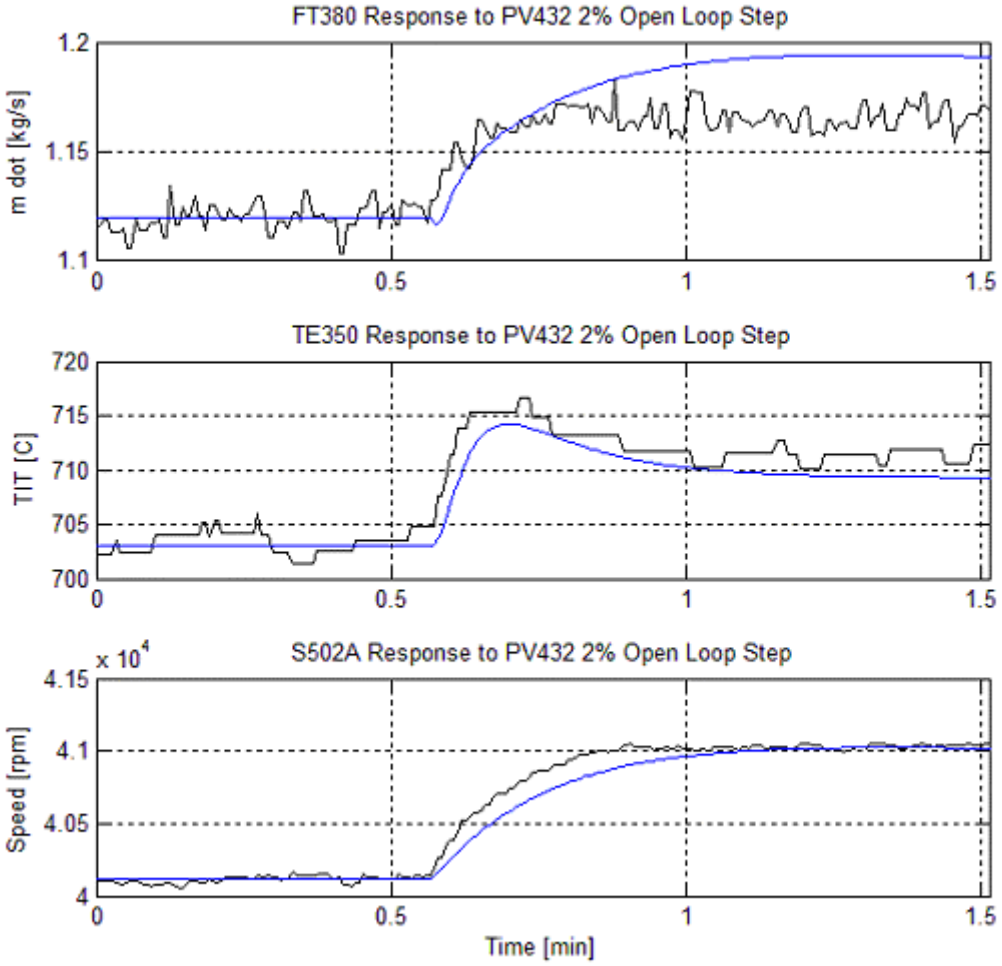

Figure 4.23 Fuel Valve Open Loop Step Response

When the 5x5 matrix is analyzed, large RGA numbers appear in the matrix elements. This is indicative of an ill-conditioned plant that is extremely difficult to control. The condition number for this plant was in fact $\kappa = 253.5$, too high for adequate control. As a comparison, literature suggests that condition numbers in the range between 10-20 are feasible plants to control. As will be further discussed, convergence of the state space robust algorithm was unsuccessful for the 5x5 system, proof of the need for additional inputs, and loss of controllability.

It was stated that the original 5x5 Transfer Function matrix was reduced to a 3x3 system. The simplified version consists of the CA, HA, and fuel valve actuator inputs, and the FC mass flow rate, TIT, and turbine speed outputs, as expressed in Eq.4.1.2. One of the main rationales for the revision is the physical inability to successfully control the plenum temperature without the use of an additional bypass valve. All the existing valves have a strong influence on the plenum flow, but not on temperature in an uncoupled manner. Also, the plenum pressure is more constrained by the difference in pressure across the electrolyte membrane of a fuel cell, rather than on the cathode side route.

The BA valve has shown to be more effective in mitigating emergency transient effects, such as avoidance of compressor stall/surge, than as a mass flow rate control actuator that would be used under normal operation. The load bank input on the other hand is best modeled as a disturbance rather than a command signal, as would be the case in real life.

Equation 4.1.29 shows a disturbance model matrix that will be used as part of the controller shown in the upcoming sections. The disturbance model incorporates both the load bank and the fuel valve as inputs. The fuel valve TF is used in the disturbance model because FC disturbance heat is superimposed on the combustor heat when the syngas FC model is in use. The syngas model activates the fuel valve in response to measured HyPer variables. A steady heat flow however is always required to run the turbine at nominal speed. This matrix is incorporated into the Simulink control configuration shown in section 4.1.5.2.

$$\begin{bmatrix} \dot{m}_{FT380} \\ T_{T350} \\ \Omega_{S505} \end{bmatrix} = \begin{bmatrix} G_{14}(s) & G_{15}(s) \\ G_{44}(s) & G_{45}(s) \\ G_{54}(s) & G_{55}(s) \end{bmatrix} \cdot \begin{bmatrix} FV_{PV432} \\ LB_{kW} \end{bmatrix} \qquad \text{Eq.4.1.29}$$

4.3 RGA and System Singular Values

Equation 4.1.30 shows the Relative Gain Array values of the Transfer Function matrix of Eq.4.1.2, evaluated at zero frequency. According to this matrix, the plenum airflow is best controlled with the HA valve, the turbine inlet temperature with the CA and fuel valves, and the turbine speed with the fuel valve. The negative numbers indicate cross couplings to avoid, if decentralized control is attempted. Note that the order of rows are: $\dot{m}_{FC}$, TIT, Ω, and the order of the columns are: CA, HA, and fuel valve. Figure 5.24 displays the RGA values as a function of frequency. These values are obtained by evaluating the RGA matrix one frequency at a time, and expressing the complex results as positive scalars i.e. absolute values. Hence the figure illustrates times at which coupling between inputs and outputs have fully developed, and have the greatest impact on each other. Each of the plotted lines corresponds to the absolute value of one of the 9 elements of the RGA matrix. Shown in red is element (1,2), mass flow rate as a function of HA bypass valve opening.

$$RGA(0) = \begin{bmatrix} -1.3156 & 2.4300 & -0.1144 \\ 2.3327 & -1.3868 & 0.0541 \\ -0.0171 & -0.0432 & 1.0603 \end{bmatrix} \qquad \text{Eq.4.1.30}$$

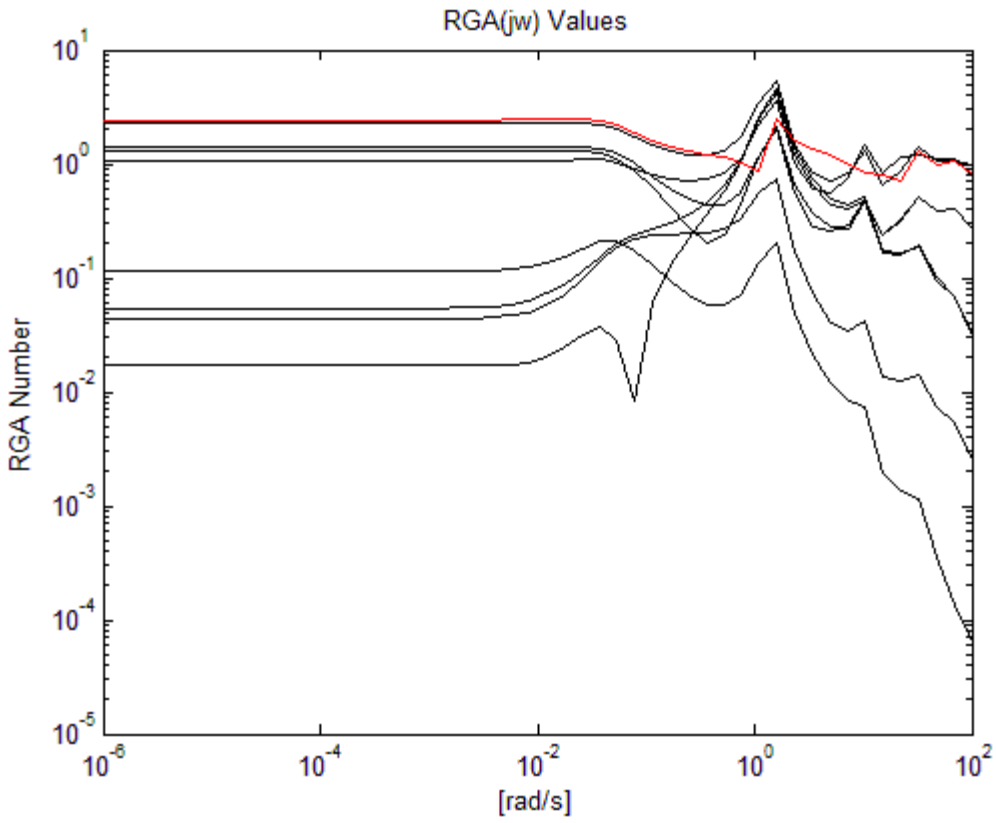

Figure 4.24 Relative Gain Array

Figure 4.24 illustrates the development of full system coupling at frequencies between 0.01rad/s and 0.1rad/s. The values below these frequencies pertain to the absolute value of the elements in Eq.4.1.30. The high frequency region above 1rad/s gives no valuable information, in terms of the effective coupling between variables, mostly because the frequencies are physically unattainable. The distorted contour in this range is a consequence of the mathematical computation of the RGA matrix.

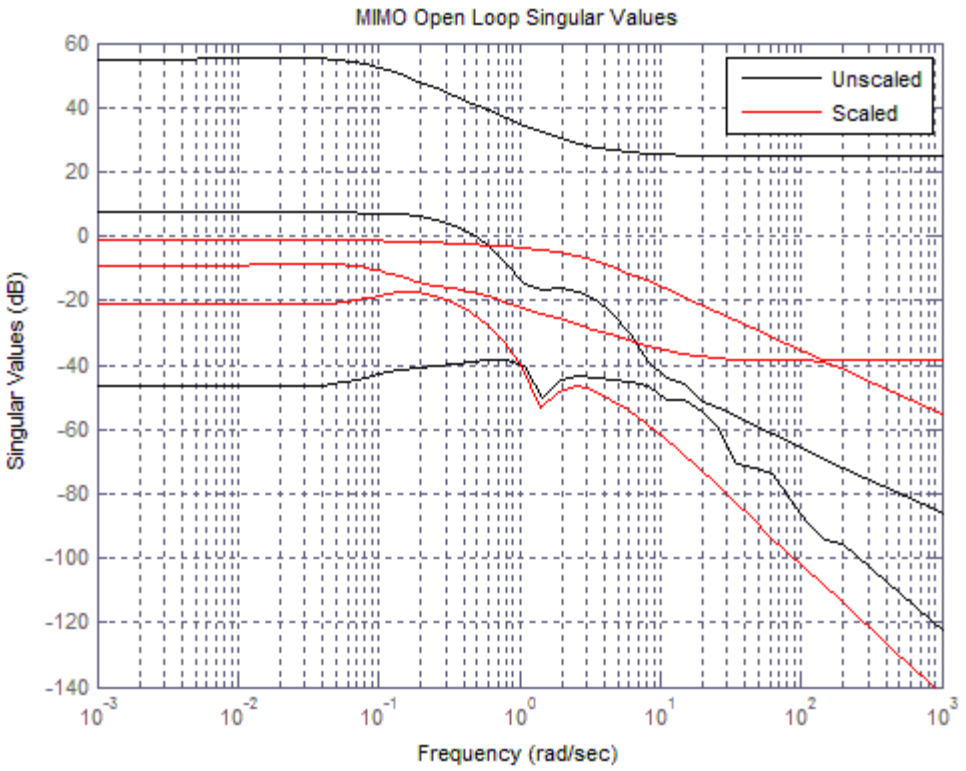

Figure 4.25 Scaled and Unscaled Open Loop Singular Values

When analyzing the plant, scaling is of the utmost importance, for without it, there is no equative degree of comparison between individual disturbances. Figure 4.25 is a plot of the scaled and unscaled singular values of the matrix of Eq.4.1.2 as a function of frequency. The black lines are the singular values of the 3x3 matrix, whereas the red lines correspond to the scaled singular values. Scaling is necessary to properly interpret and manipulate the sensitivity function. An unscaled sensitivity function is of no value when deriving a controller because of the disparate representation of the system gains. It also lessens the effort of designing and selecting shaping weights, as described in the following sections. By pre and post multiplication of input and output scaling matrices to the open loop matrix, a bounded unitary response can thus be attributed to the maximum allowable value a certain output can have, for a bounded unitary input. Equations 4.1.31-4.1.33 give the scaling factor matrices, where W_{pre} contains the allowable output deviations, and W_{post}, the allowable input deviations.

$$G_{scaled}(s) = W_{pre}^{-1} \cdot G_p(s) \cdot W_{post} \qquad \text{Eq.4.1.31}$$

$$W_{pre} = diag(\Delta\dot{m}_{FC}, \Delta T_{TIT}, \Delta\Omega) = diag\left(0.3\frac{kg}{s}, 50K, 1500rpm\right) \qquad \text{Eq.4.1.32}$$

$$W_{post} = diag(\Delta CA, \Delta HA, \Delta PV) = diag(10\%, 10\%, 1\%) \qquad \text{Eq.4.1.33}$$

Figure 4.26 shows the sensitivity function of Equation 4.1.31. It is clearly seen that the scaled plant is sensitive to low frequency perturbations, as noted by the upper singular value peak above 0dB. The plot also shows that there is poor reference tracking due to the position of the open loop gain singular values being dispersed as well. The scaled system is sensitive to disturbances because $\overline{\sigma} > 0dB$ at all tested frequencies.

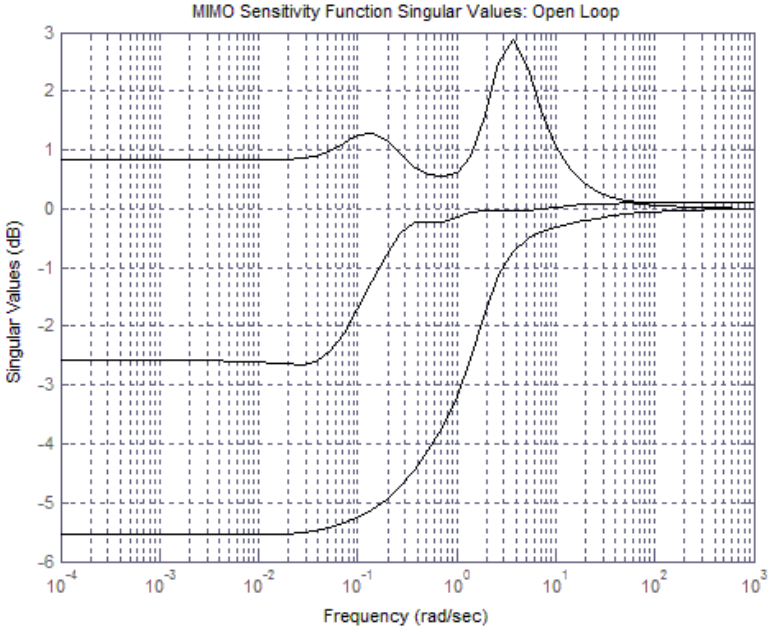

Figure 4.26 Open Loop Sensitivity Function

4.4 Loop Gain Weight Selection

In order to properly select the loop gain weights as described in the procedure of Chapter 3, time delays and RHP zeros must first be determined for the MIMO plant. These

constitute restrictions on the performance weights in terms of achievable control bandwidth. A transmission zero of z = 0.1455rad/s was found to limit the first order Transfer Function weight given in Equation 4.1.34. The RHP zero is given by ω_c , while ω_s is a small arbitrarily chosen frequency. With the use of ω_s computational errors in the solution of the Hamiltonian matrices of the H_∞ algorithm are avoided. Equation 4.1.34 gives the lower bound for the control performance criteria that must be met. In this case, the crossover frequency is that of the RHP zero. The zero of Eq.4.1.34 is placed at 10 decades before the crossover frequency to allow enough margin for all the singular values to roll off before ω_c. This gives a crossover slope of –20dB/dec when multiplied to the open loop plant singular values.

$$W_S = \frac{(s + 0.1 \cdot \omega_c)}{(2 \cdot s + \omega_s)},\ \omega_c \to RHPzero,\ \omega_s \approx 0.0001 \qquad \text{Eq.4.1.34}$$

An upper admissible bound for system robustness is given in Eq.4.1.35. To make this Transfer Function weight proper, a zero is included two decades after the weight pole, located at $100\omega_c$. The inclusion prevents the weight from affecting the plant dynamics. Figure 4.27 shows the upper and lower bounds, together with the scaled open loop singular values. The blue line corresponds to the performance weight of Eq.4.1.34, and the red line to the robustness weight of Eq.4.1.35, in particular W_T^{-1}.

$$W_T = \frac{\left(\frac{1}{\omega_c} \cdot s + 1\right)^2}{\left(\frac{1}{100 \cdot \omega_c} \cdot s + 1\right)} \qquad \text{Eq.4.1.35}$$

The goal of the controller as seen in the frequency domain, is to manipulate the loop gain singular values, shown in black, to lay within the area encapsulated by the intersection of the upper and lower bounds.

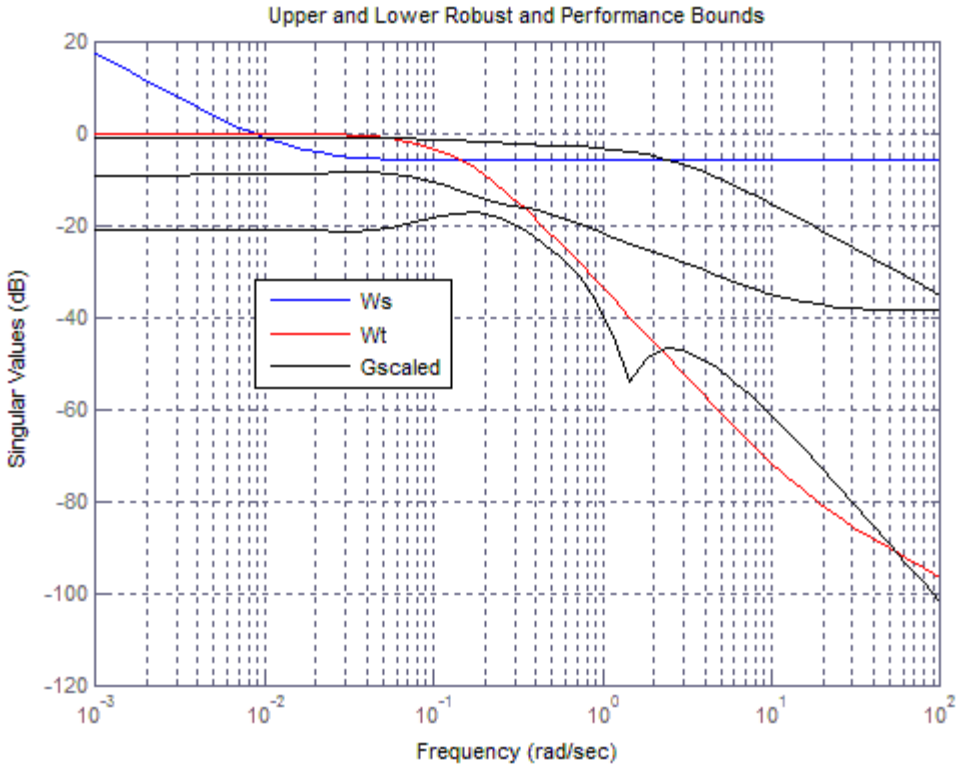

Figure 4.27 Performance and Robustness Bounds

According to the algorithm detailed in Chapter 3, the open loop Transfer Function scaled matrix is first multiplied by a dynamic weight, to shape the loop gain. The performance weight is given in Equation 4.1.36. This weight includes double poles at ω_s so that the low frequency gain is increased at a rate of 40dB/dec. The pole at $0.05\omega_n$ rolls off the compensated singular values at –40dB/dec, right before the uncertainty frequency limit pertaining to the highest frequency tested of 1Hz. The dynamics of the weight is equally introduced in all the input channels with the diagonal identity matrix. Finally, the constant A adjusts the weight's magnitude, so that the zero at $0.02\omega_c$ can smoothly roll off the singular values at the crossover frequency. The value of A is 0.0024.

$$W_P(s) = \frac{A \cdot (s + 0.02 \cdot \omega_c)}{(s + \omega_s)^2 \cdot (s + 0.051 \cdot \omega_n)^2} \cdot I \qquad \text{Eq.4.1.36}$$

$$\omega_n \approx 2 \cdot \pi \cdot f \ , \ f = 1[Hz]$$

Once the singular values of the open loop matrix are shaped with the use of the dynamic compensator W_p, they must be brought close together around the crossover frequency in order to meet the performance and robustness bounds simultaneously. Glad and Ljung propose a method by which a specific SV loop gain can be moved to the vicinity of an adjacent SV. Eq.4.1.37 defines the loop gain, where L_L is evaluated at half the crossover frequency. This constant gain matrix W_1 is given by Eq.4.1.41, U and V being the output and input direction matrices of the singular value decomposition representation.

$$L_L = G_p \cdot W_p = U_L \cdot \Sigma_L \cdot V_L^* \qquad \text{Eq.4.1.37}$$

$$U_L = \begin{bmatrix} -0.8605 & -0.1652 & -0.4819 \\ -0.4851 & -0.0229 & 0.8741 \\ -0.1554 & 0.9860 & -0.0604 \end{bmatrix} \qquad \text{Eq.4.1.38}$$

$$\Sigma_L = \begin{bmatrix} \sigma_1 & 0 & 0 \\ 0 & \sigma_2 & 0 \\ 0 & 0 & \sigma_3 \end{bmatrix} = \begin{bmatrix} 0.2298 & 0 & 0 \\ 0 & 0.0690 & 0 \\ 0 & 0 & 0.0269 \end{bmatrix} \qquad \text{Eq.4.1.39}$$

$$V_L = \begin{bmatrix} -0.8295 & -0.2450 & 0.5018 \\ -0.5281 & 0.0519 & -0.8476 \\ -0.1817 & 0.9681 & 0.1724 \end{bmatrix} \qquad \text{Eq.4.1.40}$$

$$W_1 = I + \frac{(\sigma_1 - \sigma_3)}{\sigma_3} \cdot V \cdot V^T \qquad \text{Eq.4.1.41}$$

$$W_1 = \begin{bmatrix} 2.8959 & -3.2024 & 0.6514 \\ -3.2024 & 6.4092 & -1.1003 \\ 0.6514 & -1.1003 & 1.2238 \end{bmatrix} \qquad \text{Eq.4.1.42}$$

The pre-compensated gain matrix above is post multiplied to the loop gain of Eq.4.1.37 as shown in Eq.4.1.43. It is this new compensated loop gain L that is represented in state space form and subsequently used as the plant in the robust H_∞ algorithm.

$$L = G_{scaled} \cdot W_P(s) \cdot W_1 \qquad \text{Eq.4.1.43}$$

4.5 Controller Performance

The current section presents the results of the Glover-McFarlane H_∞ algorithm, for two slightly distinct versions, one proposed by Glad and Ljung (2000), and the other by Skogestad and Postlewaithe (2005) Appendix E lists the MatLab m-files that generate the robustification solution described in Chapter 3. The infinity norms of the Glover-McFarlane, and the Co-Prime algorithms were $\gamma = 1.9111$, and $\gamma = 1.7374$ respectively. These values, being less than 4, indicate a successful derivation of a robust controller.

4.5.1 Compensated Singular Values

Figure 4.28 shows the loop gain singular values of the compensated plant. It can be seen that all lay within the performance and robust bounds, with a transition slope of approximately –20dB/dec at the crossover frequency. The singular values are also closer at the crossover. This is the best shape achievable under the RHP zero limitation. A closer look at the plot shows of singular values lumped together within a third of a decade.

Figures 4.29 and 4.30 display the compensated sensitivity and co-sensitivity function singular values. There is a smooth decay of both functions for the low and high frequency ranges, as desired. This means that disturbance rejection and good tracking is achieved for the low frequencies, and uncertainties due to un-modeled dynamics are taken care of. Comparison between Figures 4.26 and 4.29 demonstrates the effectiveness of the methodology in rejecting disturbances.

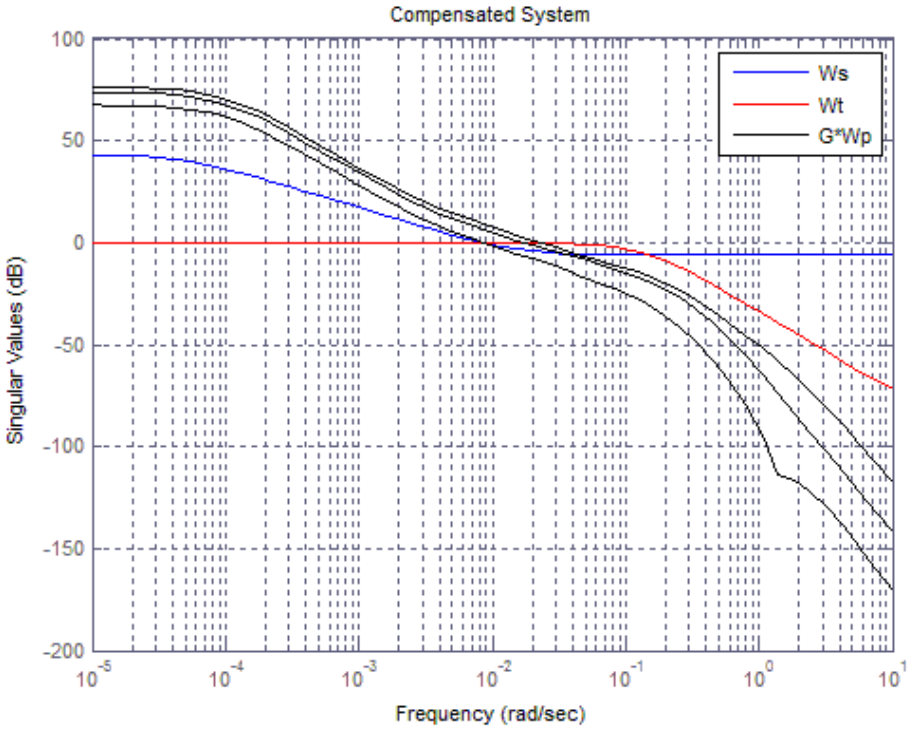

Figure 4.28 Compensated Loop Gain Singular Values

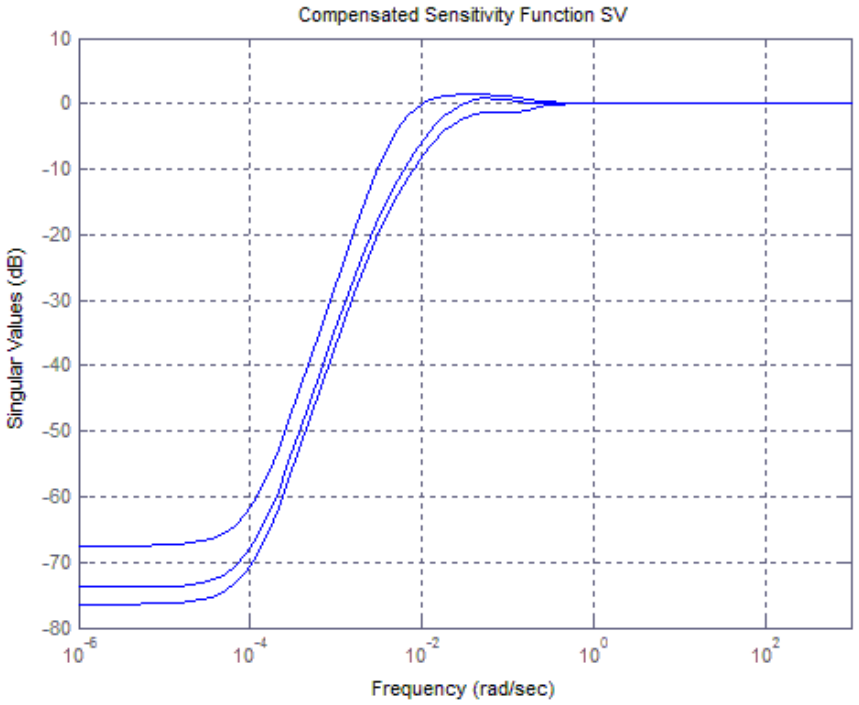

Figure 4.29 Compensated Sensitivity Function Singular Values

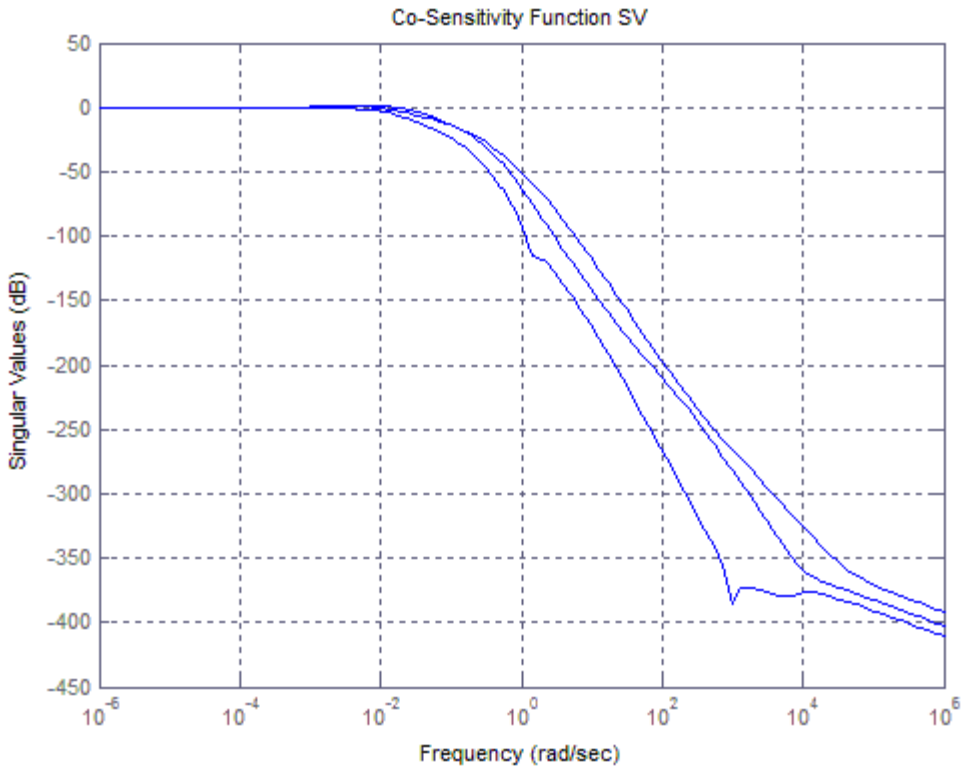

Figure 4.30 Compensated Complementary Sensitivity Function SV

4.5.2 Controller Implementation

The controller detailed in Chapter 3 is implemented in the Simulink environment, shown in Figure 4.31. Skogestad and Postlewaite suggest the given configuration with the use of a pre-filter K_c, used in the forward path, preceding the control loop. This pre-filter is nothing but the H_∞ controller evaluated at dc, and is given in Eq.4.1.44. It is placed outside the control loop to avoid large overshoots that would result from excitation of the reference signals. The location of this pre-filter does not affect the dynamics of the robust controller in the feedback loop (Skogestad 2005).

$$K(0) = \begin{bmatrix} -0.3253 & -0.5454 & 0.0298 \\ -0.5558 & 0.3355 & -0.0136 \\ -0.0115 & -0.0180 & -0.6244 \end{bmatrix} \qquad \text{Eq.4.1.44}$$

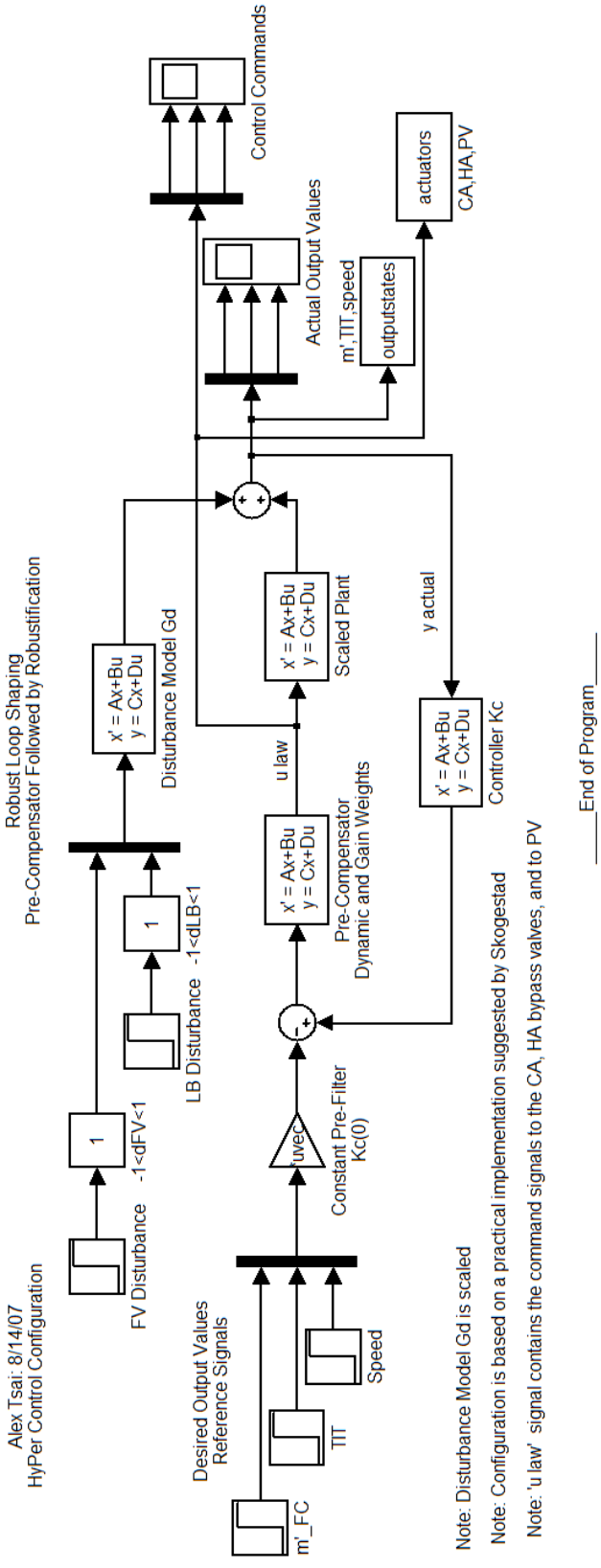

Figure 4.31 Simulink Control Configuration

4.5.3 Reference Tracking and Regulation

Figures 4.32 to 4.43 plot various cases of the compensated system's simultaneous response for plenum airflow, TIT, and turbine speed, to fuel and load disturbances as well as for desired output tracking commands. Plots of the actuator control signals for the CA, HA, and fuel valve are also given. The values shown are for the scaled plant, thus the CA and HA valves must be multiplied by a factor of 10 in order to scale back to the actual valve positions. The fuel valve position shown is the actual valve value, because the scale factor used was 1. Note that tracking is to step input signals. The actual outputs must be scaled back to real values by piecewise multiplication of Eq.4.1.32. Speed of response, once again, is affected by the transmission MIMO zero. The largest time constant observed for a transient event is approximately 2min for the speed output signal. On average, the time constants of the output responses lay within 1min.

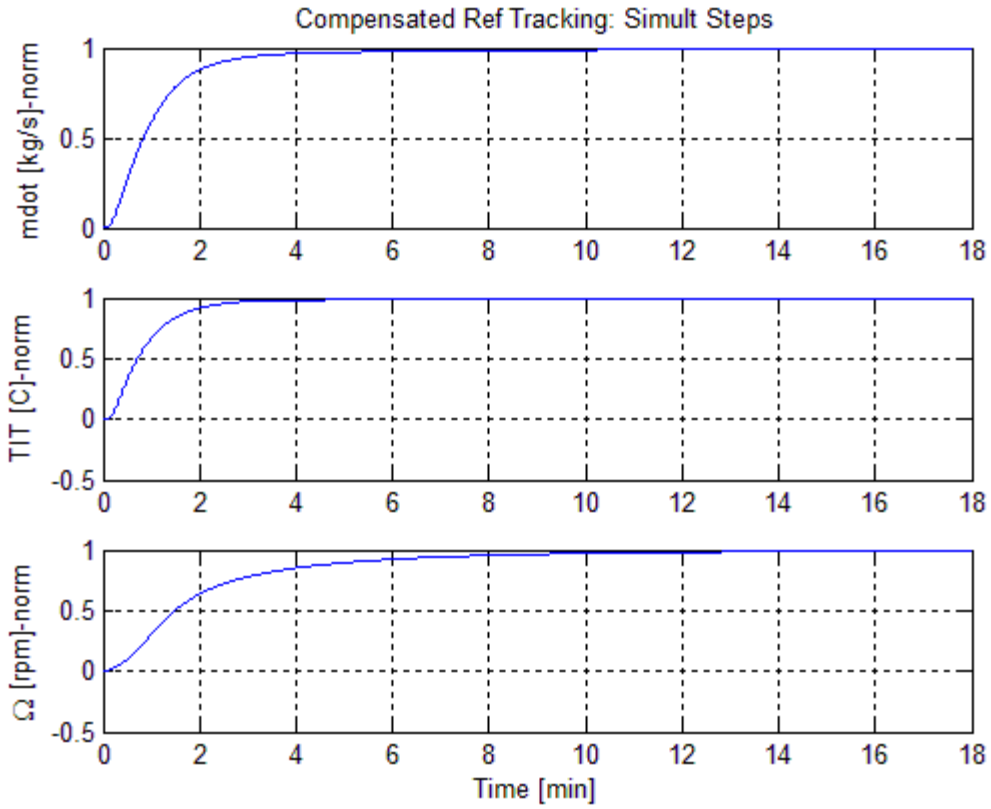

Figure 4.32 Signal Reference Tracking: Step Command

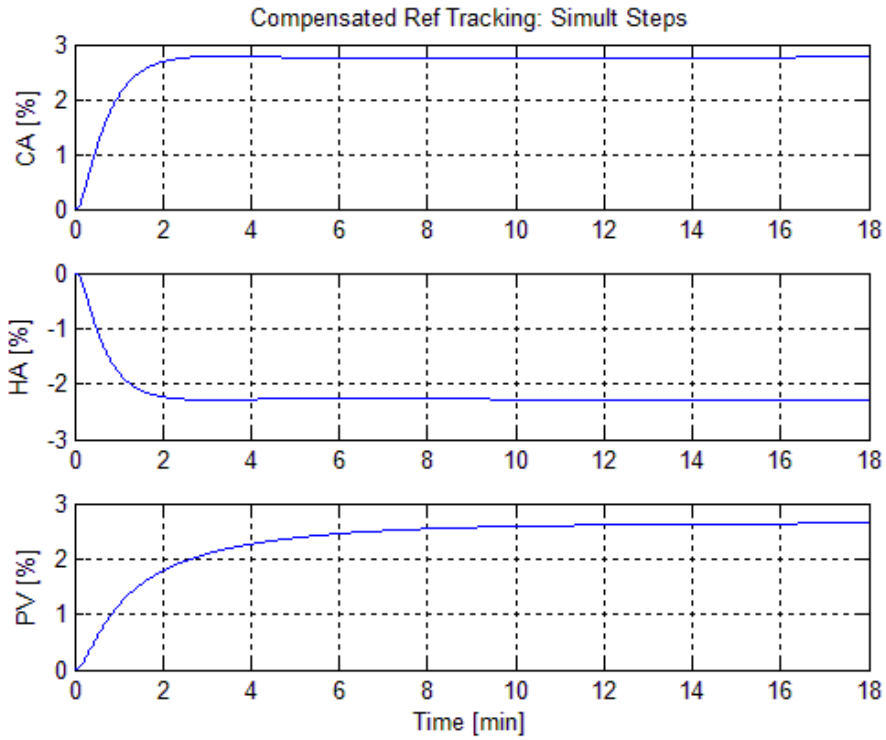

Figure 4.33 Control Signal: Simultaneous Step Tracking

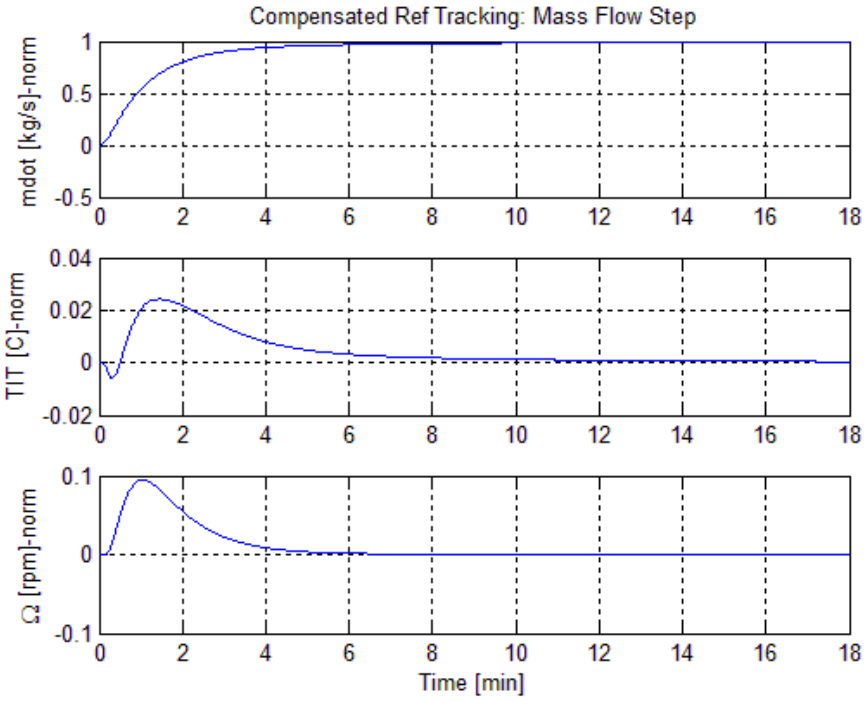

Figure 4.34 Signal Tracking: $\dot{m}_{FC}$

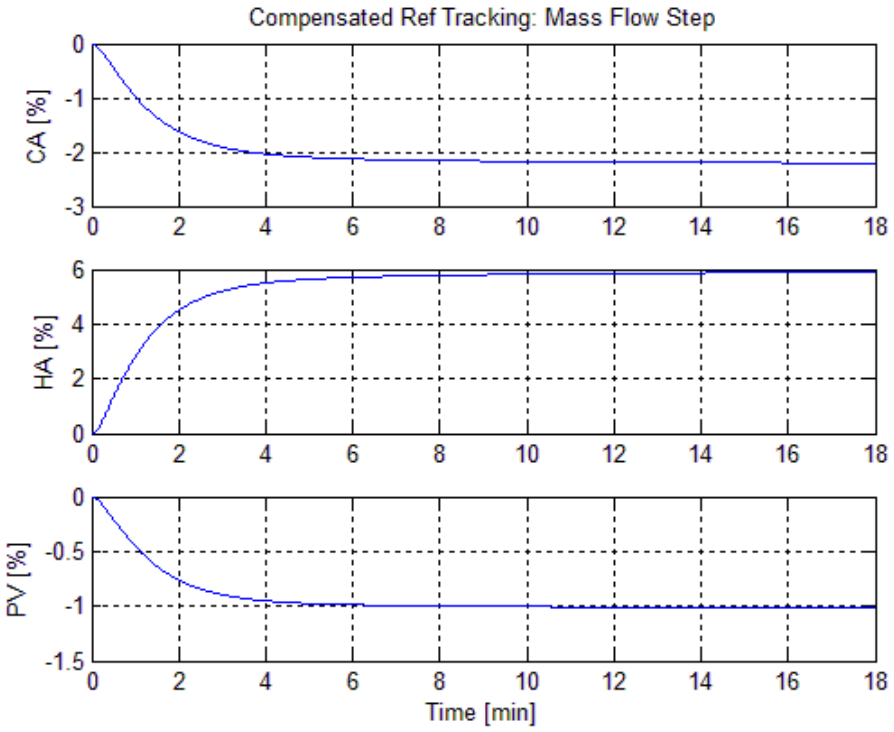

Figure 4.35 Control Signal: $\dot{m}_{FC}$ Tracking

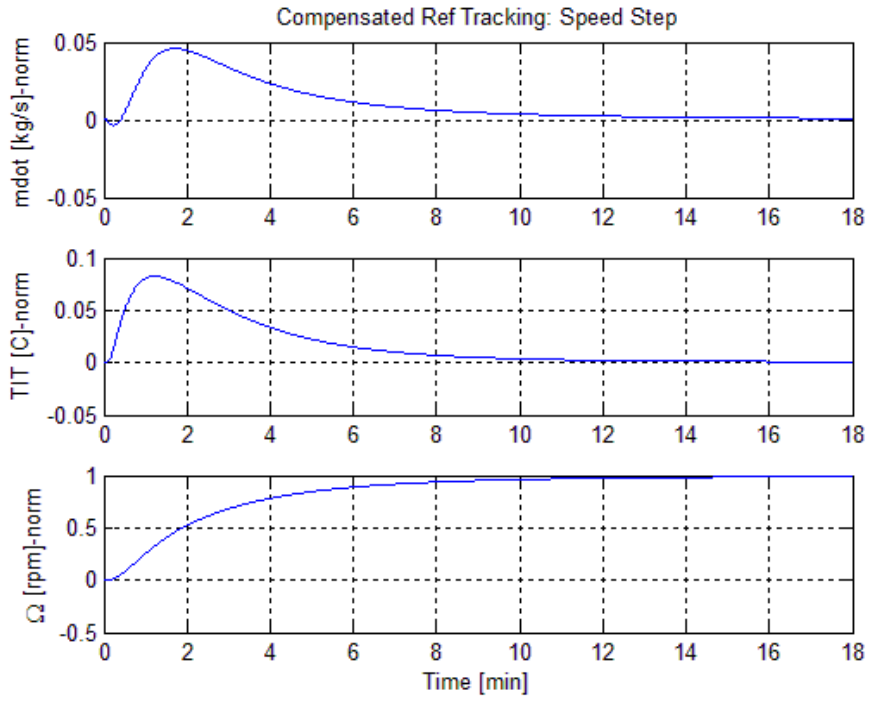

Figure 4.36 Signal Tracking: Ω

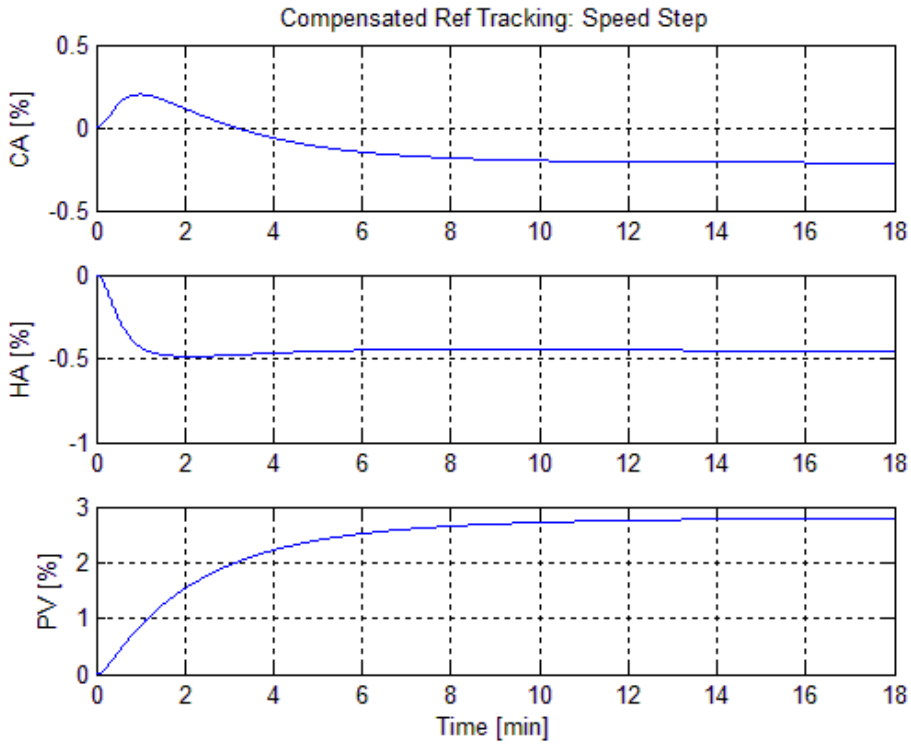

Figure 4.37 Control Signal: Ω Tracking

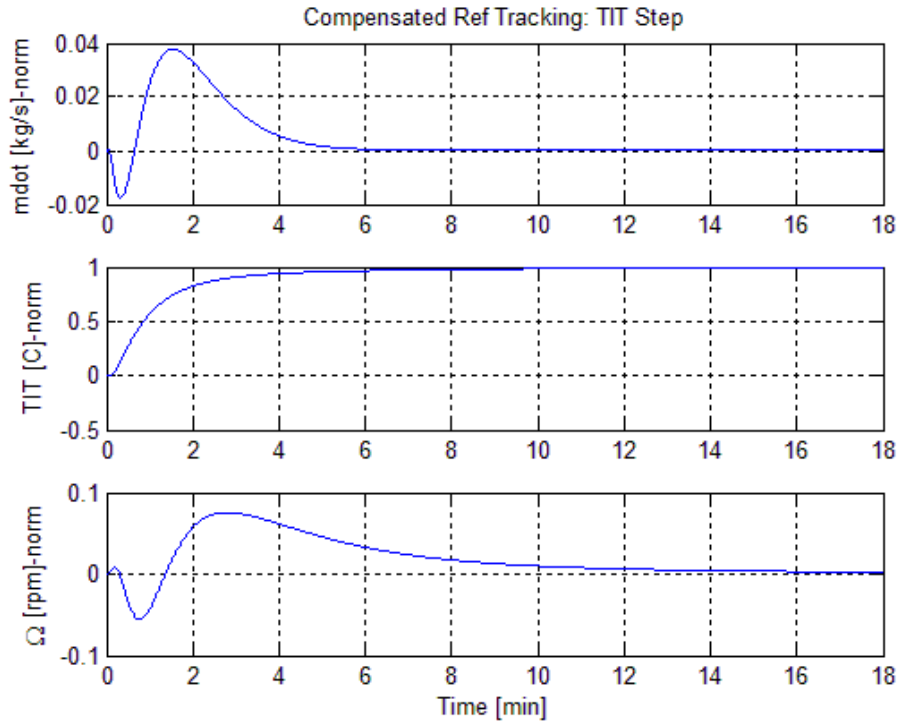

Figure 4.38 Signal Tracking: TIT

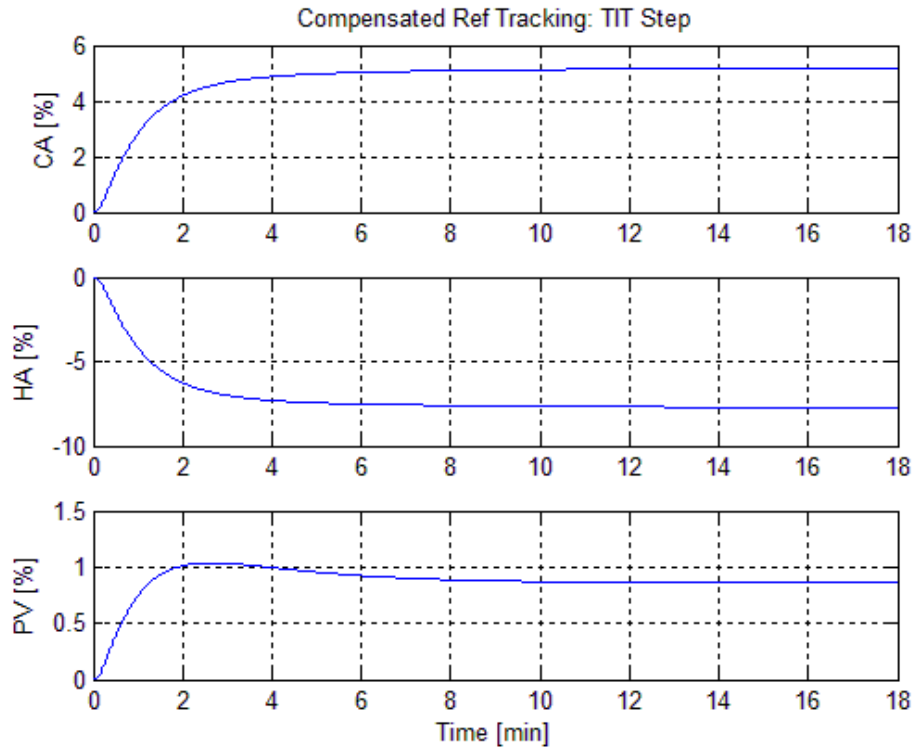

Figure 4.39 Control Signal: TIT Tracking

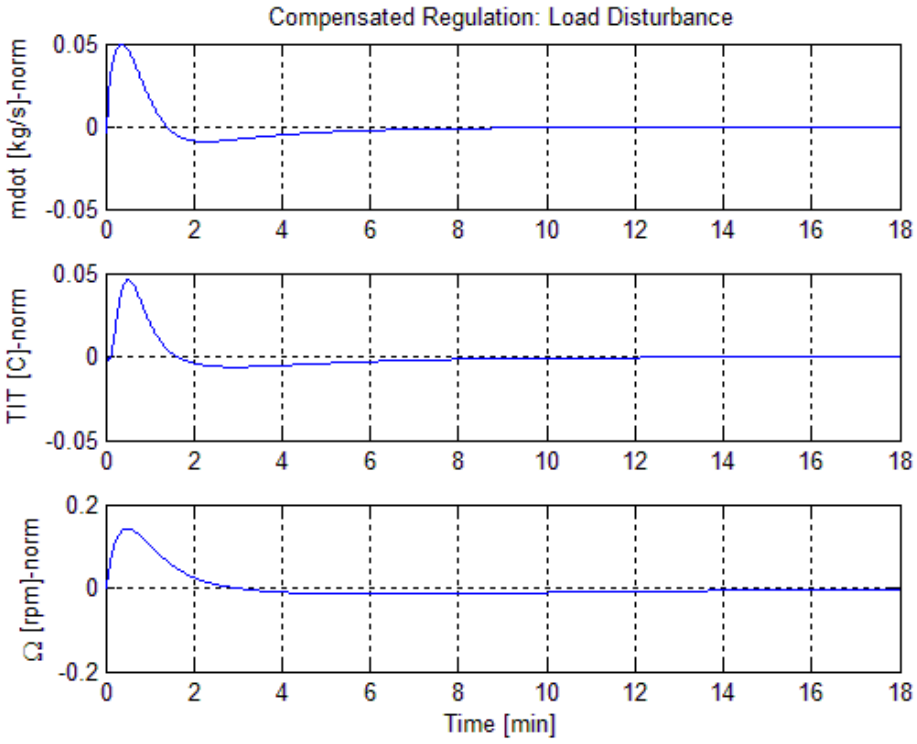

Figure 4.40 Load Step Disturbance Attenuation

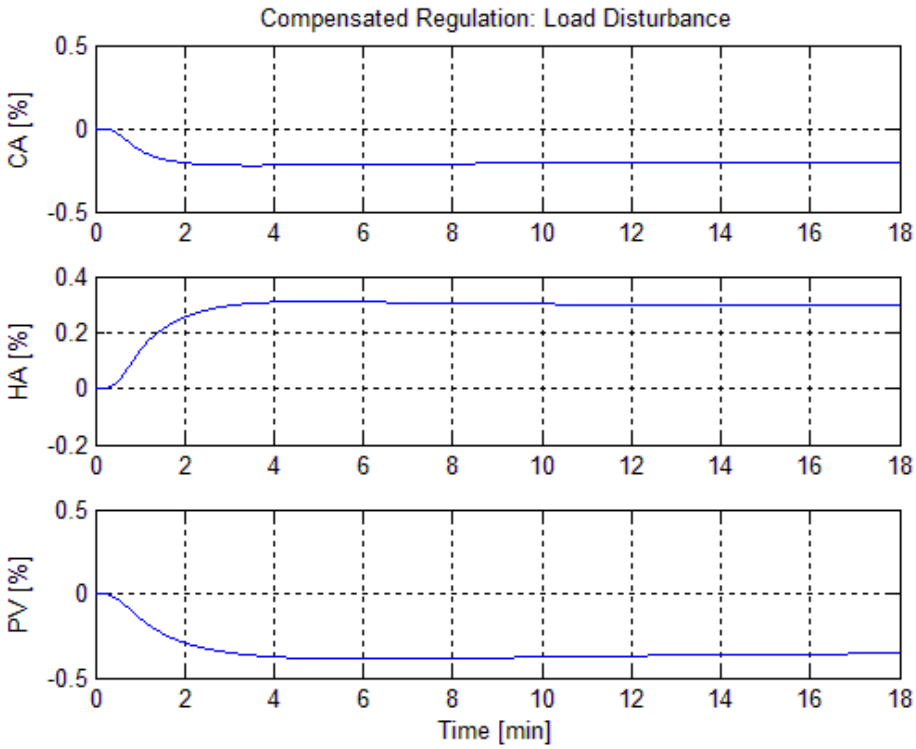

Figure 4.41 Control Signal: Load Disturbance

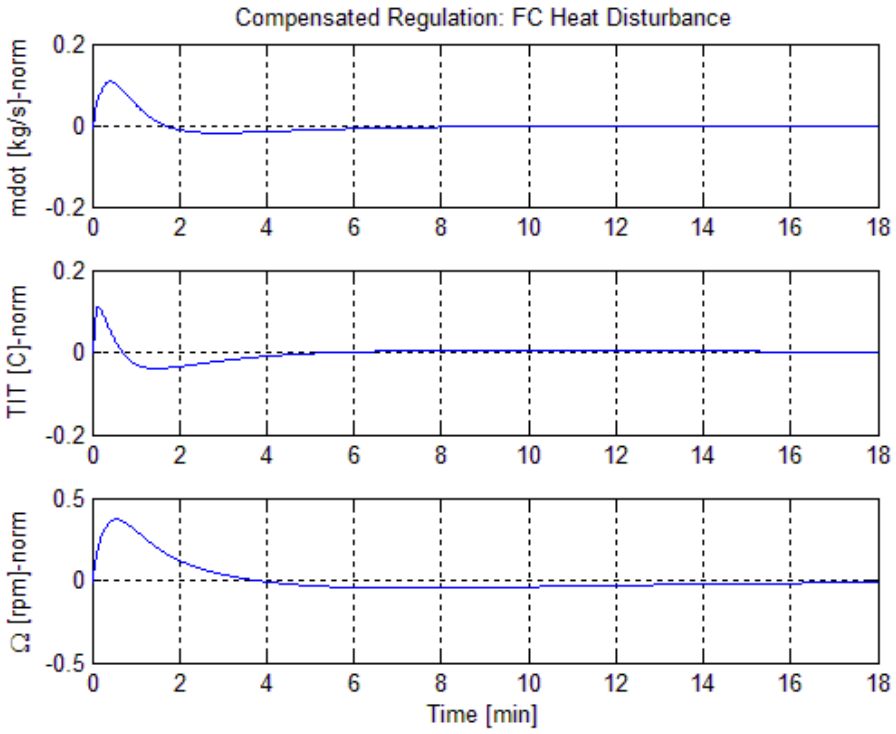

Figure 4.42 Heat Step Disturbance Attenuation

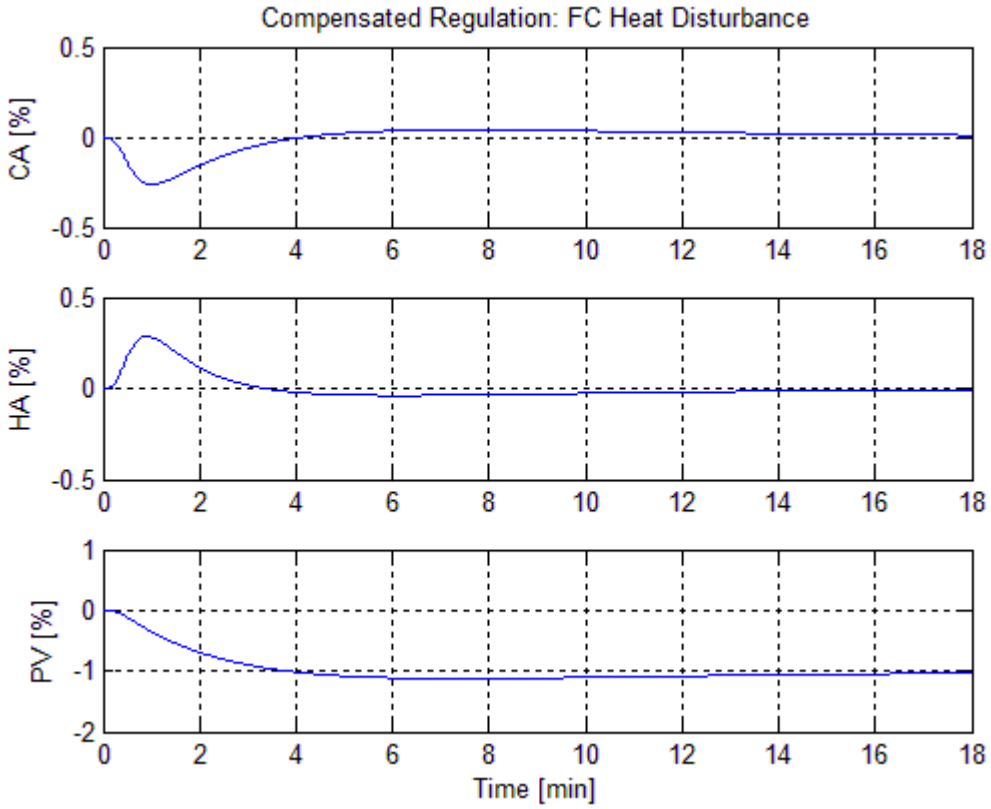

Figure 4.43 Control Signal: Heat Disturbance

In Figures 4.32 to 4.43 the input signals of CA, HA, and PV are scaled, hence their true values are obtained by multiplying factors of 10, 10, and 1 to each signal respectively. Thus in Figure 4.33 for example, the CA, HA, and PV actual steady state valve percentages are approximately 27% opened, 23% closed, and 2.6% opened from their nominal operating values, defined by the zero set point. The mass flow rate, TIT, and turbine speed must be multiplied by factors of 0.3kg/s, 50K, and 1500rpm to scale back to their true values.

Figure 4.32 shows the system response to simultaneous steps in mass flow, TIT, and turbine, while Figure 4.33 the respective control law. In the same manner, plots of system response and consequent actuator response are given for individual one at a time reference steps. In Figure 4.35 for example, a mass flow step increase of 0.3kg/s is

commanded, causing the CA valve to decrease by 20%, the HA valve to increase by 60%, and the PV valve to decrease by 1% from their nominal values. It might seem counter intuitive to open the HA this much, but a closer look indicates this is necessary if TIT and turbine speed response are to remain unvaried. When the fuel valve decreases by 1%~26kW, the TIT becomes colder as seen in Figure 4.34. It is then necessary to increase the HA valve to compensate for this and to increase speed at the same time, while closing the CA to augment airflow into the cathode. The result of the multivariate control law is that the mass flow tracks the command signal, regulating TIT and turbine speed at the same time, as seen in Figure 4.34.

In Figure 4.37, the detrimental effect of the RHP zero is seen as the system tracks a step increase in speed of 1500rpm. For this scenario the CA valve decreases by 2%, the HA decreases by 5%, and the fuel valve increases by 2.8%~74kW, or 24.7% of the fuel cell power. This results in almost negligible mass flow and TIT peaks, at the expense of controller tracking speed. This is the slowest response observed for the fuel valve, with a time constant of approximately 2.5min. It is possible that the sluggish behavior of the fuel valve for this scenario can be corrected by a shift of the RHP zero to a different output channel of least importance. This is further discussed in Chapter 6.

Figure 4.39 shows the control law response to a TIT command step of 50K. In this case, CA increases by 50%, fuel valve increases by 1%~26kW or 10% of the fuel cell power, while HA decreases by 75%. Closing the HA by this amount is not possible if the nominal operating valve opening is at 40%. If possible, closing the HA would maintain cathode airflow constant as seen in Figure 4.38. This indicates the necessary inclusion of an anti windup scheme that would compensate for valve saturation effects such as this one. The CA increase helps mitigate TIT overshoots by cooling it down, while increasing the cathode airflow. It is because of this additional increment in cathode airflow due to the CA opening, that the HA valve responds so drastically.

In Figures 4.40 to 4.43 the system response to input disturbances of generator load and fuel cell exhaust are seen. Figure 4.40 demonstrates the effectiveness in mitigating a

5kW~5% increase in electrical load. For this case, the fuel valve closes slightly, approximately 0.4%~10kW, while the HA valve opens to 3% to speed up the turbine. To regulate airflow to the cathode, the CA valve closes 2.5%. Similarly, Figures 4.42 and 4.43 show control regulation when a 1%~26kW step in fuel cell heat exhaust occurs. This heat increase is close to 10% of the total fuel cell power output. For this case, the CA and HA valves activate initially, but eventually drop to their nominal operating values. The fuel valve on the other hand, decreases by 1%, the same amount required to counteract the heat increase effect.

4.5.4 Uncertainty Analysis and Regulation

Model uncertainty is mostly expressed as parametric or unstructured uncertainty. Parametric uncertainty assigns a probability range to a set of variables within the model, mainly the poles and zeros of the Transfer Functions. In unstructured uncertainty, a frequency dependent bound is defined via a first order Transfer Function, such that the un-modeled dynamics are accounted for, similar to the post multiplication of the dynamic compensator in the robust algorithm. The approach used in this work is that of parametric uncertainty due to the seeming repeatability of poles and zeros in the derived Transfer Functions. By varying a common pole or zero that is present in various Transfer Functions, one can determine the analytical model accuracy needed for a certain identified balance of plant component. The complete MatLab script that analyzes uncertainty can be found in Appendix E.

In the written code, one or several Transfer Functions can be parametrically varied with the use of MatLab's "ultidyn" function. This function allows the user to build an uncertain linear time invariant dynamic model that contains varied poles and zeros. It is because of this that a wide variety of pole/zero combinations can be studied and examined for any divergence effects in the robust algorithm. Figure 4.44 shows one such combination, where all the poles and zeros of one particular Transfer Function were varied by 10%. There are 20 plotted lines representing 20 various random values of the

10% pole/zero variation. The controller allows for up to 41% variation in the poles and zeros of the particular Transfer Function.

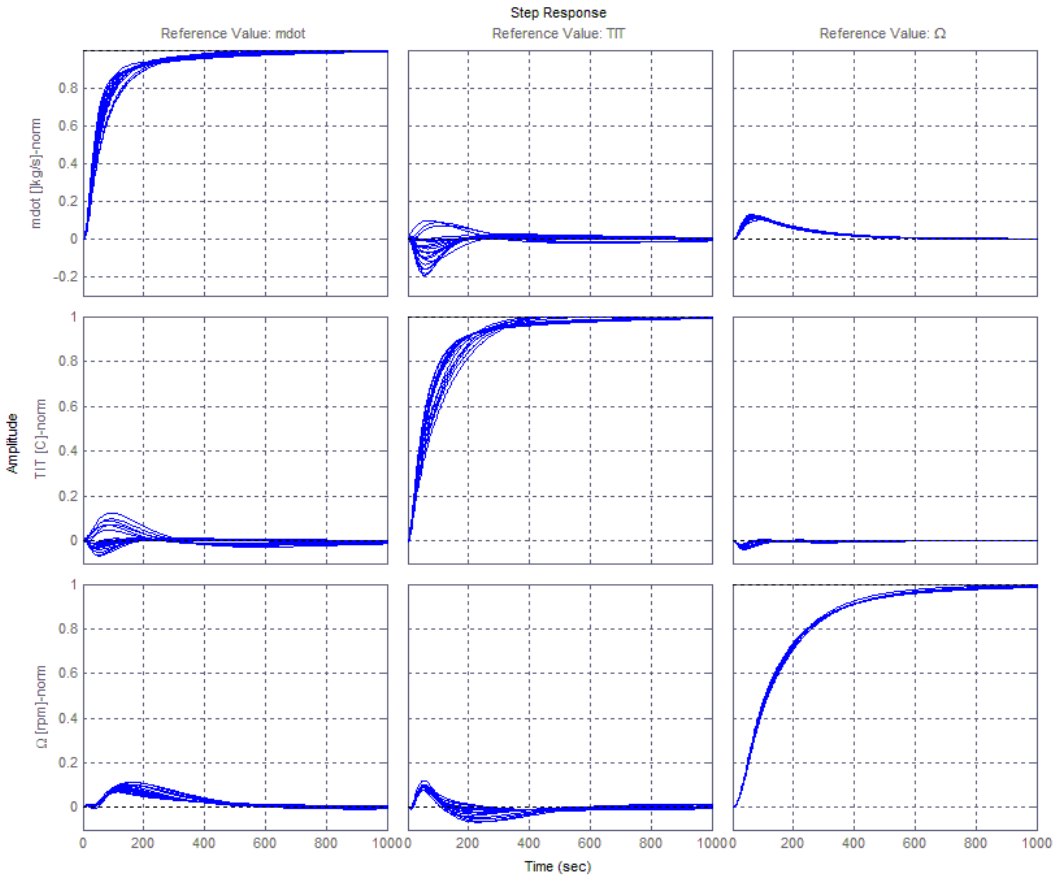

Figure 4.44 Step Response to 10% Zero/Pole Parametric Uncertainty

The actuator dynamics can also be incorporated into the uncertainty model by the use of multiplicative uncertainties. This is accomplished by multiplying the nominal plant by a first order diagonal weight that has high and low frequency uncertainty percent values. Equations 4.1.45 to 4.1.47 express this relationship, where Δ_I is the multiplicative diagonal matrix containing the scalar perturbations for each input channel, τ is the time constant where there is 100% uncertainty, r_0 the relative dc uncertainty magnitude, and r_∞ the high frequency weight magnitude (Skogestad et al. 2005).

$$G_{unc} = G_{nom} \cdot \left(I + W_I \cdot \Delta_I\right) \qquad \text{Eq.4.1.45}$$

$$\Delta_I = diag\{\delta_I\},\ W_I = diag\{\varpi_I\} \qquad \text{Eq.4.1.46}$$

$$\varpi_I = \frac{(\tau \cdot s + r_0)}{\left(\left(\frac{\tau}{r_\infty}\right) \cdot s + 1\right)} \qquad \text{Eq.4.1.47}$$

The MatLab command "makeweight" produces a first order state space system similar to that of Equation 4.1.46 and 4.1.47. Low and high frequency uncertainties can then be combined with each actuator's bandwidth to represent input uncertainty for all channels.

5 Analytical Model

The nonlinear model is comprised of ordinary differential equations stemming from energy, continuity, and momentum balances. The HyPer facility is virtually built in a Simulink-MatLab environment, in which subsystem block components interconnect in the same way piping elements route the airflow path in the hardware facility. In particular, this model does not make use of the compressor maps utilized on the simple cycle Brayton model. This allows for a simulation run that starts at a much lower rpm, approximating the actual rpm's at ignition. Although Chapter 2 had described the HyPer assembly in general, Appendix H provides the facility's Process and Instrumentation Diagram. This model is built in parallel to the empirical plant, and is intended as a complementary tool to the analysis presented in Chapter 3.

5.1 Brayton Cycle

The simple gas turbine cycle was described in Chapter 2 as the Brayton cycle. The ideal behavior of this cycle produces the highest thermal efficiency for isentropic and adiabatic processes enabling the comparison of other cycle efficiencies to this one. The main difference between this and the HyPer model is the large amount of volume inserted between the compressor and the turbine, as well as the heat recuperation scheme for the latter. As an initial means of comparison between the simple cycle and the more complex hybrid cycle, a model of the Brayton cycle was constructed using compressor maps. The HyPer model was then built upon the simple cycle by the addition of subsystem blocks, symbolizing the various system pipes, plenums, and recuperators. As will be later noted, the compressor maps were replaced with algebraic equations. Due to the fact that some subsystems of the simple cycle are used in the nonlinear model, these will be further presented in the BOP model section instead. System response plots will be shown in Chapter 5 for open and closed loop tests.

Figure 5.1 shows a schematic of a simple gas turbine cycle. The 250 kW APU used in the HyPer facility has an air intake at point "a". A two-stage centrifugal compressor

provides approximately a 4:1 pressure ratio with a 200°C temperature rise at point "b". The combustor ignites this flow to 1600°F by the use of a 1MW heat source at point "c" before it expands in the turbine. The hot gasses exhaust at point "d", where they are routed to a stack, kept at atmospheric conditions. Work is extracted from the turbine mainly for running the compressor and generating electrical power if connected to a generator.

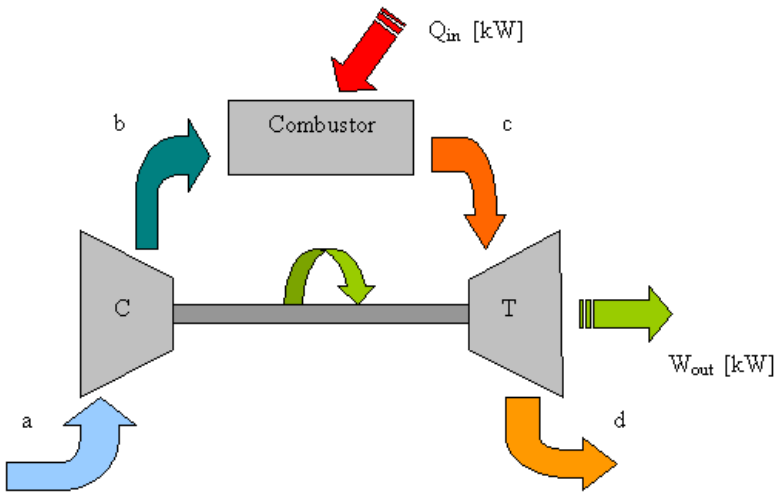

Figure 5.1 Gas Turbine Brayton Cycle

Figure 5.2 shows a graphical wire up of the gas turbine components as they appear in the Simulink workspace. Each block represents a subsystem that houses algebraic or differential equations. The arrangement is fashioned according to the Brayton Cycle schematic shown in Figure 5.1. This model receives two heat sources as inputs, along with ambient temperature and pressure. "Q_{in} " is the 950 kW heat source that ignites at once when the model is started, while "Q_{in} Inc" is an incremental change in heat, specified as a percentage of "Qin" at some instant of time. This is done to test the stability and validity of the model response to sudden perturbations of the heat source. Each subsystem and its corresponding set of equations will be described in the following figures.

One thing to note is that the representation given is that for an open loop system. No feedback loop is present and no relationship has been shown for fuel flow vs. heat input. For the time being the heat source will be applied as a constant as is the case for the ambient pressure and temperature conditions. Also, there is no controller of any type or transducer transfer function. These will be added, once all pertinent components are added.

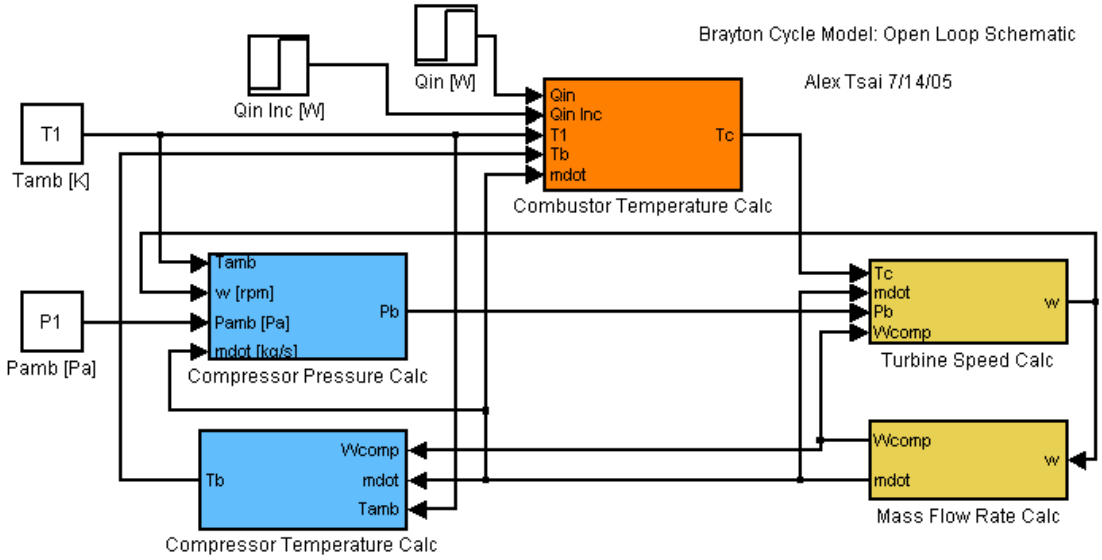

Figure 5.2 Gas Turbine Simulink Model

The state variables of interest for the compressor are the pressure ratio and the temperature of compression. These two signals and their respective equations in Simulink are presented below (Saad 1997). The compressor efficiency is set to 65%.

$$T_b = T_{amb} + \frac{\dot{W}}{\eta_{comp} C_p \dot{m}} \qquad \text{Eq.5.1.1}$$

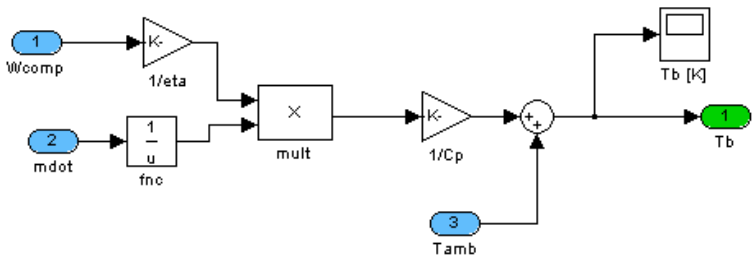

Figure 5.3 Compressor Temperature Subsystem

Inputs to the subsystem are shown in blue, while outputs are in green. Occasionally scopes or numeric displays are placed along the signal path to graph signals of interest. These are shown in gray.

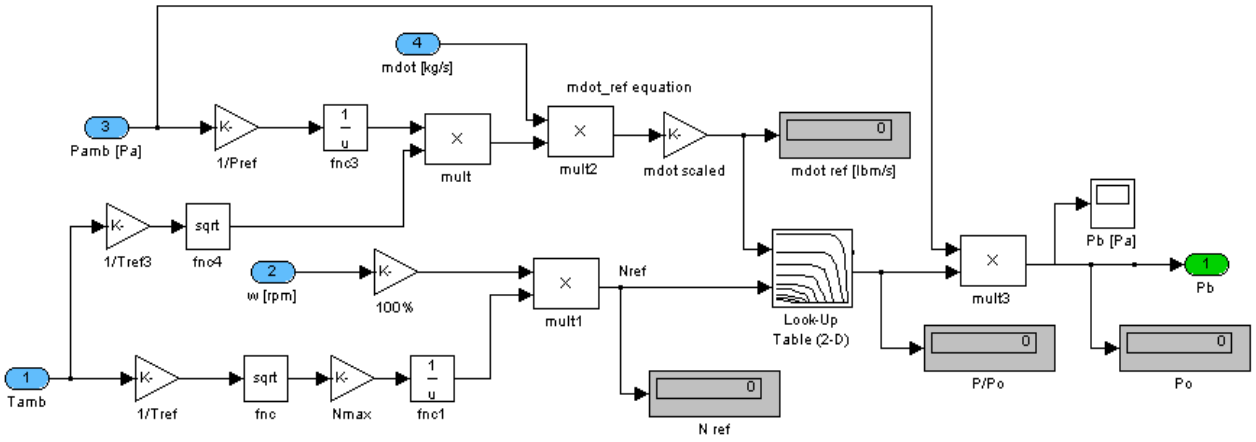

Figure 5.4 Compressor Pressure Subsystem

Figure 5.4 shows the contents of the compressor pressure subsystem. A lookup table takes in referred mass flow and percentage speed values in terms of a reference pressure and temperature of 101.3kPa and 293.15K, and outputs pressure ratio. The table used is given in Appendix B. The equations that comprise most of Figure 5.4 are those to convert calculated mass flow rate to the referred flow from the graph, which is in English units as well. Below are the conversion factors (Larminie et al. 2003).

$$\dot{m}_{ref} = \dot{m} \cdot \frac{\sqrt{\frac{T_a}{T_{ref}}}}{\frac{P_a}{P_{ref}}} \qquad N_{ref} = \frac{N_{speed}}{N_{\max} \cdot \sqrt{\frac{T_a}{T_{ref}}}} \qquad \text{Eq.5.1.2}$$

The combustor wire up is given in Figure 5.5, with the corresponding 1st order differential equation outlined in Eq.5.1.3-5.1.5. Here, the thermal resistance is calculated in a MatLab script file in Appendix E and shown here as a gain. Although not shown, the integrator has the ambient temperature as an initial condition.

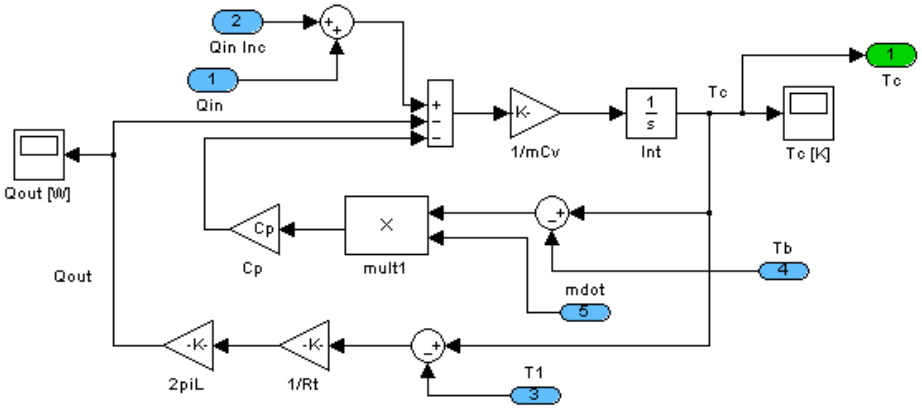

Figure 5.5 Combustor Temperature Subsystem

$$\dot{Q}_{in} - \dot{Q}_{out} = m \cdot C_v \cdot \dot{T}_c + \dot{m} \cdot C_p \cdot (T_c - T_b) \qquad \text{Eq.5.1.3}$$

$$\dot{Q}_{out} = \frac{2 \cdot \pi \cdot L \cdot (T_c - T_a)}{R_t} \qquad \text{Eq.5.1.4}$$

$$R_t = 2 \cdot \pi \cdot L \cdot \left(\frac{1}{h_0 \cdot A_{\sin}} + \frac{1}{h_{amb} \cdot A_{sout}} \right) + \frac{\ln\left(\frac{r_2}{r_1}\right)}{k_1} + \frac{\ln\left(\frac{r_3}{r_2}\right)}{k_2} \qquad \text{Eq.5.1.5}$$

In Eq.5.1.4, T_c is sometimes expressed as the average of T_b and T_c instead. In Eq.5.1.3, T_c is the only temperature differentiated in time since the volume and the mass within this volume is relatively small, and it is thus assumed that T_c has a greater rate of change due to $\dot{Q}_{in}$ than does T_b (Incropera et al. 1990). It is also worth noting that the convection coefficient inside and outside the combustor is set as a constant. The inner h_0 is in the upper range for forced convection of a gas, while h_{amb} is within the upper bound for free convection.

Figure 5.6 shows Eq.5.1.6-5.1.7 in the Simulink workspace. This essentially is a power balance between the output shaft torque produced by the turbine and all the combined loads that counteract this shaft torque. An electrical load of 45 kW is given as a constant input, since this is the base case resistive loading as defined by the HyPer group. The windage losses are lumped into other losses that will be modeled explicitly later, since windage loss is not the only loss mechanism and the compressor is not isentropic. These factors will be taken into account eventually.

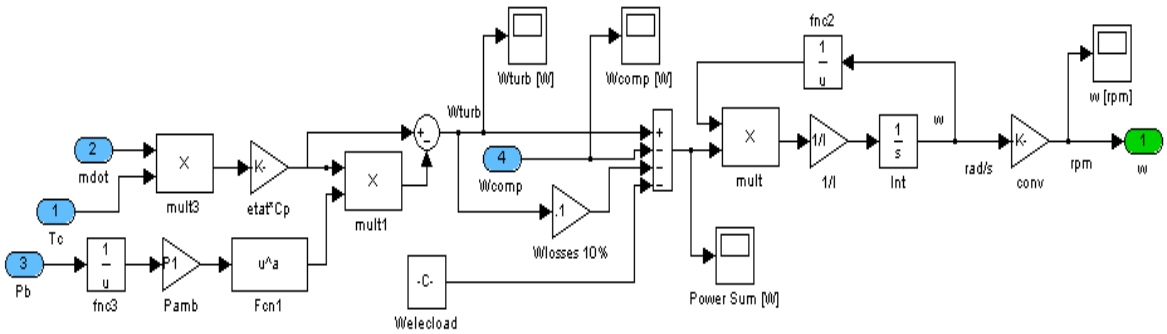

Figure 5.6 Turbine Power Subsystem

$$Power = \Delta K.E. = \frac{d}{dt}\left(\frac{1}{2}\cdot I\cdot \omega^2\right) = Torque\cdot\omega = \left(I\cdot\dot{\omega}\right)\cdot\omega \qquad \text{Eq.5.1.6}$$

$$\omega I\dot{\omega} = \dot{W}_{turb} - \dot{W}_{comp} - \dot{W}_{losses} - \dot{W}_{elec} \qquad \text{Eq.5.1.7}$$

$$\dot{W}_{turb} = \eta\cdot\dot{m}\cdot C_p\cdot T_c\cdot\left(1-\left(\frac{P_d}{P_c}\right)^{\frac{k-1}{k}}\right) \qquad \text{Eq.5.1.8}$$

In Eq.5.1.8 air is assumed to be an ideal gas, undergoing a polytropic process (Lindeburg 2002). The values for the constants and their meaning are given in the MatLab m-file, Appendix E. The turbine efficiency is set to 70%. As noted earlier, some subsystems such as the "Mass Flow Rate" and the "Combustor Temperature" blocks are utilized in

the subsequent HyPer model, and are omitted here to avoid redundancy. To finalize the simple cycle modeling, a PID controller is affixed to maintain turbine speed, as shown in Figures 5.7 and 5.8 (Katsuhiko 2002).

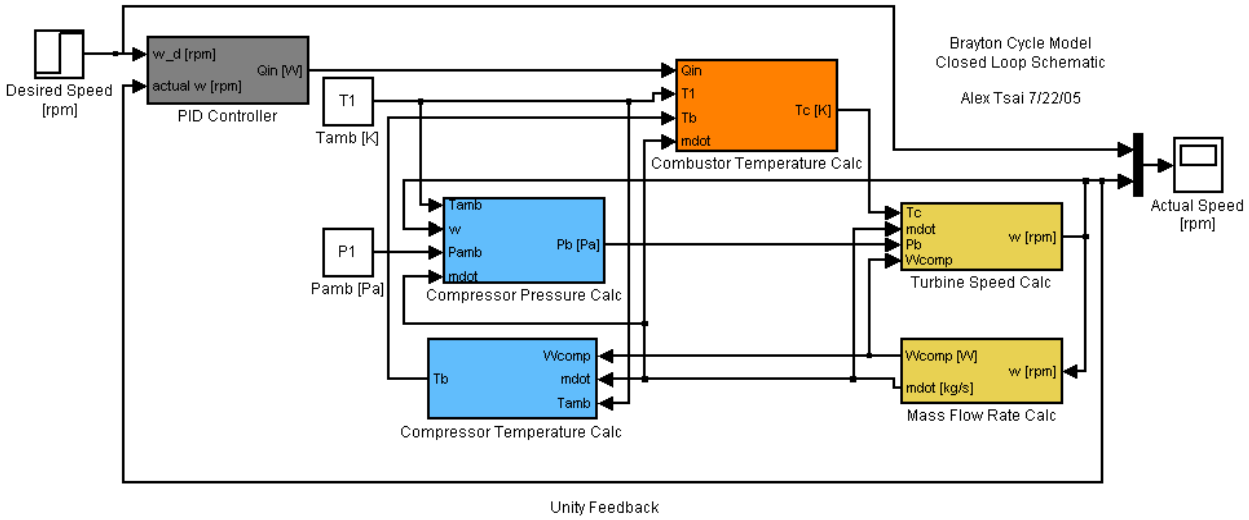

Figure 5.7 Gas Turbine Components with Speed Feedback Control

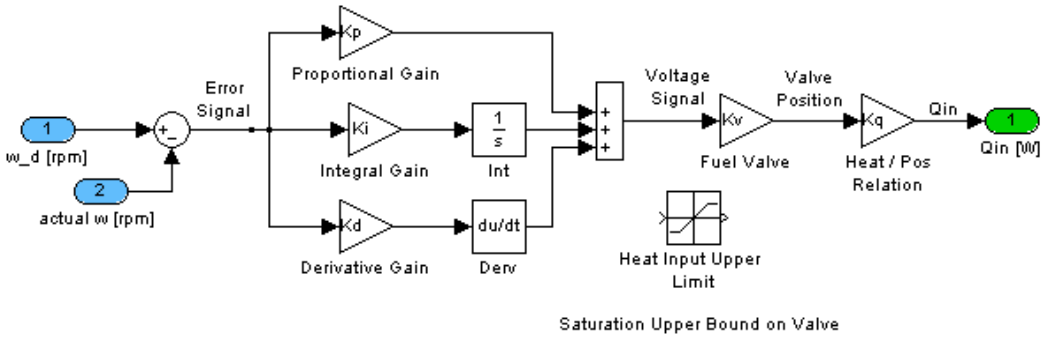

Figure 5.8 PID Controller Subsystem

5.2 Balance of Plant

Figure 5.9 shows the Simulink nonlinear model of the HyPer facility. It is composed of subsystems that represent the analytical equations described in later sections. Each subsystem has a hierarchy of inner subsystems as will be shown. The outermost layer of

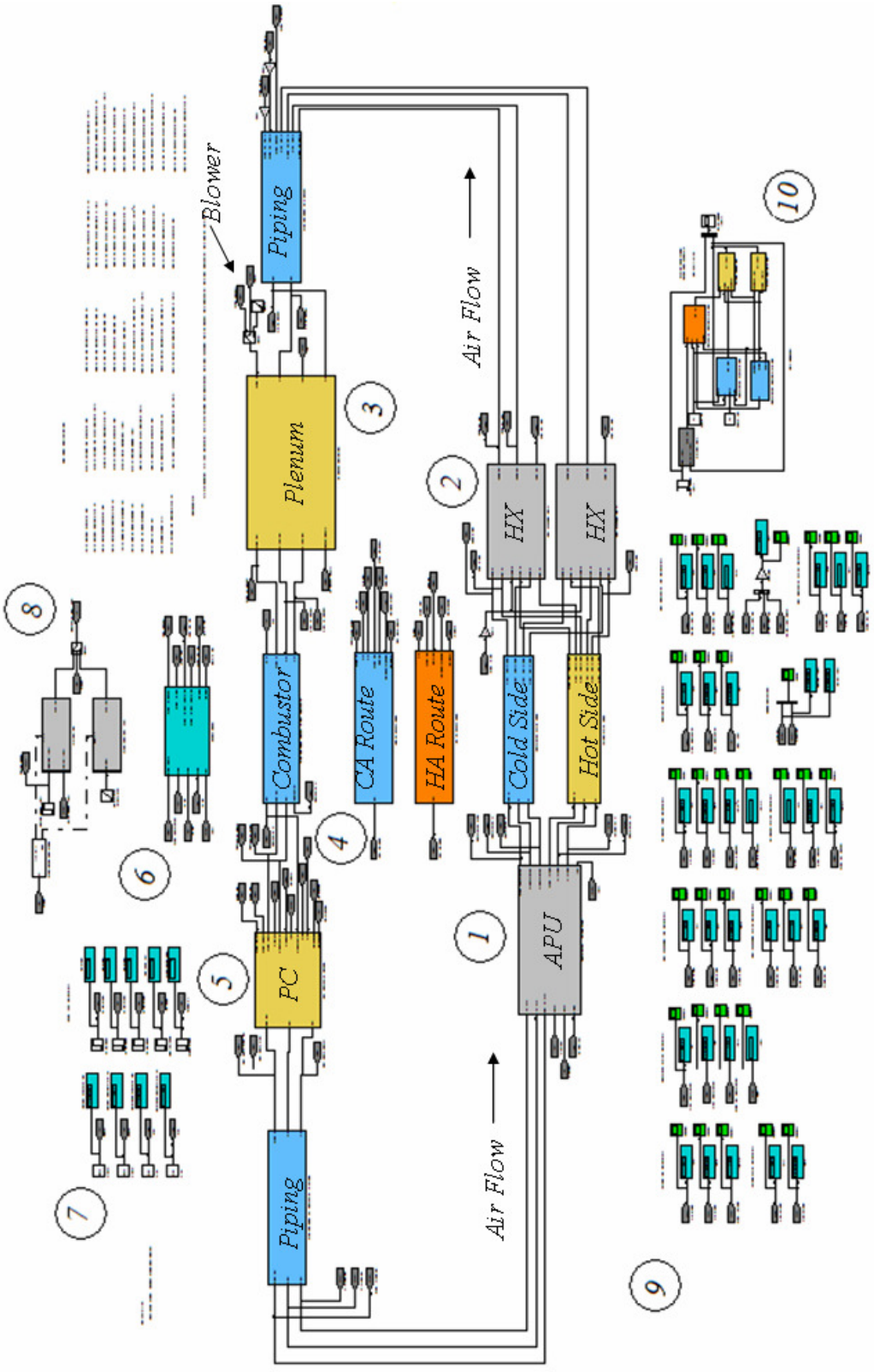

Figure 5.9 Simulink Nonlinear Model

the model has the main piping routes, heat exchangers, post combustor, valve logic, and gas turbine subsystems presented. The schematic of Fig.5.9 has numbers assigned to identify the various components. These regions are:

1. Gas Turbine/ Compressor Model
2. Primary Surface Recuperator Model
3. Air Plenum, representative of Fuel Cell Cathode Volume
4. Combustor Subsystem
5. Post Combustor Subsystem
6. Mass Flow Rate Distribution
7. Input Parameters: Valve Positions, Load, Ambient Conditions
8. Fuel Valve Mode: Open Loop or Closed Loop
9. Displays and Scopes
10. Brayton Cycle Reference Model

All other subsystems represent the different piping routes between the main components. The following figures show how the piping is assembled according to the process and instrumentation diagram as built. Appendix I shows the inner routing of the piping main subsystems.

In Appendix I, the blue subsystems have the temperature and pressure loss equations for straight pipes within, while the yellow systems represent the pressure drop due to minor losses from pipe bends, geometry changes, expansions and the like. The model runs under the following logic:

- Starting at 1000rpm, the air plenum receives a ramp input which represents the blower mass flow rate i.e. input blocks before “3” in Figure 4.9. This is actually intended for the case where the model begins at a lower initial velocity, and the combustor is not ignited. The mass flow ramp input allows for an increase in plenum temperature and pressure that would enable the turbine to reach ignition speed prior to combustor activation.

- When the turbine speed reaches 9000rpm, the mass flow rate into the plenum switches from the ramp input to the mass flow assigned by the valve logic subsystem in “6”. This flow rate depends on whether any bypass valves are opened and is sequentially connected to the compressor exit mass flow rate through the heat exchanger path. All the input parameters can be changed while the model is running via the use of step blocks located at “7”. In “7” there are step blocks for the cold air (CA), hot air (HA), and bleed air (BA) percent openings, as well as electrical load and model mode inputs.
- The model mode allows the model to run under open or closed loop operation in the subsystem of region “8” of Figure 5.9. There, the fuel valve can either have a saturated ramp opening if in open loop mode, or can respond to a PID controller signal under a selected desired speed if closed loop mode is chosen. Ambient pressure and temperature are also included in region “7” for parametric studies. As a reference, the original Brayton cycle is included in region “10”, as a means to compare expected simple cycle results, to those due to the volumetric expansion between compressor and turbine. Detailed models, equations and their operational logic will be presented in subsequent sections.

The gas turbine model follows the same isentropic relations as those for the simple cycle to calculate exit pressure and temperatures. Mass flow rate is derived from a vectorial analysis of the compressor blade and geometry. The equations and their respective Simulink representation are given below and represent subsystem “1” in Fig.5.9.

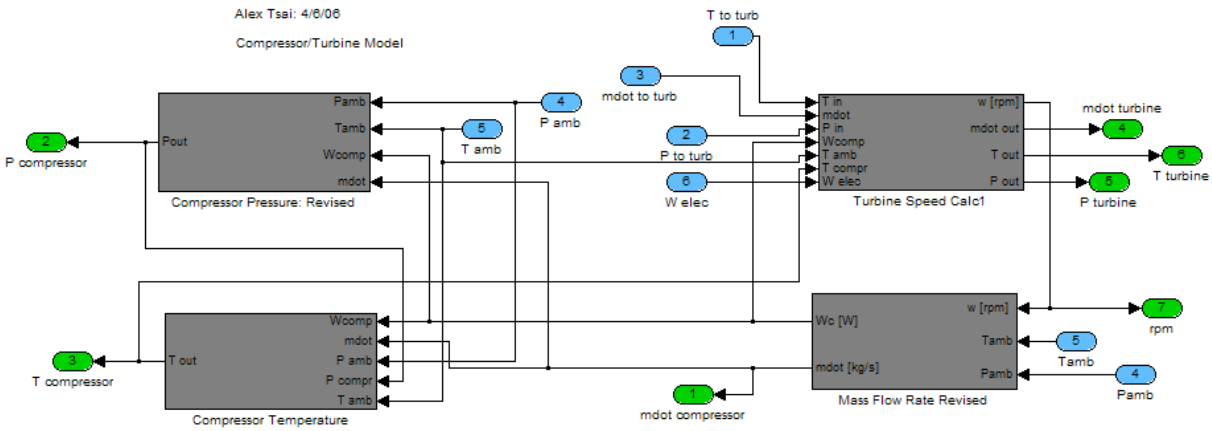

Figure 5.10 Gas Turbine Simulink Model

The gas turbine model is composed of four subsystems. This model can be used for a simple cycle just as long as the inlet pressure, temperature and mass flow rates of the turbine are those corresponding to outlet conditions of the compressor.

5.3 Compressor Model

The mechanical power of a turbo machine is given by the dot product of the angular velocity of the rotor and the applied shaft torque as (Fox et al. 1992):

$$\dot{W}_{mech} = \omega \cdot T_{shaft} \qquad \text{Eq.5.3.1}$$

The angular momentum principle states that the rate of change of the angular momentum denoted by "H" is equal to the total torque exerted by the surroundings on the system. In essence, Eq.5.3.2 expresses the time variation of the system extensive property "H" in terms of its change associated to a specified control volume. The extensive property of angular momentum is defined as $\vec{H} = (\vec{r} \times \vec{v}) \cdot m$, while its intensive property η is given by $\eta = (\vec{r} \times \vec{v})$.

The first term of Eq.5.3.2 corresponds to the time rate of change of the total amount of angular momentum for an element of mass within the control volume, whereas the second term pertains to the net rate of flux of the extensive property "H" through the

control surface. The symbol "∘" denotes the dot product of terms. The terms on the right hand side of Eq.5.3.3 correspond to pressure surface moments, gravitational moments and shaft torques respectively. If the first two effects of Eq.5.3.3 are neglected, Eq.5.3.2 can be reduced to the Euler Turbo Machine equation for steady flow. This equation is applicable to all turbo machines and is given by Eq.5.3.10 (Fox et al. 1992). Figure 5.11 shows the control volume representation to be used in deriving Eq.5.3.10 from Eq.5.3.2 and Eq.5.3.3.

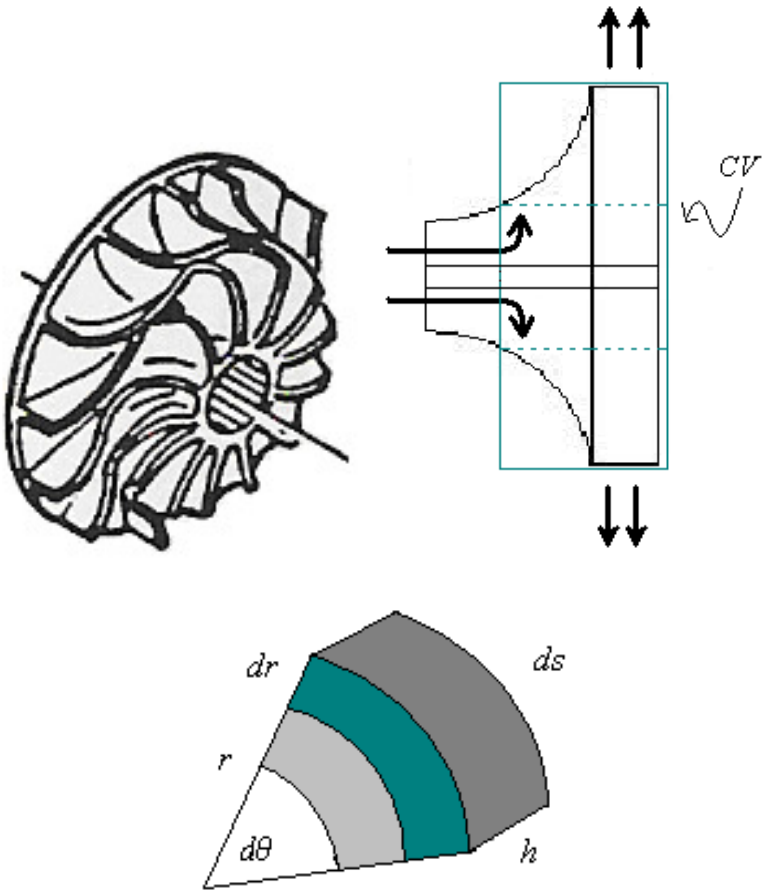

Figure 5.11 Compressor Blades, Control Volume, and Infinitesimal Volume Element

$$\vec{T}_{total} = \left.\frac{d\vec{H}}{dt}\right|_{syst} = \frac{\partial}{\partial t}\int_{CV}(\vec{r}\times\vec{v})\cdot\rho\cdot dV + \oint_{CS}(\vec{r}\times\vec{v})\cdot\rho\cdot\vec{v}\circ d\vec{A} \qquad \text{Eq.5.3.2}$$

$$\left.\frac{d\vec{H}}{dt}\right|_{syst} = \left(\vec{r}\times\vec{F}_s\right) + \int_{CV}\left(\vec{r}\times\vec{g}\right)\cdot\rho\cdot dV + \vec{T}_{shaft} \qquad \text{Eq.5.3.3}$$

As stated previously, the first term of Eq.5.3.2 is the rate of change of the angular momentum within the control volume, and can be expressed in scalar form as:

$$\frac{d}{dt}\int_{CV}\left(r\times\vec{v}\right)\rho\cdot dV = \tilde{\rho}\cdot\int_{CV}\left(r^2\cdot\omega\right)\cdot dV = \tilde{\rho}\cdot\int_{r,\theta}\left(r^2\cdot\omega\right)\cdot r\cdot h\cdot d\theta\cdot dr \qquad \text{Eq.5.3.4}$$

where $\tilde{\rho}$ is a density approximation of inlet and outlet conditions, as: $\tilde{\rho} = \frac{\left(\rho_1+\rho_2\right)}{2}$.

Following with the derivation of Eq.5.3.4, for unsteady flow, the rate of change of "H" is given by Eq.5.3.6.

$$2\cdot\pi\cdot\tilde{\rho}\cdot h\cdot\omega\cdot\int_r r^3\cdot dr = 2\cdot\pi\cdot\tilde{\rho}\cdot h\cdot\omega\cdot\left.\frac{r^4}{4}\right|_{r_1}^{r_2} = \frac{\pi\cdot\tilde{\rho}\cdot h\cdot\omega}{2}\cdot\left[r_2^4 - r_1^4\right] \qquad \text{Eq.5.3.5}$$

$$\frac{d}{dt}\int_{CV}\left(r\times\vec{v}\right)\cdot\rho\cdot dV \cong \frac{\pi}{2}\cdot\tilde{\rho}\cdot h\cdot\left[r_2^4 - r_1^4\right]\cdot\frac{d\omega}{dt} \qquad \text{Eq.5.3.6}$$

For the second term of Eq.5.3.2, the net flux of "H" across the control surface in scalar form is derived in Eq.5.3.7-5.3.8, noting that the incoming flow profile is assumed to be uniform and perpendicular to the surface area, hence inlet mass flows have a negative sign convention.

$$\oint_{CS}\left(r\times\vec{v}\right)\cdot\rho\cdot\vec{v}\circ dA = -r_1\cdot v_{t1}\cdot\left[\rho\cdot v_{n1}\cdot A_1\right] + r_2\cdot v_{t2}\cdot\left[\rho\cdot v_{n2}\cdot A_2\right] \qquad \text{Eq.5.3.7}$$

$$\oint_{CS}\left(r\times\vec{v}\right)\cdot\rho\cdot\vec{v}\circ dA = \dot{m}\cdot\left(r_2\cdot v_{t2} - r_1\cdot v_{t1}\right) \qquad \text{Eq.5.3.8}$$

Combining Eq.5.3.3 through Eq.5.3.8 gives the total torque exerted by a turbo machine as:

$$T_{shaft} = \frac{\pi}{2}\cdot\tilde{\rho}\cdot h\cdot\left[r_2^4 - r_1^4\right]\cdot\frac{d\omega}{dt} + \dot{m}\cdot\left(r_2\cdot v_{t2} - r_1\cdot v_{t1}\right) \qquad \text{Eq.5.3.9}$$

Since the compressor impeller dimensions are quite small, the first unsteady term of Eq.5.3.9 can be discarded with no loss of accuracy, and so Eq.5.3.9 reduces to the Euler Turbo Machine equation Eq.5.3.10 (Fox et al. 1992).

$$T_{shaft} = \dot{m} \cdot \left(r_2 \cdot v_{t2} - r_1 \cdot v_{t1} \right) \qquad \text{Eq.5.3.10}$$

The velocities of Eq.5.3.10 are tangential components of the absolute velocity entering and exiting the compressor blades. The components of the absolute air velocity at inlet and outlet sections of a radial compressor are shown schematically in Figure 5.12.

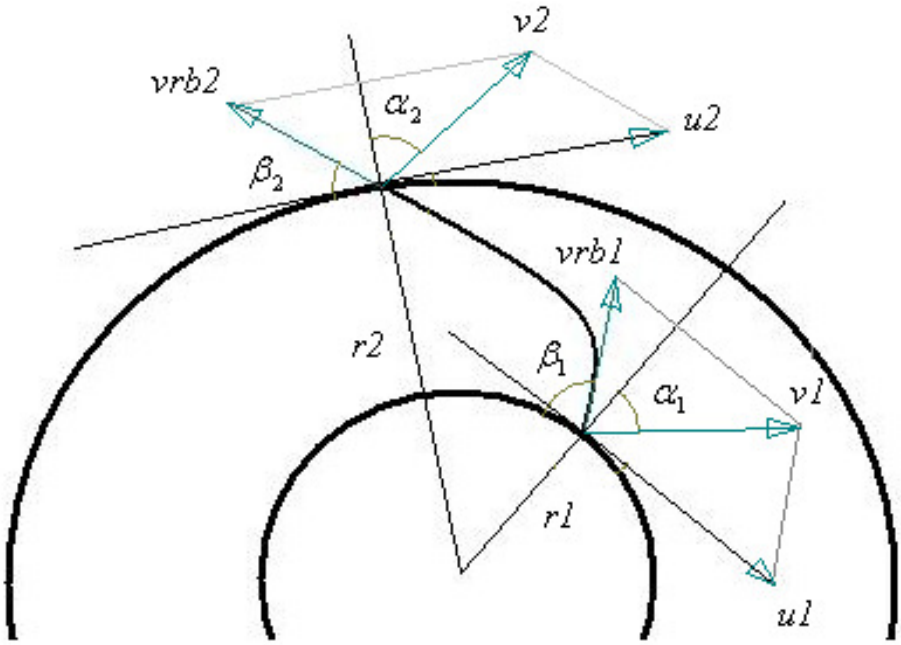

Figure 5.12 Velocity polygons of a radial flow compressor [31]

Subscripts 1 and 2 denote the entrance and exit ports of the compressor, v_{rb} and u are the flow velocity relative to the blade, and the runner speed that is specified by impeller geometry and rotational speed, α and β are angles of velocity vectors relative to normal and tangential blade directions, $v1$ and $v2$ are the absolute velocities of the air, and ω, is the rotor's rotational speed. The normal component of the velocity at section 2, v_{n2}, is

derived from the conservation of mass equation at inlet and outlet ports, as will be shown shortly. The tangential components of the absolute velocity are the only ones capable of doing work according to Eq.5.3.10. Figure 5.13 shows the inlet segment of the compressor blades with v_t and v_n being the tangential and normal components of the absolute velocity of the air. Eq.5.3.11 through Eq.5.3.14 give the geometric relationships used to obtain v_{n1} and v_{t1}.

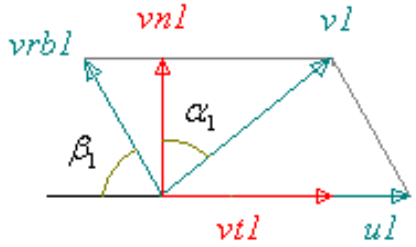

Figure 5.13 Absolute velocities in terms of relative and rotor velocities [31]

$$\tan(\alpha_1)=\frac{v_{t1}}{v_{n1}}\ ,\ \cot(\beta_1)=\frac{(u_1-v_{t1})}{v_{n1}} \qquad \text{Eq.5.3.11}$$

$$v_{n1}\cdot\cot(\beta_1)=u_1-v_{n1}\cdot\tan(\alpha_1) \qquad \text{Eq.5.3.12}$$

$$v_{n1}=\frac{u_1}{(\tan(\alpha_1)+\cot(\beta_1))}=\frac{r_1\cdot\omega}{(\tan(\alpha_1)+\cot(\beta_1))} \qquad \text{Eq.5.3.13}$$

$$v_{t1}=v_1\cdot\sin(\alpha_1)=\frac{v_{n1}}{\cos(\alpha_1)}\cdot\sin(\alpha_1)=v_{n1}\cdot\tan(\alpha_1) \qquad \text{Eq.5.3.14}$$

In order to obtain the tangential and normal components of the velocities at section 2, the continuity equation is used in conjunction with the polygon analysis as shown in Eq.5.3.15 to Eq.5.3.16.

$$\left.\frac{dM}{dt}\right|_{sys}=0=\frac{d}{dt}\int_{CV}\rho\cdot dV+\oint_{CS}\rho\cdot v\circ dA \qquad \text{Eq.5.3.15}$$

$$0=V\cdot\frac{d\rho}{dt}-\dot{m}_{in}+\dot{m}_{out}=V\cdot\frac{d\rho}{dt}-(\rho\cdot v\cdot A)_{in}+(\rho\cdot v\cdot A)_{out} \qquad \text{Eq.5.3.16}$$

$$V \cdot \frac{d\rho}{dt} = \rho_{in} \cdot v_{n1} \cdot \left(\frac{\pi}{4} \cdot \left(d_2^2 - d_1^2 \right) \right) - \rho_{out} \cdot v_{n2} \cdot \left(\pi \cdot d_2 \cdot h \right) \qquad \text{Eq.5.3.17}$$

$$v_{n2} = \frac{1}{\pi \cdot \rho_{out} \cdot d_2 \cdot h} \cdot \left[\frac{\pi}{4} \cdot \rho_{in} \cdot v_{n1} \cdot \left(d_2^2 - d_1^2 \right) - V \cdot \frac{d\rho}{dt} \right] \qquad \text{Eq.5.3.18}$$

$$v_{t2} = v_{n2} \cdot \tan\left(\alpha_2 \right) \qquad \text{Eq.5.3.19}$$

The mass flow rate leaving the compressor can be calculated with Eq.5.3.20, where "h" is the average blade height, and d_2 is the outer diameter.

$$\dot{m}_{out} = \rho_{out} \cdot v_{n2} \cdot \left(\pi \cdot d_2 \cdot h \right) \qquad \text{Eq.5.3.20}$$

For this case, it is assumed that the absolute velocity of the air at the inlet enters radially and hence $\alpha_1=0°$. This assumption holds true whenever the inlet flow is swirl free. Also, because changes in density within the relatively small control volume of the compressor are difficult to conceptualize, and the system is mostly analyzed as a quasi-steady state condition, the last term of Eq.5.3.18 can be neglected with no appreciable loss of accuracy. It is not uncommon to assume incompressible flow of air at standard conditions in developing compressor equations, considering benchmark models have used this assumption with no loss of generality i.e. Greitzer (1976a). Further vectorial analysis and accompanying MathCAD file are shown in Appendix D. Below is the Simulink subsystem that calculates compressor work and mass flow rate.

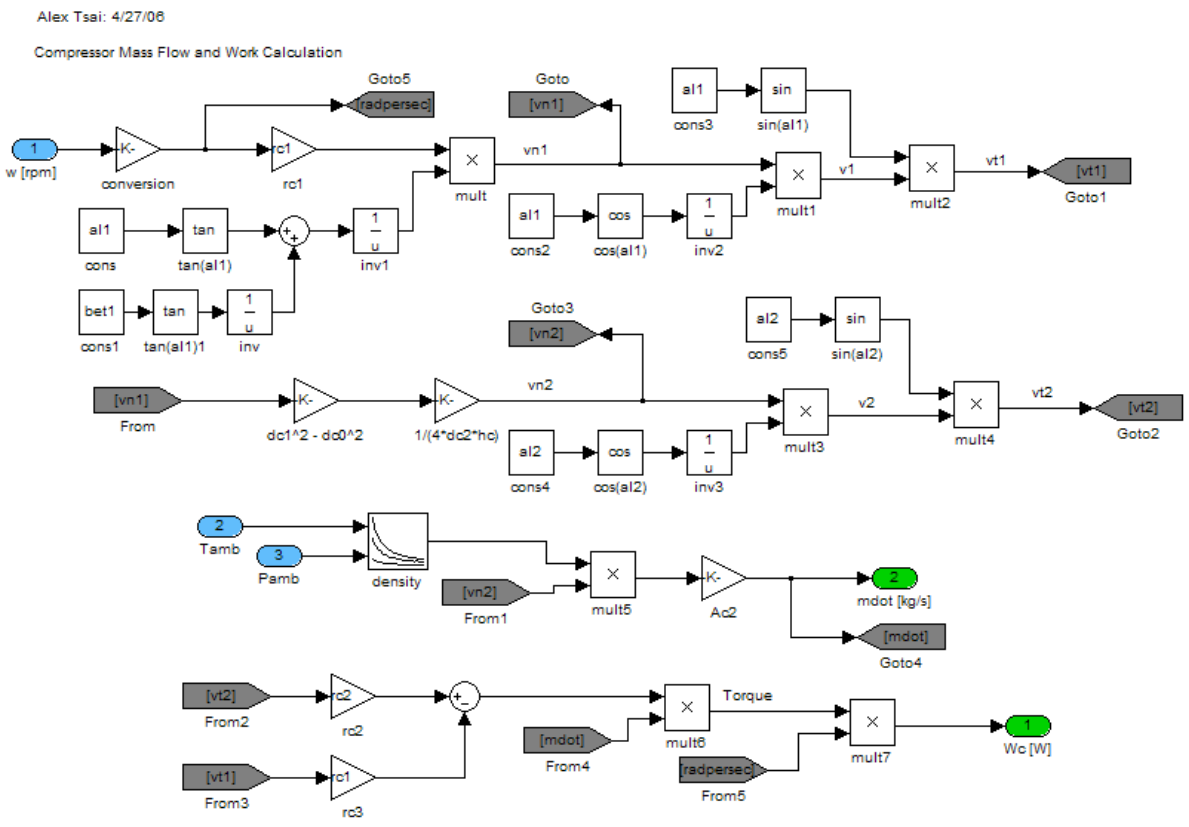

Figure 5.14 Mass Flow Rate and Compressor Work Subsystem

The compressor outlet pressure is calculated from the isentropic relation below as:

$$P_{out} = P_{amb} \cdot \left[1 + \frac{\eta_{comp} \cdot \dot{W}_{comp}}{\dot{m} \cdot C_p \cdot T_{amb}} \right]^{\frac{k}{k-1}} \qquad \text{Eq.5.3.21}$$

In Eq.5.3.21, "k" is the specific heat ratio and for air as an ideal gas it is assigned a value of 1.4. The efficiency of the compressor should ideally be obtained from maps provided by the manufacturer. However, for this approach it is assigned a constant value of 75%, as observed for the constrained speed range window of the compressor map. Below is the Simulink subsystem for the pressure output.

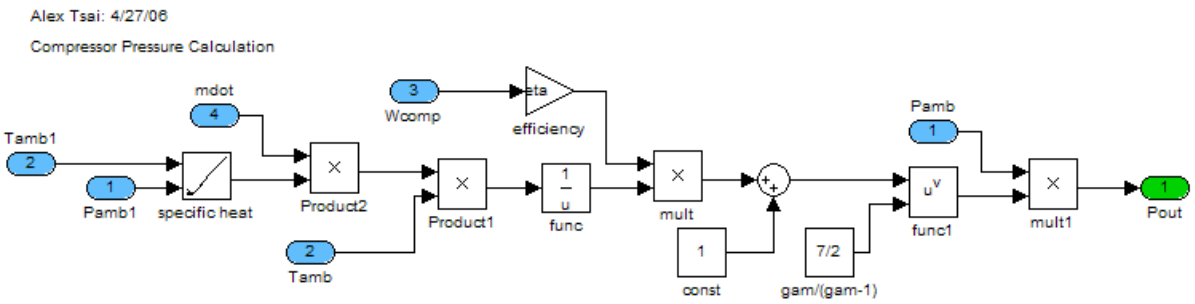

Figure 5.15 Compressor Pressure Subsystem

The temperature out of the compressor is also given by the isentropic relationship as:

$$T_{out} = T_{amb} + \frac{\dot{W}_{comp}}{\dot{m} \cdot C_p \cdot \eta_{comp}} \qquad \text{Eq.5.3.22}$$

The Simulink block diagram is given in Figure 5.16.

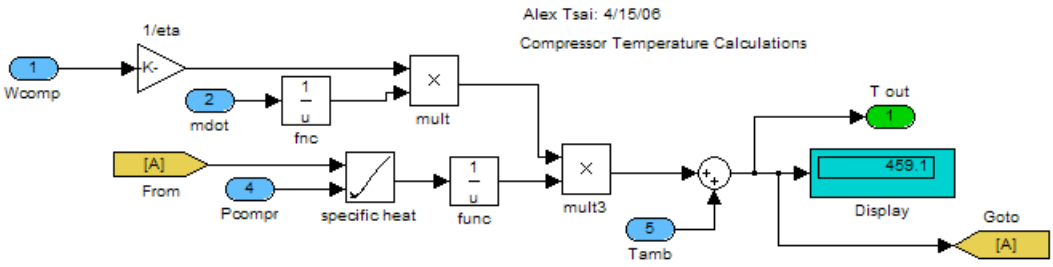

Figure 5.16 Compressor Temperature Subsystem

5.4 Turbine Model

The turbine work equation is given by the isentropic relationship of Eq.5.4.1, and modeled in Simulink in Figure 5.17. This figure also includes the speed calculation, as well as the temperature and pressure outputs. The combined mechanical energies of the turbine and compressor, and the energy related to the electrical load and irreversible heat losses are incorporated into Eq.5.4.4. The turbine back pressure is a function of an empirical curve that is dependent on shaft speed.

$$\dot{W}_{turb} = \eta_{turb} \cdot \dot{m} \cdot C_p \cdot T_{in} \cdot \left[1 - \frac{P_{back}}{P_{in}} \right]^{\frac{\gamma-1}{\gamma}} \qquad \text{Eq.5.4.2}$$

$$T_{out} = T_{in} \cdot \left(\frac{P_{back}}{P_{in}} \right)^{\frac{\gamma-1}{\gamma}} \qquad \text{Eq.5.4.3}$$

$$\omega \cdot I \cdot \frac{\partial \omega}{\partial t} = \dot{W}_{turb} - \dot{W}_{comp} - \dot{W}_{elec} - \dot{W}_{losses} \qquad \text{Eq.5.4.4}$$

In the previous equations, γ is the ratio of specific heats as noted by $\gamma = \frac{c_p}{c_v}$. T_{out} refers to the turbine exhaust temperature, T_{in} to the turbine inlet temperature, and P_{in} to the inlet turbine pressure. All the power losses are a constant value of the turbine power, set at 10%, while the electrical power $\dot{W}_{elec}$ losses are assigned during the model run, according to a particular scenario.

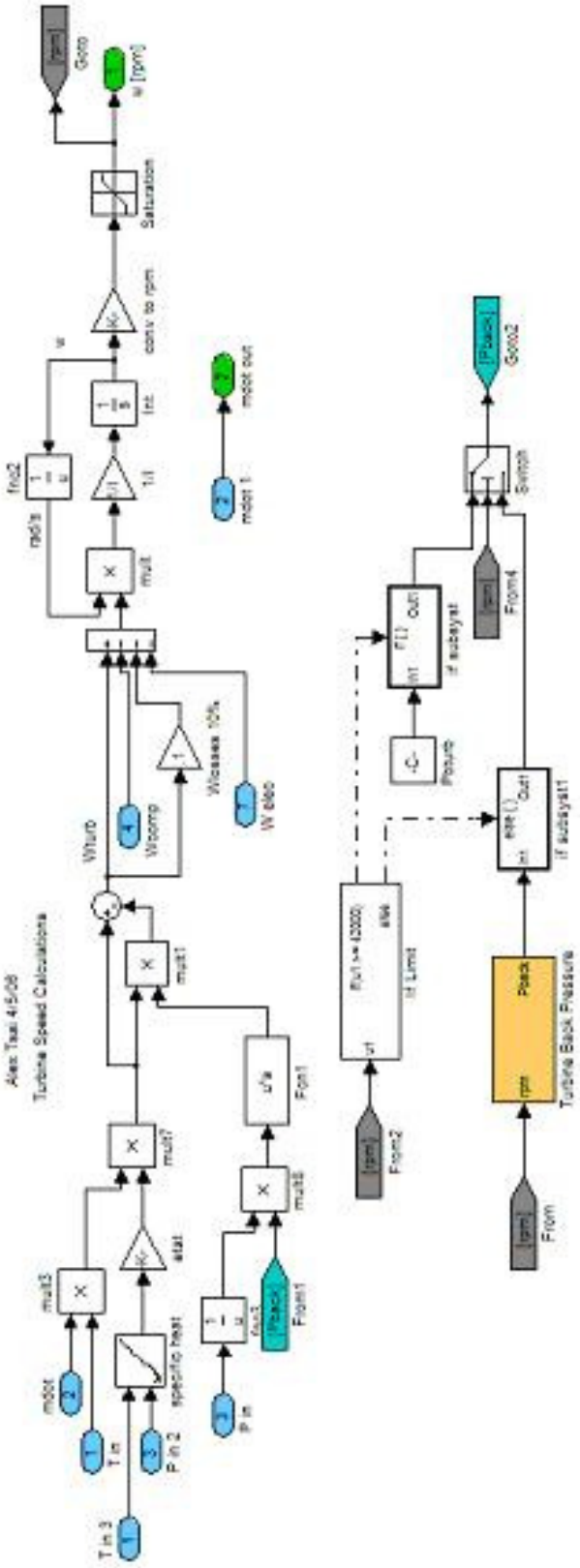

Figure 5.17 Turbine Equation Subsystem

5.5 Air Plenum Model

The continuity equation states that the sum of the rate of change of mass within a control volume and the mass flux crossing the control surface boundary are equal to zero. In integral form, this equation is given by:

$$\left.\frac{dM}{dt}\right|_{syst} = 0 = \frac{\partial}{\partial t}\int_{CV}\rho \cdot dV + \oint_{CS}\rho \cdot \vec{v} \circ d\vec{A} \qquad \text{Eq.5.5.1}$$

$$\dot{m}_{stored} = \dot{m}_{in} - \dot{m}_{out} \qquad \text{Eq.5.5.2}$$

$$V_{CV} \cdot \frac{\partial \rho}{\partial t} = \dot{m}_{in} - \dot{m}_{out} \qquad \text{Eq.5.5.3}$$

In this case the vessel volume is fixed, and thus the variable becomes the plenum density. The mass flow out of a vessel is dependent on the pressure difference across the outlet section and the discharge coefficient of the orifice, given by:

$$\dot{m}_{out} = \rho \cdot C_d \cdot A_c \cdot \sqrt{\frac{2 \cdot \left(P_{CV} - P_{out}\right)}{\rho}} \qquad \text{Eq.5.5.4}$$

$$P = \rho \cdot R \cdot T \qquad \text{Eq.5.5.5}$$

where the pressure inside is calculated by the ideal gas law relationship given above. The vessel's backpressures are curved fitted from experimental data relating the outlet pressure as a function of turbine speed. This data is provided in Appendix A.

5.5.1 Energy Conservation Equations: Plenum Control Volume

The first law of thermodynamics states that the rate of change of total energy within a system is equal to the heat transfer rate minus the rate of work done on or by the system. If heat is added to the system Q takes a positive value, whereas W is positive, if work is done by the system on its surroundings. The intensive property of energy is denoted by

"e" and is equal to the internal, kinetic and potential energies combined. The integral form of the first law is given by:

$$\left.\frac{dE}{dt}\right|_{syst} = \left(\dot{Q}_{in} - \dot{Q}_{out}\right) - \left(\dot{W}_{in} - \dot{W}_{out}\right) = \frac{\partial}{\partial t}\int_{CV} e \cdot \rho \cdot dV + \oint_{CS}\left(e + p \cdot v\right) \cdot \rho \cdot \vec{v} \circ d\vec{A} \qquad \text{Eq.5.5.6}$$

$$e = u + \frac{v^2}{2} + g \cdot z \qquad \text{Eq.5.5.7}$$

For the plenum, the potential energy is neglected as well as work done by or on the system. If no external heat is introduced, for steady flow in and out of the vessel the energy equation becomes:

$$-\dot{Q}_{out} = \frac{\partial}{\partial t}\left(e \cdot \rho \cdot V_{CV}\right) - \dot{m}_{in} \cdot \left(h_{in} + \frac{v_{in}^2}{2}\right) + \dot{m}_{out} \cdot \left(h_{out} + \frac{v_{out}^2}{2}\right) \qquad \text{Eq.5.5.8}$$

where the enthalpy "h" is the sum of the internal energy and the pressure energy "pv". The first term on the right of Eq.5.5.8 can be evaluated by using the chain rule as:

$$\frac{\partial}{\partial t}\left(e \cdot \rho \cdot V_{CV}\right) = \frac{\partial}{\partial t}\left(u \cdot \rho \cdot V_{CV}\right) = \rho \cdot V_{CV} \cdot \frac{\partial u}{\partial t} + u \cdot V_{CV} \cdot \frac{\partial \rho}{\partial t} \qquad \text{Eq.5.5.9}$$

$$\partial u = C_V \cdot \partial T \qquad \text{Eq.5.5.10}$$

Substitution of Eq.5.5.9 and Eq.5.5.10 into Eq.5.5.8 gives the ordinary differential equation that is solved for the temperature inside of the plenum as shown in Eq.5.5.11.

$$\rho \cdot V_{CV} \cdot C_v \cdot \frac{\partial T}{\partial t} = -\dot{Q}_{out} - u \cdot V_{CV} \cdot \frac{\partial \rho}{\partial t} - \dot{m}_{out} \cdot \left(h_{out} + \frac{v_{out}^2}{2}\right) + \dot{m}_{in} \cdot \left(h_{out} + \frac{v_{in}^2}{2}\right) \qquad \text{Eq.5.5.11}$$

$$C_v = C_p - R_{gas} \qquad \text{Eq.5.5.12}$$

$$v_{in} = \frac{\dot{m}_{in}}{\rho_{in} \cdot A_{cin}} \qquad \text{Eq.5.5.13}$$

It is easily seen that Eq.5.5.11 is dependent on the amount of heat lost to the environment. This heat flux is assumed to be constant, and calculated via a partial heat transfer

coefficient that extends from the inside surface of the vessel to the ambient medium at the outside of the plenum. These equations are given by:

$$\dot{Q}_{out} = Q''_{flux} \cdot A_{surf} = U_{partial} \cdot A_{surf} \cdot \left(T_{surf} - T_{amb}\right) \qquad \text{Eq.5.5.14}$$

$$A_{surf\_in} = \pi \cdot d_{in} \cdot L_{plenum} \qquad \text{Eq.5.5.15}$$

$$U_{partial} = \frac{1}{d_{in} \cdot \frac{\ln\left(\frac{d_{out}}{d_{in}}\right)}{k_{metal}} + d_{in} \cdot \frac{\ln\left(\frac{d_{ins}}{d_{out}}\right)}{k_{ins}} + \frac{d_{in}}{d_{ins}} \cdot \frac{1}{h_{amb}}} \qquad \text{Eq.5.5.16}$$

5.5.2 Energy Conservation Equation: Plenum Shell Control Volume

In order to solve for Eq.5.5.14, the plenum's surface temperature must be known. Thus an energy balance is performed for a control volume that surrounds the plenum's solid shell. Equations 5.5.17 and 5.5.18 give the heat balance and temperature equation for the solid shell respectively. This equation is coupled to Eq.5.5.11 and both temperatures are solved for simultaneously.

The plenum in this case is simulated as a very wide pipe, whose bulk inner velocity is assumed to be very small. In this manner a convection coefficient can be approximated and a surface temperature obtained from the aforementioned equations. Figure 5.19 shows the plenum subsystem in its entirety, and Figure 5.18 the simplified cross-section of the plenum with the corresponding thermal resistances.

In Figure 5.18 the heat flux is denoted by Q", while the thermal resistances of the shell surface, insulation, and ambient air are denoted by R2, R3, and R4 respectively. These thermal resistances are defined in the denominator of Eq.5.5.17. The surface temperature of Eq.5.5.18 corresponds to Ts1 in Figure 5.18.

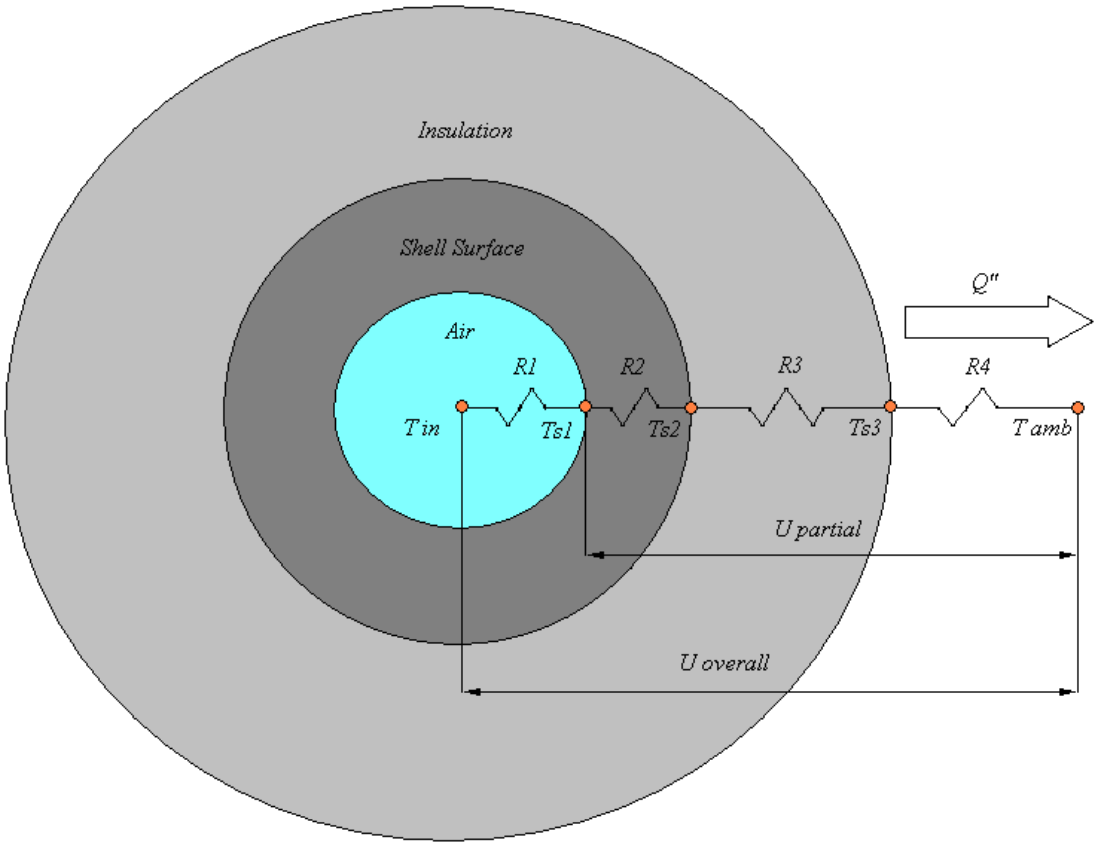

Figure 5.18 Cross-Section of Air Plenum

$$\dot{Q}_{stored} = \dot{Q}_{in} - \dot{Q}_{out} = h_{conv} \cdot A_{surf\_in} \cdot \left(T_{air} - T_{surf}\right) - Q''_{flux} \cdot A_{surf\_in} \qquad \text{Eq.5.5.17}$$

$$\rho_{metal} \cdot C_p \cdot V_{metal} \cdot \frac{\partial T_{surf}}{\partial t} = A_{surf\_in} \cdot \left[h_{conv} \cdot \left(T_{air} - T_{surf}\right) - U_{partial} \cdot \left(T_{surf} - T_{amb}\right)\right] \qquad \text{Eq.5.5.18}$$

$$h_{conv} = \frac{k_{air} \cdot Nu}{d_{in}} \qquad \text{Eq.5.5.19}$$

$$Nu = 0.023 \cdot \mathrm{Re}^{\frac{4}{5}} \cdot \mathrm{Pr}^{\frac{1}{3}} \qquad \text{Eq.5.5.20}$$

$$\mathrm{Re} = \frac{\rho \cdot d_{in} \cdot v_{plen}}{\mu} \qquad \text{Eq.5.5.21}$$

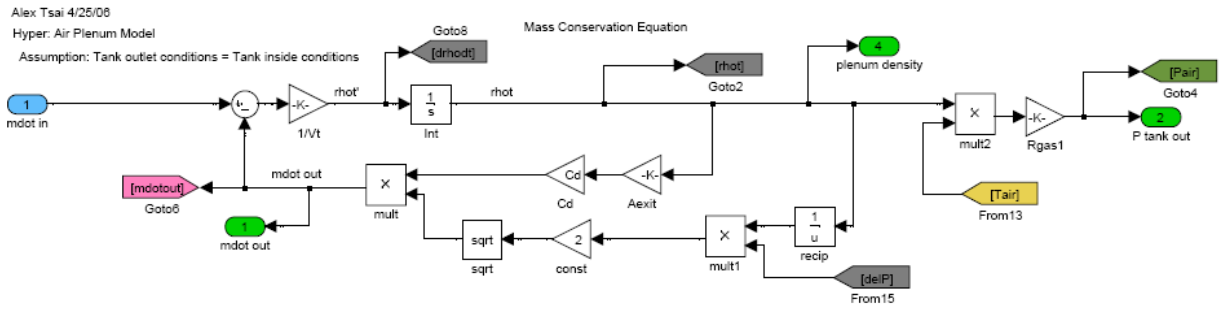

Figure 5.19 Air Plenum Subsystem: Mass Conservation

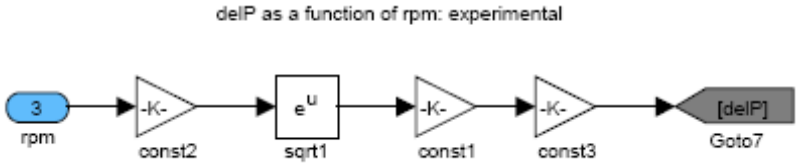

Figure 5.20 Air Plenum Subsystem: Empirical Backpressure

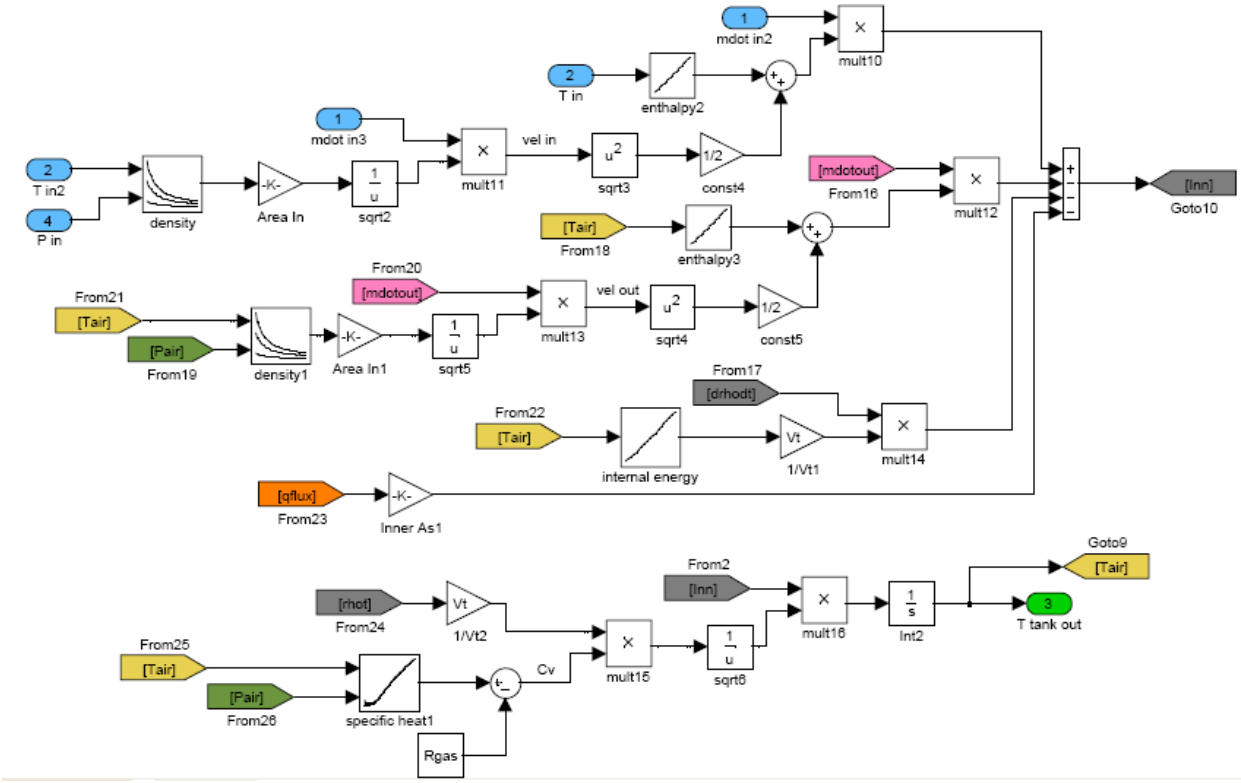

Figure 5.21 Air Plenum Subsystem: Energy Conservation

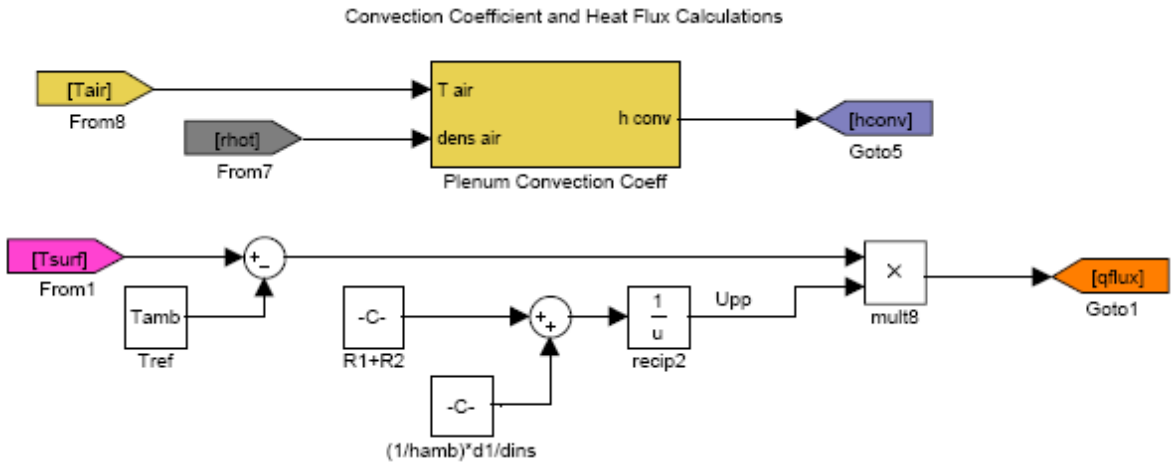

Figure 5.22 Air Plenum Subsystem: Heat Flux and Convection Coefficient

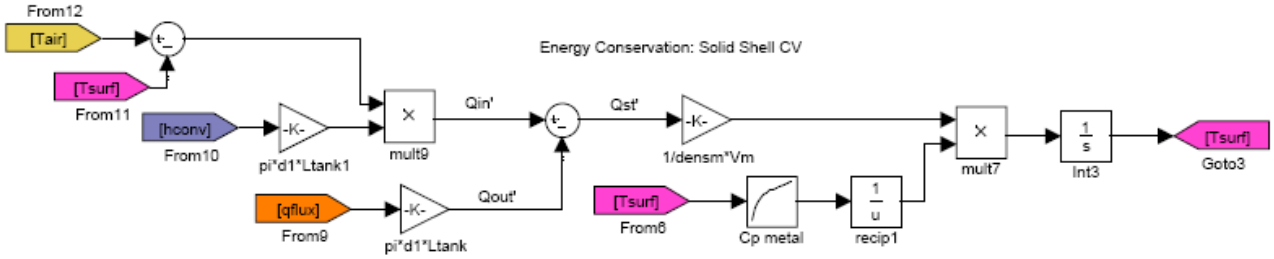

Figure 5.23 Air Plenum Subsystem: Solid Shell Energy Conservation

5.6 Piping Model

The piping model consists of temperature and pressure subsystem equation blocks that are combined for straight pipe routing segments of the HyPer system. Figure 5.25 is a Simulink schematic showing one pipe segment and its corresponding geometry.

5.6.1 Temperature Equation

The energy equation of Eq.5.6.1 is applied to all the system piping. In this case, there is no control volume of the air inside the pipe because the residence time of the air at the operating mass flows is almost negligible for each pipe segment. A control volume is then fixed to the pipe shell where the pipe's surface temperature is calculated from the

usual energy balance equation. A constant flux assumption allows for the calculation of the exit pipe temperature of the fluid. For this analysis, an overall and a partial heat transfer coefficient are used, where the difference lies in the exclusion of the insulation and ambient thermal resistances in the partial heat transfer coefficient term. Figure 5.24 shows a schematic of the pipe cross-section, and the relevant parameters.

$$\rho_m \cdot C_{pm} \cdot V_m \cdot \frac{\partial T_{surf}}{\partial t} = \dot{m} \cdot C_{pa} \cdot \left(T_{in} - T_{out}\right) - Q''_{flux} \cdot \pi \cdot d_{in} \cdot L \qquad \text{Eq.5.6.1}$$

$$T_{out} = T_{surf} + \frac{Q''_{flux}}{U_{partial}} \qquad \text{Eq.5.6.2}$$

$$Q''_{flux} = U_{overall} \cdot \left(T_{in} - T_{amb}\right) \qquad \text{Eq.5.6.3}$$

$$U_{overall} = \frac{1}{\frac{1}{h_{conv}} + d_{in} \cdot \frac{\ln\left(\frac{d_{out}}{d_{in}}\right)}{2 \cdot k_{metal}} + d_{in} \cdot \frac{\ln\left(\frac{d_{ins}}{d_{out}}\right)}{2 \cdot k_{ins}} + \frac{d_{in}}{d_{ins}} \cdot \frac{1}{h_{amb}}} \qquad \text{Eq.5.6.4}$$

$$U_{partial} = \frac{1}{\frac{1}{h_{conv}} + d_{in} \cdot \frac{\ln\left(\frac{d_{out}}{d_{in}}\right)}{2 \cdot k_{metal}}} \qquad \text{Eq.5.6.5}$$

Following are the Simulink subsystems for Equations 5.6.1 to 5.6.5.

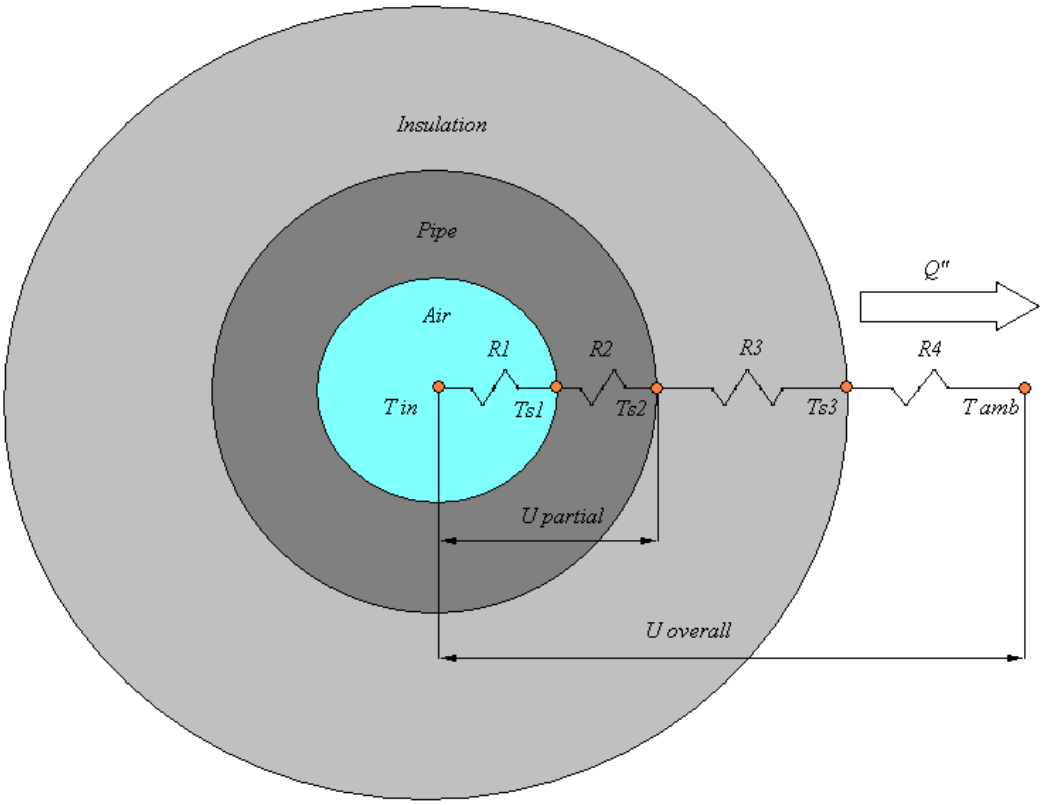

Figure 5.24 Pipe Cross-Sectional Schematic

In Figure 5.24, the radial heat flux is indicated by Q", while the thermal resistances for the inlet air, metal pipe, insulation, and ambient air are shown as R1, R2, R3, and R4 respectively. These resistances are defined in the denominator of Eq.5.6.3. In Eq.5.6.1, T_{surf} is the surface temperature Ts2 shown in the diagram, while T_{in} is the inner temperature of the air, at the outlet of the pipe section. The contact resistances between the insulation and the pipe are omitted in the diagram, and excluded from the analysis.

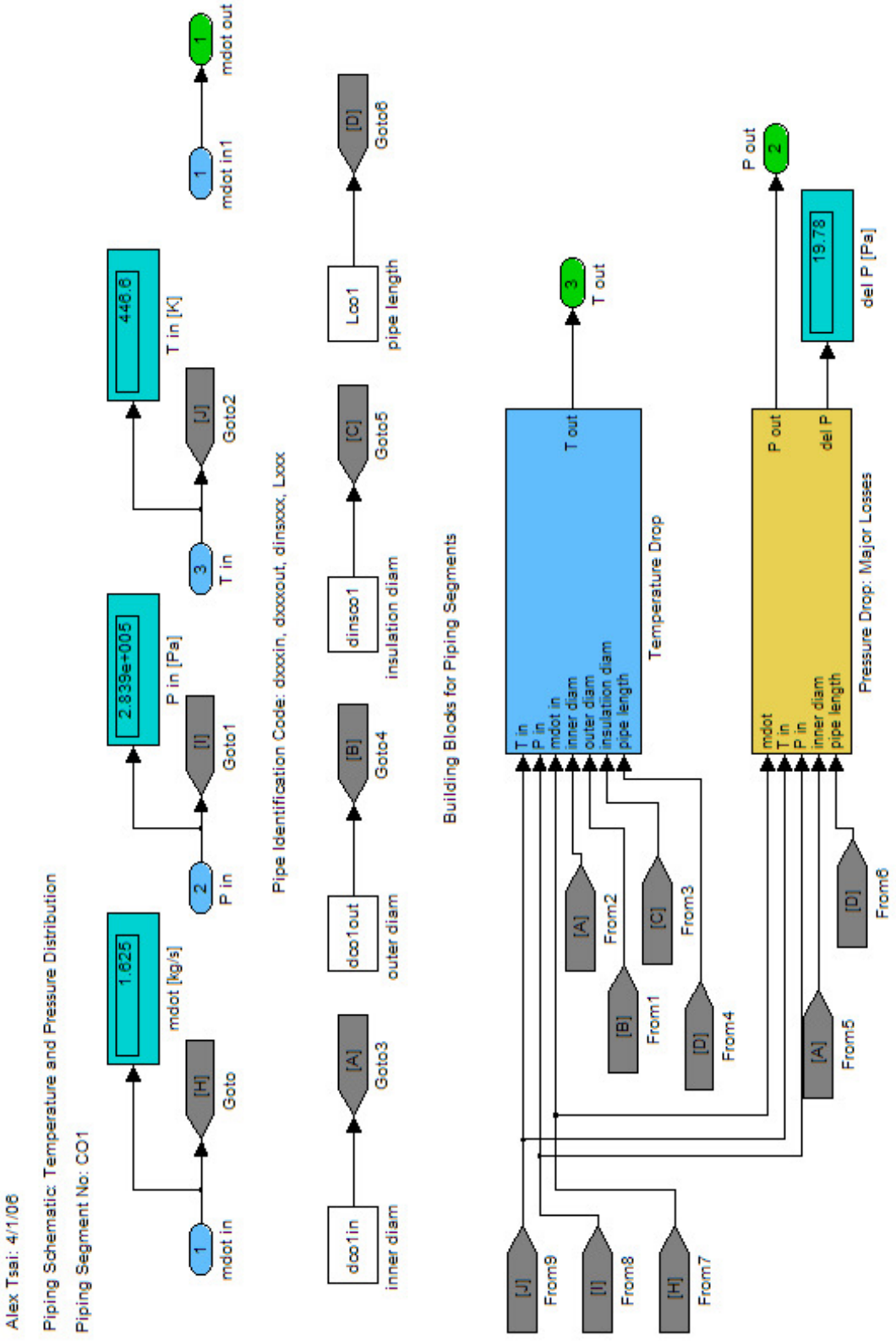

Figure 5.25 Pipe Element: Temperature and Pressure Subsystems

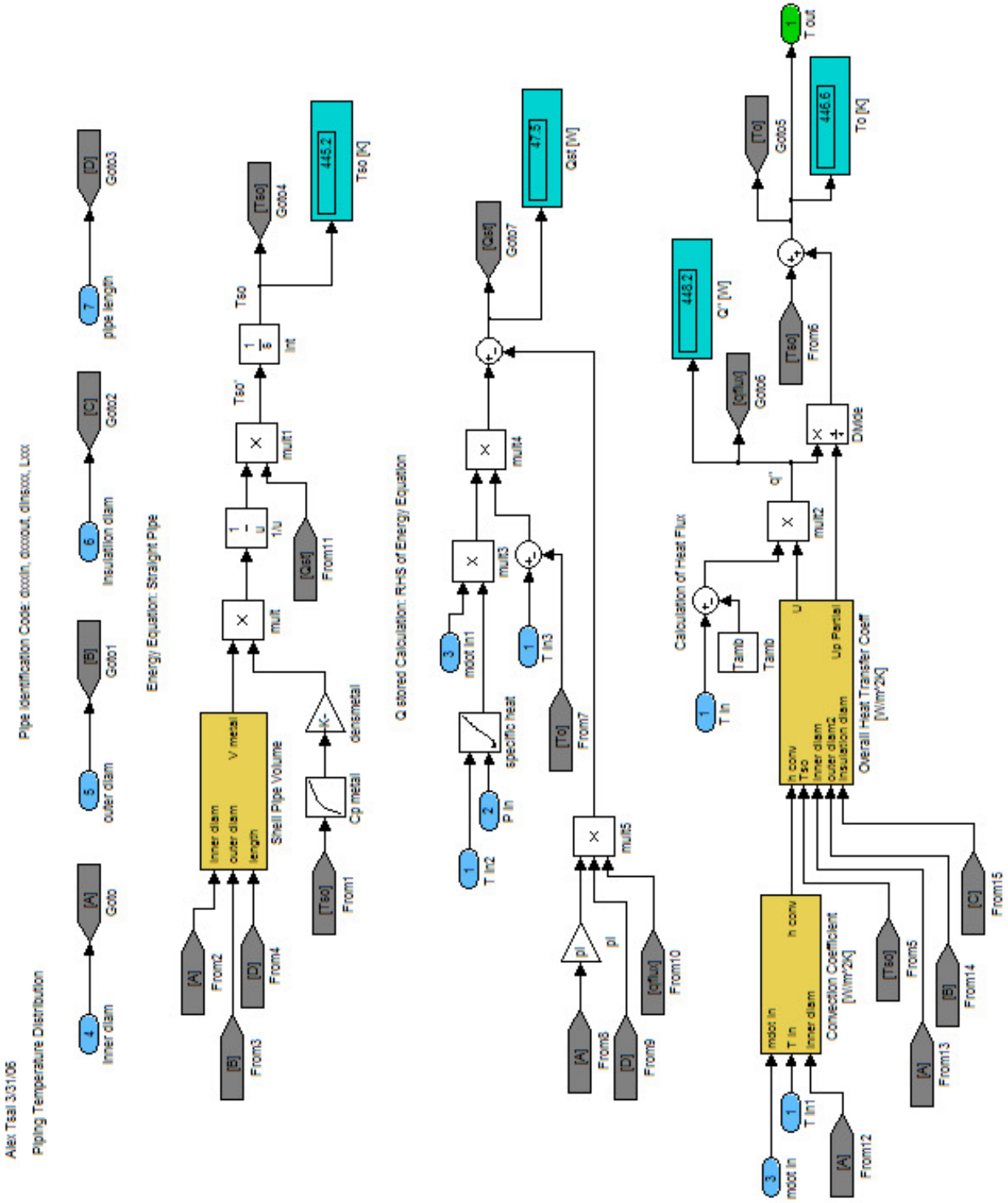

Figure 5.26 Temperature Equation Subsystem

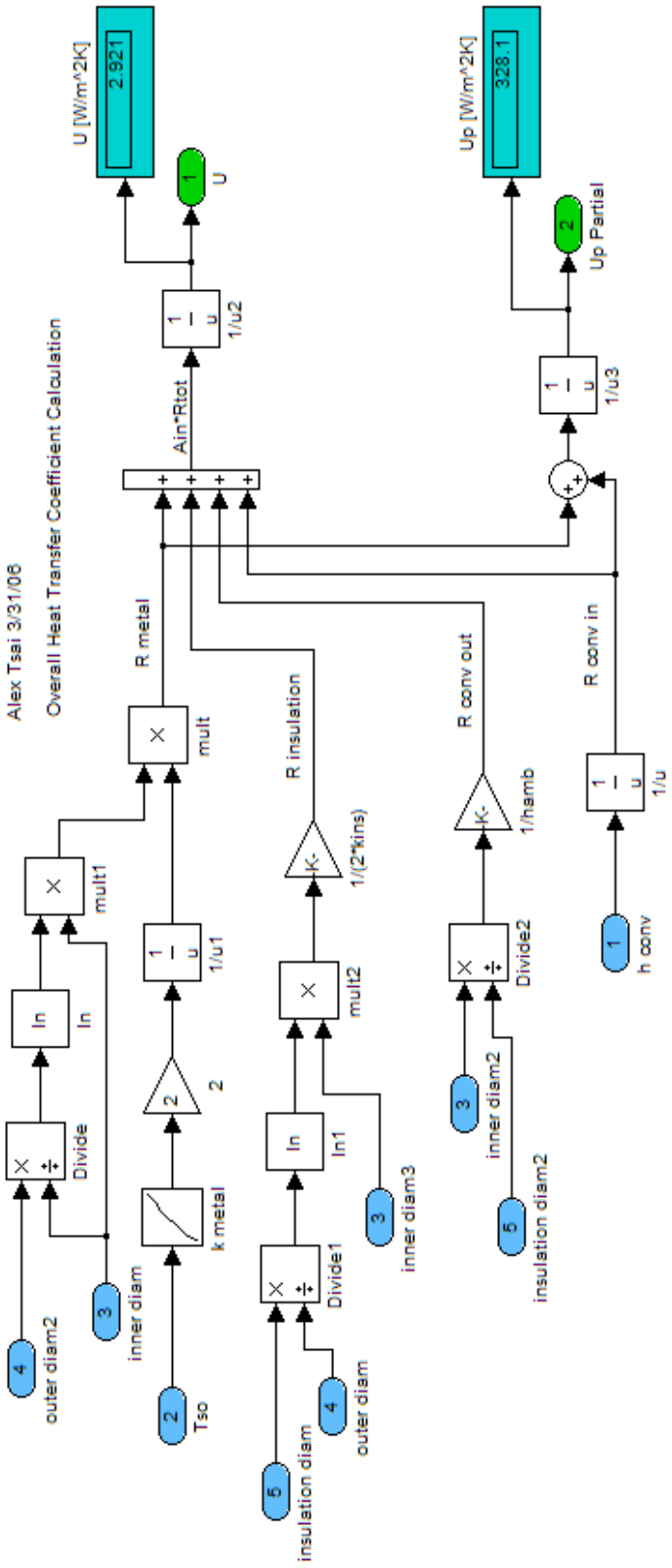

Figure 5.27 Overall and Partial Heat Transfer Coefficient Subsystem

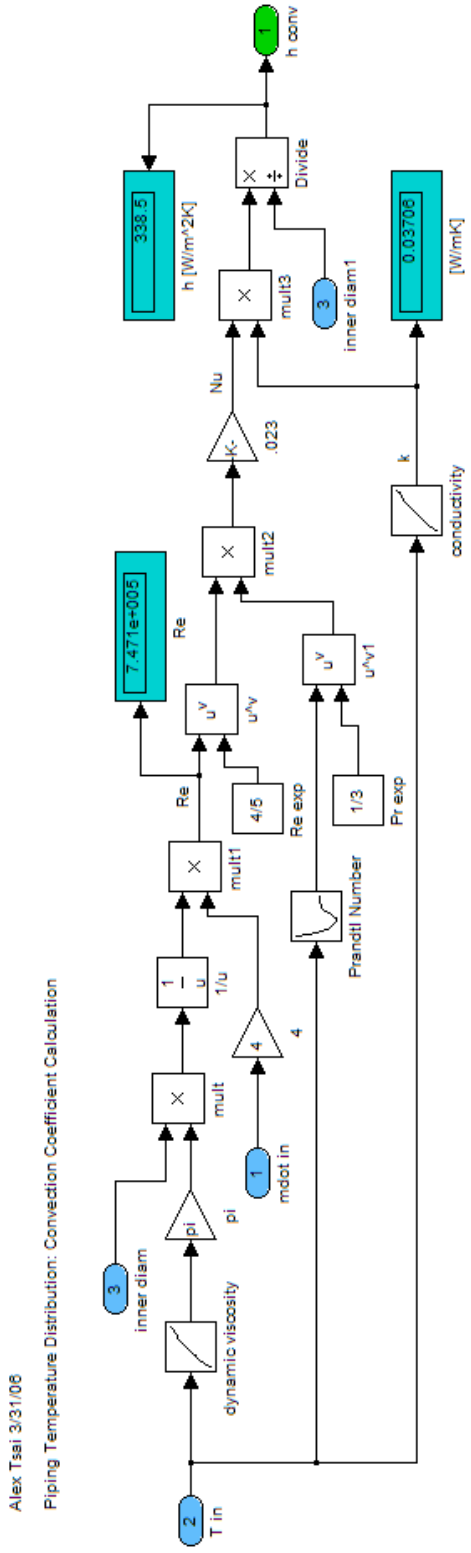

Figure 5.28 Convection Coefficient Subsystem

5.6.2 Pressure Equation

The pressure drop of the air within each pipe segment is calculated from the derivation of the energy equation Eq.5.5.6 considering incompressible flow with variable density. It is assumed that the pressure is uniform along cross sectional areas of the piping and that the flow is steady flow. With no work done or heat added, the energy equation becomes:

$$\left(\frac{P_{in}}{\rho}+\alpha_{in}\cdot\frac{v_{in}^2}{2}+g\cdot z_{in}\right)-\left(\frac{P_{out}}{\rho}+\alpha_{out}\cdot\frac{v_{out}^2}{2}+g\cdot z_{out}\right)=\left(u_2-u_1\right)-\frac{\partial Q}{dm} \qquad \text{Eq.5.6.6}$$

The terms in parenthesis on the left hand side of Eq.5.6.6 correspond to the mechanical energy per unit mass at inlet and outlet sections. The velocity term is multiplied by a kinetic energy coefficient "α". This term approaches unity with high Reynolds numbers but may be influential for developing flows (Fox et al. 1992). For our purpose $\alpha_1=\alpha_2$, and this coefficient is equal to 1. The right hand side of Eq.5.6.6 represents the difference in mechanical energy between inlet and outlet sections of a pipe, and can be related via the Buckingham π Theorem to Eq.5.6.8. This energy dissipation can be expressed as a "head loss" composed of major and minor frictional effects. Major effects are frictional losses in piping having constant cross sectional area, whereas minor losses are associated with loss due to pipefittings, geometry changes and the like. Eq.5.6.8 expresses the head loss in terms of major "h_l" and minor "h_{lm}" frictional losses (Fox et al. 1992).

$$P_{out}=P_{in}-\rho\cdot h_l \qquad \text{Eq.5.6.7}$$

$$h_l=f\cdot\frac{L}{d_{in}}\cdot\frac{v^2}{2} \quad , \quad h_{lm}=K\cdot\frac{v^2}{2} \qquad \text{Eq.5.6.8}$$

$$K=K_{loss}, K=\left(\frac{L_e}{d}\right), K=\frac{1}{d_{in}}\cdot\left(L_{equiv}\right) \qquad \text{Eq.5.6.9}$$

$$v=\frac{4\cdot\dot{m}}{\rho\cdot\pi\cdot d_{in}^2} \qquad \text{Eq.5.6.10}$$

The friction factor is a function of the relative roughness of the pipe ε/d, and Reynolds number for the most general case. There are various correlations for the friction factor, but the Miller (Fox et al. 1992) correlation provides results with no iterative loop calculations.

$$f = \frac{0.25}{\left[\ln\left(\frac{\varepsilon / d_{in}}{3.7} + \frac{5.74}{\mathrm{Re}^{0.9}}\right)\right]^2} \qquad \text{Eq.5.6.11}$$

In order to develop a model that is faithful to the process and instrumentation diagram of the HyPer facility, all the piping routes were traced to record pipe diameters, lengths, fittings, expansions and contractions. They Hyper model includes three different loss factors for different minor loss cases. Appendix C show spreadsheets containing all pipe data.

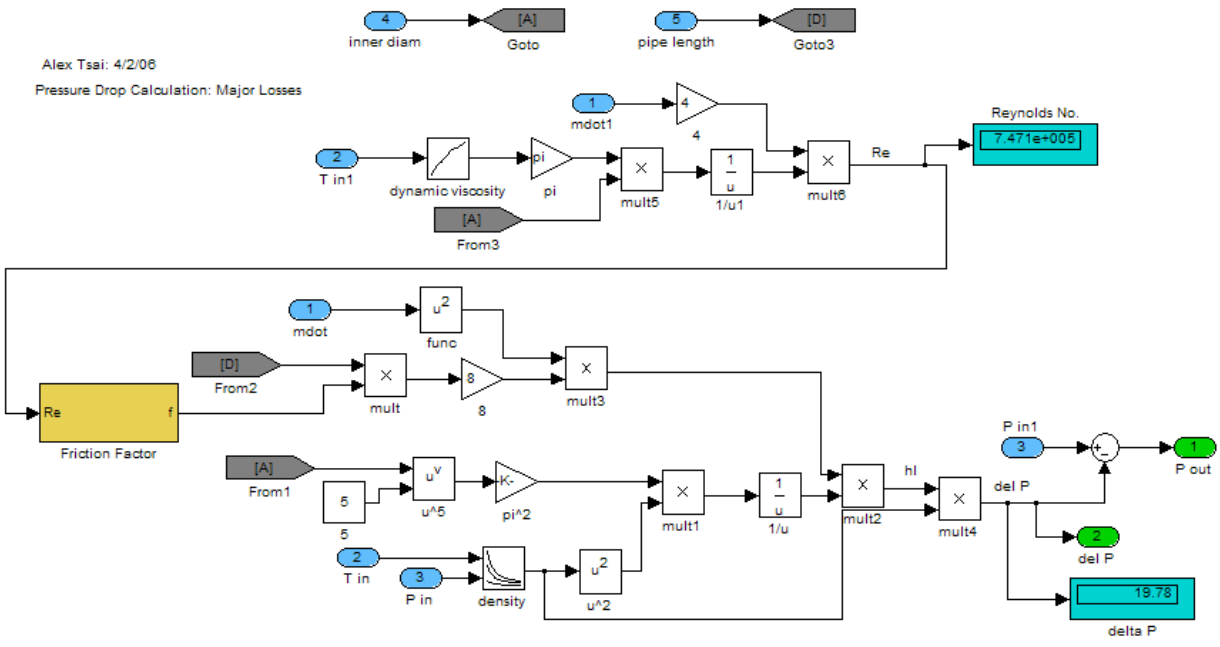

Figure 5.29 Pressure Major Losses in Straight Pipe

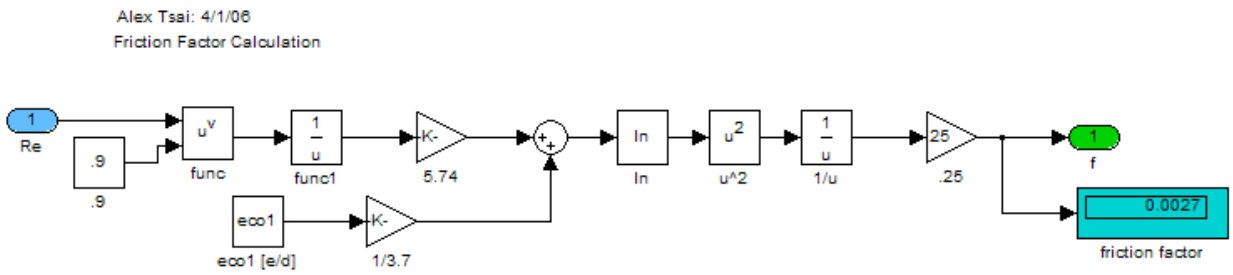

Figure 5.30 Friction Factor Subsystem

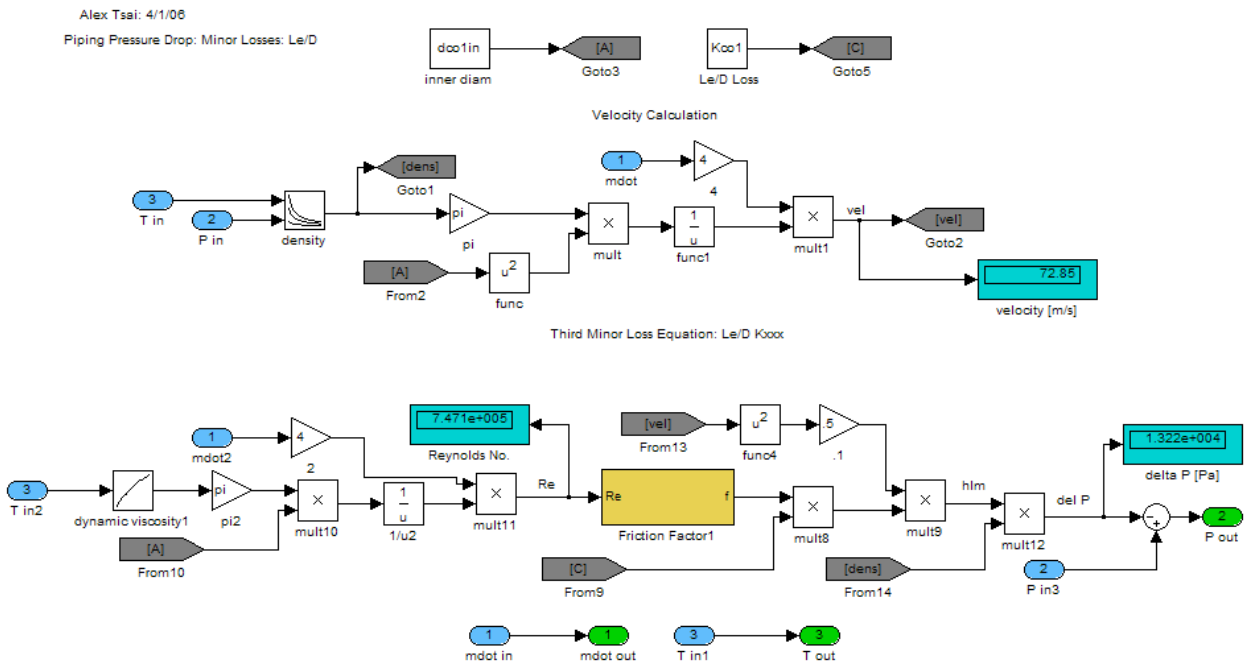

Figure 5.31 Minor Pressure Losses Subsystem: Le/D Case

5.7 Heat Exchanger Model

The heat exchangers are analyzed with the use of the number of transfer units' method, the NTU method (Incropera 1990). Under steady state operation, this method calculates a maximum heat transfer rate based on a minimum heat capacity rate C_{min} between the hot and cold air sides. The heat exchangers in use are primary surface recuperators that

combine cross and counter flows. The bulk of the exchanger is counter flow, and thus the effectiveness given by Eq.5.7.4 uses the correlation of counter flow behavior. All heat exchanger data is approximated on the basis of geometry and exchanger type.

$$q_{actual} = \varepsilon \cdot q_{\max} \qquad \text{Eq.5.7.1}$$

$$q_{\max} = C_{\min} \cdot \left(T_{HotIn} - T_{ColdIn}\right) \qquad \text{Eq.5.7.2}$$

$$C_{\min} \le \left[\left(\dot{m}_{cold} \cdot C_{pcold}\right) \cup \left(\dot{m}_{hot} \cdot C_{phot}\right)\right] \qquad \text{Eq.5.7.3}$$

$$\varepsilon = f\left(NTU, C_r\right) \qquad \text{Eq.5.7.4}$$

$$\varepsilon = \frac{1 - e^{\left[-NTU \cdot (1 - C_r)\right]}}{1 - C_r \cdot e^{\left[-NTU \cdot (1 - C_r)\right]}} \qquad \text{Eq.5.7.5}$$

For a counter flow heat exchanger, Eq.5.7.5 gives the NTU-effectiveness relationship.

$$NTU = \frac{U \cdot A}{C_{\min}} \quad , \quad C_r = \frac{C_{\min}}{C_{\max}} \qquad \text{Eq.5.7.6}$$

The overall heat transfer coefficient U, and the gas-side surface area A, must be obtained from the manufacturer, through experimental data, or approximated from geometry. The heat capacity rates C_{min} and C_{max} are determined by Eq.5.7.3, where C_{min} is the smaller of the two capacity values between the cold and hot air sides. The exit temperatures for both sides are given as:

$$T_{ColdOut} = T_{ColdIn} + \frac{q_{actual}}{\dot{m}_{cold} \cdot C_{pcold}} \qquad \text{Eq.5.7.7}$$

$$T_{HotOut} = T_{HotIn} - \frac{q_{actual}}{\dot{m} \cdot C_{phot}} \qquad \text{Eq.5.7.8}$$

During transient operation the heat in and out of the heat exchanger wall are computed according to a sequential logic described later in the paper, using the equations below.

$$\dot{Q}_{in} = \left(h_{conv} \cdot A_{surf}\right)_{hot} \cdot \left(T_{hot} - T_{wall}\right) + \left(h_{conv} \cdot A_{surf}\right)_{cold} \cdot \left(T_{cold} - T_{wall}\right) \qquad \text{Eq.5.7.9}$$

$$\dot{Q}_{out} = 0 \text{ or } \dot{Q}_{out} = \left(h_{conv} \cdot A_{surf}\right)_{cold} \cdot \left(T_{wall} - T_{cold}\right) \qquad \text{Eq.5.7.10}$$

The first heat rate in Eq.5.7.10 is for $T_{wall}<T_{cold}$, while the second is for $T_{wall}>T_{cold}$. Figures 5.32-5.39 show the heat exchanger subsystem and logic.

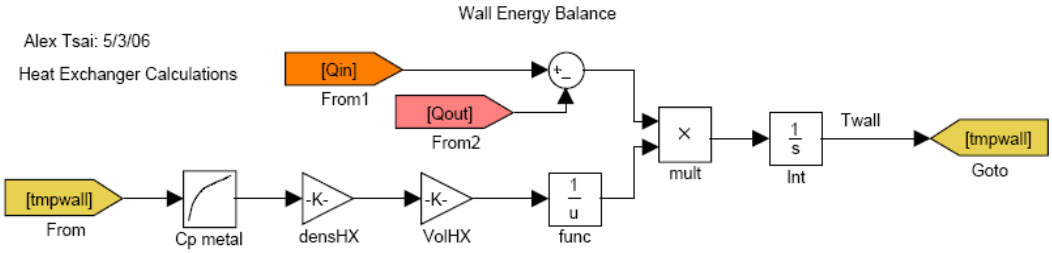

Figure 5.32 Heat Exchanger Subsystem: Wall Balance

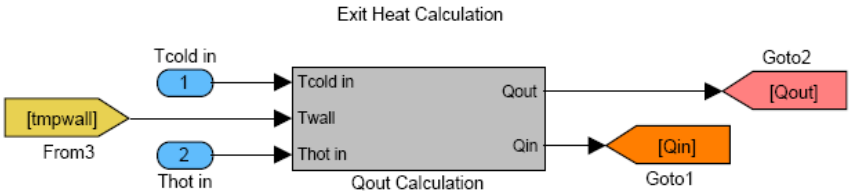

Figure 5.33 Heat Exchanger Subsystem: Heat Calculation

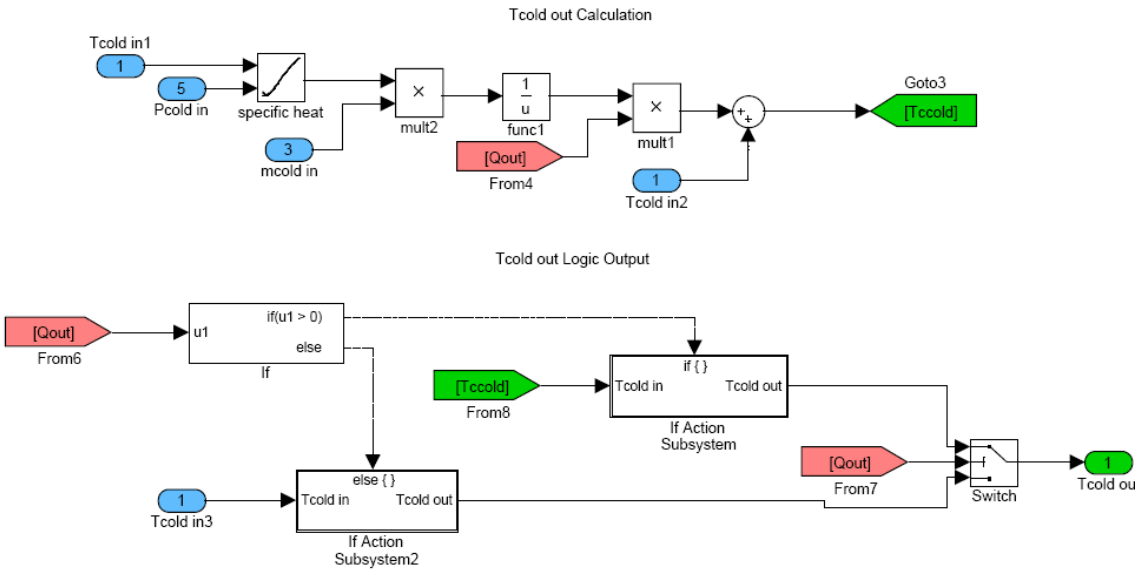

Figure 5.34 Heat Exchanger Subsystem: Cold Side Temperature Equation

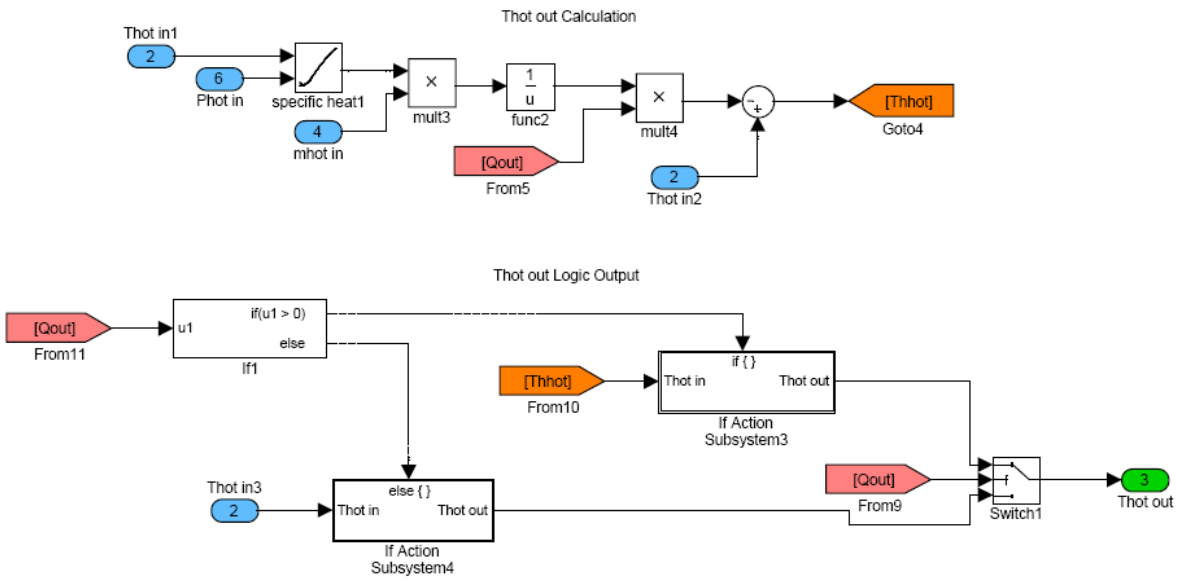

Figure 5.35 Heat Exchanger Subsystem: Hot Side Temperature Equation

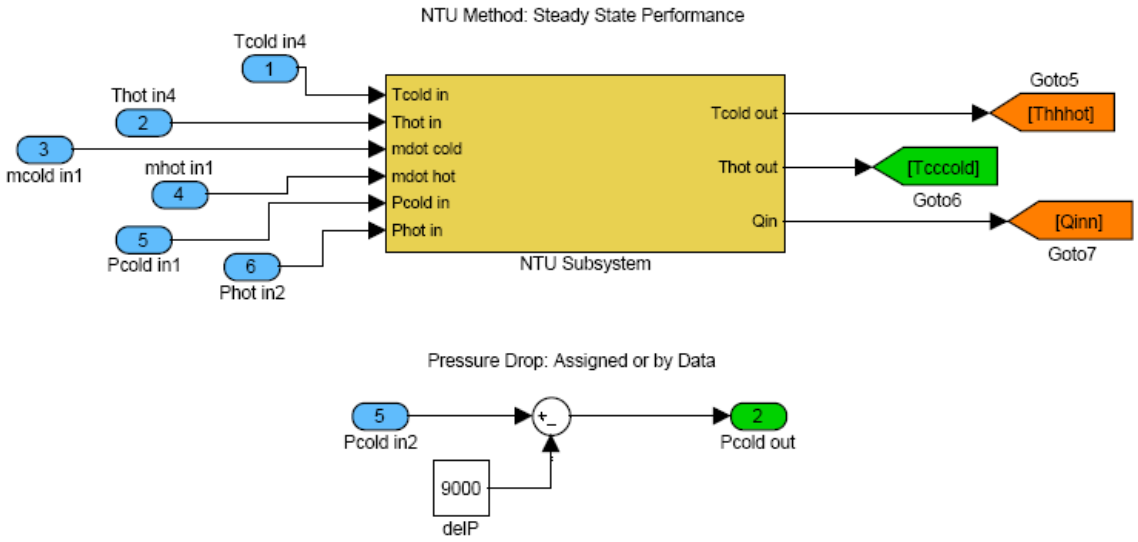

Figure 5.36 Heat Exchanger Subsystem: NTU Block

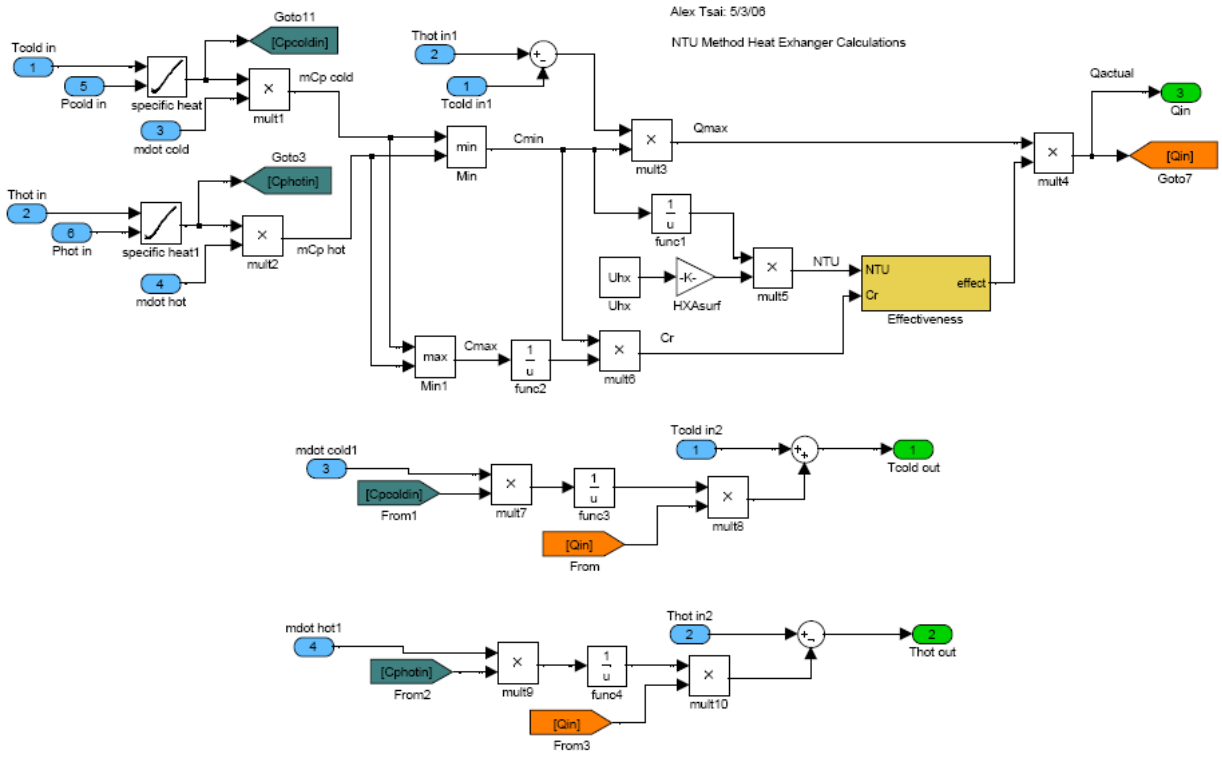

Figure 5.37 Heat Exchanger Subsystem: NTU Subsystem

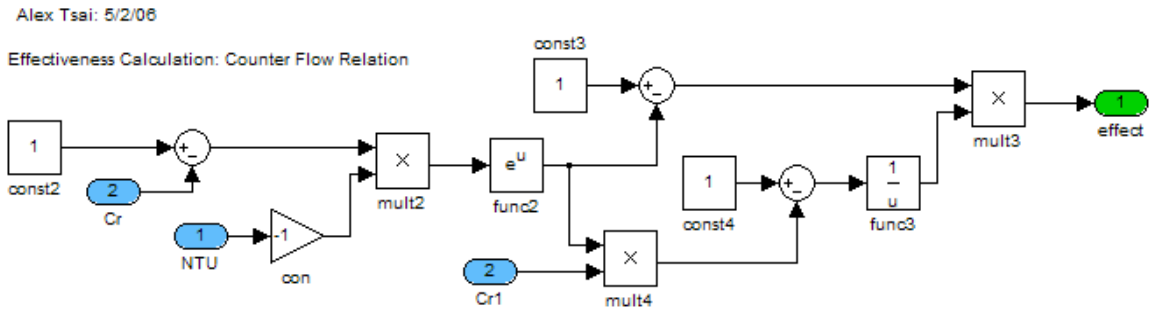

Figure 5.38 NTU Effectiveness Equation

The convection coefficient is approximated from heat exchanger cross sectional passage geometry, wetted flow perimeter and Nusselt number for fully developed laminar flow. Manufacturer data is still required to obtain a more accurate model and thus analysis.

In order to allow the heat exchanger metal to heat up properly during system startup, a logic subsystem compares the cold side air temperature with the heat exchanger "wall" temperature. During transient periods, both the hot and cold air streams heat the wall. Therefore, heat in or out of the wall is assigned accordingly to whether the comparison condition holds true. The equations for Q_{in} and Q_{out} are given in Eq.5.7.9 and Eq.5.7.10. Once at steady state, the NTU method is activated until system shutdown, when the temperature condition is again revised and a heat input or output assigned.

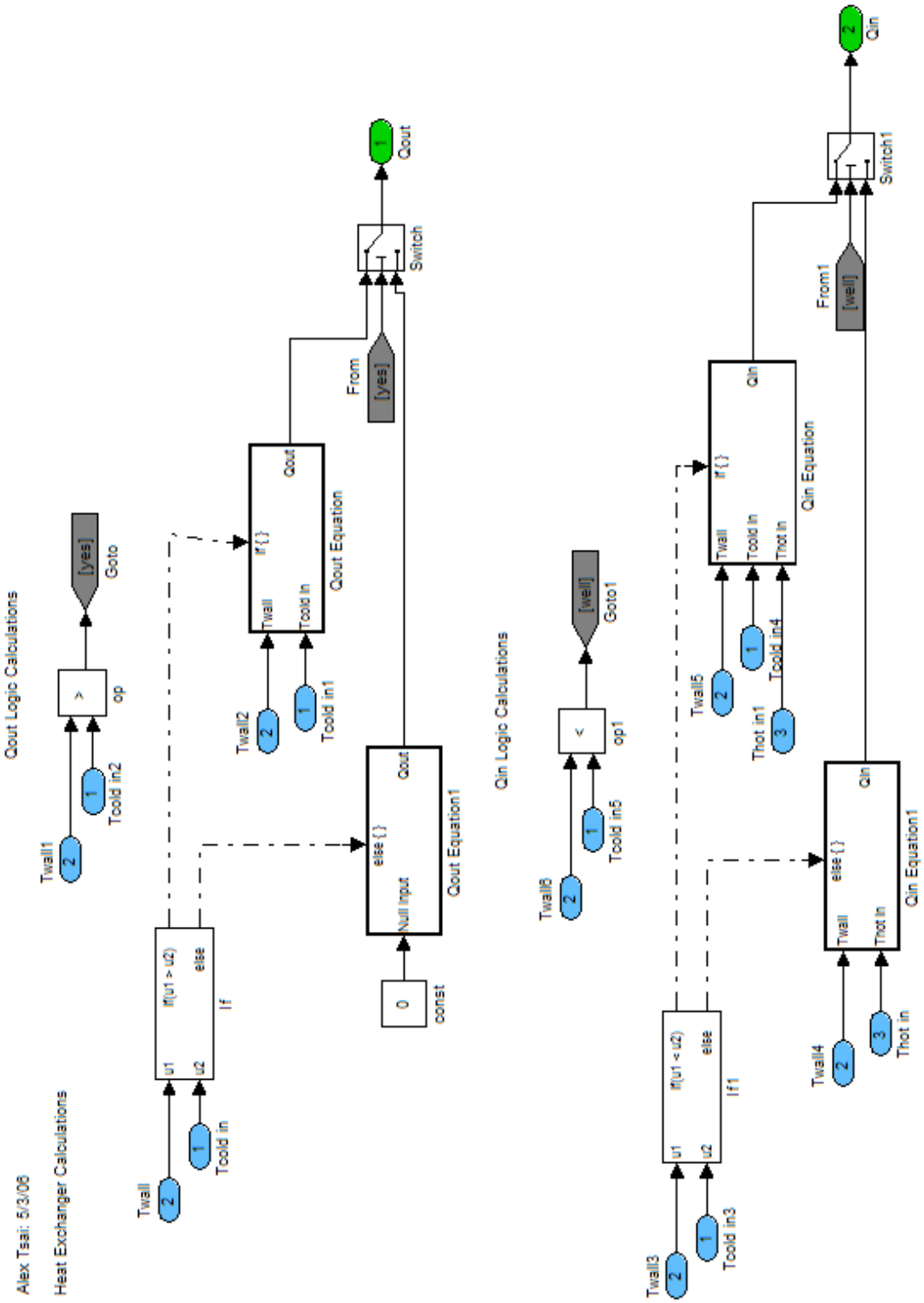

Figure 5.39 Heat Flux Calculation Logic

5.8 Combustor Model

The combustor is modeled as a cylindrical can lying within the inner layers of the piping that connects to the post combustor. The combustion process itself is not modeled, but rather the temperature rise is derived by a simplification of the energy equation Eq.5.5.6, in which work input and changes in density within the can are neglected. Because the change in kinetic energy is insignificant compared to the change in enthalpy within the control volume of the canister, the energy equation becomes (Incropera 1990):

$$\dot{Q}_{in} = \frac{\partial}{\partial t} \cdot (e \cdot \rho \cdot V) - \dot{m} \cdot (h_{out} - h_{in}) \qquad \text{Eq.5.8.1}$$

$$e = u + \frac{v^2}{2} \qquad \text{Eq.5.1.78}$$

Applying the chain rule to the first term in the right hand side of Eq.5.8.1, and assuming T_{in}=constant, gives:

$$\frac{\partial}{\partial t}(e \cdot \rho \cdot V) = \left(u + \frac{v^2}{2}\right) \cdot \left(V \cdot \frac{\partial \rho}{\partial t}\right) + \frac{\partial}{\partial t}\left(u + \frac{v^2}{2}\right) \cdot \rho \cdot V \qquad \text{Eq.5.8.2}$$

$$\frac{\partial}{\partial t}\left(u + \frac{v^2}{2}\right) \cdot \rho \cdot V = \left(\frac{\partial u}{\partial t} + \frac{1}{2} \cdot \frac{\partial (v^2)}{\partial t}\right) \cdot \rho \cdot V \qquad \text{Eq.5.8.3}$$

$$\rho \cdot C_v \cdot V \cdot \frac{\partial T_{out}}{\partial t} = \dot{Q}_{in} - \rho \cdot V \cdot \frac{1}{2} \cdot \frac{\partial (v_{in}^{\ 2})}{\partial t} - \dot{m} \cdot (h_{out} - h_{in}) \qquad \text{Eq.5.8.4}$$

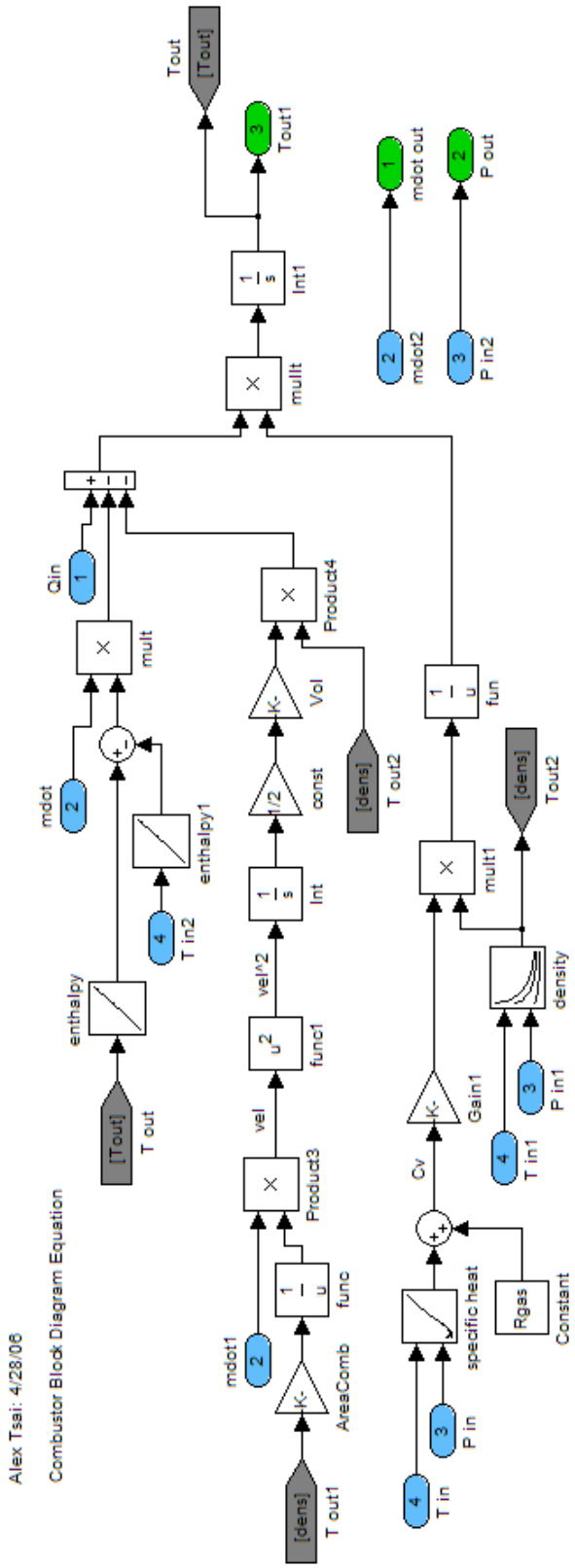

Figure 5.40 Combustor Block Diagram

5.9 Post Combustor Model

The continuity and energy equations for the post combustor are derived in a similar fashion as the ones for the air plenum. In this case, there are now more inlet ports connecting the combustor route with the cold air and hot air bypass routes. These equations are presented below, where $\dot{Q}_{st}$ is the stored heat within the post combustor control volume, and Q''_{flux} is the heat loss radially through the post combustor skin. The index "i"= 1,2,3 corresponds to combustor, cold air, and hot air terms respectively.

$$\dot{m}_{st} = \dot{m}_{inComb} + \dot{m}_{inCA} + \dot{m}_{inHA} - \dot{m}_{out} \qquad \text{Eq.5.9.1}$$

$$\dot{Q}_{st} = \dot{Q}_{in} - \dot{Q}_{out} = \left(\dot{Q}_{inComb} + \dot{Q}_{inCA} + \dot{Q}_{inHA}\right) - \left(\dot{Q}_{out} + Q''_{flux}\right) \qquad \text{Eq.5.9.2}$$

For simplicity, all incoming routes will be examined at the same elevation, thus canceling the potential energy terms as shown in Eq.5.9.3.

$$\dot{Q}_i = \dot{m}_i \cdot \left(h_i + \frac{v_i^2}{2}\right) \qquad \text{Eq.5.9.3}$$

$$\rho \cdot C_v \cdot V \cdot \frac{\partial T}{\partial t} = -\dot{Q}_{flux} - u \cdot V \cdot \frac{\partial \rho}{\partial t} - \dot{m}_{out} \cdot \left(h_{out} + \frac{v_{out}^2}{2}\right) + \sum_{i=1}^{3} \dot{Q}_i \qquad \text{Eq.5.9.4}$$

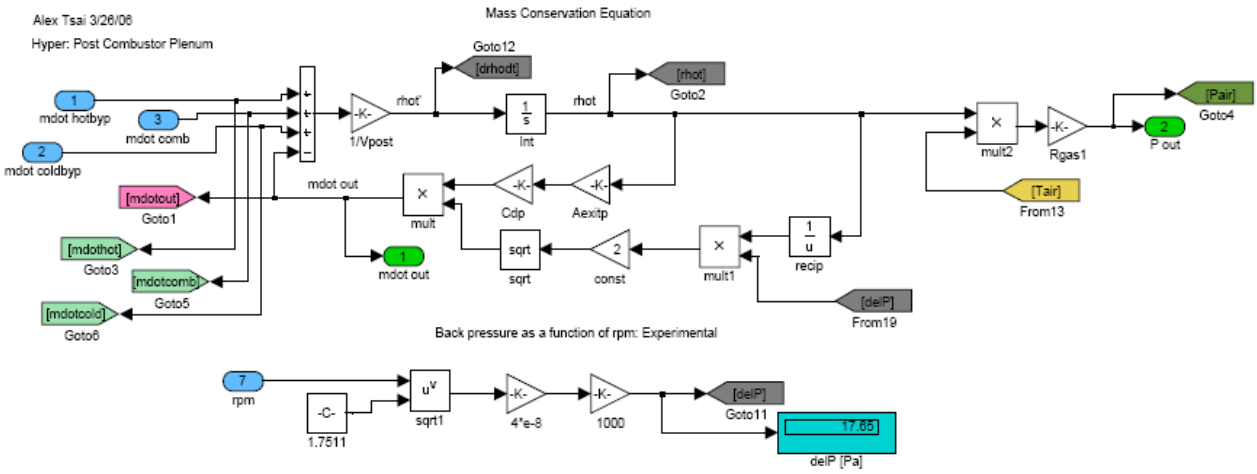

Figure 5.41 Post Combustor Subsystem: Mass Conservation

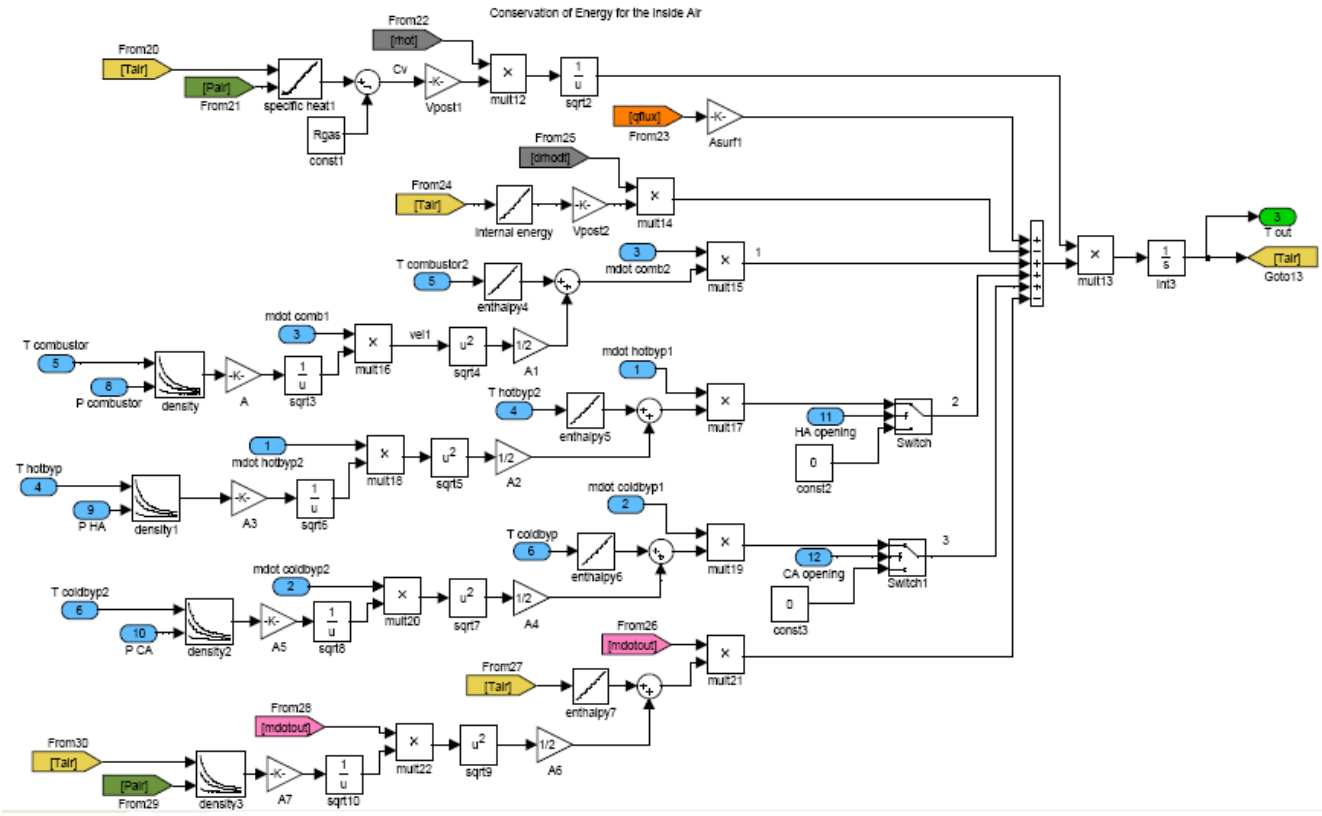

Figure 5.42 Post Combustor Subsystem: Inlet Air Energy Conservation

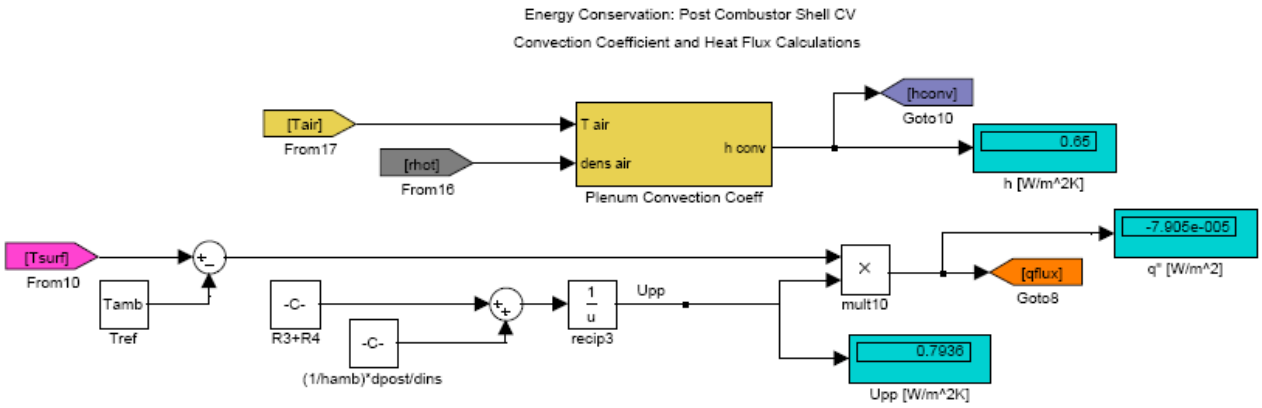

Figure 5.43 Post Combustor Subsystem: Shell CV

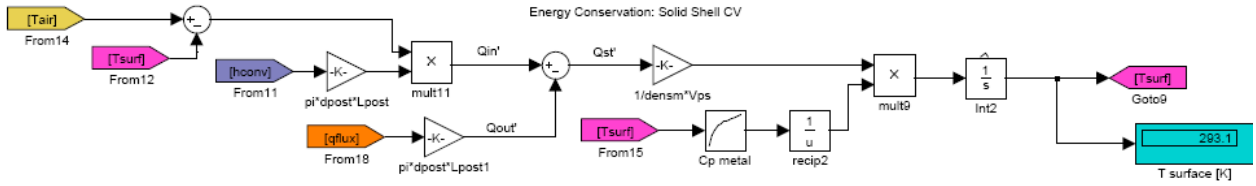

Figure 5.44 Post Combustor Subsystem: Energy Equation

5.10 Bypass Valve Mass Flows

The valve subsystem assigns a mass flow rate to the heat exchangers, air plenum and post combustor depending on whether any of the three bypass valves are activated. Each valve was empirically characterized for pressure drop and mass flow rate across it. Look-up tables in Simulink provide the pressure and flow for all the valves. The cold and hot air piping routes are shown in Appendix I. Temperature, pressure and mass flow are redirected throughout the piping routes, when a corresponding bypass valve is either opened or closed. The post combustor subsystem receives routed flows upon bypass valve activation.

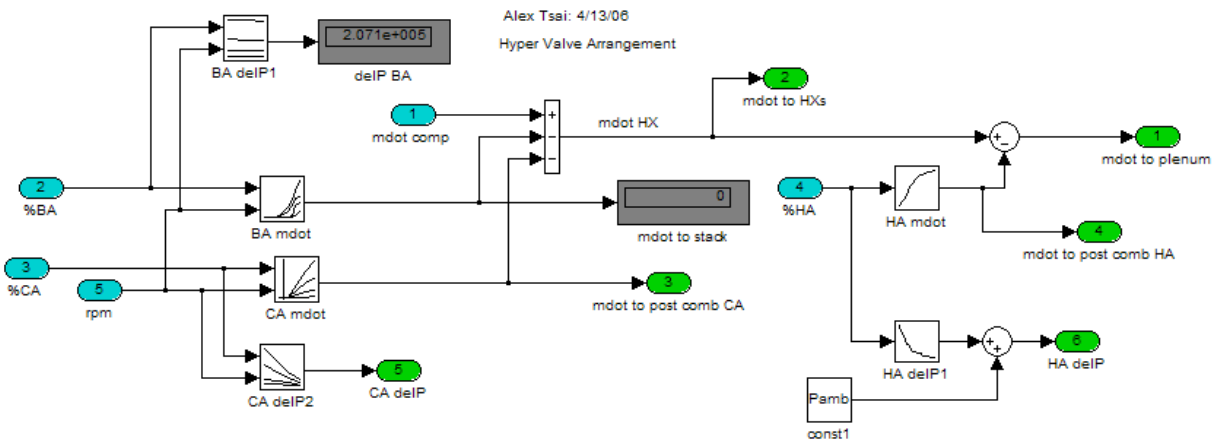

Figure 5.45 Bypass Valve Mass Flow Characteristics

5.11 Fuel Valve Logic

The fuel valve can be used in either open loop or closed loop mode. Figure 5.46 shows both subsystems, and Figures 5.47 and 5.48 the inner workings of the closed loop block.

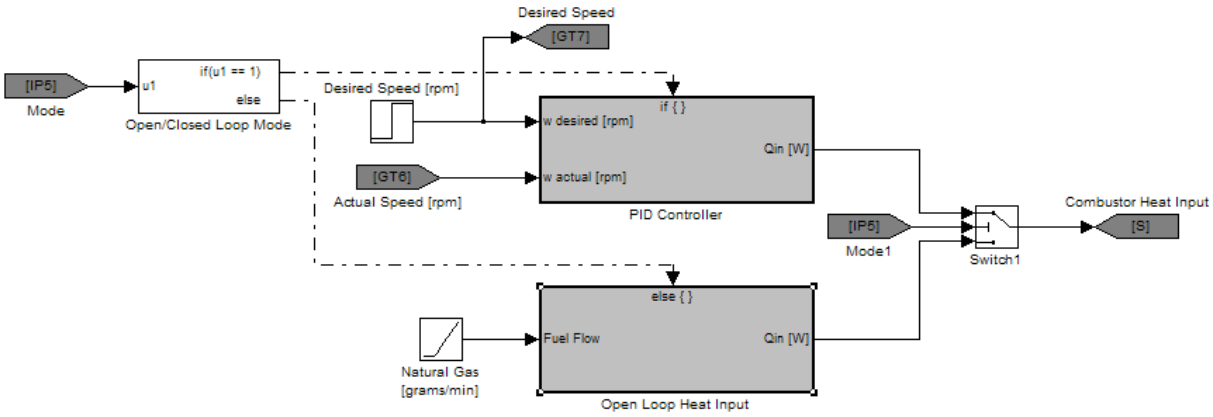

Figure 5.46 Combustor Heat Input Logic

The output of either one block is the calculated heat in kW that goes to the combustor. Regardless of what mode is chosen, the model always begins with the blower providing mass flow rate to the air plenum. This blower is modeled as a ramp with a pre-determined slope, which spins the turbine before the combustor is activated. Once

9000rpms are reached, the combustor ignites from either closed loop or open loop fuel flow control mode.

5.11.1 Open Loop Command

In Figure 4.9 region "7" allows the user to select a system "mode" from a step input block. If open loop is chosen, the fuel valve, modeled as a ramp input sends a signal at a predetermined ramp slope, representing the fuel valve flow rate. This signal is amplified by a slider gain that has the empirical flow rate limits. Heat input into the combustor is then modeled according to the LHV of the natural gas.

5.11.2 Closed Loop Command

If in turn the closed loop mode is chosen, the fuel valve is activated by a PID controller, which resembles the actual speed controller the HyPer system utilizes. Turbine speed response is dependent on the gains chosen for the proportional, integral and derivative controller terms. Figure 5.48 includes the PID gains, and the fuel valve dynamics as described in the polynomial equation. This translates valve demand in percentage, to fuel flow in [g/s]. The LHV is multiplied to this flow, yielding heat in [kW].

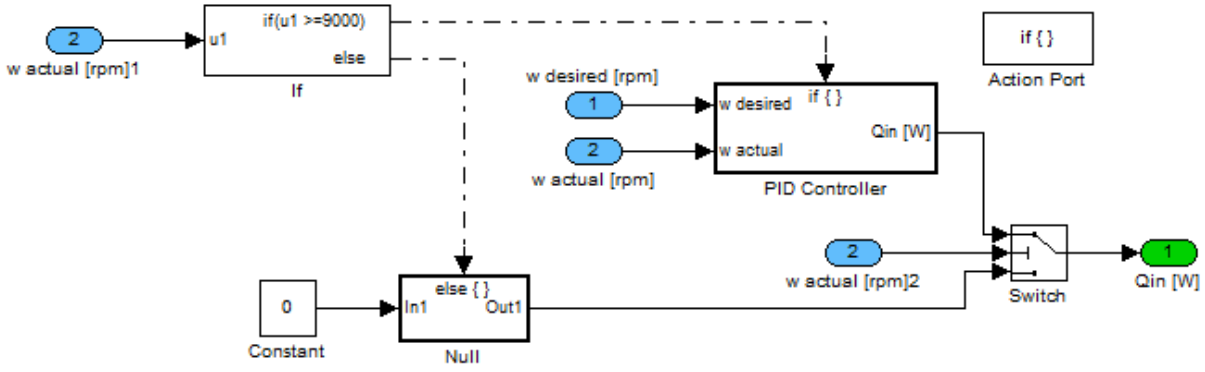

Figure 5.47 PID Controller Subsystem

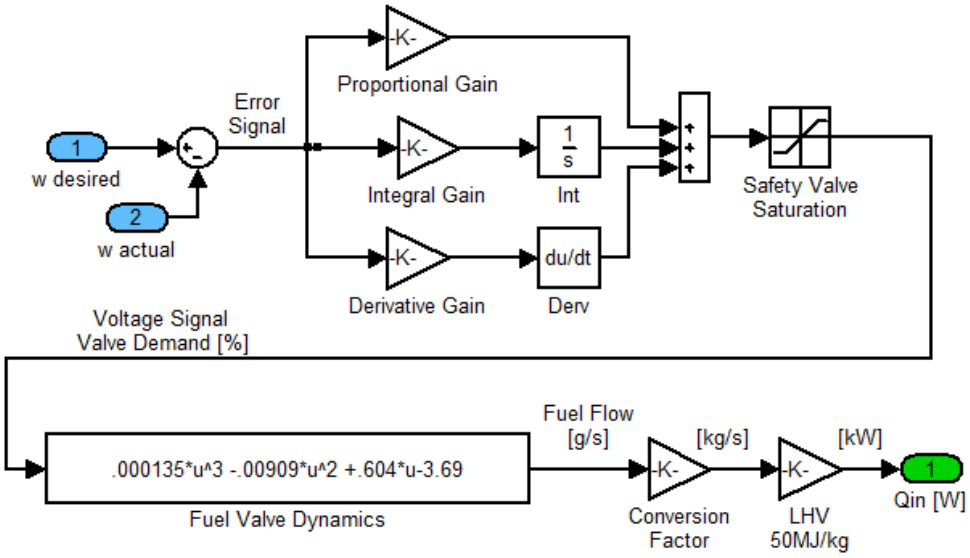

Figure 5.48 PID Controller Subsystem Inner Works

5.12 Analytical Model Results

As described in Chapter 4, the analytical nonlinear model of the HyPer facility was built in the Simulink/MatLab platform as a tool for both system scale up and control testing. This parallel effort to the work conducted in Chapter 3, proved to be quite challenging. The complexity of the model, in its numerous assumed parameters has lead to the need of further revision and work. In the upcoming chapter, the pros and cons of the current version will be discussed, and ideas for its improvement detailed. The immediate sections however, present model validation plots for various experimental tests carried at NETL.

5.12.1 Ramp Rate Startup Tests

One attractive feature the nonlinear model possesses is the ability to be run at close to zero speed, as compared to that of the plant's nominal value of 40,500rpm. Startup profiles for speeds of approximately 2% of nominal are shown in Figures 5.49 and 5.51, for four different test runs. The plots show the startup blower effect on turbine speed up to 9000rpm. After the purge cycle the PI controller takes command of the fuel valve, up

to the start of the test procedure, where the valve can be toggled between open loop, closed loop, or fuel cell model control. The different colors represent turbine speeds for various combinations of proportional and integral gains, black being the model data. It is important to note that the gains used in the GAP software are based on the measured turbine speed, and not the error signal. Thus the real system uses a proportional gain of 0.001, and an integral of 0.00075, whereas the model utilizes a variety of gains based on the error signal. Figure 5.51 for example, shows the speed response to a PI controller having a proportional gain of 40, and an integral of 2.

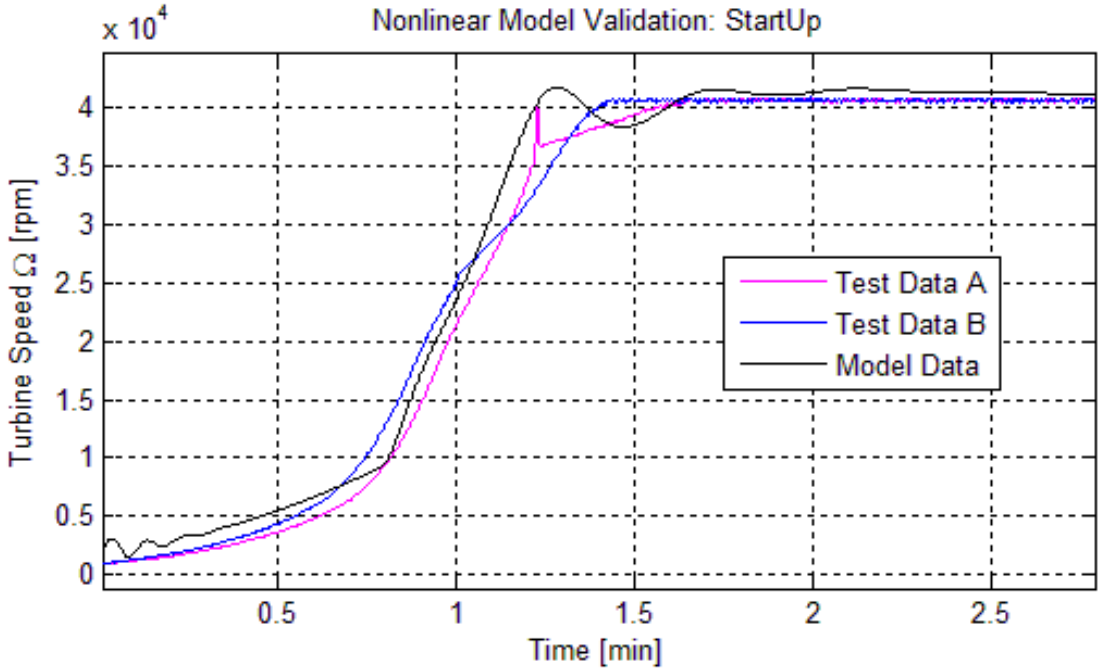

Figure 5.49 Startup Profile: PID Controller in Model

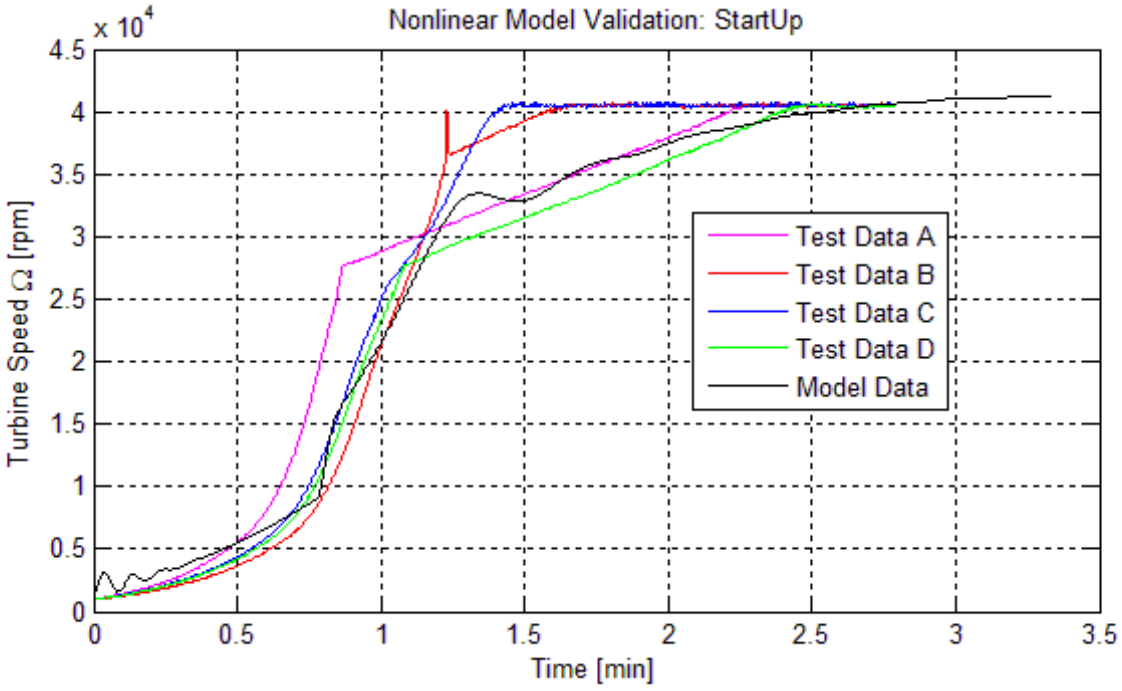

Figure 5.50 Startup Profile PI Controller in Model

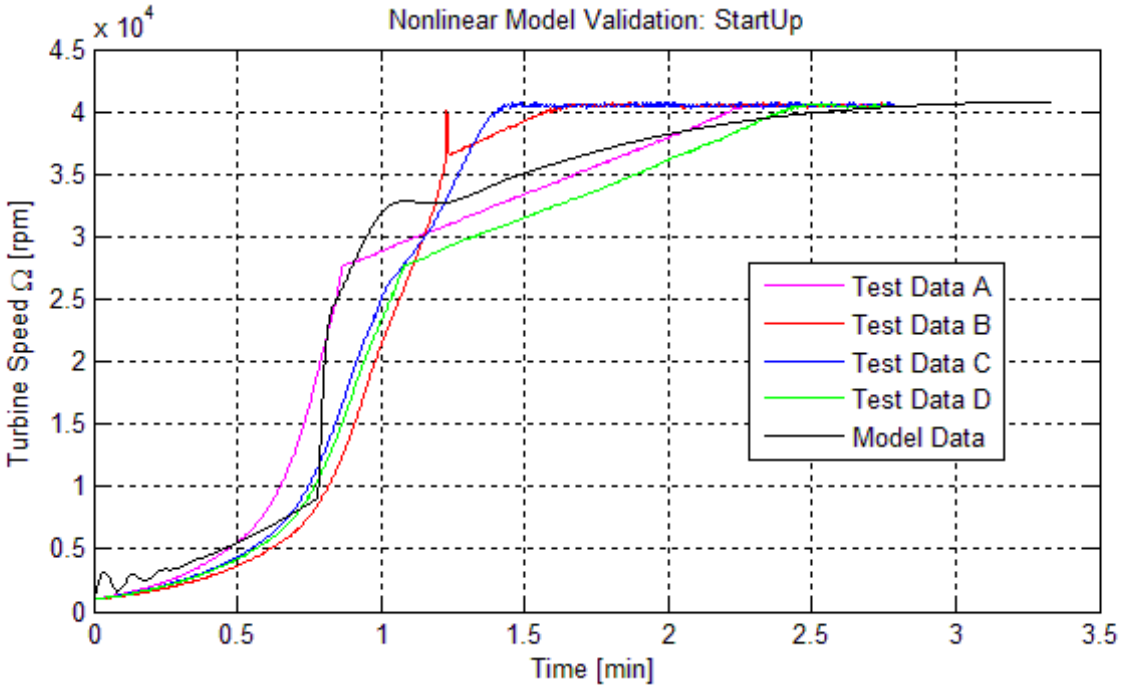

Figure 5.51 Startup Profile PI Controller in Model

5.12.2 Bypass Valve Simulation

Figures 5.52 to 5.56 show the model response to a 25% CA step increase. The various outputs plotted show a moderate agreement with the test data during the transient periods. The gain combinations described in the previous section, and the compressor geometric angles, are the model parameters that mostly influence the startup response of the plant. Here it is seen, that the model overshoots and undershoots at the time the CA is opened, but eventually converges after some time. The magnitude of the peaks is still great compared to those of the actual data,

Besides the obvious discrepancies, the model does show the expected trends of response for the majority of the outputs shown. As an example, Figure 5.56 has the turbine inlet temperature drop when the CA is opened, as well as Figure 5.52, which demonstrates that the plenum airflow decreases with the use of the bypass valve, very similarly to the experimental data.

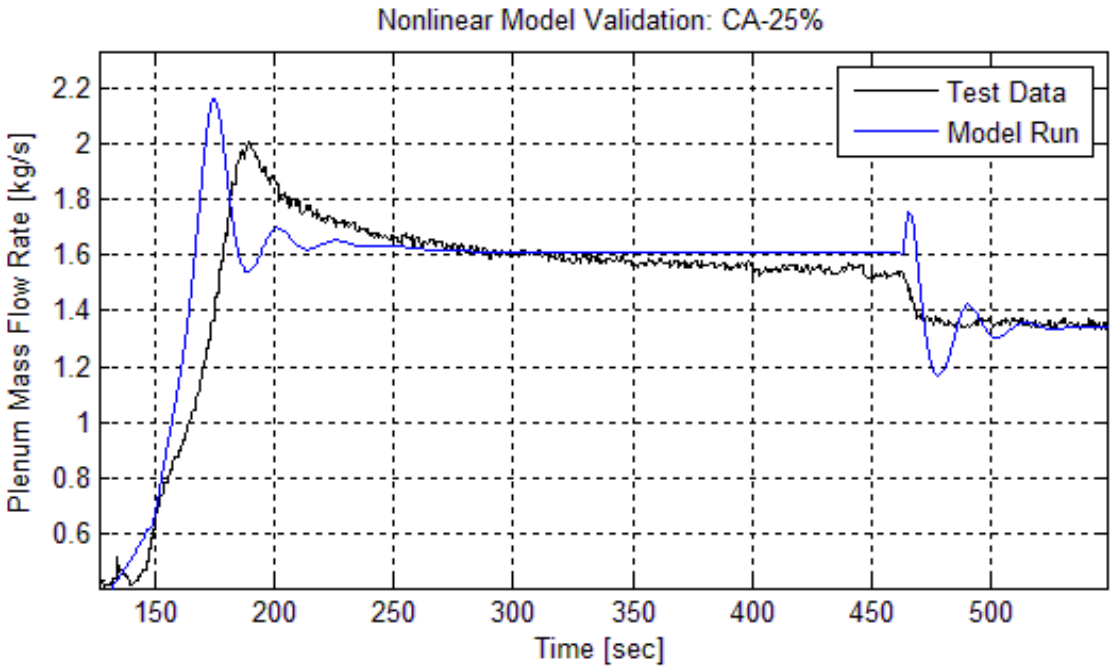

Figure 5.52 Plenum Airflow Response to CA Step Increase: 25%

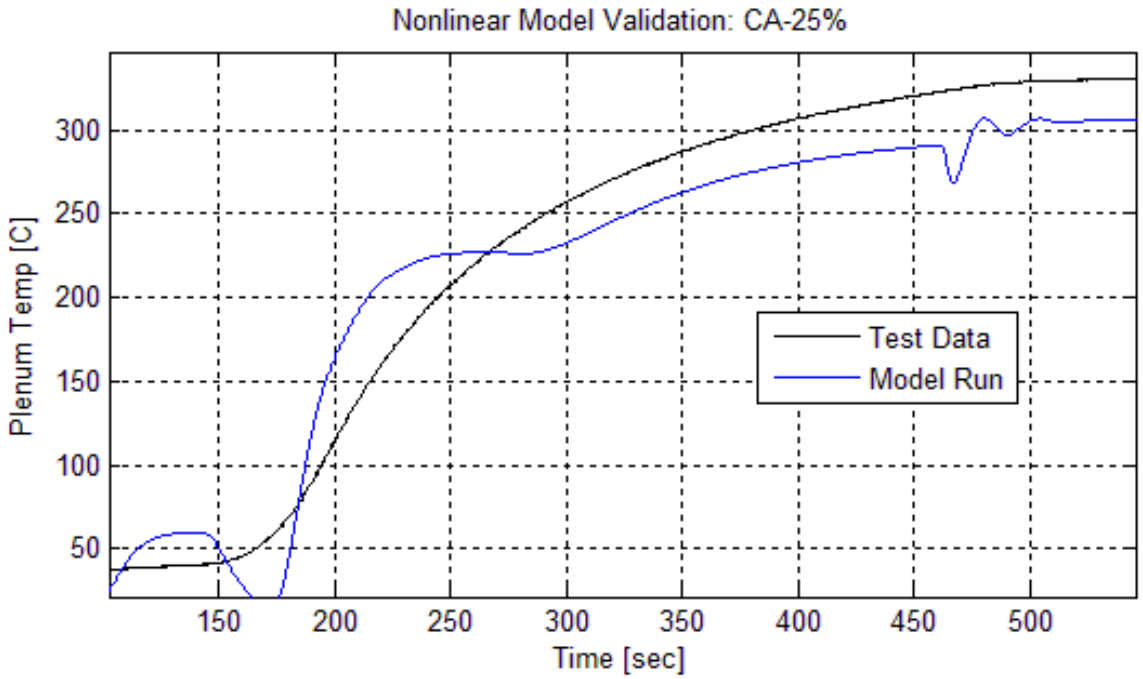

Figure 5.53 Plenum Temperature Response to CA Step Increase: 25%

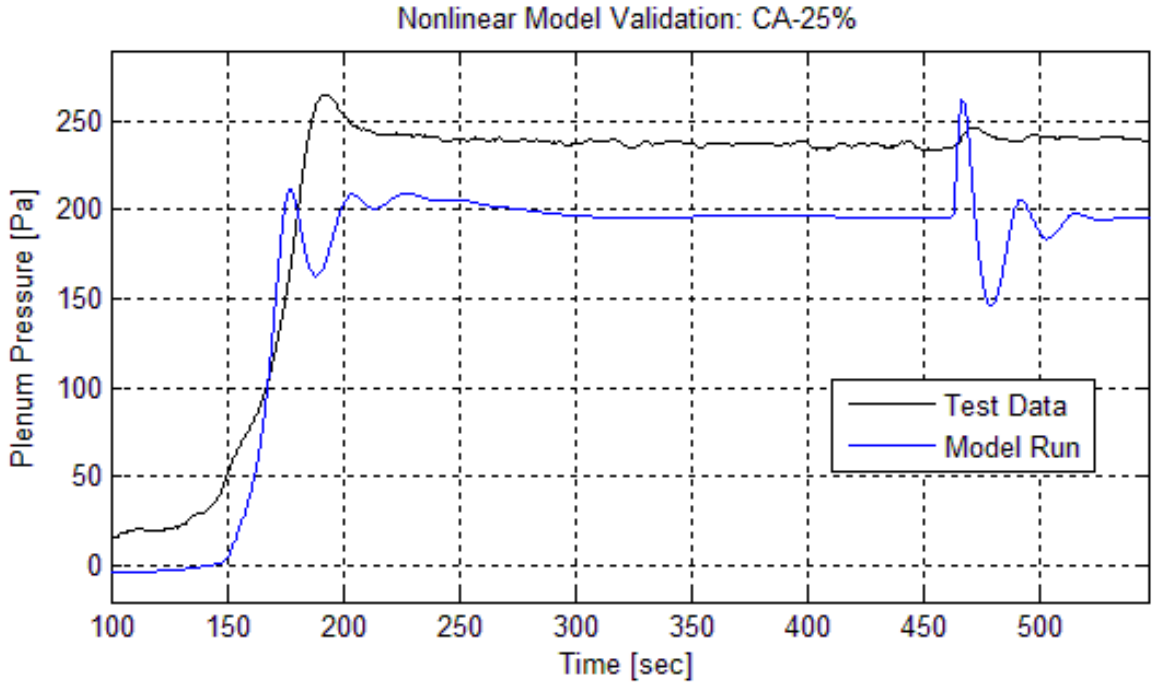

Figure 5.54 Plenum Pressure Response to CA Step Increase: 25%

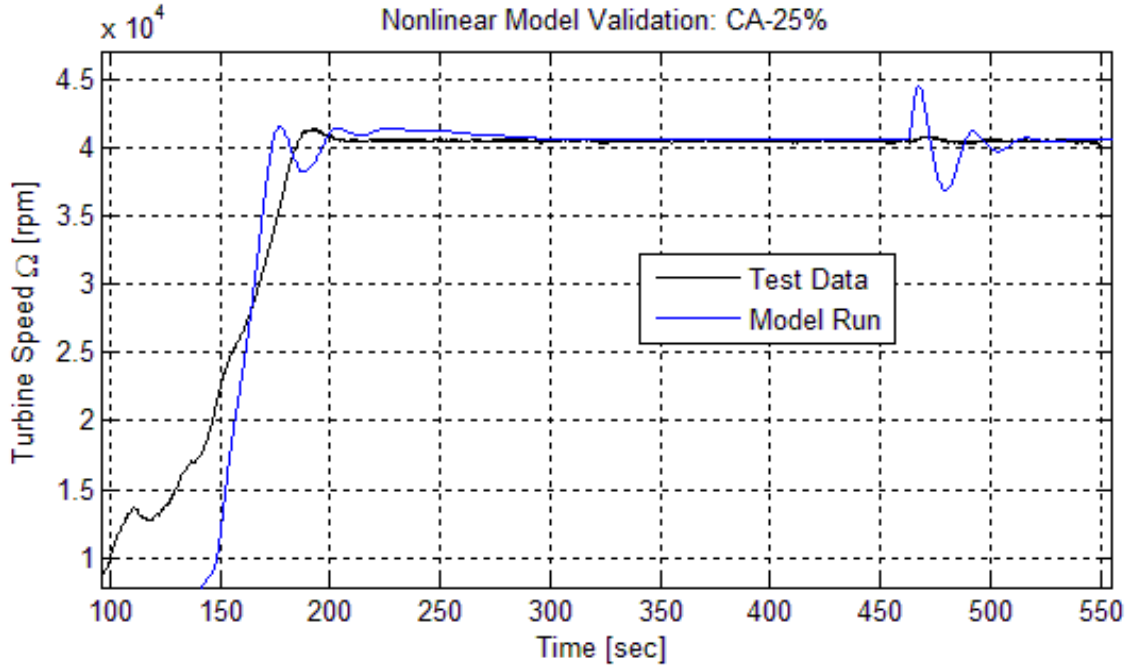

Figure 5.55 Turbine Speed Response to CA Step Increase: 25%

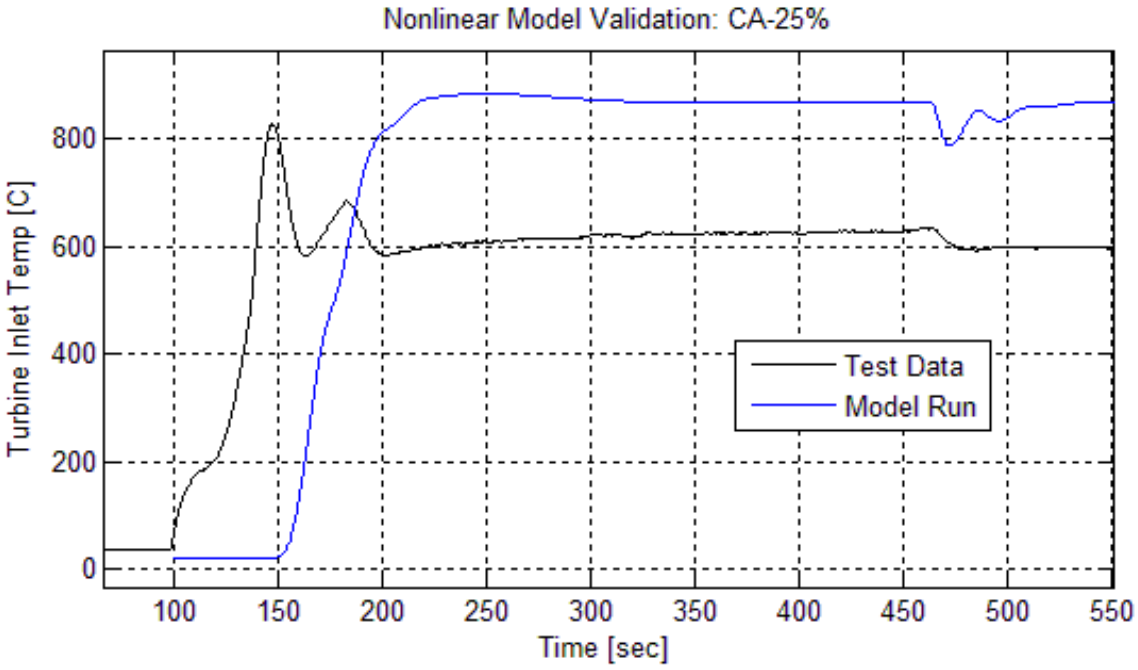

Figure 5.56 TIT Response to CA Step Increase: 25%

5.12.3 Electrical Load Simulation

The nonlinear model also allows for the successive addition of resistive load to the turbine shaft. Figures 5.57 to 5.61 show the combined effect of BA and electrical load disturbance. There are three instances where the transients are applied, namely one at 60s, and two at 250s and 350s. The first excitation is that of the BA valve, with a step increase of 13%, and the two subsequent, load bank step increments of 15kW each. Once again, there are notable differences between model and data, still sharing the expected dynamic trend. The one recurring phenomena in all the plots is the large overshoot in speed, plenum pressure, and mass flow rate. Figures 5.59 and 5.61 show increasing oscillatory peaks when the two 15kW loads combine, whereas Figures 5.58 and 5.61 display a smoother transition of their dynamic response, despite the magnitude difference between them.

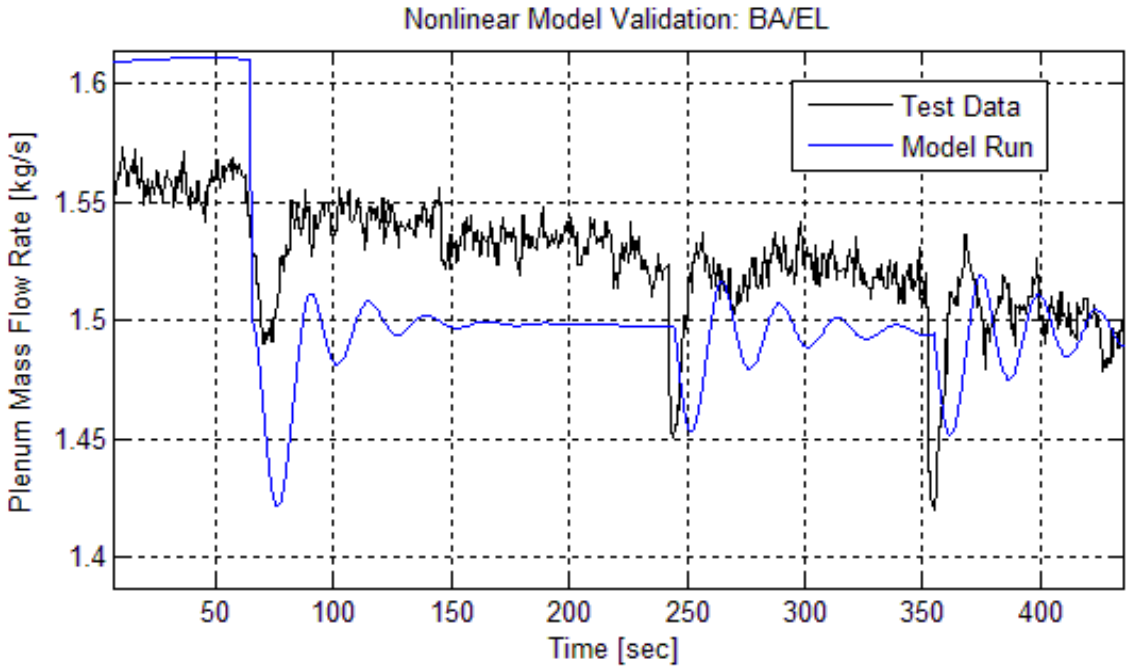

Figure 5.57 Plenum Airflow Response to BA and EL Steps: PID

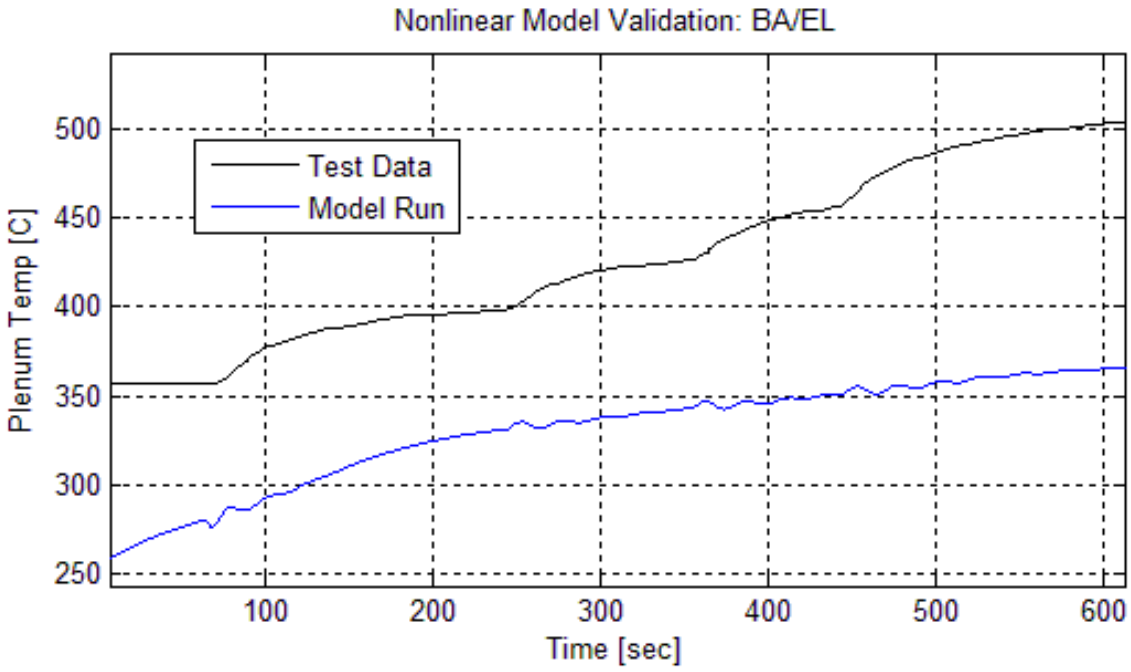

Figure 5.58 Plenum Temp Response to BA and EL Steps: PID

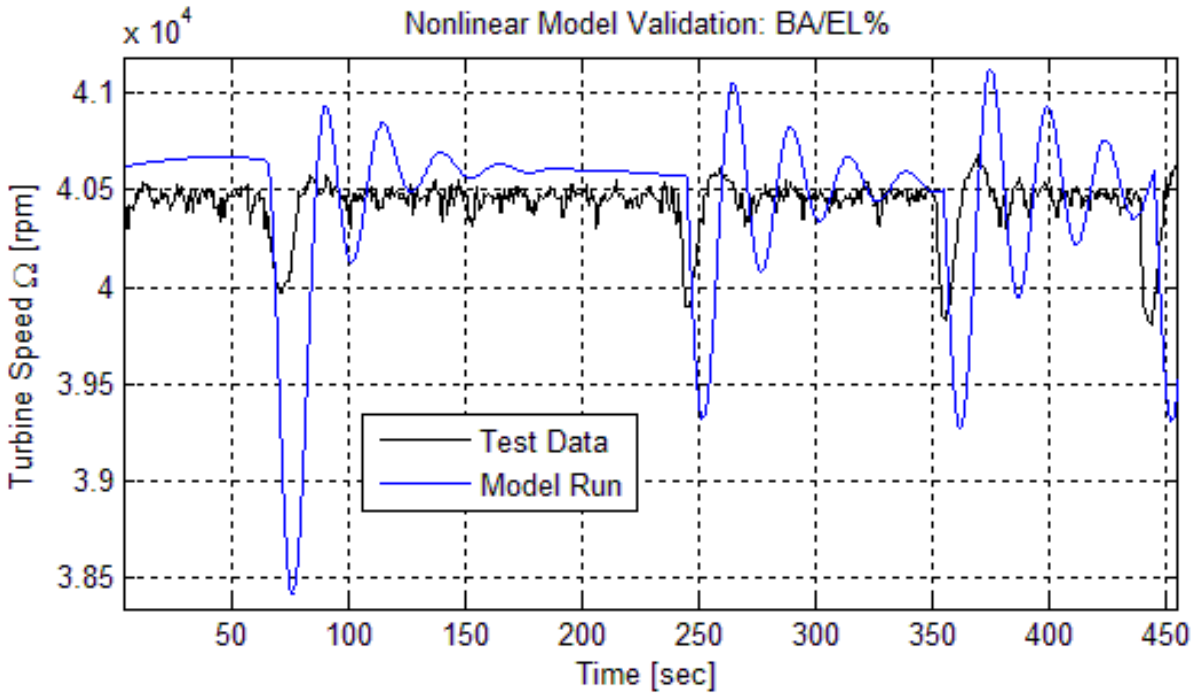

Figure 5.59 Turbine Speed Response to BA and EL Steps: PID

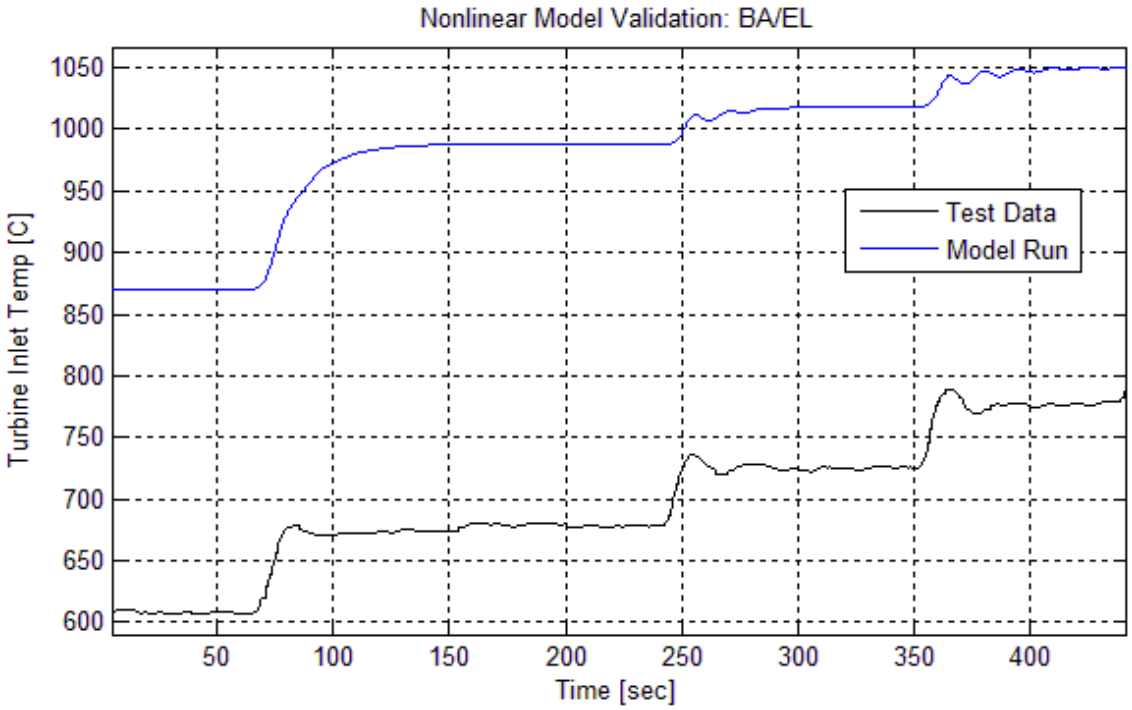

Figure 5.60 TIT Response to BA and EL Steps

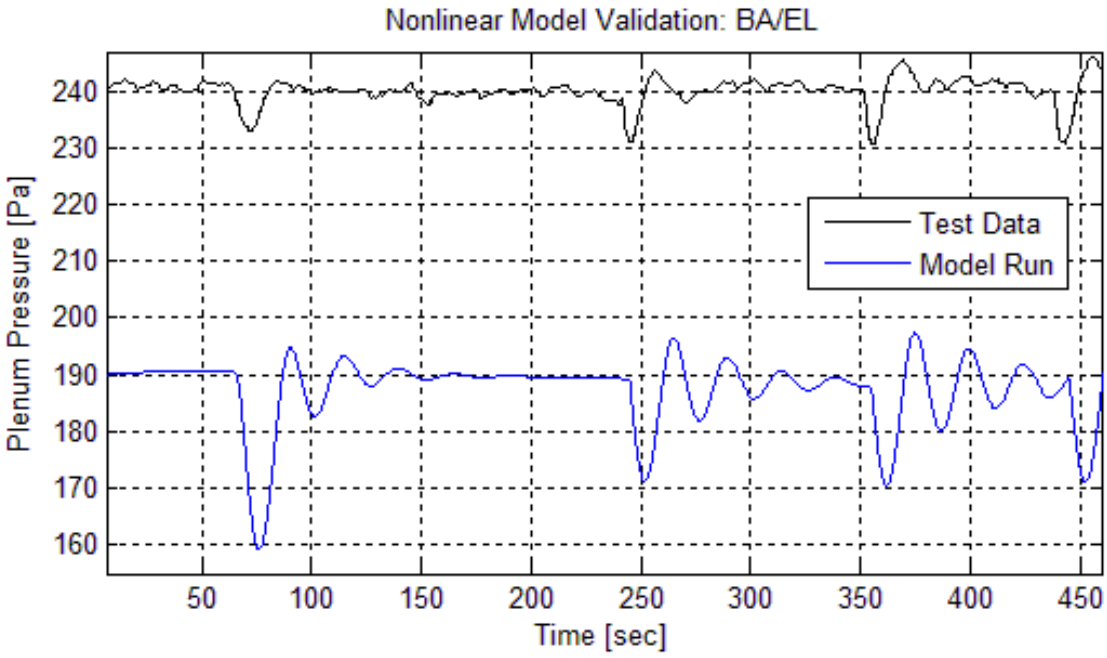

Figure 5.61 Plenum Press Response to BA and EL Steps: PID

6 Conclusions and Discussion

The results presented in the previous chapter are discussed in the sections to follow, for both the empirical system model and the analytical nonlinear model. System response to the chosen control methodology for the given hybrid configuration is favorable for the reduced order plant matrix. More work is still required in the analytical model, if the behavior of this, or another control algorithm, is to be accurately depicted prior to any real time implementation.

6.1 Multivariate Transfer Function Matrix

In order to build the empirical MIMO system, frequency response data was first generated as described in Chapter 3. The tests prove that the open loop response is stable under the window of excitation each signal undergoes, when the phase margins are examined. If it weren't, no sinusoid could have been sustained at steady state, without the occurrence of an unbounded system response. It is clearly seen that Figures 4.6 to 4.14 show a positive phase margin for all the Bode plots, indicating a stable system. The thermal system also exhibits large delays, which are evident in the phase plots. These steep phase roll-off rates are indicative of non-minimum phase behavior, and can be expressed as pure exponentials, as described in Chapter 3.

Actuator and instrumentation bandwidths can also be described with the use of the Bode plots, as is seen in Figures 4.10, 4.12, 4.14, and 4.16, where in the latter the fuel flow transmitter is characterized as a function of fuel valve command signal. Although not given, the Transfer Function correlating the fuel valve transmitter to the command signal gave insight into the proper selection of the input used in the FFT algorithm i.e. the choice between the fuel valve signal over the transmitter signal, based on the instrument's bandwidth restriction.

The Bode plots can also provide steady state error detection as defined by the static position, static velocity, and static acceleration error constants described in linear control

theory (Katsuhiko 2002). By observing the dc gain of each magnitude plot, and the corresponding slope at the low frequencies, the steady state error can be calculated for step inputs when the system type is formulated from the derived Transfer Functions. In the derived equations, the system type is 0, meaning there are no free integrators in the open loop characteristic equation. The resulting steady state error is then defined as: $e_{SS} = \frac{1}{1+K_{dc}}$ for each separate Bode plot.

The individual Transfer Functions were derived manually from the Bode plots with the methodology for LTI systems. Figures 4.16 to Figure 4.20 demonstrate that the derived equations fit the data well. Useful and noisy data ranges are distinguished by color, red crosshairs being unreliable data. The bandwidth of each valve, based on experimental data, serves as the threshold where the data is considered to be reliable or not, as shown in Figures 4.18 and 4.20. Hence the derived Transfer Functions are valid up to the actuator and sensor bandwidths, although the latter was not taken into consideration during the analysis. Unfortunately, because of the nature of the TF approximation, being manual, estimating the error and model accuracy is primarily left to the observable fit between data and model, and not on a least squares calculation, where the model would instead be derived from a minimization of the error signal. Analytical identification of the physical parameters that generate the Transfer Function poles and zeros would eventually refine the existing equations. It is likely that some of the singularities will be found to repeat and one or more of the functions will be adjusted. For example, note that G_{24}, G_{34} and G_{54} all have a pole at s = -0.04, so it is possible that the pole in G_{14} currently assigned to s = -0.033 might not rather be at s = -0.04 instead. One way of interpreting the origins of the poles and zeros is to isolate each physical component's input/output frequency data, deriving thus an internal Transfer Function. In doing so, a pole can then be attributed to the time constant of a particular component such as the air plenum, post combustor, or heat exchanger.

The original plant model was based on all of the physical input actuators, and five particular outputs of interest, mainly air plenum inlet conditions, and the turbo machinery

states of TIT and turbine speed. A study of the RGA matrix, the condition number, and the loop gain singular values, proved that the selected control variables could not robustly control all of the chosen outputs of interest simultaneously for the 5x5 plant. For instance, the RGA of the 5x5 matrix contained large numbers, relating to strong coupling between input and output channels, as well as numerous negative matrix elements, hinting to difficulties in controllability of the system.

The condition number, defined as the ratio of upper and lower singular values was found to be $\kappa = 253.5$, much too high for control, as compared to values suggested in literature of one to two orders in magnitude less (Skogestad 2005). Simplification of the matrix to a 3x3 plant reduced the condition number to $\kappa = 12.5$.

As noted in Chapter 3, the open loop SV are indicative of maximum and minimum induced gains of a MIMO plant. The more singular values a system has, the more complex their contour in the frequency domain is, and the harder it becomes to manipulate all of them at one frequency, when loop-shaping techniques are utilized. As an example, robust loop shaping requires that dynamic compensators shape the scaled singular values prior to conversion to state space and insertion into the Hamiltonian equations. Closeness of the SV is also desired at the crossover frequency, so that all the input channels have approximately the same bandwidth. When there are many, separated SV, each with its own frequency response, it is extremely problematic to derive the pre-compensation gain matrix of Glad/Ljung that accomplishes closeness at the crossover frequency. Hence, even if a weight gain matrix is derived to produce a desired loop gain shape, the Hamiltonian matrices will most often not converge, and the closed loop Transfer Functions will be unstable. A fallback to H_∞ control is that a solution does not always exist for the choice of weights or size of plant.

Asides from the problems that arise from the logistics of the control algorithm, a physical handicap stems from an insufficient number of actuators. Due to the strong system coupling, it is not possible to efficiently control one state variable without affecting drastically another, under the current built configuration. For example, the temperature at

the inlet of the plenum cannot be controlled without affecting turbine speed, or TIT, or plenum flow. This is because the bypass valves, which redirect airflow, must be used to regulate plenum temperature, if the speed is to be kept synchronous and steady. This restriction forbids the practical regulation of temperature, and it is why this output state is removed from the original Transfer Function matrix. One possible fix is the addition of yet another valve that can bypass the heat exchangers, thus relaxing the coupling issue between actuators.

Plenum pressure has also been excluded from the original matrix as an output of interest due to the relative significance it has on the cathode path of the fuel cell, in comparison to the combined anode/cathode sides, and corresponding pressure differential. It has been determined that the pressure differential across the fuel cell electrolyte is much more critical to fuel cell performance and safety, than longitudinal pressure across one membrane alone, i.e. cathode or anode sides separately. Note that the HyPer facility symbolizes the physical cathode volume of a fuel cell, and accompanying balance of plant components.

One final reason that weighted on the decision to exclude the plenum pressure signal is its relation to mass flow. Pressure is inversely related to mass flow rate, and hence controlling mass flow would indirectly control pressure. The inclusion of pressure, as a controlled variable is then unjustified, as it not only affects the degree of complexity and convergence of the model, but it becomes a redundant state for control.

Reducing the matrix order to a square system implied removing the BA and load bank inputs as well. The BA exclusion is justified by its own purpose. This valve is mainly used during a fuel cell thermal transient event, where a BA opening would attenuate a sudden increase in turbine speed in response to this extra heat input, by imposing a load on the shaft. The BA also helps increase the stall/surge margin by decreasing the pressure drop across the system. In both of these cases, the valve is used as an emergency device, triggered by unexpected transient behavior, and it is not considered in

use for normal control purposes of plenum flow, or turbine speed regulation. This valve can then be used in a decentralized PID loop for such unplanned cases.

The last signal to be removed as a control signal was that of the resistive load bank. Instead, the load bank is used in the disturbance model, because in the present hybrid configuration, the turbine speed is meant to run synchronously. Real life scenarios would typically involve unexpected disturbances from the load bank side, which is connected to the power grid.

When the simplified 3x3 Transfer Function is analyzed, it is seen that the RGA, condition number, and open loop SV all improve greatly. The RGA matrix elements of Equation 4.1.30 corroborate the intuition that plenum mass flow rate is best controlled with the HA valve, the TIT with the CA valve, and turbine speed with the fuel valve. This new matrix given in Equation 4.1.2 is validated against open loop data, and is seen to predict well the dynamic behavior of the system, as seen in Figures 4.21-4.23. It is important to note that adjustments to the derived Transfer Functions were made during the comparison of the open loop step response data. For example, the dc gain of the TF pertaining to Figure 4.23 was increased to better depict the speed response. Step response comparisons thus aids in the adjustments of parameters.

One interesting observation of the open loop step tests was that for the HA valve response of Figure 4.22 the step signal was actually stepped down in the TF model, rather than up. This valve is adjacent to the air plenum, but on a different airflow path, that is parallel to the main airflow stream as noted in Figure 3.2 and 3.11. Hence an opening of the valve would decrease plenum airflow and temperature, and vice versa. This seems to indicate that the HA bypass Transfer Function data is inversely related to valve opening. Model data fits very well the experimental data when the role of the valve is reversed.

The control implementation of Figure 4.31 proved to be effective in both rejecting fuel cell heat transients and resistive load disturbances, and in following reference signals, as shown in Figures 4.32 to 4.43. The time scale is in minutes, and the abscissa axes are

scaled according to Equations 4.1.32 and 4.1.33. Thus the actuator and output signals must be multiplied by Equations 4.1.32 and 4.1.33 respectively in order to scale back to the real state values.

This controller is also proven to be robust for a variety of uncertain pole/zero combinations in the Transfer Functions. The MatLab script found in Appendix E allows the user to randomly select zero/pole uncertainty ranges to determine the degree of system robustness before instability ensues. One at a time, or all simultaneous Transfer Function equations can be tested under the uncertain plant model. One such combination, assigned a 10% uncertainty to all the poles and zeros of an individual Transfer Function. The m-file outputs the maximum allowable variation possible for a stable result, which in this case resulted in 41% allowed variation. This means robustness is assured for the MIMO system, even if one Transfer Function has close to 50% uncertain poles/zero parameters. A large number of combinations can be thus examined, resulting in a test tool that can be used to help build analytical models in lessening the bounds of accuracy for system parameters.

In conclusion, this work has theoretically proven the functionalilty of a robust, stable, multivariable controller for a simulated SOFC/GT hybrid plant, based on an empirical mathematical formulation. The controller successfully tracks command signals, rejects generator load and fuel cell heat disturbances, and demonstrates to perform robustly under plant uncertainty. This work demonstrates that the up to date tacit assumption of base loading a hybrid system to achieve controllability by manipulating turbine speed is not necessarily valid. Furthermore, this work proposes a multivariate state space method that manages fuel cell airflow solely with the use of bypass valves. Hence the more realistic scenario of maintaining turbine/generator constant load for grid-connected systems is realizable under the proposed control methodology. This is a desireable control feature if the proposed methodology is to be scaled and implemented in larger sized plants having similar hybrid configurations.

6.2 Nonlinear Analytical Model

The analytical model response plots of Chapter 5 indicate that the model closely matches experimental data for some variables, and deviates in magnitude for others. Even though there is much room for improvement, overall, the model predicts well the dynamic trends of a transient event. As an example, Figure 5.49 shows a very good match of the turbine speed response, considering the model complexity and the fact that it is run at almost zero speed. No other model thus far built for the HyPer facility can predict startup speed profiles at such a low rpm. The closest tested model can only predict speeds beginning at more than half the steady state nominal value of 40,500rpm.

Startup profiles in the model are heavily dependent on the closed loop controller gains, and the compressor geometric blade angles. Figures 5.50 and 5.51 are two very different contours from that of Figure 5.49. They only differ in the type of controller used i.e. PI vs. PID, and the value of their gains. The real facility uses a PI speed controller based on the configuration given in Figure 6.1, where the proportional gain is $k_P = 0.001$, and the integral gain is $k_I = 0.75k_P$. This PI controller has as its input the difference between the measured speed signal, and the signal itself after integration. The integration block has a saturation limit, given as the nominal speed of 40,500rpm. In contrast, the nonlinear model arrangement shown in Figure 5.48 is a function of the error signal between the set point and the measured speed, having gains of $k_P = 0.00022$, and $k_I = 0.6k_P$, and $k_D = 0.007$. This last set of values produces the more realistic response of Figure 5.49.

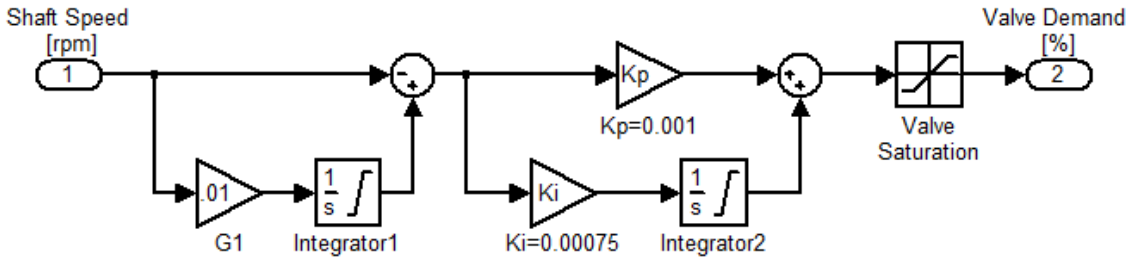

Figure 6.1 Actual HyPer PI Scheme

When the bypass valves are tested, there is a greater error margin, as seen in the responses of Figures 5.52 and 5.56. While the plenum pressure and temperature vary less than 50kPa and 50 degrees each before the transient, the TIT response varies by more than 100 degrees. In the first two cases, the model under predicts the temperature, whereas in the latter it over predicts it. This may be due to the possible fluctuation in the LHV parameter. The LHV is assumed to remain constant in the model, even though it varies from day to day. Lowering this value could possibly decrease the error margin, and maintain the plenum pressure and temperature unaffected. This is because the heat exchangers have yet to reach their effectiveness level i.e. the HX time constant is approximately 10min.

Compared to the test data, the model transient behavior assimilates correctly the change in direction of an output, but not the magnitude trend. The model overshoots and undershoots every time for all outputs, to various degrees. It is possible that the subsystem logic of the CA bypass-piping route is at fault, or that the tabulated valve characterization data is inaccurate. The model applies a series of assumptions via logic blocks, downstream of the bypass valve whenever a valve is opened or closed, as described in Chapter 5. For instance, if the CA valve is closed, the temperature at the very end of that piping route is assumed to be that of the post combustor temperature. When the valve opens, there is temperature drop distributed downstream of the pipe. However, there are far more complex dynamics involved in real life, which are not taken into account in the model. This is a major source of error when the valves are either entirely shut or entirely opened.

The model response to electrical load perturbations was also examined, and shown in Figures 5.57 to 5.61. Once again, the model trend appears to follow that of real life, except for the magnitude gap and overshoot peaks. Figure 5.58 exhibits the greatest margin of error, with an augmenting value. This may be the result of erroneous heat exchanger parameters, since the times shown should have displayed some sort of activity from the recuperators. Most of these parameters are assumed, such as the overall heat

transfer coefficient, the effective surface area, and the mass of the primary surface recuperators.

Other possible sources of error can be found within the turbine/compressor model subsystem. The compressor and turbine efficiency for example, are assumed to be constant at all speeds. This is obviously incorrect, but needed if the model was to be free of compressor/turbine maps. These maps are computationally troublesome at low speeds, and their avoidance makes it possible to model startup profiles that begin at approximately 2% of the turbine nominal speed. Un-modeled generator winding losses, which are a function of speed, also contribute to model error. The last chapter of this work addresses these issues and suggests possible fixes for the improvement of the model.

7 Future Work

The accomplishments garnered in this work can be further expanded to produce an implementable controller that can be tested on the physical facility, once it is validated in the nonlinear analytical model. It is therefore necessary to correct the sources of error in the model before any controller-induced response is studied. An immediate controller validation can be carried out with the use of existing HyPer models, such as the lumped parameter model described in the literature review section.

One such model improvement would include the substitution of the air plenum and post combustor backpressure empirical equations, which are currently a function of turbine speed, with an assumed pressure, that is updated constantly. An iterative process can assign the value of the backpressure by verifying if the downstream pressure of the stack pipe exhaust is atmospheric. A positive match of atmospheric pressures at this point would then indicate that the assumed pressure value is correct, if the all the losses between the plenum and the stack exhaust are adequately modeled.

Minor and less time consuming fixes are those pertaining to the physical parameters of the balance of plant components, such as the ones for pipes, heat exchangers, and vessels. Thermal conductivity constants, pressure loss coefficients, relative roughness factors and the like, are all possible sources of error. These variables were chosen conservatively mostly from literature, and sometimes, as is the case with the heat exchangers, they were simply assumed for lack of information. This work is currently ongoing.

With regard to the empirically derived Transfer Functions, the poles and zeros can be further analyzed to identify what are the plant components attributable to their respective locations, and what is the physical significance of this. If for instance a particular pole is correlated to the heat exchanger time constant, and the heat exchanger is removed, would this change affect all the other poles as well? Due to the strong system coupling, would a change in one pole result in several zero changes? Note that even though zeros are

generally indicative of rates of change of input signals, or initial conditions, they can also stem indirectly from poles, if system has inner loops, similar to the well known positive and negative feedback loop block diagrams.

Scaling is yet another issue worth considering in the study of the system poles and zeros. It would be interesting to determine whether a larger size plant can be accurately described by the same set of Transfer Functions, solely by the inclusion of a scaling factor for each pole and zero combination. The relative dc gain can be easily modified as well, and it is likely to be the case.

The frequency response techniques discussed in this work can also be compared to alternate methods for gathering magnitude and phase data. One way would be to apply colored noise to a fast acting actuator, as in the case of the fuel valve. Theory requires the use of white noise, but this is unobtainable in bandwidth-limited actuators. Nonetheless, close to white noise signals could be attained with the fast acting fuel valve, where the Transfer Functions would then be derived as the ratio between the covariance matrix of input and output signals. Exercising this test procedure could reduce testing times by orders of magnitude i.e. each individual Bode plot required a point by point steady state data window, lasting an approximate 10hr/test for all points in the studied frequency range.

It is important to note that the frequency response Bode Plot generated data is for the nominal operating point of the HyPer facility. This work can be extended to address a broader operating envelope at various operating points. A design of experiments test plan can be developed to further expand the frequency response database.

Concerning the controller, it can also be modified with an anti-windup scheme, in order to avoid large actuator signal overshoots that can otherwise saturate the valves. Other dynamic compensating shaping weights can be implemented for enhanced performance. The detrimental effect of the RHP zero in one output channel for example, can be moved to another output channel, by manipulating the diagonal independent weight bandwidths.

The physical addition of heat exchanger bypass valve to control plenum temperature, can aid the controllability of the system, lessening the weight selection criteria constraints.

Finally, there is a real need to demonstrate the proven theoretical results in the HyPer working testbed. The control algorithm can be modified to include additional states from the fuel cell cathode and anode sides, with the use of a high fidelity fuel cell model incorporated into the control scheme. Fuel cell inlet temperature and cathode/anode pressure gradient are examples of important states that will most likely require added control input signals. Irrespective of the number of added states, multivariable control holds the promise of a practical, implementable, robust design suited for optimal performance of hybrid systems.

There are still vast amounts of tasks that can complement the present work. This paper serves as the starting point to multivariate robust control of mathematically empirically based hybrid plant models.

Bibliography

Belanger, P. *Control Engineering: A Modern Approach*. USA: Saunders College Publishing, 1995.

Blanchini, F., D. Micheli, P. Giannattasio, P. Pinamonti. "Limits and Trade-Off in the Control of Compressor Surge" *ASME Turbo Expo*: Amsterdam, The Netherlands, 3-6 June 2002. ASME, GT2002-30538.

Boyd, S. "H_∞ Optimal Control Theory" *Information Systems Laboratory CDC Workshop*, Electrical Engineering Department, Stanford University, 1987.

Brogan, W. *Modern Control Theory, Third Edition*. New Jersey: Prentice Hall, 1991.

Carlson, E. *Solid Oxide Fuel Cell Manufacturing Cost Model: Simulating Relationships Between Performance, Manufacturing, and Cost of Production*, National Energy Technology Report. 20 Apr 2004.

Cochin, I., W. Cadwallender. *Analysis and Design of Dynamic Systems, Third Edition*. New York: Addison Wesley, 1997.

Dorf, R., R. Bishop. *Modern Control Systems, Eighth Edition*. California: Addison Wesley, 1998.

Doyle, J., B. Francis, A. Tannenbaum. *Feedback Control Theory*. New York: Macmillan, 1992.

Ferrari, M., A. Traverso, L. Magistri, A. Massardo. "Influence of Anodic Recirculation Transient Behavior on the SOFC Hybrid System Performance" *Journal of Power Sources* 149 (2005): 22-32.

Ford, C., et al. "Evaluation of Methods for Thermal Management in a Coal Based SOFC Hybrid through Numerical Simulation" Seventh International Colloquium on Environmentally Preferred Advanced Power Generation: Irvine, CA, 5-8 Sept. 2006.

Fox, R., A. McDonald. *Introduction to Fluid Mechanics, Fourth Edition*. New York: John Wiley & Sons, 1992.

Franklin G., J. Powell, A. Emami-Naeini. *Feedback Control of Dynamic Systems, Fifth Edition*. New Jersey: Prentice Hall, 2006.

Franklin, G., J. Powell, M. Workman. *Digital Control of Dynamic Systems, Third Edition*. California: Addison Wesley, 1998.

Glad, T., L. Ljung. *Control Theory: Multivariable and Nonlinear Methods*. London: Taylor and Francis, 2000.

Goodwin, G., S. Graebe, M. Salgado. *Control System Design*. New Jersey: Prentice Hall, 2001.

Gravdahl, J., O. Egeland. "A moore-Greizer Axial Compressor Model with Spool Dynamics" Proceedings of the 36th Conference on Decision and Control: San Diego, CA, Dec 1997.

Green, M., D. Limebeer. *Linear Robust Control*. New Jersey: Prentice Hall, 1995.

Greitzer, E. "Surge and Rotating Stall in Axial Flow Compressors, Part I: Theoretical Compression System Model" *Journal of Engineering for Power* 98 (1976): 190-198.

Greitzer, E. "Surge and Rotating Stall in Axial Flow Compressors, Part II: Experimental Results and Comparison with Theory" *Journal of Engineering for Power* 98 (1976): 199-211.

Hahn, A. *Modeling and Control of Solid Oxide Fuel Cell Gas Turbine Power Plant Systems*, Masters Thesis: University of Pittsburgh, April 2004.

Hansen, K., P. Jørgensen, P. Larsen. "Experimental and Theoretical Study of Surge in a Small Centrifugal Compressor" *Journal of Fluids Engineering* 103 (1981): 391-395.

Incropera, F., D. DeWitt. *Fundamentals of Heat and Mass Transfer, Third Edition*. New York: John Wiley & Sons, 1990.

Iwasaki, T., S. Hara. "Robust Control Synthesis with General Frequency Domain Specifications: Static Gain Feedback Case" *Proceedings of the 2004 American Control Conference*: Boston, MA, 30 June – 2 July, 2004. 4613-4618

Karvountzi G., et al. "Comparison of Molten Carbonate and Solid Oxide Fuel Cells for Integration in a Hybrid System for Cogeneration or Tri-generation" *Proceedings of the International Mechanical Engineering Congress and Exposition*: Anaheim, CA, 13-20 Nov 2004. ASME, IMECE2004-59927.

Katsuhiko, Ogata. *Modern Control Engineering, Fourth Edition*. USA: Prentice Hall, 2002.

Larminie, James, Andrew Dicks. *Fuel Cell Systems Explained, Second Edition*. England: John Wiley & Sons, 2003.

Levine, W. *The Control Handbook*. USA: CRC Press, 1996.

Lewis, F. *Applied Optimal Control and Estimation: Digital Design and Implementation*. New Jersey: Prentice Hall, 1992.

Lindeburg, Michael. *Engineer-In-Training Reference Manual, Eighth Edition*. California: Professional Publications, 2002.

Lundberg, W., S. Veyo, M. Moeckel. "A High Efficiency Solid Oxide Fuel Cell Hybrid Power System Using the Mercury 50 Advanced Turbine Systems Gas Turbine" *Journal of Engineering for Gas Turbines and Power* 125 (2003): 51-58.

McFarlane, D., K. Glover. "A Loop Shaping Design Procedure Using H_∞ Synthesis" *Transactions on Automatic Control* 37 (1992): 759-769.

Mishra, M., P. Das, S. Sarangi. "Transient Behavior of Crossflow Heat Exchangers with Longitudinal Conduction and Axial Dispersion" *Journal of Heat Transfer* 126 (2004): 425-433.

Morgans, A., A. Dowling. "Model Based Control of Combustion Instabilities" *Proceedings of the ASME Turbo Expo*: Reno-Tahoe, NV, 6-9 June, 2005. ASME, GT2005-68897.

Mueller, F., F. Jabbari, J. Brouwer, J. Tobias, H. Ghezel-Ayagh. "Linear Quadratic Regulator for a Bottoming Solid Oxide Fuel Cell Gas Turbine Hybrid System" *Proceedings of the International Colloquium on Environmentally Preferred Advanced Power Generation*: Newport Beach, CA, 5-8 Sept. 2006. ASME, ICEPAG2006-24018.

National Fuel Cell Research Center, "Hybrid Fuel Cell Systems" 2007. *NFCRC*,<http://www.nfcrc.uci.edu/2/ACTIVITIES/RESEARCH_STUDIES/Hybrid_Fuel_Cell_Systems/Analyses_of_Hybrid_FC_Gas_Turbine_Systems/Index.aspx>, Accessed Oct. 17 2007.

Nise, N. *Control Systems Engineering, Second Edition*. New York: Addison Wesley, 1995.

Pukrushpan, J., A. Stefanopoulou, H. Peng. "Control of Fuel Cell Breathing" *IEEE Control Systems Magazine*, Apr 2004: 30-46.

Rancruel, D., M. Spakovsky. "Investigation of Control Strategy Development Using an Integrated Model of a SOFC Based APU Under Transient Conditions" *ASME International Mechanical Engineering Congress and Exposition*: Anaheim, CA, 13-20 Nov 2004. ASME, IMECE2004-62372.

Rao, A., G. Samuelsen. "A Thermodynamic Analysis of Tubular Solid Oxide Fuel Cell Based Hybrid Systems" *Journal of Engineering for Gas Turbines and Power* 125 (2003): 59-66.

Rivera, J., R. Gemmen. "Development of Dynamic Modeling Tools for Solid Oxide and Molten Carbonate Hybrid Fuel Cell Gas Turbine Systems" Submitted for presentation in the: *ASME International Gas Turbine Institute Meeting*: 8-12 May, 2000

Saad, Michael. *Thermodynamics, Principles and Practice*. New Jersey: Prentice Hall, 1997.

Samuelsen, G., A. Verma, A. Rao. "Sensitivity Analysis of a Vision 21 Coal Based Zero Emission Power Plant" *Journal of Power Sources* 158 (2006): 417-427.

Shelton, M., E. Liese. "A Transient Model of a Hybrid Fuel Cell Gas Turbine Test Facility Using Simulink" *Proceedings of the ASME Turbo Expo*: Reno-Tahoe, NV, 6-9 June 2005. ASME, GT2005-68467.

Skogestad, S., I. Postlethwaite. *Multivariable Feedback Control: Analysis and Design, Second Edition*. England: John Wiley & Sons, 2005.

Smith, T. *Hardware Simulation of Fuel Cell / Gas Turbine Hybrids*, Doctoral Dissertation: Georgia Institute of Technology, May 2007.

Smith, T., E. Liese. "A Dynamic Bulk SOFC Model Used in a Hybrid Turbine Controls Test Facility" *Proceedings of the ASME Turbo Expo*: Barcelona, Spain, 8-11 May 2006. ASME, GT2006-90383.

Stengel, R. *Optimal Control and Estimation*. New York: Dover Publications, 1994.

Stiller, C., B. Thorud, O. Bolland, R. Kandepu, L. Imsland. "Control Strategy for a Solid Oxide Fuel Cell Gas Turbine Hybrid System" *Journal of Power Sources* 158 (2005): 303-315.

Traverso, A., F. Calzolari, A. Massardo. "Transient Analysis of and Control System for Advanced Cycles Based on Micro Gas Turbine Technology" *Journal of Engineering for Gas Turbines and Power* 127 (2005): 340-347.

Traverso, A., M. Ferrari, L. Magistri, A. Massardo. "Control System for Solid Oxide Fuel Cell Hybrid Systems" *Proceedings of the ASME Turbo Expo*: Reno-Tahoe, NV, 6-9 June 2005. ASME, GT2005-68102.

Tsai, A., L. Banta, D. Tucker, L. Lawson. "Determination of an Empirical Transfer Function of a Solid Oxide Fuel Cell Gas Turbine Hybrid System Via Frequency Response Analysis" *Proceedings of ASME Fuel Cell, Engineering, and Technology Conference:* New York, NY, 18-20 June 2007. FuelCell2007-25099.

Tucker, D., E. Liese. "Fuel Cell Gas Turbine Hybrid Simulation Facility Design" *ASME International Mechanical Engineering Congress and Exposition*: New Orleans, LA, 2003.

Tucker, D., J. Kislear, A. Akinbobuyi. "Examination of Ambient Pressure Effects on Hybrid Solid Oxide Fuel Cell Turbine System Operation Using Hardware Simulation" *Proceedings of the ASME Turbo Expo:* Barcelona, Spain, 8-11 May 2006. ASME, GT2006-91291.

Tucker, D., L. Lawson, R. Gemmen. "Characterization of Air Flow Management and Control in a Fuel Cell Turbine Hybrid Power System Using Hardware Simulation" *Proceedings of the ASME Turbo Expo*: Chicago, IL, 5-7 April 2005. ASME, PWR2005-50127.

Tucker, D., T. Smith, L. Lawson. "Characterization of Bypass Control Methods in a Coal-Based Fuel Cell Turbine Hybrid" *Proceedings of the International Colloquium on Environmentally Preferred Advanced Power Generation*: Newport Beach, CA, 5-8 Sept., 2006. ASME, ICEPAG2006-24008.

Tucker, D., T. Smith. "Hardware-Based Simulation of a Fuel Cell Turbine Hybrid Response to Imposed Fuel Cell Load Transients" *Proceedings of IMECE2006 International Mechanical Engineering Congress and Exposition*: Chicago, IL, 5-10 Nov. ASME, IMECE2006-13978

Umez-Eronini, E. *System Dynamics and Control*. New York: Brooks Publishing, 1999.

Vaes, D., J. Swevers, P. Sas. "Optimal Decoupling for MIMO Controller Design with Robust Performance" *Proceedings of the 2004 American Control Conference*: Boston, MA, 30 June – 2 July, 2004. Vol.5 4601-4606

Veyo, S., W. Lundberg, S. Vora, K. Litzinger. "Tubular SOFC Hybrid Power System Status" *ASME Turbo Expo*: Atlanta, GA, 16-19 June 2003. ASME, GT2003-38943

Wächter, C., R. Lunderstädt, F. Joos. *Dynamic Model of a Pressurized SOFC/Gas Turbine Hybrid Power Plant for the Development of Control Concepts*, Power Engineering Laboratory of Turbo-Machinery, University of Armed Forces, Hamburg, Germany. 2 June, 2006

Weibel, H., M. Beukenberg, M. Brodmann, D. Müller. "Design of State Space Controllers for Industrial Twin Shaft Gas Turbines" *Proceedings of the ASME Turbo Expo*: Reno-Tahoe, NV, 6-9 June 2005. ASME, GT2005-68167.

Woodward Industrial Controls. *Designed Training Course Manual,* Mar 2002.

Wylie, R., L. Barret. *Advanced Engineering Mathematics, Sixth Edition*. USA: McGraw-Hill, 1995.

Appendix A

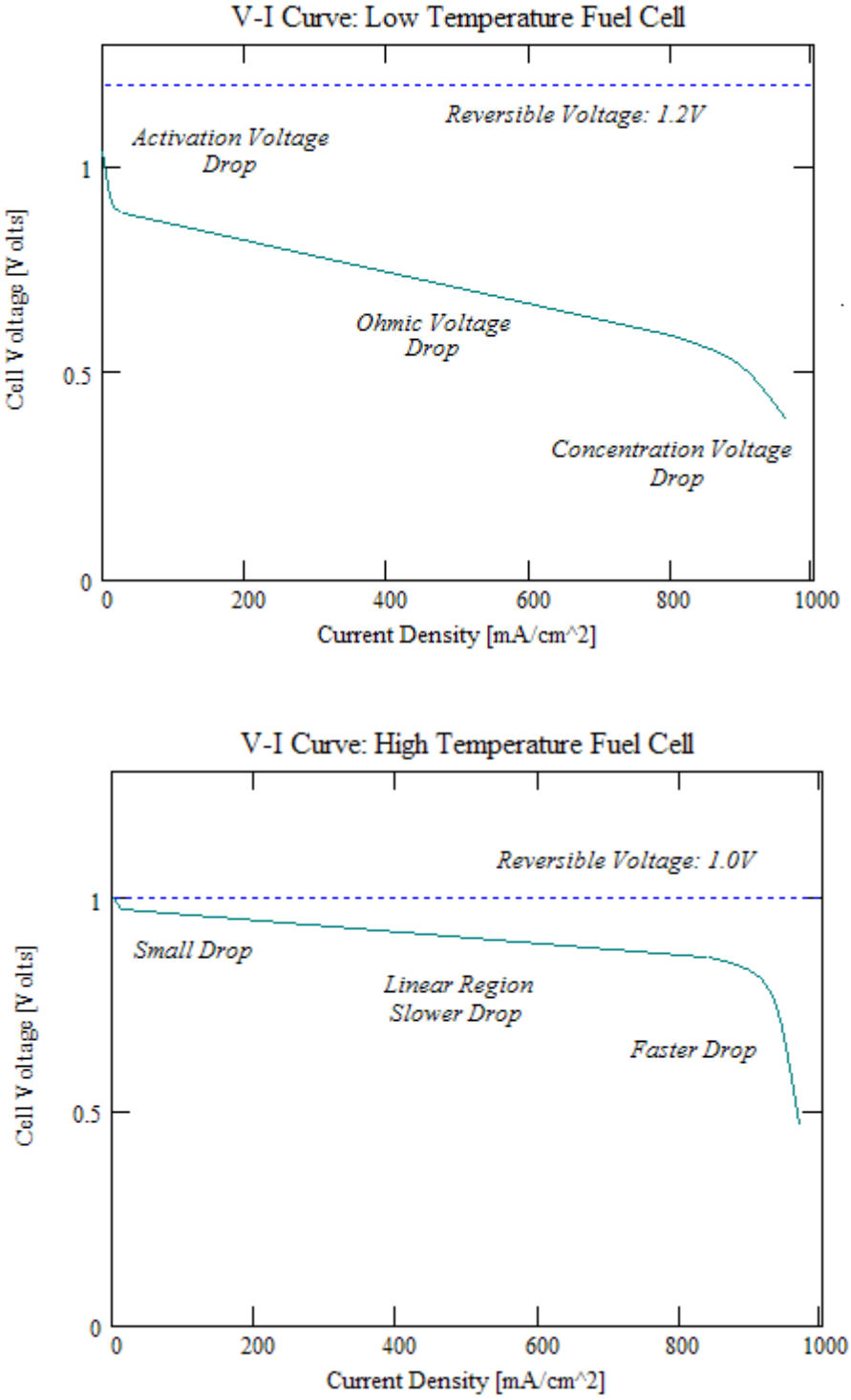

Typical Fuel Cell Voltage Losses for High and Low Temperature Fuel Cells

Appendix B

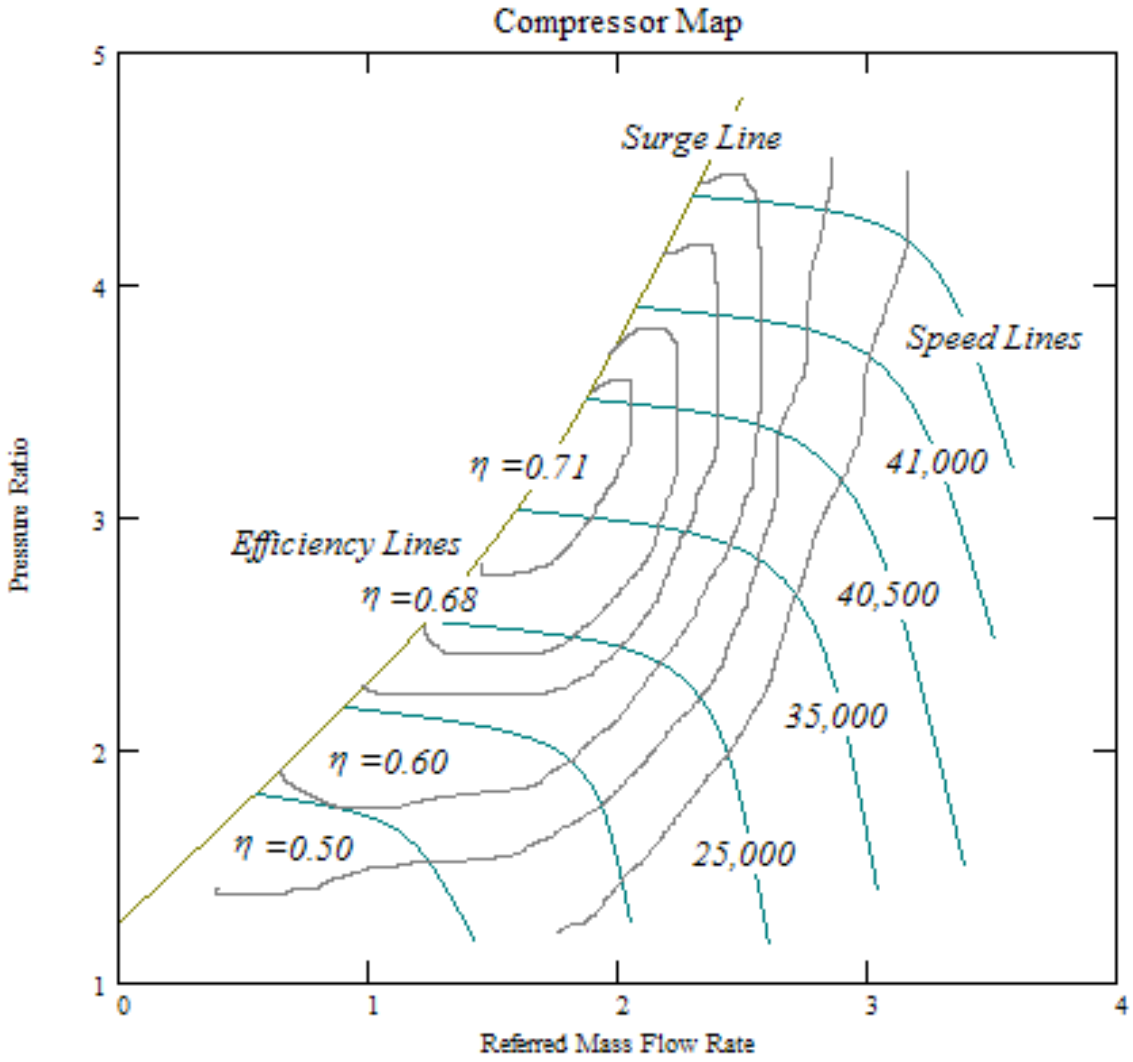

Sample Generic Compressor Map

Note: The Referred Mass Flow Rate has Units of $\left[\frac{kg}{s}\cdot\frac{K^{\frac{1}{2}}}{Pa}\right]$

Compressor Pressure Ratio

	% N referred								
$\dot{m}_{ref}$	20	30	40	50	60	70	80	90	100
0	1.12	1.2	1.35	1.6	1.8	2.22	2.7	3.3	4.12
0.2	1.12	1.2	1.35	1.6	1.8	2.22	2.7	3.3	4.12
0.4	1.11	1.2	1.35	1.6	1.8	2.22	2.7	3.3	4.12
0.6	1.1	1.2	1.35	1.6	1.8	2.22	2.7	3.3	4.12
0.8	1.09	1.18	1.34	1.6	1.8	2.22	2.7	3.3	4.12
1	1.05	1.16	1.3	1.6	1.8	2.22	2.7	3.3	4.12
1.2	1	1.15	1.29	1.6	1.8	2.22	2.7	3.3	4.12
1.4	1	1.12	1.27	1.55	1.8	2.22	2.7	3.3	4.12
1.6	1	1.08	1.24	1.5	1.8	2.22	2.7	3.3	4.12
1.8	1	1.06	1.2	1.48	1.78	2.22	2.7	3.3	4.12
2	1	1	1.18	1.45	1.75	2.22	2.7	3.3	4.12
2.2	1	1	1.15	1.4	1.73	2.22	2.7	3.3	4.12
2.4	1	1	1.1	1.35	1.72	2.2	2.7	3.3	4.12
2.6	1	1	1	1.25	1.7	2.19	2.7	3.3	4.12
2.8	1	1	1	1	1.65	2.17	2.7	3.3	4.12
3	1	1	1	1	1.55	2.15	2.69	3.3	4.12
3.2	1	1	1	1	1.32	2.1	2.68	3.3	4.12
3.4	1	1	1	1	1	2	2.65	3.3	4.12
3.6	1	1	1	1	1	1.7	2.6	3.29	4.12
3.8	1	1	1	1	1	1.5	2.55	3.27	4.12
4	1	1	1	1	1	1.3	2.5	3.26	4.12
4.2	1	1	1	1	1	1	2.25	3.25	4.12
4.4	1	1	1	1	1	1	1.9	3.15	4.1
4.6	1	1	1	1	1	1	1.35	3.05	4.05
4.8	1	1	1	1	1	1	1	2.9	4.03
5	1	1	1	1	1	1	1	2.75	4.01
5.2	1	1	1	1	1	1	1	2.3	3.9
5.4	1	1	1	1	1	1	1	1.6	3.8
5.6	1	1	1	1	1	1	1	1	3.5
5.8	1	1	1	1	1	1	1	1	3
6	1	1	1	1	1	1	1	1	1

Generated Compressor Map: Pressure Ratio Table

Appendix C

Alex Tsai 3/28/06
Hyper Piping Data

Conversion: 0.0254

dap=air plenum
dpc=post combustor

Assumed

Nomenclature:
co=compressor outlet
ho=heat exchanger outlet
po=plenum outlet
cb=compressor bypass outlet
to=turbine outlet
ti=turbine inlet

	Pipe No.	din [in]	din [m]	thick [in]	thick [m]	dout [in]	dout [m]	ins thick [in]	ins thick [m]	dins [in]	dins [m]	L [in]	L [m]	Material	specific roughn	specify as: eXXX relative roughness
1	dco1	4.37	0.110998	0.065	0.001651	4.5	0.1143	1	0.0254	6.5	0.1651	5	0.127	304L SS	0.000015	0.000135138
2	dco2	6.375	0.161925	0.125	0.003175	6.625	0.168275	1	0.0254	8.625	0.219075	31	0.7874	304L SS	0.000015	9.26355E-05
3	dco3	6.375	0.161925	0.125	0.003175	6.625	0.168275	1	0.0254	8.625	0.219075	10	0.254		0.000015	9.26355E-05
4	dco4	4.37	0.110998	0.065	0.001651	4.5	0.1143	1	0.0254	6.5	0.1651	31	0.7874		0.000015	0.000135138
5	dco5	4.37	0.110998	0.065	0.001651	4.5	0.1143	1	0.0254	6.5	0.1651	31	0.7874		0.000015	0.000135138
6	dco6	4.37	0.110998	0.065	0.001651	4.5	0.1143	1	0.0254	6.5	0.1651	26	0.6604		0.000015	0.000135138
7	dco7	4.37	0.110998	0.065	0.001651	4.5	0.1143	1	0.0254	6.5	0.1651	26	0.6604		0.000015	0.000135138
8	dho1	6.065	0.154051	0.28	0.007112	6.625	0.168275	2	0.0508	10.625	0.269875	24	0.6096	SCH40	0.000015	9.73704E-05
9	dho2	6.065	0.154051	0.28	0.007112	6.625	0.168275	2	0.0508	10.625	0.269875	27	0.6858	SCH40	0.000015	9.73704E-05
10	dho3	6.065	0.154051	0.28	0.007112	6.625	0.168275	2	0.0508	10.625	0.269875	20	0.508	SCH40	0.000015	9.73704E-05
11	dho4	6.065	0.154051	0.28	0.007112	6.625	0.168275	2	0.0508	10.625	0.269875	10	0.254	SCH40	0.000015	9.73704E-05
12	dpo1	6.065	0.154051	0.28	0.007112	6.625	0.168275	2	0.0508	10.625	0.269875	57	1.4478	SCH40	0.000015	9.73704E-05
13	dpo2	6.065	0.154051	0.28	0.007112	6.625	0.168275	2	0.0508	10.625	0.269875	38	0.9652	SCH40	0.000015	9.73704E-05
14	dpo3	7.625	0.193675	0.5	0.0127	8.625	0.219075	2	0.0508	12.625	0.320675	36	0.9144	Incaloy	0.000015	7.74493E-05
15	dti1	7.625	0.193675	0.5	0.0127	8.625	0.219075	2	0.0508	12.625	0.320675	9	0.2286	SCH80	0.000015	7.74493E-05
16	dti2	7.625	0.193675	0.5	0.0127	8.625	0.219075	2	0.0508	12.625	0.320675	16	0.4064	SCH80	0.000015	7.74493E-05
17	dcb1	4.026	0.10226	0.237	0.00602	4.5	0.1143	2	0.0508	8.5	0.2159	18	0.4572	SCH40	0.000015	0.000146684
18	dcb2	6.065	0.154051	0.28	0.007112	6.625	0.168275	2	0.0508	10.625	0.269875	44	1.1176	SCH40	0.000015	9.73704E-05
19	dcb3	6.065	0.154051	0.28	0.007112	6.625	0.168275	2	0.0508	10.625	0.269875	13	0.3302	SCH40	0.000015	9.73704E-05
20	dcb4	6.065	0.154051	0.28	0.007112	6.625	0.168275	2	0.0508	10.625	0.269875	44	1.1176	SCH40	0.000015	9.73704E-05
21	dcb5	6.065	0.154051	0.28	0.007112	6.625	0.168275	2	0.0508	10.625	0.269875	20	0.508	SCH40	0.000015	9.73704E-05
22	dcb6	6.065	0.154051	0.28	0.007112	6.625	0.168275	2	0.0508	10.625	0.269875	62	1.5748	SCH40	0.000015	9.73704E-05
23	dcb7	7.981	0.202717	0.322	0.008179	8.625	0.219075	2	0.0508	12.625	0.320675	12	0.3048	SCH40	0.000015	7.39946E-05
24	dcb8	7.981	0.202717	0.322	0.008179	8.625	0.219075	2	0.0508	12.625	0.320675	180	4.572	SCH40	0.000015	7.39946E-05
25	dcb9	6.065	0.154051	0.28	0.007112	6.625	0.168275	2	0.0508	10.625	0.269875	12	0.3048	SCH40	0.000015	9.73704E-05
26	dcb10	6.065	0.154051	0.28	0.007112	6.625	0.168275	2	0.0508	10.625	0.269875	12	0.3048	SCH40	0.000015	9.73704E-05
27	dcb11	7.625	0.193675	0.5	0.0127	8.625	0.219075	2	0.0508	12.625	0.320675	37	0.9398	SCH80	0.000015	7.74493E-05
28	dcb12	7.625	0.193675	0.5	0.0127	8.625	0.219075	2	0.0508	12.625	0.320675	64	1.6256	SCH80	0.000015	7.74493E-05
29	dto1	7.834	0.198984	0.083	0.002108	8	0.2032	2	0.0508	12	0.3048	37	0.9398	318L SS	0.000015	7.53831E-05
30	dto2	7.834	0.198984	0.083	0.002108	8	0.2032	2	0.0508	12	0.3048	20	0.508	304SS	0.000015	7.53831E-05
31	dto3	7.834	0.198984	0.083	0.002108	8	0.2032	2	0.0508	12	0.3048	14	0.3556	304SS	0.000015	7.53831E-05
32	dto4	7.834	0.198984	0.083	0.002108	8	0.2032	2	0.0508	12	0.3048	17	0.4318	304SS	0.000015	7.53831E-05
33	dto5	7.834	0.198984	0.083	0.002108	8	0.2032	2	0.0508	12	0.3048	17	0.4318	304SS	0.000015	7.53831E-05
34	dto6	7.834	0.198984	0.083	0.002108	8	0.2032	2	0.0508	12	0.3048	23	0.5842	304SS	0.000015	7.53831E-05
35	dto7	7.834	0.198984	0.083	0.002108	8	0.2032	2	0.0508	12	0.3048	23	0.5842	304SS	0.000015	7.53831E-05
36	dto8	7.981	0.202717	0.322	0.008179	8.625	0.219075	1	0.0254	10.625	0.269875	15	0.381		0.000015	7.39946E-05
37	dto9	7.981	0.202717	0.322	0.008179	8.625	0.219075	1	0.0254	10.625	0.269875	15	0.381		0.000015	7.39946E-05
38	dto10	7.981	0.202717	0.322	0.008179	8.625	0.219075	1	0.0254	10.625	0.269875	16	0.4064		0.000015	7.39946E-05
39	dto11	7.981	0.202717	0.322	0.008179	8.625	0.219075	1	0.0254	10.625	0.269875	16	0.4064		0.000015	7.39946E-05
40	dto12	7.981	0.202717	0.322	0.008179	8.625	0.219075	1	0.0254	10.625	0.269875	9	0.2286	SCH40	0.000015	7.39946E-05
	dap	48	1.2192	1	0.0254	50	1.27	2	0.0508	54	1.3716	96	2.4384			
	dpc	18	0.4572	1	0.0254	20	0.508	2	0.0508	24	0.6096	54	1.3716	Incaloy		

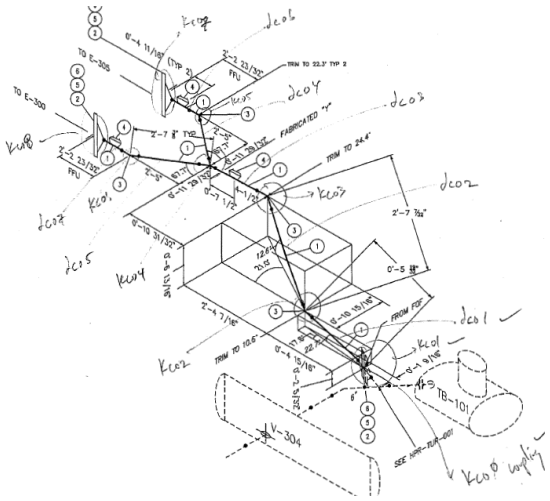

Sample Sketch of Pipe Routing Data: Compressor Exit Route

		Alex Tsai 3/28/06										
			co=compressor outlet					conversion:	0.0254			
		Ref: EIT, Fox McDonald	ho=heat exchanger outlet									
			po=plenum outlet									
	Assumed		cb=compressor bypass outlet									
			to=turbine outlet									
			ti=turbine inlet									
	Fittings Pressure Losses: Kloss or Lequiv											
							d1<d2			d1<d2		
	Fitting No.	Description	Kloss	Lequiv [in]	Lequiv [m]	Le/D <angl bend	Expan d1	Expan d2	Kexp	Cont d1	Cont d2	Kcont
1	Kco0	flange coupling		7.8	0.19812				#DIV/0!			#DIV/0!
2	Kco1	annular compressor exit can			0	400			#DIV/0!			#DIV/0!
3	Kco2	tee flow thru stem		252	6.4008				#DIV/0!			#DIV/0!
4	Kco3	obtuse bend, 10			0	2			#DIV/0!			#DIV/0!
5	Kco4	flow split 45 in between			0	12			#DIV/0!			#DIV/0!
6	Kco5	obtuse bend, 23			0	5			#DIV/0!			#DIV/0!
7	Kco6	obtuse bend, 23			0	5			#DIV/0!			#DIV/0!
8	Kco7	flange coupling		7.8	0.19812				#DIV/0!			#DIV/0!
9	Kco8	flange coupling		7.8	0.19812				#DIV/0!			#DIV/0!
10	Kcb1	54 elbow			0	20			#DIV/0!			#DIV/0!
11	Kcb2	6"x4" reducer			0		4	6	0.308642			#DIV/0!
12	Kcb3	flange coupling		7.8	0.19812				#DIV/0!			#DIV/0!
13	Kcb4	90 elbow			0	30			#DIV/0!			#DIV/0!
14	Kcb5	tee flow thru branch			0	20			#DIV/0!			#DIV/0!
15	Kcb6	bleed air valve: ball valve fully opened			0	3			#DIV/0!			#DIV/0!
16	Kcb7	reducing tee flow 8"x6"			0	20			#DIV/0!			#DIV/0!
17	Kcb8	cold air valve: ball valve			0	3			#DIV/0!			#DIV/0!
18	Kcb9	tee flow thru branch			0	60			#DIV/0!			#DIV/0!
19	Kcb10	90 elbow			0	30			#DIV/0!			#DIV/0!
20	Kcb11	flange coupling		7.8	0.19812				#DIV/0!			#DIV/0!
21	Kcb12	post comb entrance			0		8	60	0.96476			#DIV/0!
22	Kho1	reducer 6"x4"			0		4	6	0.308642			#DIV/0!
23	Kho2	reducer 6"x4"			0		4	6	0.308642			#DIV/0!
24	Kho3	90 elbow			0	30			#DIV/0!			#DIV/0!
25	Kho4	90 elbow			0	30			#DIV/0!			#DIV/0!
26	Kho5	tee smooth			0	50			#DIV/0!			#DIV/0!
27	Kho6	flange coupling		7.8	0.19812				#DIV/0!			#DIV/0!
28	Kho7	plenum entrance			0		6	48	0.968994			#DIV/0!
29	Kho8	hot air valve: ball valve			0	3			#DIV/0!			#DIV/0!
30	Kho9	flange coupling		7.8	0.19812				#DIV/0!			#DIV/0!
31	Kho10	expansion joint, special			0		5	6	0.093364			#DIV/0!
32	Kho11	post comb entrance			0		6	18	0.790123			#DIV/0!
33	Kpo1	flange coupling		7.8	0.19812				#DIV/0!			#DIV/0!
34	Kpo2	90 elbow			0	30			#DIV/0!			#DIV/0!
35	Kpo3	flange coupling		7.8	0.19812				#DIV/0!			#DIV/0!
36	Kpo4	reducer 8"x6"			0		6	8	0.191406			#DIV/0!
37	Kpo5	flange coupling		7.8	0.19812				#DIV/0!			#DIV/0!
38	Kpo6	flange coupling		7.8	0.19812				#DIV/0!			#DIV/0!
39	Kpo7	post comb entrance			0		8	60	0.96476			#DIV/0!
40	Kti1	flange coupling		7.8	0.19812				#DIV/0!			#DIV/0!
41	Kti2	35 elbow			0	10			#DIV/0!			#DIV/0!
42	Kti3	flange coupling		7.8	0.19812				#DIV/0!			#DIV/0!
43	Kti4	turbine clamp			0	10			#DIV/0!			#DIV/0!
44	Kto1	expansion joint, 8"			0		6	8	0.191406			#DIV/0!
45	Kto2	23 elbow			0	5			#DIV/0!			#DIV/0!
46	Kto3	27 elbow			0	8			#DIV/0!			#DIV/0!
47	Kto4	flow split 90 in between			0	24			#DIV/0!			#DIV/0!
48	Kto5	45 elbow			0	16			#DIV/0!			#DIV/0!
49	Kto6	45 elbow			0	16			#DIV/0!			#DIV/0!
50	Kto7	reducer 9.5"x8"			0		8	9.5	0.084599			#DIV/0!
51	Kto8	reducer 9.5"x8"			0		8	9.5	0.084599			#DIV/0!
52	Kto9	flange coupling		7.8	0.19812				#DIV/0!			#DIV/0!
53	Kto10	flange coupling		7.8	0.19812				#DIV/0!			#DIV/0!
54	Kto11	45 elbow			0	16			#DIV/0!			#DIV/0!
55	Kto12	45 elbow			0	16			#DIV/0!			#DIV/0!
56	Kto13	tee flow in			0	40			#DIV/0!			#DIV/0!
57	Kto14	flange coupling		7.8	0.19812				#DIV/0!			#DIV/0!
58	Kto15	tee flow thru branch			0	60			#DIV/0!			#DIV/0!

Piping Pressure Loss Coefficient for Minor Losses

Appendix D

Alex Tsai: 4/27/06

Compressor Torque Equation: Euler Turbomachine Equation

$rev := 2\cdot\pi\cdot rad \qquad \omega := 40500\cdot\frac{rev}{min} \qquad \omega = 4.241\times 10^{3}\,Hz \qquad \rho := 1.2\cdot\frac{kg}{m^3}$

Compressor Inlet Conditions:

$\alpha 1 := 0\cdot deg \qquad \beta 1 := 48\cdot deg \qquad d1 := 4.354\cdot in \qquad d0 := 1.572\cdot in$

$dave := d1 - d0 \qquad dave = 0.071\,m \qquad r1 := \frac{dave}{2} \qquad r1 = 0.035\,m$

$A1 := \frac{\pi}{4}\cdot\left(d1^2 - d0^2\right) \qquad A1 = 8.354\times 10^{-3}\,m^2$

$vn1 := \frac{r1\cdot\omega}{\tan(\alpha 1) + \cot(\beta 1)} \qquad v1 := \frac{vn1}{\cos(\alpha 1)} \qquad vt1 := v1\cdot\sin(\alpha 1)$

$vn1 = 166.421\,\frac{m}{s} \qquad v1 = 166.421\,\frac{m}{s} \qquad vt1 = 0\,\frac{m}{s} \qquad mdot1 := \rho\cdot vn1\cdot A1 \qquad mdot1 = 1.668\,\frac{kg}{s}$

Compressor Outlet Conditions:

$h := .659\cdot in \qquad d2 := 6.605\cdot in \qquad r2 := \frac{d2}{2} \qquad A2 := \pi\cdot d2\cdot h \qquad A2 = 8.822\times 10^{-3}\,m^2$

$\alpha 2 := 70\cdot deg \qquad \beta 2 := 110\cdot deg$

$vn2 := \frac{vn1\cdot\left(d1^2 - d0^2\right)}{4\cdot d2\cdot h} \qquad vn2 = 157.582\,\frac{m}{s} \qquad v2 := \frac{vn2}{\cos(\alpha 2)} \qquad vt2 := v2\cdot\sin(\alpha 2)$

$vt2 = 432.954\,\frac{m}{s} \qquad mdot := \rho\cdot vn2\cdot A2 \qquad mdot = 1.668\,\frac{kg}{s}$

$T := (r2\cdot vt2 - r1\cdot vt1)\cdot mdot$

$Wc := T\cdot\omega \qquad Wc = 2.57\times 10^{5}\,W \qquad vn2 = 157.582\,\frac{m}{s}$

This equation was the original one for vn2: $vnn := \frac{r2\cdot\omega}{\tan(\alpha 2) + \cot(\beta 2)}$

The second vnn is obtained from continuity $vnn = 149.26\,\frac{m}{s} \qquad mdott := \rho\cdot vnn\cdot A2 \qquad mdott = 1.58\,\frac{k}{}$

Continuity is used now to calculate vn2 instead of the "w" equation, thus the flow is the same. Adjust beta1 to match mdots and compressor power

Appendix E

M-file to Generate Transfer Functions from Bode Plots: Fuel Flow Input

```
% Alex Tsai: 10/2/06
% Generate Transfer Function
clc; clear all; close all

% Note: Zeroes and Poles are given in [rad/s]
%_____________________________________________________________________________
% First Transfer Function: FT380/FT432
% Open Loop Gain
Kol1=10^(-22.5/20);
% Zeroes
z11=.021; z21=.3;
% Poles
p11=.033; p21=.061;
% Transfer Function
num1=Kol1*p11*p21*conv([1 z11],[1 z21]);
den1=z11*z21*conv([1 p11],[1 p21]);
TF1=tf(num1,den1);
TF1.inputdelay=1.4;
%_____________________________________________________________________________
% Second Transfer Function: PT305/FT432
% Open Loop Gain
Kol2=10^(26/20);
% Zeroes
z12=.03; z22=1;
% Poles
p12=.04; p22=.1;
% Transfer Function
num2=Kol2*p12*p22*conv([1 z12],[1 z22]);
den2=z12*z22*conv([1 p12],[1 p22]);
TF2=tf(num2,den2);
TF2.inputdelay=.8;
%_____________________________________________________________________________
% Third Transfer Function: TE326/FT432
% Open Loop Gain
Kol3=10^(-12/20);
% Zeroes
z13=.01; z23=.015;
% Poles
p13=.04; p23=.05; p33=.1; p43=.15;
% Transfer Function
num3=Kol3*p13*p23*p33*p43*conv([1 z13],[1 z23]);
den3=z13*z23*conv(conv(conv([1 p13],[1 p23]),[1 p33]),[1 p43]);
TF3=tf(num3,den3);
TF3.inputdelay=.5;
% Approximated Bode Plots
wmin=.0063; wmax=1;
subplot(1,3,1)
bode(TF1,{wmin,wmax}); title('TF1 Gen FT380/FT432')
grid on
```

```
subplot(1,3,2)
bode(TF2,{wmin,wmax}); title('TF2 Gen PT305/FT432')
grid on
subplot(1,3,3)
bode(TF3,{wmin,wmax}); title('TF3 Gen TE326/FT432')
grid on
%_____________________________________________________________________________
% End of Program
```

M-file to Create Bode Plots from Frequency Response Data

```
% Alex Tsai: 9/25/06
% Final Bode Plot
clc; clear all; close all
%_____________________________________________________________________
% Input Frequency 0.001Hz

datalogdot001=dlmread('logdot001.txt');

time28=datalogdot001(:,1);
signal28=datalogdot001(:,31);
PV432_28=datalogdot001(:,2);

FT432_28=datalogdot001(:,3);
PT305_28=datalogdot001(:,7);
FT380_28=datalogdot001(:,8);
TE326_28=datalogdot001(:,21);

fs=12.5; fdot001=.001;
Ndot001=length(time28);

FFT_FT432dot001=fft(FT432_28); ft432magdot001=abs(FFT_FT432dot001);
FFT_PT305dot001=fft(PT305_28);
FFT_FT380dot001=fft(FT380_28);
FFT_TE326dot001=fft(TE326_28);

TF1dot001=FFT_FT380dot001./FFT_FT432dot001;
TF2dot001=FFT_PT305dot001./FFT_FT432dot001;
TF3dot001=FFT_TE326dot001./FFT_FT432dot001;

df_dot001=fs/Ndot001;
faxisdot001=0:df_dot001:df_dot001*(Ndot001-1);

edot001=fdot001*.4;
indexdot001=find(faxisdot001 < fdot001+edot001 & faxisdot001 > fdot001-edot001);

magTF1dot001=abs(TF1dot001(indexdot001));
magTF2dot001=abs(TF2dot001(indexdot001));
magTF3dot001=abs(TF3dot001(indexdot001));

dBTF1dot001=20*log10(magTF1dot001);
dBTF2dot001=20*log10(magTF2dot001);
dBTF3dot001=20*log10(magTF3dot001);

phase_radTF1dot001=angle(TF1dot001(indexdot001));
phase_radTF2dot001=angle(TF2dot001(indexdot001));
phase_radTF3dot001=angle(TF3dot001(indexdot001));

phase_degTF1dot001=phase_radTF1dot001*180/pi;
phase_degTF2dot001=phase_radTF2dot001*180/pi;
phase_degTF3dot001=phase_radTF3dot001*180/pi;

dB_dot001=[dBTF1dot001 dBTF2dot001 dBTF3dot001];
phase_dot001=[phase_degTF1dot001 phase_degTF2dot001 phase_degTF3dot001];
```

```
[ACFdot001,Lagsdot001,Boundsdot001] = autocorr(FT432_28,Ndot001-1,[],5);

entdot001=length(ACFdot001);
for i=1:entdot001
   bdot001(:,i)=Boundsdot001;
end

figure;
subplot(3,2,1,'align')
plot(time28,signal28,'k'); hold on; plot(time28,PV432_28)
title('Command and PV432: 0.001Hz');
ylabel('Percent [%]'); xlabel('[sec]')

subplot(3,2,3,'align')
plot(time28,FT432_28); ylabel('FT432 [g/s]'); xlabel('[sec]')

subplot(3,2,5,'align')
plot(ACFdot001); hold on; plot(Lagsdot001,ACFdot001,Lagsdot001,bdot001)
ylabel('AutoCorr FT432'); xlabel('Lag \tau')

subplot(3,2,2,'align')
plot(time28,FT380_28);
title('FT380'); ylabel('[kg/s]')

subplot(3,2,4,'align')
plot(time28,PT305_28)
title('PT305'); ylabel('[kPag]')

subplot(3,2,6,'align')
plot(time28,TE326_28); title('TE326')
ylabel('[C]'); xlabel('[sec]')

%_____________________________________________________________________
```

{The above code is repeated for 28 frequencies up to 1Hz}

```
%_____________________________________________________________________
% Final Empirical Bode Plot

dBTF1_final=[dB_dot001(1); dB_dot002(1); dB_dot003(1); dB_dot004(1);dB_dot005(1); dB_dot006(1);
dB_dot007(1); dB_dot008(1); dB_dot009(1);dB_dot01(1); dB_dot02(1); dB_dot03(1); dB_dot04(1);
dB_dot05(1);dB_dot06(1); dB_dot07(1); dB_dot08(1); dB_dot09(1); dB_dot1(1); dB_dot2(1); dB_dot3(1);
dB_dot4(1); dB_dot5(1); dB_dot6(1); dB_dot7(1); dB_dot8(1); dB_dot9(1); dB_1(1)];

dBTF2_final=[dB_dot001(2); dB_dot002(2); dB_dot003(2); dB_dot004(2); dB_dot005(2); dB_dot006(2);
dB_dot007(2); dB_dot008(2); dB_dot009(2); dB_dot01(2); dB_dot02(2); dB_dot03(2); dB_dot04(2);
dB_dot05(2); dB_dot06(2); dB_dot07(2); dB_dot08(2); dB_dot09(2); dB_dot1(2); dB_dot2(2);
dB_dot3(2); dB_dot4(2); dB_dot5(2); dB_dot6(2); dB_dot7(2); dB_dot8(2); dB_dot9(2); dB_1(2)];

dBTF3_final=[dB_dot001(3); dB_dot002(3); dB_dot003(3); dB_dot004(3); dB_dot005(3); dB_dot006(3);
dB_dot007(3); dB_dot008(3); dB_dot009(3); dB_dot01(3); dB_dot02(3); dB_dot03(3); dB_dot04(3);
dB_dot05(3); dB_dot06(3); dB_dot07(3); dB_dot08(3); dB_dot09(3); dB_dot1(3); dB_dot2(3);
dB_dot3(3); dB_dot4(3); dB_dot5(3); dB_dot6(3); dB_dot7(3); dB_dot8(3); dB_dot9(3); dB_1(3)];
```

```
angleTF1_final=[phase_dot001(1); phase_dot002(1); phase_dot003(1); phase_dot004(1); phase_dot005(1); phase_dot006(1); phase_dot007(1); phase_dot008(1); phase_dot009(1); phase_dot01(1); phase_dot02(1); phase_dot03(1); phase_dot04(1); phase_dot05(1); phase_dot06(1); phase_dot07(1); phase_dot08(1); phase_dot09(1); phase_dot1(1); phase_dot2(1); phase_dot3(1); phase_dot4(1); phase_dot5(1); phase_dot6(1); phase_dot7(1); phase_dot8(1); phase_dot9(1); phase_1(1)];

angleTF2_final=[phase_dot001(2); phase_dot002(2); phase_dot003(2); phase_dot004(2); phase_dot005(2); phase_dot006(2); phase_dot007(2); phase_dot008(2); phase_dot009(2); phase_dot01(2); phase_dot02(2); phase_dot03(2); phase_dot04(2); phase_dot05(2); phase_dot06(2); phase_dot07(2); phase_dot08(2); phase_dot09(2); phase_dot1(2); phase_dot2(2); phase_dot3(2); phase_dot4(2); phase_dot5(2); phase_dot6(2); phase_dot7(2); phase_dot8(2); phase_dot9(2); phase_1(2)];

angleTF3_final=[phase_dot001(3); phase_dot002(3); phase_dot003(3); phase_dot004(3); phase_dot005(3); phase_dot006(3); phase_dot007(3); phase_dot008(3); phase_dot009(3); phase_dot01(3); phase_dot02(3); phase_dot03(3); phase_dot04(3); phase_dot05(3); phase_dot06(3); phase_dot07(3); phase_dot08(3); hase_dot09(3); phase_dot1(3); phase_dot2(3); phase_dot3(3); phase_dot4(3); phase_dot5(3); phase_dot6(3); phase_dot7(3); phase_dot8(3); phase_dot9(3); phase_1(3)];

faxis_final=[fdot001; fdot002; fdot003; fdot004; fdot005; fdot006; fdot007; fdot008; fdot009; fdot01; dot02; fdot03; fdot04; fdot05; fdot06; fdot07; fdot08; fdot09; fdot1; fdot2; fdot3; fdot4; fdot5; fdot6; fdot7; fdot8; fdot9; f1]

xx=faxis_final; yy=dBTF1_final; zz=dBTF2_final; ww=dBTF3_final; dd=angleTF1_final; ee=angleTF2_final; hh=angleTF3_final;

figure;
subplot(2,3,1)
semilogx(xx(1:20),yy(1:20),xx(21:28),yy(21:28),'r+')
title('TF1: FT380(s)/FT432(s)')
ylabel('Magnitude [dB]'); xlabel('[Hz]');

subplot(2,3,2)
semilogx(xx(1:20),zz(1:20),xx(21:28),zz(21:28),'r+')
title('TF2: PT305(s)/FT432(s)')
ylabel('Magnitude [dB]'); xlabel('[Hz]');

subplot(2,3,3)
semilogx(xx(1:20),ww(1:20),xx(21:28),ww(21:28),'r+')
title('TF3: TE326(s)/FT432(s)')
ylabel('Magnitude [dB]'); xlabel('[Hz]');

subplot(2,3,4)
semilogx(xx(1:20),dd(1:20),xx(21:28),dd(21:28),'r+')
ylabel('Phase [deg]'); xlabel('[Hz]')

subplot(2,3,5)
semilogx(xx(1:20),ee(1:20),xx(21:28),ee(21:28),'r+')
ylabel('Phase [deg]'); xlabel('[Hz]')

subplot(2,3,6)
semilogx(xx(1:20),hh(1:20),xx(21:28),hh(21:28),'r+')
ylabel('Phase [deg]'); xlabel('[Hz]')

% Plots in [rad/s]

xxx=xx.*2*pi; % conversion
```

```
figure;
subplot(2,3,1)
semilogx(xxx(1:20),yy(1:20),xxx(21:28),yy(21:28),'r+')
title('TF1: FT380(s)/FT432(s)')
ylabel('Magnitude [dB]'); xlabel('[rad/s]');

subplot(2,3,2)
semilogx(xxx(1:20),zz(1:20),xxx(21:28),zz(21:28),'r+')
title('TF2: PT305(s)/FT432(s)')
ylabel('Magnitude [dB]'); xlabel('[rad/s]');

subplot(2,3,3)
semilogx(xxx(1:20),ww(1:20),xxx(21:28),ww(21:28),'r+')
title('TF3: TE326(s)/FT432(s)')
ylabel('Magnitude [dB]'); xlabel('[rad/s]');

subplot(2,3,4)
semilogx(xxx(1:20),dd(1:20),xxx(21:28),dd(21:28),'r+')
ylabel('Phase [deg]'); xlabel('[rad/s]')

subplot(2,3,5)
semilogx(xxx(1:20),ee(1:20),xxx(21:28),ee(21:28),'r+')
ylabel('Phase [deg]'); xlabel('[rad/s]')

subplot(2,3,6)
semilogx(xxx(1:20),hh(1:20),xxx(21:28),hh(21:28),'r+')
ylabel('Phase [deg]'); xlabel('[rad/s]')

%_____________________________________________________________________
% End of Program
```

M-file of Nonlinear Brayton Cycle

```
% Hybrid Model Parameters
% Alex Tsai 7/13/05
clc; clear all;
pi=3.1416;

% Mass Flow Rate Constants

convlen=.0254; % Inches to meters
convang=.0175; % Deg to radians
d2=6.605; % Outer impeller diam [in]
d2si=d2*convlen; % [m] / Conversion
r2si=d2si/2; % Outer impeller radius / Compressor [m]
d1=4.354; % Inner diameter of impeller [in]
d1si=d1*convlen; % [m] / Conversion
r1si=d1si/2; % Radius [m]
alp2=60; % Absolute fluid velocity angle at outlet of compressor blade [deg]
alp2si=alp2*convang; % [rad] / Conversion
bet2=60; % Blade outlet angle [deg]
bet2si=bet2*convang; % [rad] / Conversion
alp1=45; alp1si=alp1*convang; bet1=45; bet1si=bet1*convang;
rho2=1.3; % Density of air leaving compressor blade [kg/m^3]
n=13; % Number of blades
theta=2*pi/n; % Angle between 2 blades
s=r2si*theta; % Arc length of outlet of compressor
h=.659; % Height of outlet compressor blade [in]
hsi=h*convlen; % [m]
A2=s*hsi; % Cross sectional area of outlet of compressor between 2 blades

% Compressor Pressure Constants

T1=293.15; % Ambient temperature [K]
P1=101300; % Ambient pressure [Pa]
mslope=2.26; % Slope of linear region of compressor map [s/kg]
bint=8; % y-intercept
Pref=101300; % Reference pressure / Ambient [Pa]
Tref=293.15; % Reference temperature / Ambient [K]
%mdot=1.767; % Mass flow rate [kg/s]
data=dlmread('data.txt'); % Reads txt matrix of compressor map values
Nmax=40500; % Max speed [rev/min]
datamass=dlmread('Book2.txt'); % Reads column vector of mdot increments
betalines=dlmread('beta.txt'); % Reads beta line matrix
datamassbeta=dlmread('datamassbeta.txt'); % Outputs beta line no.: 68 rows
datamassPR=dlmread('datamassPR.txt'); % Outputs PR; 12 rows
datamassbeta71905=dlmread('datamassbeta71905.txt'); % Adds 0-20 speed
datamassPR71905=dlmread('datamassPR71905.txt'); % Adds 0-20 speed correction
datamassoriginal71905=dlmread('datamassoriginal71905.txt'); % Mass flow, N outputs PR from 0-110
data72005=dlmread('data72005.txt'); % original PR fixed
data72005rows=dlmread('data72005rows.txt'); % rows of this PR
ajullir=dlmread('ajullir.txt');
ajullir2=dlmread('ajullir2.txt');

% Compressor Temperature Constants
```

```
%vout=154; % Normal velocity component at compressor outlet [m/s]
%vin=104.8; % Normal vel component at comp inlet [m/s]
Cp=1160; % Specific heat [J/kgK]
eta=.65; % Compressor efficiency
%Wcomp=129809; % Compressor backwork [W]

% Combustor Temperature Constants

dcomb=8.625; % Combustor outer diam [in]
dcombsi=dcomb*convlen;
dcomi=8.125; % Combustor inner diam [in]
dcomisi=dcomi*convlen;
insthick=2; % Insulation thickness [in]
insthicksi=insthick*convlen;
dcominssi=dcombsi+2*insthicksi; % Diam of insulation [m]
Lcom=12; % Combustor length [in]
Lcomsi=Lcom*convlen;
Asin=pi*dcomisi*Lcomsi; % Inlet surface area of combustor [m^2]
Asout=pi*dcominssi*Lcomsi; % Outer surface area including insulation [m^2]
LHV=50000000; % Lower heating value of fuel [J/kg]
mdotfuel=.019; % Mass flow rate of fuel [kg/s]
Qin=mdotfuel*LHV; % Fuel valve input [W]
%Qin=800000;
%Tb=473.15; % Compressor outlet temperature
Areacomb=(pi*dcomisi^2)/4; % Cross sectional area of combustor [m^2]
Vol=Areacomb*Lcomsi; % Volume of combustor [m^3]
rhocomb=2.986; % Assign density as outlet of compressor / temporary
m=rhocomb*Vol; % Mass of air inside combustor [kg]

% Thermal Resistance Constants

ho=250; % Inner fluid convection coefficient [W/m^2K] / Forced convection
ha=25; % Outer convection coefficient [W/m^2K] / Free convection
kk1=80; % Incaloy thermal conductivity [W/mK]
kk2=.075; % Insulation Microtherm thermal conductivity [W/mK]
Cv=872.2; % Specific heat constant volume / Plenum [J/kgK]
Rt=2*pi*Lcomsi*(1/(ho*Asin) + 1/(ha*Asout)) + (log(dcombsi/dcomisi))/kk1 +
(log(dcominssi/dcombsi))/kk2; % [mK/W]

% Turbine Constants

%Tc=900; % Temperature out of combustor [K]
%Pb=4*P1; % Outer pressure of compressor [Pa]
k=Cp/Cv; % Gamma ratio
a=(k-1)/k; % Simplified exponent
etat=.7; % Turbine efficiency
I=.027; % Shaft inertia [kgm^2]
Welecload=45000; % Electrical load on shaft [W]
percentage=.5; % Percent for initial speed
rpm=percentage*Nmax; % Initial velocity [rpm]
rpmact=rpm; % Used in the step input for the controller
wini=rpm*2*pi/60; % Initial velocity of turbine [rad/s]
percntdes=.7; % Desired percent of speed
rpmdes=percntdes*Nmax; % Desired speed [rpm]
wdes=rpmdes*2*pi/60; % Desired speed [rad/s] / Not needed
```

```
% Controller Parameters

Kp=100; % Proportional Gain
Ki=5; % Integral Gain
Kd=10; % Derivative Gain
Kv=1; ; % Valve opening position per voltage
Kq=10; % Heat input per valve position / Characterization

% Plots of Nonlinear Block Diagram: Linear Compressor Pressure

% Load command is after running the Simulink model, then saving
load linearvalues  % After the "save linearvalues" command in workspace
N=size(Wcomp.signals.values);
t=1:N;
t1=t/26.5;
subplot(3,1,1)
plot(t1,Wcomp.signals.values,t1,Wturb.signals.values)
title('Wcomp,Wturb Plots');
ylabel('kW');
legend('Wcomp','Wturb')
subplot(3,1,2)
plot(t1,mdot.signals.values)
title('Mass Flow Rate')
ylabel('[kg/s]')
subplot(3,1,3)
plot(t1,Tblinear.signals.values,t1,Tclinear.signals.values)
title('Tb, Tc Temperatures')
ylabel('[K]')
legend('Tb','Tc')
xlabel('Seconds')
figure;
plot(t1,rpm.signals.values)
title('Shaft Speed')
ylabel('[rpm]')
xlabel('Seconds')

% Nonlinar Simulation

load nonlinearvalues

N=size(Wcomp1.signals.values);
t=1:N;
t1=t/26.5;
subplot(3,1,1)
plot(t1,Wcomp1.signals.values,t1,Wturb1.signals.values)
title('Wcomp,Wturb Plots');
ylabel('kW');
legend('Wcomp','Wturb')
subplot(3,1,2)
plot(t1,mdot1.signals.values)
title('Mass Flow Rate')
ylabel('[kg/s]')
subplot(3,1,3)
plot(t1,Tb1.signals.values,t1,Tc1.signals.values)
title('Tb, Tc Temperatures')
```

```
ylabel('[K]')
legend('Tb','Tc')
xlabel('Seconds')
figure;
plot(t1,w1.signals.values)
title('Shaft Speed')
ylabel('[rpm]')
xlabel('Seconds')

% Nonlinear Simulation with Feedback Control

load controlvalues

N=size(Wcomp3.signals.values);
t=1:N;
t1=t/32.6;
subplot(3,1,1)
plot(t1,Wcomp3.signals.values,t1,Wturb3.signals.values)
title('Wcomp,Wturb Plots');
ylabel('kW');
legend('Wcomp','Wturb')
subplot(3,1,2)
plot(t1,mdot3.signals.values)
title('Mass Flow Rate')
ylabel('[kg/s]')
subplot(3,1,3)
plot(t1,Tb3.signals.values,t1,Tc3.signals.values)
title('Tb, Tc Temperatures')
ylabel('[K]')
legend('Tb','Tc')
xlabel('Seconds')
figure;
plot(t1,w3.signals.values,t1,step1.signals.values)
legend('Actual w','Desired w')
title('Shaft Speed')
ylabel('[rpm]')
xlabel('Seconds')
```

M-file of Nonlinear “Hyper” Facility

```
% Alex Tsai 3/28/06
% NETL Hyper Project: Nonlinear Model
% Accompanying m.file: Physical Data
%_____________________________________________________________________________
clc; clear all % Remember to leave as comment when plotting from Simulink
%_____________________________________________________________________________
% Conversion Factors

convlen=.0254; % Inches to meters
convang=.0175; % Degrees to radians
%_____________________________________________________________________________
% Ambient and Reference Conditions

Tref=600;%394.95;%293.15; % [K] Reference temperature: Ambient
Pref=101300; % [Pa] Reference pressure: Ambient
T1=Tref; % [K] Ambient temperature
P1=Pref; % [Pa] Ambient pressure
% Linear Version Data
mslope=2.26; % [s/kg] Slope of linear region of compressor map
bint=8; % [P/Pref] Y-intercept
%
%_____________________________________________________________________________
% Initial Conditions at ".88kg/s" from experimental data
densPCini=1.3; % [kg/m^3]
TPCini=924.71; % [K]
Tcombini=747.5; % [K]
Tplenumini=362.96; % [K]
Tplenuminisurf=297.01; % [K]
densplenumini=2.394; % [kg/m^3]
TinletHX=381.77; % [K]
Tcompressorini=394.95; % [K]
TPCsurfini=713.53; % [K]
Treflast=1126; % [K] Last piping segment after PC, from data @ 20250rpm

%_____________________________________________________________________________
% Organized Initial Conditions by Piping Label

Tamb=293.15; % [K]
Tpipe1=Tamb; % Piping out of Compressor: Air
Tpipe1surf=Tamb; % Surface
Tpipe2=Tamb; % Piping out of HXs: Air
Tpipe2surf=Tamb; % Surface
Tpipe3=Tamb; % Piping out of Plenum: Air
Tpipe3surf=Tamb; % Surface
Tcombustini=Tamb; % Combustor Air
Tpipe4=Tamb; % Piping out of Post Combustor: Air
Tpipe4surf=Tamb; % Surface
Tpipe5=Tamb; % Piping out of Turbine
Tpipe5surf=Tamb; % Surface
Tplenini=Tamb; % Air inside Plenum
Tplensurfini=Tamb; % Surface Plenum
Tpostini=Tamb; % Air inside Post Combustor
Tpostsurfini=Tamb; % Surface Post Combustor
```

```
Tcold1=Tamb; % Piping of CA: Air
Tcold1surf=Tamb; % Surface
Thot1=Tamb; % Piping of HA: Air
Thot1surf=Tamb; % Surface
winitial=100;%943; % rad/s initial of turbine
densityiniplen=1.3; % Plenum density
densityinipost=1.3; % Post density

%_____________________________________________________________________________
% Piping Diameters and Lengths: See Excel Spreadsheet for Nomenclature

% Inside Diameters [m]
dco1in=.110998; dco2in=.161925; dco3in=.161925; dco4in=.110998;
dco5in=.110998; dco6in=.110998; dco7in=.110998; dho1in=.154051;
dho2in=.154051; dho3in=.154051; dho4in=.154051; dpo1in=.154051;
dpo2in=.154051; dpo3in=.193675; dti1in=.193675; dti2in=.193675;
dcb1in=.10226; dcb2in=.154051; dcb3in=.154051; dcb4in=.154051;
dcb5in=.154051; dcb6in=.154051; dcb7in=.201727; dcb8in=.202717;
dcb9in=.154051; dcb10in=.154051; dcb11in=.193675; dcb12in=.193675;
dto1in=.198984; dto2in=.198984; dto3in=.198984; dto4in=.198984;
dto5in=.198984; dto6in=.198984; dto7in=.198984; dto8in=.202717;
dto9in=.202717; dto10in=.202717; dto11in=.202717; dto12in=.202717;
% Outside Diameters [m]
dco1out=.1143; dco2out=.16828; dco3out=.16828; dco4out=.1143;
dco5out=.1143; dco6out=.1143; dco7out=.1143; dho1out=.16828;
dho2out=.16828; dho3out=.16828; dho4out=.16828; dpo1out=.16828;
dpo2out=.16828; dpo3out=.21908; dti1out=.21908; dti2out=.21908;
dcb1out=.1143; dcb2out=.16828; dcb3out=.16828; dcb4out=.16828;
dcb5out=.16828; dcb6out=.16828; dcb7out=.21908; dcb8out=.21908;
dcb9out=.16828; dcb10out=.16828; dcb11out=.21908; dcb12out=.21908;
dto1out=.2032; dto2out=.2032; dto3out=.2032; dto4out=.2032;
dto5out=.2032; dto6out=.2032; dto7out=.2032; dto8out=.21908;
dto9out=.21908; dto10out=.21908; dto11out=.21908; dto12out=.21908;
% Insulation Diameters [m]
dinsco1=.1651; dinsco2=.21908; dinsco3=.21908; dinsco4=.1651;
dinsco5=.1651; dinsco6=.1651; dinsco7=.1651; dinsho1=.26988;
dinsho2=.26988; dinsho3=.26988; dinsho4=.26988; dinspo1=.26988;
dinspo2=.26988; dinspo3=.32068; dinsti1=.32068; dinsti2=.32068;
dinscb1=.2159; dinscb2=.26988; dinscb3=.26988; dinscb4=.26988;
dinscb5=.26988; dinscb6=.26988; dinscb7=.32068; dinscb8=.32068;
dinscb9=.26988; dinscb10=.26988; dinscb11=.32068; dinscb12=.32068;
dinsto1=.3048; dinsto2=.3048; dinsto3=.3048; dinsto4=.3048;
dinsto5=.3048; dinsto6=.3048; dinsto7=.3048; dinsto8=.26988;
dinsto9=.26988; dinsto10=.26988; dinsto11=.26988; dinsto12=.26988;
% Lengths [m]
Lco1=.127; Lco2=.7874; Lco3=.254; Lco4=.7874; Lco5=.7874; Lco6=.6604;
Lco7=.6604; Lho1=.6096; Lho2=.6858; Lho3=.508; Lho4=.254; Lpo1=1.4478;
Lpo2=.9652; Lpo3=.9144; Lti1=.2286; Lti2=.4064; Lcb1=.4572; Lcb2=1.1176;
Lcb3=.3302; Lcb4=1.1176; Lcb5=.508; Lcb6=1.5748; Lcb7=.3048; Lcb8=4.572;
Lcb9=.3048; Lcb10=.3048; Lcb11=.9398; Lcb12=1.6256; Lto1=.9398; Lto2=.508;
Lto3=.3556; Lto4=.4318; Lto5=.4318; Lto6=.5842; Lto7=.5842; Lto8=.381;
Lto9=.381; Lto10=.4064; Lto11=.4064; Lto12=.2286;
%_____________________________________________________________________________
% Piping Parameters for Temperature and Pressure Calculations

% tempvec=dlmread('tempvec.txt'); % temperature vector values
```

```
% tempsteel=dlmread('tempsteel.txt'); % temp vector for steel pipe prop
% visc=dlmread('visc.txt'); % kinematic viscosity nu
% viscu=dlmread('viscu.txt'); % dynamic viscosity mu
% kcond=dlmread('kcond.txt'); % air conductivity as funct of temp
% Cp=dlmread('Cp.txt'); % air heat capacitance
% Prndtl=dlmread('Prndtl.txt'); % Prandlt number
% dens=dlmread('dens.txt'); % air density as a function of temp
% cmetal=dlmread('cmetal.txt'); % stainless steel Cp [J/kgK]
% kmetal=dlmread('kmetal.txt'); % metal conductivity [W/mK]
densmetal=7900; % [kg/m^3] steel metal density
convlen=.0254; % Inches to meters
d1=convlen*4; % inner diameter of first section of pipe
d2=convlen*4.5; % pipe outer diameter / thickness 1/4"
d3=convlen*8.5; % insulation outer diameter
L=convlen*60; % length of one segment of pipe / 5ft
hout=10; % free outside convection
r1=d1/2; r2=d2/2; r3=d3/2;
ka=80; kb=.075; % metal and insulation conductivities respectively
matR=(r1/ka)*log(r2/r1)+(r1/kb)*log(r3/r2);
outR=(r1/r3)/hout;
Rcomb=matR+outR; % combined resistances
Ah=40; % area calculated as in example pg. 665

effNTU=dlmread('effNTU.txt'); % vector column of NTU values
effCr=dlmread('effCr.txt'); % row vector of Cr
effect=dlmread('effect.txt'); % table values of effectiveness
% f=.03; % this value needs to be calculated from Re / e/D=.004
% Kloss=2; % loss coefficients
%
% % properties dependent on both temperature and pressure
% tempvector=dlmread('tempvector.txt');
% density=dlmread('density.txt');
% pressure=dlmread('pressure.txt');
% specificheat=dlmread('specificheat.txt');
%Tamb=300;
%Pamb=405300;

%_____________________________________________________________________________
% Minor Pressure Loss Coefficients for Piping Elements

% Equivalent Length: Le [m]
Kco0=.1981; Kco2=6.401; Kco7=.1981; Kco8=.1981; Kcb3=.1981; Kcb11=.1981;
Kho6=.1981; Kho9=.1981; Kpo1=.1981; Kpo3=.1981; Kpo5=.1981; Kpo6=.1981;
Kti1=.1981; Kti3=.1981; Kto9=.1981; Kto10=.1981; Kto14=.1981;
% Le/D
Kco1=800; Kco3=2; Kco4=12; Kco5=5; Kco6=5; Kcb1=20; Kcb4=30; Kcb5=20;
Kcb6=3; Kcb7=20; Kcb8=3; Kcb9=60; Kcb10=30; Kho3=30; Kho4=30; Kho5=50;
Kho8=3; Kpo2=30; Kti2=10; Kti4=10; Kto2=5; Kto3=8; Kto4=24; Kto5=16;
Kto6=16; Kto11=16; Kto12=16; Kto13=40; Kto15=60;
% K Factor
Kcb2=.3086; Kcb12=.9648; Kho1=.3086; Kho2=.3086; Kho7=.969; Kho10=.0934;
Kho11=.7901; Kpo4=.1914; Kpo7=.9648; Kto1=.1914; Kto7=.0846; Kto8=.0846;

%_____________________________________________________________________________
% Relative Roughness
eco1=1.35e-4; eco2=9.26e-5; eco3=9.26e-5; eco4=1.35e-4; eco5=1.35e-4;
```

```
eco6=1.35e-4; eco7=1.35e-4; eho1=9.74e-5; eho2=9.74e-5; eho3=9.74e-5;
eho4=9.74e-5; epo1=9.74e-5; epo2=9.74e-5; epo3=7.74e-5; eti1=7.74e-5;
eti2=7.74e-5; ecb1=1.47e-4; ecb2=9.74e-5; ecb3=9.74e-5; ecb4=9.74e-5;
ecb5=9.74e-5; ecb6=9.74e-5; ecb7=7.4e-5; ecb8=7.4e-5; ecb9=9.74e-5;
ecb10=9.74e-5; ecb11=7.74e-5; ecb12=7.74e-5; eto1=7.54e-5; eto2=7.54e-5;
eto3=7.54e-5; eto4=7.54e-5; eto5=7.54e-5; eto6=7.54e-5; eto7=7.54e-5;
eto8=7.4e-5; eto9=7.4e-5; eto10=7.4e-5; eto11=7.4e-5; eto12=7.4e-5;
%_____________________________________________________________________
% Air Plenum V-301 Physical Data [m]

% dapin=1.2192; dapout=1.27; dinsap=1.3716; Lap=2.4384; % This is of tank
dapin=1.2192; dapout=1.2319; dinsap=1.3335; Lap=1.524; % New Info
% Conversion Factors, Gas, Metal and Insulation Properties
conv=.0254; % [in to m]
Rgas=286; % [J/kgK] Universal Gas Constant
densm=7900; % [kg/m^3] Density of metal
kins=.075; % [kg/m^3] Insulation conductivity
kmetal=80; % [kg/m^3] Metal conductivity : This conflicts with kmetal matrix
hamb=10; % [W/m^2K] Free outside convection coefficient
Pamb=101325; % [Pa] Ambient pressure
velaire=10; % [ft/s] Velocity of air inside plenum: Assumed
velair=velaire*conv*12; % [m/s]

% Ambient and Initial Conditions
Tamb=293.15; % [K] Ambient temperature
rhotankini=1.3; % [kg/m^3] Initial density of air in tank
rhotankini2=2.4; % [kg/m^3] Initial dens from 89C, 148kPag at "wini" experimental
rhotankini3=.5;
rhotankini4=2.394; % @ TinIC and PinIC start simulation
Ttankini=Tamb; % [K] Tank initial temperature
Tsini=Tamb; % [K] Initial surface area temperature
Pback=225100; % [Pa] Initial back pressure of vessel
Tin=723; % [K] Incoming plenum temperature, At component practice level
TinIC=362.96; % [K] Temp @ .88kg/s start simulation ~89.81C
PinIC=Pref+148590; % [Pa] Press @ .88kg/s start simulation

% Air Plenum Physical Data
% dapinn=dapin*conv; This was WRONG!
% dapoutt=dapout*conv;
% Lapp=Lap*conv;
% thicke=1; % [in] Thickness of vessel: Old Measurement
thicke=.25; % [in] New Measurement
thick=thicke*conv; % [m]
thickinse=2; % [in] Thickness of insulation
thickins=thickinse*conv; % [m]
dtanke=48.5; % [in] Outer diameter of air vessel
dtank=dtanke*conv; % [m]
dins=dtank+2*thickins; % [m] Insulation diameter
d1=dtank-2*thick; % [m], Internal diameter of plenum
Ltanke=60;   %96; % [in] Length of vessel
Ltank=Ltanke*conv; % [m]
Vt=(pi*(d1^2)/4)*Ltank; % [m^3] Volume of air plenum: inside
Asin=pi*d1*Ltank; % [m^2], Inner surface area of air plenum
dexite=6; % [in] Exit diameter of tank
dexit=dexite*conv; % [m]
Aexit=(pi*dexit^2)/4; % [m^2] Exit area of tank
```

```
AreaIn=Aexit; % Assume inlet cross sectional area is the same
Cd=.61; % Discharge coefficient for tank: Sharp edge exit REF: EIT
R1=d1*log(dtank/d1)/kmetal; % Resistance of metal shell
R2=d1*log(dins/dtank)/kins; % Resistance of insulation
dellP=225100; % delP added to Pref to equate plenum back P


Up=1/((dtank/2)*log(dins/dtank)/kins+(1/hamb)); % Partial overall heat transfer coefficient

Vmout=((pi*dtank^2)/4)*Ltank; % Outer volume of plenum
Vmin=((pi*d1^2)/4)*(Ltank-2*thick); % Inner volume of plenum
Vm=Vmout-Vmin; % [m^3], Volume of metal plenum

tempvecenthalpy=dlmread('tempvecenthalpy.txt'); % Temperature vector values for enthalpy
enthalpy=dlmread('enthalpy.txt'); % Enthalpy table dependent on Temp

% Properties dependent on both temperature and pressure

tempvectorTP=dlmread('tempvectorTP.txt'); % temp vector for Temp and Press dependent variables
density=dlmread('density.txt');
pressure=dlmread('pressure.txt');
specificheat=dlmread('specificheat.txt');
%
temp=dlmread('temp.txt'); % Temperature vector for Temp dependent variables
tempmetal=dlmread('tempmetal.txt'); % Temp vector for metal
Cpmetal=dlmread('Cpmetal.txt'); % [J/kgK] Cp for metal
kmetal=dlmread('kmetal.txt'); % [W/mK] Conductivity of metal
%
visc=dlmread('visc.txt'); % [m^2/s] kinematic viscosity nu
viscu=dlmread('viscu.txt'); % [Ns/m^2] dynamic viscosity mu
kcond=dlmread('kcond.txt'); % [W/mK] air conductivity as funct of temp
Prndtl=dlmread('Prndtl.txt'); % Prandlt number

Tinternal=dlmread('Tinternal.txt'); % [K] Temp vector for internal energy values
internal=dlmread('internal.txt'); % [J/kgK] Internal energy values


%_____________________________________________________________________________
% Post Combustor V-304 Physical Data [m] : Note: Material is Incaloy

% Double check these dimensions, they might not correspond to actual
% dpcin=.4572; dpcout=.508; dinspc=.6096; Lpc=1.3716; Older Values
dpcin=.813; dpcout=.864; dinspc=.965; Lpc=1.219;
kpc=80; % [W/mK] Thermal conductivity of post combustor: Incaloy

Vpost=(pi*(dpcin^2)/4)*Lpc; % [m^3] Volume of inside of post combustor: air
Aexitp=(pi*dti1in^2)/4; % [m^2] Area exit post combustor
Cdp=.68; % Post combustor discharge coefficient: Assumed
Asurf=pi*dpcin*Lpc; % [m^2] Surface area of inside post combustor
R3=dpcin*(log(dpcout/dpcin))/kpc; % Sheet metal resistance: Should be f(T)
R4=dpcin*(log(dinspc/dpcout))/kins; % Insulation resistance
dpost=dpcin; % Inner post comb diameter
velairp=.1; % Inner post comb air velocity: Assumed
Lpost=Lpc; % Length of post comb
Vps=pi*(dpcout^2-dpcin^2)*Lpc/4; % Volume post comb of sheet metal
Tpcwini=362.15; % [K] Initial PC temp from exp data @ wini condition
```

```
%_____________________________________________________________________
% Heat Exhanger E-300, E-305 Physical Data

densHX=7900; % [kg/m^3] Density of stainless steel
heightHX=.7697; lengthHX=2.67; widthHX=1.27; % [ft]
hHX=.2346; lHX=.81382; wHX=.3871; % [m]
HXsolidVol=.30; % [%] Percent of volume that is solid: Approximate
VolHX=hHX*lHX*wHX*HXsolidVol; % [m^3] HX approximated mass volume
THXini=Tamb;
Nplates=10; % Approximate number of plates in HX
HXAsurf=2*hHX*wHX*Nplates; % [m^2] Surface Area of HX
Uhx=20; % Approximate from internet [W/m^2K]
HXVolHot=(VolHX/HXsolidVol)*.35; % Approximate bulk volume of hot side [m^3]
HXAcrossCold=lHX*wHX*.8; % [m^2] Cold Side Approx Cross sectional area
HXAcrossHot=HXAcrossCold;
HXVolCold=HXVolHot;
Perimeter=wHX*2+lHX*2;%.02+.01; % [m] Wetted perimeter of one entrance: 1cm=width, .5cm=height
Acc=HXAcrossCold*.5;%5e-5; % [m^2] cross sect area of one entrance
Dh=4*Acc/Perimeter; % [m] Hydraulic Diameter of rectangle cross sect area

%_____________________________________________________________________
% Compressor C-100 Parameters

d2=6.605; % [in] Outer impeller diameter
d2si=d2*convlen; % [m] Conversion
r2si=d2si/2; % [m] Compressor outer impeller radius
d1=4.354; % [in] Inner diameter of impeller
d1si=d1*convlen; % [m] Conversion
r1si=d1si/2; % [m] Radius
alp2=60;%64 %60; % [deg] Absolute fluid velocity angle at outlet of compressor blade
alp2si=alp2*convang; % [rad] Conversion
bet2=60;%80 %60; % [deg] Blade outlet angle
bet2si=bet2*convang; % [rad] Conversion
alp1=45; alp1si=alp1*convang; bet1=45; bet1si=bet1*convang;
rho2=1.3; % [kg/m^3] Density of air leaving compressor blade
n=13; % Number of blades
theta=2*pi/n; % [rad] Angle between 2 blades
s=r2si*theta; % [m] Arc length of outlet of compressor
h=.659; % [in] Height of outlet compressor blade
hsi=h*convlen; % [m] Conversion
A2=s*hsi; % [m^2] Cross sectional area of outlet of compressor between 2 blades
mdotwini=.9; % [kg/s] Minimum mdot at "wini" speed

% Compressor Data and .txt Files

% data=dlmread('data.txt'); % Reads txt matrix of compressor map values
% datamass=dlmread('Book2.txt'); % Reads column vector of mdot increments
% betalines=dlmread('beta.txt'); % Reads beta line matrix
% datamassbeta=dlmread('datamassbeta.txt'); % Outputs beta line no.: 68 rows
% datamassPR=dlmread('datamassPR.txt'); % Outputs PR; 12 rows
% datamassbeta71905=dlmread('datamassbeta71905.txt'); % Adds 0-20 speed
% datamassPR71905=dlmread('datamassPR71905.txt'); % Adds 0-20 speed correction
% datamassoriginal71905=dlmread('datamassoriginal71905.txt'); % Mass flow, N outputs PR from 0-110
data72005=dlmread('data72005.txt'); % original PR fixed
data72005rows=dlmread('data72005rows.txt'); % rows of this PR
```

```
% ajullir=dlmread('ajullir.txt');
% ajullir2=dlmread('ajullir2.txt');

Cp=1160; % [J/kgK] Specific heat: Note: Might need to change to 1004
eta=.75;%.65; % Compressor efficiency

%_____________________________________________________________________________
% New Compressor Parameters

conversion=.0254; hh=.659; hc=hh*conversion; dd2=6.605; dc2=dd2*conversion;
rc2=dc2/2; dd1=4.354; dd0=1.572; ddd=dd1-dd0; ddd1=ddd*conversion;
rc1=ddd1/2; dc1=dd1*conversion;
degreeconversion=2*pi/360; al1=0; bb1=48; bet1=bb1*degreeconversion;
aal2=70; al2=aal2*degreeconversion; bb2=110; bet2=bb2*degreeconversion;
Ac2=pi*dc2*hc; dc0=dd0*conversion;
% changed again bb1 from 55 to 48
% changed al1 from 0 to 10

%
% rc1=.035;
% al1=0; bet1=.837758; rc2=.0838835; al2=1.2217;
% dc2=.167767; hc=.0167386;
% Ac2=pi*dc2*hc; dc1=.1105916; dc0=.0399288;


%_____________________________________________________________________________
% Combustor Data

dcomb=8.625; % Combustor outer diam [in]
dcombsi=dcomb*convlen;
dcomi=8.125; % Combustor inner diam [in]
dcomisi=dcomi*convlen;
insthick=2; % Insulation thickness [in]
insthicksi=insthick*convlen;
dcominssi=dcombsi+2*insthicksi; % Diam of insulation [m]
Lcom=12; % Combustor length [in]
Lcomsi=Lcom*convlen;
Asin=pi*dcomisi*Lcomsi; % Inlet surface area of combustor [m^2]
Asout=pi*dcominssi*Lcomsi; % Outer surface area including insulation [m^2]
LHV=34600000; % Lower heating value of fuel [J/kg]
mdotfuel=.019; % Mass flow rate of fuel [kg/s]
Qin=mdotfuel*LHV; % Fuel valve input [W]
%Qin=800000;
%Tb=473.15; % Compressor outlet temperature
Areacomb=(pi*dcomisi^2)/4; % Cross sectional area of combustor [m^2]
Vol=Areacomb*Lcomsi; % Volume of combustor [m^3]
rhocomb=2.986; % Assign density as outlet of compressor / temporary
m=rhocomb*Vol; % Mass of air inside combustor [kg]


ho=250; % Inner fluid convection coefficient [W/m^2K] / Forced convection
ha=25; % Outer convection coefficient [W/m^2K] / Free convection
kk1=80; % Incaloy thermal conductivity [W/mK]
kk2=.075; % Insulation Microtherm thermal conductivity [W/mK]
Cv=872.2; % Specific heat constant volume / Plenum [J/kgK]
```

```
Rt=2*pi*Lcomsi*(1/(ho*Asin) + 1/(ha*Asout)) + (log(dcombsi/dcomisi))/kk1 +
(log(dcominssi/dcombsi))/kk2; % [mK/W]

%_____________________________________________________________________________
% Turbine T-101 Parameters

Nmax=40500; % [rev/min] Max turbine speed
%Tc=900; % Temperature out of combustor [K]
%Pb=4*P1; % Outer pressure of compressor [Pa]
k=Cp/Cv; % Gamma ratio
a=(k-1)/k; % Simplified exponent
etat=.7; % Turbine efficiency
I=.027; % Shaft inertia [kgm^2]
Welecload=0; % Electrical load on shaft [W] Runs well with 15, 30 or 45kW
percentage=.222; % Percent for initial speed
rpm=percentage*Nmax; % Initial velocity [rpm]
rpmact=rpm; % Used in the step input for the controller
wini=rpm*2*pi/60; % Initial velocity of turbine [rad/s]
percntdes=1;%.7; % Desired percent of speed
rpmdes=percntdes*Nmax; % Desired speed [rpm]
wdes=rpmdes*2*pi/60; % Desired speed [rad/s] / Not needed
delPb=9000; % [Pa] Delta P of piping from outlet of turbine to exhaust stack
Pbturb=Pref+delPb; % [Pa] Turbine back pressure assumed
TIT=1033.15; % [K] Turbine inlet temperature, for 60kW case
TIP=326400; % [Pa] Turbine inlet press, for 60kW case; = 225kPag + 101.3kPa
TET=776.15; % [K] Turbine exit temp, for 60kW case
TOP=110400; % [Pa] Turbine outlet pressure, for 60kW case


%_____________________________________________________________________________
% Valve Data
CAopening=dlmread('CAopening.txt'); % Vector of 10,30,50,70% opening, used for deP block
CAopening2=dlmread('CAopening2.txt'); % -10,10,30,50,70, used for mdot block
CAspeed=dlmread('CAspeed.txt'); % Vector of 10500,20500,30500,40500 rpm
CApress=dlmread('CApress.txt'); % Vector of gage pressures [Pa]
CAopenmdot=dlmread('CAopenmdot.txt'); % Vector 30,50,70 since no readings for 10
CAmdot=dlmread('CAmdot.txt'); % CA mdot values
BAopening=dlmread('BAopening.txt'); % 0,2,4,6,8,10,12,14,16,18 % opening
BAopen=dlmread('BAopen.txt'); % 14,16,18
BApress=dlmread('BApress.txt'); % BA gage values
BAmdot=dlmread('BAmdot.txt'); % mdot values for BA
HAopenings=dlmread('HAopenings.txt'); % 10-100% in 5% increments, used for press block
HAopening2=dlmread('HAopening2.txt'); % starts from 0-100, at 5% increments, used for mdot block
HAmdot=dlmread('HAmdot.txt');
HApress=dlmread('HApress.txt');
%_____________________________________________________________________________
% Controller Parameters: Original Brayton Report

Kp=50;%10;%100; % Proportional Gain
Ki=2;%5; % Integral Gain
Kd=0;%50;%10; % Derivative Gain
Kv=1; ; % Valve opening position per voltage
Kq=1;%10; % Heat input per valve position / Characterization
%_____________________________________________________________________________
% Report Test Simulation Runs
```

```
% load xx1 xx2 xx3 xx4 xx5 xx6 xx7 xx8 xx9
% y=xx1.signals.values;
% y1=xx2.signals.values;
% y2=xx3.signals.values;
% yyy=xx8.signals.values;
% yyyy=xx9.signals.values;
% N=length(xx2.signals.values);
%
% % Compressor Parameters
% tt=1:N; t=600*tt/N;
% subplot(4,1,1);plot(t,y)
% title('Compressor Outlet Parameters')
% ylabel('Flow Rate [kg/s]'); hold on
% subplot(4,1,2); plot(t,y1)
% ylabel('Temp [K]'); hold on
% subplot(4,1,3); plot(t,y2)
% ylabel('Press [Pa]'); hold on
% subplot(4,1,4); plot(t,yyyy)
% ylabel('RPM')
% xlabel('Time [Seconds]'); hold off
%
% % Turbine and Heat Exchanger Parameters
% figure
% y3=xx4.signals.values;
% y4=xx5.signals.values;
% y5=xx6.signals.values;
% y6=xx7.signals.values;
%
% subplot(4,1,1);plot(t,y3)
% title('Turbine and Heat Exchanger Parameters')
% ylabel('Turb Temp [K]'); hold on
% subplot(4,1,2); plot(t,y4)
% ylabel('Turb Press [Pa]'); hold on
% subplot(4,1,3); plot(t,y5)
% ylabel('HX Inlet [K]'); hold on
% subplot(4,1,4); plot(t,y6)
% ylabel('HX Exit [K]')
% xlabel('Time [Seconds]'); hold off
%_____________________________________________________________________________
% End of Program
```

M-File that Generates 3x3 MIMO Plant

```
% 3x3 system: Eliminate Tfc, Pfc and LB, BA

clc; clear all

%_____________________________________________
% Individual Transfer Functions

% Nomenclature: Gij, i-output, j-input

% Input No.1: BA - Bleed Air Bypass Valve
g11=zpk([],[-.12 -.32 -.8],5.339e-4,'iodelay',2.29);
g21=zpk(-.042,[-.073 -.2 -.2 -.2],.047,'iodelay',2.56);
g31=zpk([],[-.025 -.2 -.3],3.991e-3,'iodelay',3.92);
```

```
g41=zpk([],[-.12 -.2 -.2 -.9],2.429e-3,'iodelay',1.03);
g51=zpk([-.03 -5.1],[-.046 -.09 -1.1 -.25],1.485,'iodelay',1.12);
% Input No.2: CA - Cold Air Bypass Valve
g12=zpk([-.085],[-.08 -1.91],.032,'iodelay',.51);
g22=zpk([-.015 -.085 -.4],[-.01 -.15 -.25 -.95],.099,'iodelay',3.29);
g32=zpk([-2.5 -2.5],[-.025 -.2],6.731e-4,'iodelay',2.77);
g42=zpk([],[-.32 -1.1],.788,'iodelay',.125);
g52=zpk([roots([1 7.5e-3 .0056])'],[-.077 -.082 -2],26.682,'iodelay',.66);
% Input No.3: HA - Hot Air Bypass Valve
g13=zpk([-.7],[-.91 -2.5],.04,'iodelay',.77);
g23=zpk([-.03 -.8],[-.059 -.081 -4],.178,'iodelay',1.57);
g33=zpk([-2.5 -2.5],[-.025 -.2],3.185e-4,'iodelay',1.07);
g43=zpk([],[-.2 -2],.357,'iodelay',.22);
g53=zpk([-.03],[-.06 -.09],2.543,'iodelay',.85);
% Input No.4: PV - Fuel Valve
g14=zpk([-.022 -.3],[-.033 -.061 -1 -4],.041,'iodelay',1.38);
g24=zpk([-.03],[-.04 -.07 -4],3.524,'iodelay',.43);
g34=zpk([-.005 -.015],[-.04 -.05 -.1 -.15],.024,'iodelay',3.4);
g44=zpk([-.054 -.054],[-.085 -.085 -.53 -.53],2.201,'iodelay',.18);
g54=zpk([-.03 -3],[-.04 -.07],17.495,'iodelay',.2);
% Input No.5: LB - Load Bank
g15=zpk([-.022 -.3 -1.5],[-.043 -.071 -1 -3.5 -3.5],.048,'iodelay',1.59);
g25=zpk([-.03],[-.05 -.07 -4],1.476,'iodelay',.92);
g35=zpk([-2.5 -2.5],[-.025 -.1],1e-3,'iodelay',2.71);
g45=zpk([],[-.15 -.15],.071,'iodelay',5.9);
g55=zpk([-.02],[-.04 -.06],21.339,'iodelay',.153);

%_____________________________________________
% Transfer Function Matrix

Gp=[g12 g13 g14;...
   g42 g43 g44;...
   g52 g53 g54];

% Left: Inputs - CA, HA, PV
% Left: Outputs - mdot, TIT, speed

%_____________________________________________
% Time Delay Vector

td=[2.29 .51 .77 1.38 1.59...
   2.56 3.29 1.57 .43 .92...
   3.92 2.77 1.07 3.4 2.71...
   1.03 .125 .22 .18 5.9...
   1.12 .66 .85 .2 .153]';

td_max=max(td); td_min=min(td); % Max and Min Delay Times
wd_m=1/td_max; % Frequency at Max Delay Time
```

M-File that Analyzes MIMO Plant

```
% Alex Tsai: 8/6/07
% Multivariate Bode Plot, DC Gain, RGA, SVD, Transmission Zeros
%
% The code plots the Open Loop Singular Values of the Unscaled and Scaled
```

```
% Transfer Function Matrices. It also plots the Singular Values of the Open
% Loop Sensitivity Function. The Relative Gain Array is calculated from the
% plant's DC Gain, as well as from a Frequency Dependent Loop. Singular
% Value Decomposition gives Input and Output Directions for the 5 Singular
% Values at DC Gain.
%
% The plant has been modified to 3x3 dimensions

clc; clear all

%_____________________________________________
% Loading the Unscaled and Simplified Plants
load Gp
load wd_m

%_____________________________________________
%Scaling Diagonal Input and Output Matrices

dm=0.3; dTIT=50; dS=1500; % Units: [kg/s,C,rpm]
dCA=10; dHA=10; dPV=1; % Units: [%,%,%]

post=diag([dCA dHA dPV]);
pre=diag([dm dTIT dS]);

%_____________________________________________
% Scaled Transfer Function Matrix

Gscaled=inv(pre)*Gp*post;
Gscaled=pade(Gscaled); % See Note

%_____________________________________________
% Multivariate Bode Plot for Gp, Gpscaled, S, T

figure(1) % Unscaled and Scaled SV Plots
sigma(Gp,'k'); hold on; sigma(Gscaled,'r'); hold off; grid on
title('MIMO Open Loop Singular Values'); legend('Unscaled','Scaled')

Sf=inv(eye(3)+Gscaled); % Open Loop Sensitivity Function
Tf=eye(3)-Sf; % Open Loop Complementary Sensitivity Function

figure(2) % Open Loop Sensitivity Function and Co-Sensitivity Function
w=logspace(-4,3); sigma(Sf,'k',w); grid on
title('MIMO Sensitivity Function Singular Values: Open Loop')

%_____________________________________________
% DC Gain and RGA: Unscaled and Scaled

Gpz=evalfr(Gp,0); % Gain at Steady State, Unscaled
Gpzs=evalfr(Gscaled,0); % Scaled DC Gain: See Note
RGAz=Gpz.*inv(Gpz');

%_____________________________________________
% Frequency Dependent RGA: Ref [Oskar Vivero]

w=logspace(-6,2);
Gf=freqresp(Gp,w);
```

```
for i=1:length(w);
   Grga(:,:,i)=Gf(:,:,i).*inv(Gf(:,:,i)');
end

figure(3) % RGA(jw) Plot
for i=1:3
  for j=1:3
    rgaij=Grga(i,j,:);
    rgaint=Grga(1,2,:);
    rgaijabs=abs(rgaij); rgaints=abs(rgaint);
    uplot('liv,lm',w,rgaijabs(:),'k',w,rgaints(:),'r'); grid off
    hold on
 end
end
title('RGA(jw) Values'); ylabel('RGA Number'); xlabel('[rad/s]')
hold off;

%_____________________________________________
% Input and Output Directionality: Condition Number

[U,S,V]=svd(Gpz); % Unscaled Plant at DC
[Us,Ss,Vs]=svd(Gpzs); % Scaled Plant at DC
condnum=Ss(1,1)/Ss(3,3); % See Note

%_____________________________________________
% Open Loop Transmission Zeros

Gsys=pade(Gp); Gsys=minreal(Gsys); %Gsys=minreal(Gp);
[a,b,c,d]=ssdata(Gsys);
z=tzero(a,b,c,d);
zb_high=max(z); zb_low=min(z);
index=find(z>0);
zv=z(index);
RHPfz=max(zv);RHPsz=min(zv);
wc=real(RHPsz);

%_____________________________________________
% Notes:
%   1. In the scaling diagonal matrices, 'pre' refers to the allowed errors
%   of the outputs i.e. for m' in the fuel cell, the maximum allowed change
%   in its value is +/-0.2kg/s from the nominal value. This is considered
%   to be the 'window' of operation. The 'post' refers to the allowed
%   changes from nominal of the input actuators i.e. the CA is not allowed
%   to change more than 10% from its nominal value, without causing a stall.

%   2. Pade is used on the scaled plant in order to obtain the inverse in
%   the Sensitivity calculation. To have any meaning, scaling must be done
%   prior to obtaining the Sensitivity Function. When using Pade prior to
%   the SV Plot, the actual plot is lower in magnitude than without Pade.
%   This might indicate either an approximation error, or the delays not
%   being taken into account when Pade is not used. The choice is to use
%   Pade before anything.

%   3. RGAz is the RGA evaluated at 0 frequency.

%   4. V is the unitary matrix corresponding to the input directions,
```

```
%   whereas U relates to the output directions. Will use U,S,V for the
%   unscaled plant

%   5. To track what is the Open Loop cross-over frequency, the norm
%   function can be used on the upper singular values of Gscaled

%   6. When computing the transmission zeros, it makes a difference whether
%   Pade is used or not. If its not used prior to the command 'tzero', the
%   maximum value of the Z vector is half that, when Pade is used i.e.
%   without Pade zb_high=21.9, with Pade zb_high~56

%   7. The condition number depends greatly on scaling.

%_____________________________________________
% End of Program
```

M File that Generates Controller

```
% Alex Tsai: 8/14/07
% Robust Loop Shaping followed by Robustification
% H-Infinity Algorithm: [Ref. Skogestad/Postlethwaite]

clc; clear all
%_____________________________
load Gscaled
load wc

[AA,BB,CC,DD]=ssdata(Gscaled);

%_____________________________
% Upper and Lower Admissible Bounds

s=tf('s');
wn=1*2*pi; % [1Hz] Uncertainty Bound i.e. Unmodeled Dynamics
At=wc^2/(100*wc);
Wt=(s+wc)^2/(At*(s+100*wc)); % High Frequency Weight

ee=1.e-4;
Ws=(s+.1*wc)/(2*s+ee); % Low Frequency Weight

figure(1) % Bounds and Open Loop Scaled Singular Values
w=logspace(-3,2);
sigma(Ws,'b',w); hold on; sigma(Wt^-1,'r',w);
hold on; sigma(Gscaled,'k',w); hold off
title('Upper and Lower Robust and Performance Bounds');
legend('Ws','Wt','Gscaled')
grid on

%_____________________________
% Loop Gain Dynamic Weight Wp

A=wn*ee/wc; B=10^(100/20); A=A*B; C=10^(-45/20);
A=A*C; A=A*10^(-20/20); A=A*10^(-40/20);

Wp=A*(s+.02*wc)/((s+ee)^2*(s+.051*wn)^2);
```

```
Wp=Wp*eye(3);
L=1*Gscaled*Wp;

%_____________________________
% Pre-Compensator Weight W1 [Ref. Glad/Ljung]

Gf=evalfr(L,.41*wc);
[U,S,V]=svd(Gf);

p1=1; p2=3;
alpha=(S(p1,p1)-S(p2,p2))/S(p2,p2);
W1a=eye(3)+alpha*V(:,p2)*V(:,p2)';

W11=Wp*W1a;
[x1,x2,x3,x4]=ssdata(W11);

%_____________________________
% Compensated Loop Gain

L=L*W1a;

figure(2) % Pre-Compensating Gscaled
w=logspace(-5,1);
sigma(Ws,'b',w); hold on; sigma(Wt^-1,'r',w); hold on; sigma(L,'k',w); hold off
title('Compensated System'); legend('Ws','Wt','G*Wp')
grid on

figure(3) % Sensitivity Function
S=inv(eye(3)+L);
sigma(S,'b'); title('Compensated Sensitivity Function SV'); grid on

figure(4) % Complementary Sensitivity Function
T=eye(3)-S;
sigma(T,'b'); title('Co-Sensitivity Function SV'); grid on

% _____________________________
% H-Infinity Controller Algorithm [Ref. Skogestad/Postlethwaiste]

[a,b,c,d]=ssdata(L);
gamrel=1.1;
[Ac,Bc,Cc,Dc,gammin] = coprimeunc(a,b,c,d,gamrel);

%_____________________________
% H-Infinity Controller Algorithm [Ref. Glad/Ljung]

Ar1=a'; Br1=c'; Qr1=b*b';
[X,L1,G1,report1]=care(Ar1,Br1,Qr1);
Ar2=a; Br2=b; Qr2=c'*c;
[Z,L2,G2,report2]=care(Ar2,Br2,Qr2);

lam=max(eig(X*Z));
al=1.1;
gam=al*sqrt(1+lam);
R=eye(size(X*Z))-(1/(gam^2))*(eye(size(X*Z))+Z*X);
Lc=Br2'*X;
K=inv(R)*Z*Br1;
```

```
Ke=K; Kc=Lc;

%_____________________________________
% Constant Pre-Filter Matrix: Evaluated at Steady State

[Knum1,Kden1]=ss2tf(Ac,Bc,Cc,Dc,1);
[Knum2,Kden2]=ss2tf(Ac,Bc,Cc,Dc,2);
[Knum3,Kden3]=ss2tf(Ac,Bc,Cc,Dc,3);

Gcnum={[Knum1(1,:)] [Knum2(1,:)] [Knum3(1,:)];...
      [Knum1(2,:)] [Knum2(2,:)] [Knum3(2,:)];...
      [Knum1(3,:)] [Knum2(3,:)] [Knum3(3,:)]};

Gcden={[Kden1] [Kden2] [Kden3];...
      [Kden1] [Kden2] [Kden3];...
      [Kden1] [Kden2] [Kden3]};

KKc=tf(Gcnum,Gcden); % Transfer Function Matrix
Kzc=evalfr(KKc,0); % Controller/Filter Kc(0)

%_____________________________________________
% Disturbance Model Gd

% Input No.5: LB - Load Bank
g15=zpk([-.022 -.3 -1.5],[-.043 -.071 -1 -3.5 -3.5],.048,'iodelay',1.59);
g45=zpk([],[-.15 -.15],.071,'iodelay',5.9);
g55=zpk([-.02],[-.04 -.06],21.339,'iodelay',.153);

% Input No.4: PV - Fuel Valve
g14=zpk([-.022 -.3],[-.033 -.061 -1 -4],.041,'iodelay',1.38);
g44=zpk([-.054 -.054],[-.085 -.085 -.53 -.53],2.201,'iodelay',.18);
g54=zpk([-.03 -3],[-.04 -.07],17.495,'iodelay',.2);

Gdd=[g14 g15;g44 g45;g54 g55]; % Disturbance Plant

% Scaling Factors
dL=1; dm=.3; dTIT=50; dS=1500; dPV=1;
post3=diag([dPV dL]);
pre3=diag([dm dTIT dS]);

Gddscaled=inv(pre3)*Gdd*post3; % Scaled Disturbance Matrix
Gddscaled=pade(Gddscaled);

[ALL,BLL,CLL,DLL]=ssdata(Gddscaled);

%_____________________________________
% End of Program
```

M-File that Generates Co-Prime Solution [Ref.Skogestad/Postlewaite]

```
%function [Ac,Bc,Cc,Dc,gammin] = coprimeunc(a,b,c,d,gamrel)
%
% Finds the controller which optimally robustifies a given
% shaped plant in terms of tolerating maximum coprime uncertainty.
% Used in the McFarlane-Glover H-infinity loopshaping procedure.
```

```
% --- Uses the robust control toolbox ---
%
%    a,b,c,d:     State-space description of (shaped) plant
%    gamrel:      Final gamma used is gamrel*gammin [default: gamrel=1.1]
%    Ac,Bc,Cc,Dc: State-space description of "robustifying" controller
%                 assuming positive feedback
%
% Copyright 1996-2003 Sigurd Skogestad & Ian Postlethwaite

% $Id: coprimeunc.m,v 1.2 2004/04/15 08:10:13 vidaral Exp $

function [Ac,Bc,Cc,Dc,gammin] = coprimeunc(a,b,c,d,gamrel)
if nargin <4,
  disp('usage:  [Ac,Bc,Cc,Dc] = coprimeunc(a,b,c,d,gamrel)'); return; end
if nargin <5, gamrel=1.1; end

% Find Normalized Coprime factors of the shaped plant
S=eye(size(d'*d))+d'*d;
R=eye(size(d*d'))+d*d';
Rinv=inv(R);Sinv=inv(S);

A1 = (a-b*Sinv*d'*c); R1 =S; B1=b; Q1 = c'*Rinv*c;
[X,XAMP,G,REP]=care(A1,B1,Q1,R1);
if REP == -1
   disp('The Hamiltonian matrix has jw-axis eigenvalues')
elseif REP == -2
   disp('There is no finite stabilizing solution X')
else
   sprintf('X: Frobenius norm of relative residual= %0.5g',REP)
end

A2 = A1'; Q2 = b*Sinv*b'; B2=c'; R2 = R;
[Z,ZAMP,G,REP]=care(A2,B2,Q2,R2);
if REP == -1
   disp('The Hamiltonian matrix has jw-axis eigenvalues')
elseif REP == -2
   disp('There is no finite stabilizing solution X')
else
   sprintf('Z: Frobenius norm of relative residual= %0.5g',REP);
end

% display optimal gamma
XZ = X*Z; gammin=sqrt(1+max(eig(XZ)))

% Use higher gamma
gam=gamrel*gammin; gam2 = gam*gam; gamconst = (1-gam2)*eye(size(XZ));
Lc = gamconst + XZ; Li = inv(Lc'); Fc = -Sinv*(d'*c+b'*X);
Ac = a + b*Fc + gam2*Li*Z*c'*(c+d*Fc);
Bc = gam2*Li*Z*c';
Cc = b'*X;
Dc = -d';
%---------------------------------------------------------------------
```

M-File that Compares Open Loop TF Step Response with Data

```
% Alex Tsai: 9/1/07
```

```
% Step Data for Comparison with Transfer Function Matrix
% Open Loop Step Response: Test Date 8/3/06, pg.4 PV = 39 to 41%

clc; clear all
load mdot
load TIT
load speed

% Simulink Run Workspace Values: g14
mdot_y=mdot.signals.values; mdot_y=mdot_y+1.12;
mdot_time=mdot.time;

TIT_y=TIT.signals.values; TIT_y=TIT_y+703;
speed_y=speed.signals.values; speed_y=speed_y+40120;

g14=zpk([-.022 -.3],[-.033 -.061 -1 -4],.041,'iodelay',1.38);
g44=zpk([-.054 -.054],[-.085 -.085 -.53 -.53],2.201,'iodelay',.18);
g54=zpk([-.03 -3],[-.04 -.07],17.495,'iodelay',.2);

% PV Step Input - [2%] : Note: CA was 34% Opened

%_____________________________
% FT380 = Fuel Cell Mdot

subplot(3,1,1)
FT380_mfc=dlmread('PVstepFT380.txt');
time_v=FT380_mfc(:,1);
FT380_v=FT380_mfc(:,2);

plot(time_v./60,FT380_v,'k'); hold on
plot(mdot_time./60,mdot_y); hold off; grid on
title('FT380 Response to PV432 2% Open Loop Step')
xlim([0 time_v(length(time_v))/60])
ylim([1.1 1.2])
ylabel('m dot [kg/s]')

mdotss=1.165; % From Test Data
error_mdot=(mdot_y(length(mdot_y))-mdotss)/mdotss;

%_____________________________
% TE350 = Turbine Inlet Temperature

subplot(3,1,2)
TIT_T=dlmread('PVstepTE350.txt');
time_v=TIT_T(:,1);
TE350_v=TIT_T(:,2);

plot(time_v./60,TE350_v,'k'); hold on
plot(mdot_time./60,TIT_y); hold off; grid on
title('TE350 Response to PV432 2% Open Loop Step')
xlim([0 time_v(length(time_v))/60])
ylabel('TIT [C]')

TITss=711; % From Test Data
error_TIT=(TIT_y(length(TIT_y))-TITss)/TITss;
```

```
%_____________________________
% S502A = Turbine Speed

subplot(3,1,3)
S502A=dlmread('PVstepS502.txt');
time_v=S502A(:,1);
S502_v=S502A(:,2);

plot(time_v./60,S502_v,'k'); hold on
plot(mdot_time./60,speed_y); hold off; grid on
title('S502A Response to PV432 2% Open Loop Step')
xlim([0 time_v(length(time_v))/60])
xlabel('Time [min]')
ylabel('Speed [rpm]')

speedss=41030; % From Test Data
error_speed=(speed_y(length(speed_y))-speedss)/speedss;

% Notes:
%   1.  The step is from 39%-41%. If problems arise with the model, use
%       these limits instead
%   2.  To acquire all the data, must run the Simulink file 'StepResponse',
%       save the corresponding Workspace output variables on the MatLab
%       workspace, and then run this mfile.
%   3.  Need to verify the speed transfer function in generated Bode file
%   4.  The zpk gain of the speed TF was changed from -17 to -40. There was
%       a better fit of the step response.

%_____________________________
% End of Program


% Alex Tsai: 9/1/07
% Step Data for Comparison with Transfer Function Matrix
% Open Loop Step Response: Test Date 12/15/05, pg.4 CA = 45 to 42%

clc; clear all
% Loading Simulink Workspace Output Variables
load mdotCA
load TITCA
load speedCA

% Simulink Run Workspace Values: g14
mdot_y=mdotCA.signals.values; mdot_y=mdot_y+1;
mdot_time=mdotCA.time;

TIT_y=TITCA.signals.values; TIT_y=TIT_y+662;
speed_y=speedCA.signals.values; speed_y=speed_y+40400;

% Equations that need to be Inserted in Simulink, from Pade Approx.
g12=zpk([-.085],[-.08 -1.91],.032,'iodelay',.51);
g42=zpk([],[-.32 -1.1],.788,'iodelay',.125);
g52=zpk([roots([1 7.5e-3 .0056])'],[-.077 -.082 -2],26.682,'iodelay',.66);

% CA Step Input Decrement - [3%]
```

```
%_____________________________
% FT380 = Fuel Cell Mdot

subplot(3,1,1)
FT380_mfc=dlmread('CAstepFT380.txt');
time_v=FT380_mfc(:,1);
FT380_v=FT380_mfc(:,2);

plot(time_v./60,FT380_v,'k'); hold on
plot(mdot_time./60,mdot_y); hold off; grid on
title('FT380 Response to ZC170 3% Open Loop Step Decrement')
xlim([0 time_v(length(time_v))/60])
ylabel('m dot [kg/s]')

mdotss=1.06; % From Test Data
error_mdot=(mdot_y(length(mdot_y))-mdotss)/mdotss;

%_____________________________
% TE350 = Turbine Inlet Temperature

subplot(3,1,2)
TIT_T=dlmread('CAstepT350.txt');
time_v=TIT_T(:,1);
TE350_v=TIT_T(:,2);

plot(time_v./60,TE350_v,'k'); hold on
plot(mdot_time./60,TIT_y); hold off; grid on
title('TE350 Response to ZC170 3% Open Loop Step Decrement')
xlim([0 time_v(length(time_v))/60])
ylabel('TIT [C]')

TITss=667; % From Test Data
error_TIT=(TIT_y(length(TIT_y))-TITss)/TITss;

%_____________________________
% S502A = Turbine Speed

subplot(3,1,3)
S502A=dlmread('CAstepS502.txt');
time_v=S502A(:,1);
S502_v=S502A(:,2);

plot(time_v./60,S502_v,'k'); hold on
plot(mdot_time./60,speed_y); hold off; grid on
title('S502A Response to ZC170 3% Open Loop Step Decrement')
xlim([0 time_v(length(time_v))/60])
xlabel('Time [min]')
ylabel('Speed [rpm]')

speedss=40400; % From Test Data
error_speed=(speed_y(length(speed_y))-speedss)/speedss;

% Notes:
%   1.  The step is from 45%-42%. If problems arise with the model, use
%       these limits instead
%   2.  To acquire all the data, must run the Simulink file 'StepResponse',
```

```
%       save the corresponding Workspace output variables on the MatLab
%       workspace, and then run this mfile.
%   3.  Need to verify the speed transfer function in generated Bode file
%   4.  The step decrement plot of the CA command is also in txt format
%   5.  There seems to be a lot of SNR. Find this value. The sampling
%       frequency is 25Hz or 0.04sec


%_____________________________________
% End of Program

% Alex Tsai: 9/1/07
% Step Data for Comparison with Transfer Function Matrix
% Open Loop Step Response: Test Date 1/12/06, pg.4 HA = 33 to 37%

clc; clear all
% Loading Simulink Workspace Output Variables
load mdotHA
load TITHA
load speedHA

% Simulink Run Workspace Values: g14
mdot_y=mdotHA.signals.values; mdot_y=mdot_y+.945;
mdot_time=mdotHA.time;

TIT_y=TITHA.signals.values; TIT_y=TIT_y+777.5;
speed_y=speedHA.signals.values; speed_y=speed_y+40450;

% Equations that need to be Inserted in Simulink, from Pade Approx.
g13=zpk([-.7],[-.91 -2.5],.04,'iodelay',.77);
g43=zpk([],[-.2 -2],.357,'iodelay',.22);
g53=zpk([-.03],[-.06 -.09],2.543,'iodelay',.85);

% HA Step Input Increment - [4%]

%_____________________________________
% FT380 = Fuel Cell Mdot

subplot(3,1,1)
FT380_mfc=dlmread('HAstepFT380.txt');
time_v=FT380_mfc(:,1);
FT380_v=FT380_mfc(:,2);

plot(time_v./60,FT380_v,'k'); hold on
plot(mdot_time./60,mdot_y); hold off; grid on
title('FT380 Response to ZC380 4% Open Loop Step')
xlim([0 time_v(length(time_v))/60])
ylabel('m dot [kg/s]')

mdotss=1.165; % From Test Data
error_mdot=(mdot_y(length(mdot_y))-mdotss)/mdotss;

%_____________________________________
% TE350 = Turbine Inlet Temperature

subplot(3,1,2)
```

```
TIT_T=dlmread('HAstepT350.txt');
time_v=TIT_T(:,1);
TE350_v=TIT_T(:,2);

plot(time_v./60,TE350_v,'k'); hold on
plot(mdot_time./60,TIT_y); hold off; grid on
title('TE350 Response to ZC380 4% Open Loop Step')
xlim([0 time_v(length(time_v))/60])
ylabel('TIT [C]')

TITss=711; % From Test Data
error_TIT=(TIT_y(length(TIT_y))-TITss)/TITss;

%_____________________________
% S502A = Turbine Speed

subplot(3,1,3)
S502A=dlmread('HAstepS502A.txt');
time_v=S502A(:,1);
S502_v=S502A(:,2);

plot(time_v./60,S502_v,'k'); hold on
plot(mdot_time./60,speed_y); hold off; grid on
title('S502A Response to ZC380 4% Open Loop Step')
xlim([0 time_v(length(time_v))/60])
xlabel('Time [min]')
ylabel('Speed [rpm]')

speedss=41030; % From Test Data
error_speed=(speed_y(length(speed_y))-speedss)/speedss;

% Notes:
%   1.  The step is from 45%-42%. If problems arise with the model, use
%       these limits instead
%   2.  To acquire all the data, must run the Simulink file 'StepResponse',
%       save the corresponding Workspace output variables on the MatLab
%       workspace, and then run this mfile.
%   3.  Need to verify the speed transfer function in generated Bode file
%   4.  The step decrement plot of the HA command is also in txt format
%   5.  The step increase in HA is really a step decrease in Simulink,
%       since opening the valve, reduces the flow to the fuel cell.
%_____________________________
% End of Program
```

M-File that Generates Controller Plots of Simulink Control Configuration

```
% Alex Tsai: 9/3/07
% Simulink Control Diagram Plots

clc; clear all

load outputstates
load actuators

%_____________________________
% Output State Plot
```

```
outputvalues=outputstates.signals.values;
outputtime=outputstates.time;

mdotvalue=outputvalues(:,1);
TITvalue=outputvalues(:,2);
speedvalue=outputvalues(:,3);

figure(1)
subplot(3,1,1)
plot(outputtime./60,mdotvalue); title('Compensated Ref Tracking: Simult Steps')
ylabel('mdot [kg/s]-norm'); grid on
subplot(3,1,2)
plot(outputtime./60,TITvalue);
ylabel('TIT [C]-norm'); grid on
subplot(3,1,3)
plot(outputtime./60,speedvalue);
ylabel('\Omega [rpm]-norm'); grid on
xlabel('Time [min]')

% Info on the Step Response of the States
S_mdot=stepinfo(mdotvalue,outputtime,1);
S_TIT=stepinfo(TITvalue,outputtime,1);
S_speed=stepinfo(speedvalue,outputtime,1);

%_____________________________
% Actuator Plot

actuatorvalues=actuators.signals.values;
actuatortime=actuators.time;

CAvalue=actuatorvalues(:,1);
HAvalue=actuatorvalues(:,2);
PVvalue=actuatorvalues(:,3);

figure(2)
subplot(3,1,1)
plot(actuatortime./60,CAvalue); title('Compensated Ref Tracking: Simult Steps')
ylabel('CA [%]'); grid on
subplot(3,1,2)
plot(actuatortime./60,HAvalue);
ylabel('HA [%]'); grid on
subplot(3,1,3)
plot(actuatortime./60,PVvalue);
ylabel('PV [%]'); grid on
xlabel('Time [min]')

% Info on the Step Response of the Valves
S1_CA=stepinfo(CAvalue);
S1_HA=stepinfo(HAvalue);
S1_PV=stepinfo(PVvalue);

% Note: The Simulink mdl file 'AlexLast' mus be ran first, and then the
% Workspace Variables saved on the MatLab workspace. This m-file runs
% afterwards.
```

```
%_____________________________
% End of Program
```

M-File that Analyzes Robustness to Uncertainty of Plant

```
% Alex Tsai: 8/28/07
% Uncertainty Analysis: HyPer Pant

clc; clear all

%_____________________________
% Piecewise Nominal and Perturbed Transfer Functions

% CA - Cold Air Bypass Valve

% Nominal Unperturbed TF:
 g12=zpk([-.085],[-.08 -1.91],.032,'iodelay',.51);
% g42=zpk([],[-.32 -1.1],.788,'iodelay',.125);
 g52=zpk([roots([1 7.5e-3 .0056])'],[-.077 -.082 -2],26.682,'iodelay',.66);
g12=pade(g12);
% g42=pade(g42);
g52=pade(g52);

% Perturbed TF: g12
% p=10; per='percentage';
% z12a=ureal('z12a',.085,'per',p); z12b=ureal('z12b',-3.922,'per',p);
% p12a=ureal('p12a',.08,'per',p); p12b=ureal('p12b',1.91,'per',p);
% p12c=ureal('p12c',3.922,'per',p);
%
% g12=tf(-.032*[1 (z12a+z12b) (z12a*z12b)],...
%     [1 (p12a+p12b+p12c) (p12a*p12c + p12b*p12c + p12a*p12b) (p12a*p12b*p12c)]);

% Perturbed TF: g42
p=10; per='percentage';
z42a=ureal('z42a',-16,'per',p);
p42a=ureal('p42a',.32,'per',p); p42b=ureal('p42b',1.1,'per',p);
p42c=ureal('p42c',16,'per',p);

g42=tf(-.788*[1 z42a],...
   [1 (p42a+p42b+p42c) (p42a*p42c + p42b*p42c + p42a*p42b) (p42a*p42b*p42c)]);

% Perturbed TF: g52
% p52=p;
% z52a=ureal('z52a',-3.03,'per',p52); p52a=ureal('p52a',.077,'per',p52);
% p52b=ureal('p52b',.082,'per',p52); p52c=ureal('p52c',2,'per',p52);
% p52d=ureal('p52d',3.03,'per',p52);
%
% A52=p52a+p52b+p52c;
% B52=p52a*p52c + p52b*p52c + p52a*p52b;
% C52=p52a*p52b*p52c;
% g52=tf(-26.682*[1 (z52a+.0075) (z52a*.0075+.0056) (z52a*.0056)],...
%     [1 (A52+p52d) (B52+A52*p52d) (C52+B52*p52d) (C52*p52d)]);

% HA - Hot Air Bypass Valve

% Nominal Unperturbed TF:
```

```
g13=zpk([-.7],[-.91 -2.5],.04,'iodelay',.77);
g43=zpk([],[-.2 -2],.357,'iodelay',.22);
g53=zpk([-.03],[-.06 -.09],2.543,'iodelay',.85);
g13=pade(g13);
g43=pade(g43);
g53=pade(g53);

% % Perturbed TF: g13
% z13a=ureal('z13a',.75,'per',p); z13b=ureal('z13b',-2.597,'per',p);
% p13a=ureal('p13a',.91,'per',p); p13b=ureal('p13b',2.5,'per',p);
% p13c=ureal('p13c',2.597,'per',p);
%
% g13=tf(-.04*[1 (z13a+z13b) (z13a*z13b)],...
%     [1 (p13a+p13b+p13c) (p13a*p13c + p13b*p13c + p13a*p13b) (p13a*p13b*p13c)]);

% % Perturbed TF: g43
% z43a=ureal('z43a',-9.091,'per',p);
% p43a=ureal('p43a',.2,'per',p);
% p43b=ureal('p43b',2,'per',p);
% p43c=ureal('p43c',9.091,'per',p);
%
% g43=tf(-.357*[1 z43a],...
%     [1 (p43a+p43b+p43c) (p43a*p43c + p43b*p43c + p43a*p43b) (p43a*p43b*p43c)]);

% % Perturbed TF: g53
% z53a=ureal('z53a',.03,'per',p); z53b=ureal('z53b',-2.353,'per',p);
% p53a=ureal('p53a',.06,'per',p); p53b=ureal('p53b',.09,'per',p);
% p53c=ureal('p53c',2.353,'per',p);
%
% g53=tf(-2.543*[1 (z53a+z53b) (z53a*z53b)],...
%     [1 (p53a+p53b+p53c) (p53a*p53c + p53b*p53c + p53a*p53b) (p53a*p53b*p53c)]);

% PV - Fuel Valve

% Nominal Unperturbed TF:
g14=zpk([-.022 -.3],[-.033 -.061 -1 -4],.041,'iodelay',1.38);
g44=zpk([-.054 -.054],[-.085 -.085 -.53 -.53],2.201,'iodelay',.18);
g54=zpk([-.03 -3],[-.04 -.07],17.495,'iodelay',.2);
g14=pade(g14);
g44=pade(g44);
g54=pade(g54);

% % Perturbed TF: g14
% z14a=ureal('z14a',.022,'per',p); z14b=ureal('z14b',.3,'per',p);
% z14c=ureal('z14c',-1.449,'per',p); p14a=ureal('p14a',.033,'per',p);
% p14b=ureal('p14b',.061,'per',p); p14c=ureal('p14c',1,'per',p);
% p14d=ureal('p14d',1.449,'per',p);
%
% A14=p14a+p14b+p14c;
% B14=p14a*p14c + p14b*p14c + p14a*p14b;
% C14=p14a*p14b*p14c;
% g14=tf(-.041*[1 (z14a+z14b+z14c) (z14a*z14c + z14b*z14c + z14a*z14b) (z14a*z14b*z14c)],...
%     [1 (A14+p14d) (B14+A14*p14d) (C14+B*p14d) (C14*p14d)]);

% % Perturbed TF: g44
% z44a=ureal('z44a',.054,'per',p); z44b=z44a;
```

```
% z44c=ureal('z44c',-11.11,'per',p); p44a=ureal('p44a',.085,'per',p); p44b=p44a;
% p44c=ureal('p44c',.53,'per',p); p44d=p44c; p44f=ureal('p44f',11.11,'per',p);
%
% A44=p44a+p44b+p44c;
% B44=p44a*p44c + p44b*p44c + p44a*p44b;
% C44=p44a*p44b*p44c;
% H44=A44+p44d;
% M44=B44+A44*p44d;
% N44=C44+B44*p44d;
% O44=C44*p44d;
% g44=tf(-2.201*[1 (z44a+z44b+z44c) (z44a*z44c + z44b*z44c + z44a*z44b) (z44a*z44b*z44c)],...
%     [1 (H44+p44f) (M44+p44f*H44) (N44+p44f*M44) (O44+p44f*N44) (p44f*O44)]);

% % Perturbed TF: g54
% z54a=ureal('z54a',.03,'per',p);
% z54b=ureal('z54b',-10,'per',p);
% p54a=ureal('p54a',.04,'per',p);
% p54b=ureal('p54b',.07,'per',p);
% p54c=ureal('p54c',10,'per',p);
%
% g54=tf(-17.495*[1 (z54a+z54b) (z54a*z54b)],...
%     [1 (p54a+p54b+p54c) (p54a*p54c + p54b*p54c + p54a*p54b) (p54a*p54b*p54c)]);

%_____________________________
% Disturbed Plant

Gp=[g12 g13 g14;...
   g42 g43 g44;...
   g52 g53 g54];

%_____________________________
% Scaled Plant

dm=0.3; dTIT=50; dS=1500; dCA=10; dHA=10; dPV=1;
post=diag([dCA dHA dPV]); pre=diag([dm dTIT dS]);

Gscaled=inv(pre)*Gp*post;
Gnom=Gscaled;

lfu=.05; % Low Frequency Uncertainty Percent: x100=[%] i.e. 5%
hfu=10; % High Frequency Uncertainty Percent i.e. 1000%

%_____________________________
% Including Actuator Dynamics as Uncertainty Parameters

wca=2.2; wha=1.26; pv=20; % Actuator Bandwidth: CA,HA,PV
Wca=makeweight(lfu,wca,hfu);
Wha=makeweight(lfu,wha,hfu);
Wpv=makeweight(lfu,pv,hfu);
del1=ultidyn('del1',[1 1]);
del2=ultidyn('del2',[1 1]);
del3=ultidyn('del3',[1 1]);
Gunc=Gnom*blkdiag(1+Wca*del1,1+Wha*del2,1+Wpv*del3);

load Ac Bc Cc Dc
load x1 x2 x3 x4
```

```
load Kzc

sysK=ss(Ac,Bc,Cc,Dc); % Robust Controller
sysPreC=ss(x1,x2,x3,x4); % Pre-Compensator
sysPreF=Kzc; % Pre-Filter

feedF=Gunc*sysPreC; % FeedForward Path
feedB=feedback(feedF,sysK,+1); % Feedback Path
sysCL=-Kzc*feedB; % Feedback + Pre-Compensator

figure(1)
step(sysCL); % title({'MIMO Step Response';''})

% Use the Below Commands for the Simulink Response
% figure(2)
% [ax,bx,cx,dx]=ssdata(sysCL);
% [y,x,t] = step(ax,bx,cx,dx,1);
% S=stepinfo(y,t,1);

%_____________________________
% A: Robustness Analysis: For Inclusion of Actuator Dyanmics

[stabmarg,destabu,report]=robuststab(sysCL);

% % Output Sensitivity of Uncertain System
%
% sysSen=feedback(sysK,feedF,+1);
% [maxgain,wcu]=wcgain(sysSen);
%
% figure(2)
% bodemag(sysSen.NominalValue,'b',usubs(sysSen,wcu),'r');
%
% % Closed Loop Analysis: Transmission of disturbances from plant I/O
%
% F=loopsens(feedF,-sysK);
%
% figure(3)
% bodemag(F.PSi,{1e-4 100}); title('I/O Plant Disturbance Transmission');
%
% [stabmargx,destabux,reportx]=robuststab(F.So); % Repeat for F.So
%
% figure(4)
% bodemag(F.So.NominalValue,{1e-4 100}) % Worst Case Gain Analysis
%
% [PeakNom,Freq]=norm(F.So.NominalValue,'inf');
% [maxgainS,wcuS]=wcgain(F.So);
%
% figure(5)
% step(F.To.NominalValue,usubs(F.To,wcuS));
% title('Worst Case Step Response');

%_____________________________
% B: Robustness Analysis: Unstructured Uncertainty

% wwc=1*2*pi; % Weight Cross Over Frequency
% W=makeweight(lfu,wwc,hfu);
```

```
% no_out=3; no_in=3; % Number of Outputs, Inputs
% pu=1; % Percent Uncertainty
% delta=ultidyn('delta',[no_out no_in],'Bound',pu);
% I=eye(size(Gnom));
% Gunc=Gnom*(I+W*delta); % Uncertain Plant
% % load Ac Bc Cc Dc
% load x1 x2 x3 x4
% load Kzc
%
% sysK=ss(Ac,Bc,Cc,Dc); % Robust Controller
% sysPreC=ss(x1,x2,x3,x4); % Pre-Compensator
% sysPreF=Kzc; % Pre-Filter
%
% feedF=Gunc*sysPreC;
% feedB=feedback(feedF,sysK,+1);
% sysCL=-Kzc*feedB;
%
% step(sysCL);
%
% [stabmarg,destabu,report]=robuststab(sysCL);
%
% % Output Sensitivity of Uncertain System
%
% sysSen=feedback(sysK,feedF,+1);
% [maxgain,wcu]=wcgain(sysSen);
%
% figure(2)
% bodemag(sysSen.NominalValue,'b',usubs(sysSen,wcu),'r');
%
% % Closed Loop Analysis: Transmission of disturbances from plant I/O
%
% F=loopsens(feedF,-sysK);
%
% figure(3)
% bodemag(F.PSi,{1e-4 100}); title('I/O Plant Disturbance Transmission');
%
% [stabmargx,destabux,reportx]=robuststab(F.So); % Repeat for F.So
%
% figure(4)
% bodemag(F.So.NominalValue,{1e-4 100}) % Worst Case Gain Analysis
%
% [PeakNom,Freq]=norm(F.So.NominalValue,'inf');
% [maxgainS,wcuS]=wcgain(F.So);
%
% figure(5)
% step(F.To.NominalValue,usubs(F.To,wcuS));
% title('Worst Case Step Response');
%_____________________________
% % Notes:
% %   1. The code tests range of uncertainty for poles/zeros at various
% %   transfer function combinations.
% %   2. The peturbed transfer functions have added poles/zeros
% %   corresponding to the pade approximation. See Note on 'Ub.m'
% %_____________________________
% % End of Program
```

Appendix F

Woodward GAP Programming Sheet

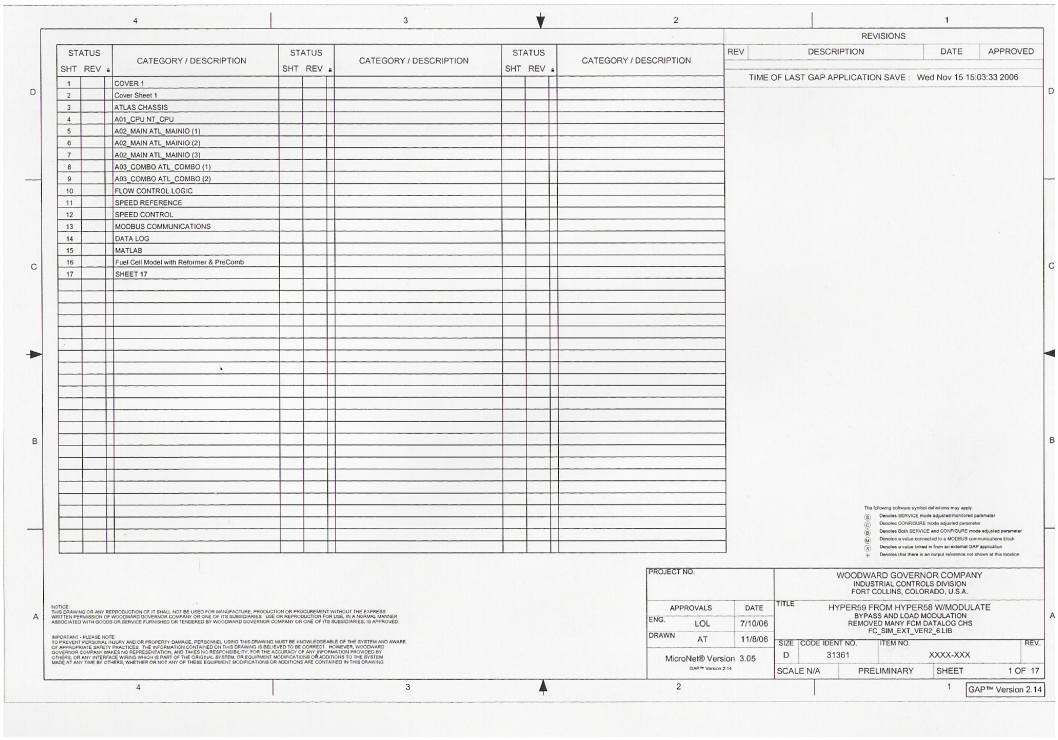

STATUS SHT	REV	CATEGORY / DESCRIPTION	STATUS SHT	REV	CATEGORY / DESCRIPTION	STATUS SHT	REV	CATEGORY / DESCRIPTION
1		COVER 1						
2		Cover Sheet 1						
3		ATLAS CHASSIS						
4		A01_CPU NT_CPU						
5		A02_MAIN ATL_MAINIO (1)						
6		A02_MAIN ATL_MAINIO (2)						
7		A02_MAIN ATL_MAINIO (3)						
8		A03_COMBO ATL_COMBO (1)						
9		A03_COMBO ATL_COMBO (2)						
10		FLOW CONTROL LOGIC						
11		SPEED REFERENCE						
12		SPEED CONTROL						
13		MODBUS COMMUNICATIONS						
14		DATA LOG						
15		MATLAB						
16		Fuel Cell Model with Reformer & PrxComb						
17		SHEET 17						

REVISIONS

REV	DESCRIPTION	DATE	APPROVED

TIME OF LAST GAP APPLICATION SAVE : Wed Nov 15 15:03:33 2006

APPROVALS	DATE
ENG. LOL	7/10/06
DRAWN AT	11/8/06

PROJECT NO.

WOODWARD GOVERNOR COMPANY
INDUSTRIAL CONTROLS DIVISION
FORT COLLINS, COLORADO, U.S.A.

TITLE: HYPER59 FROM HYPER58 W/MODULATE BYPASS AND LOAD MODULATION REMOVED MANY FCM DATALOG CHS FC_SIM_EXT_VER2_6.LIB

MicroNet® Version 3.05

SIZE	CODE IDENT NO.	ITEM NO.	REV.
D	31361	XXXX-XXX	

SCALE N/A | PRELIMINARY | SHEET 1 OF 17

GAP™ Version 2.14

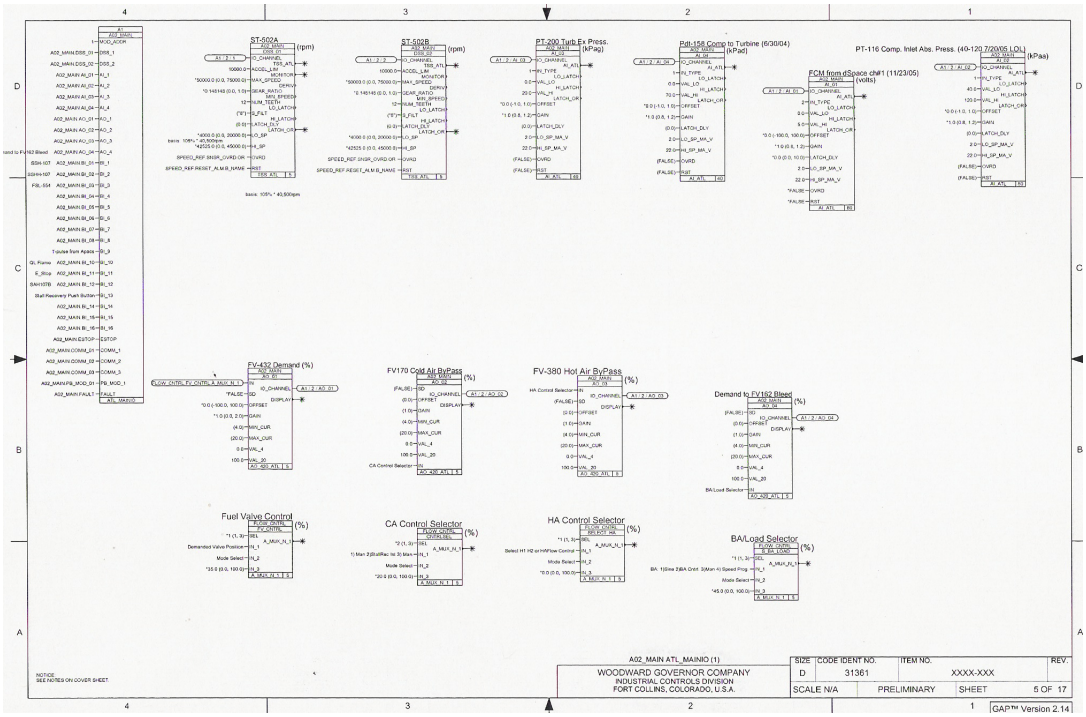

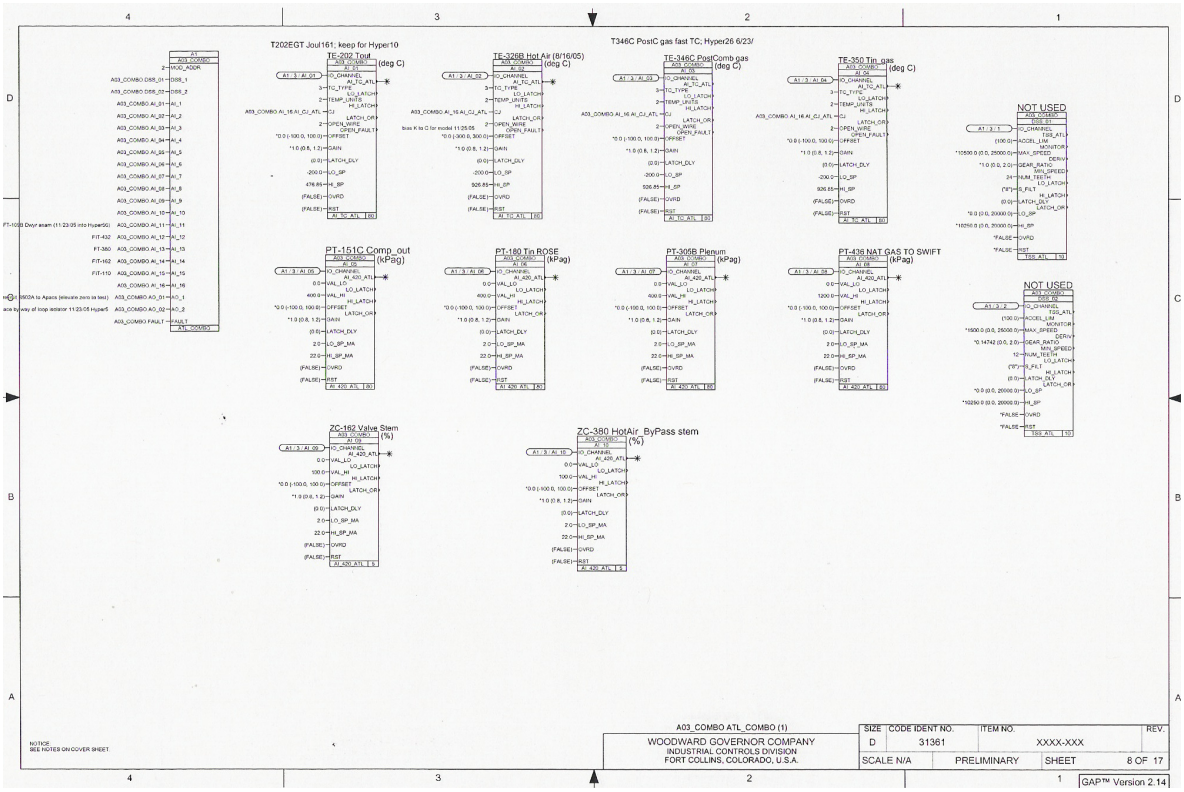
T202EGT Jou161; keep for Hyper10
TE-202 Tout
(deg C)
T346C PostC gas fast TC; Hyper26 6/23/
TE-346C PostComb gas
(deg C)
TE-326B Hot Air (8/16/05)
(deg C)
TE-350 Tin_gas
(deg C)
NOT USED
PT-151C Comp_out
(kPag)
PT-180 Tin ROSE
(kPag)
PT-306B Plenum
(kPag)
PT-436 NAT GAS TO SWIFT
(kPag)
NOT USED
ZC-162 Valve Stem
(%)
ZC-380 HotAir_ByPass stem
(%)
A03_COMBO ATL_COMBO (1)
WOODWARD GOVERNOR COMPANY
INDUSTRIAL CONTROLS DIVISION
FORT COLLINS, COLORADO, U.S.A.
SIZE D
CODE IDENT NO. 31361
ITEM NO. XXXX-XXX
REV.
SCALE N/A
PRELIMINARY
SHEET 8 OF 17
NOTICE
SEE NOTES ON COVER SHEET.
GAP™ Version 2.14

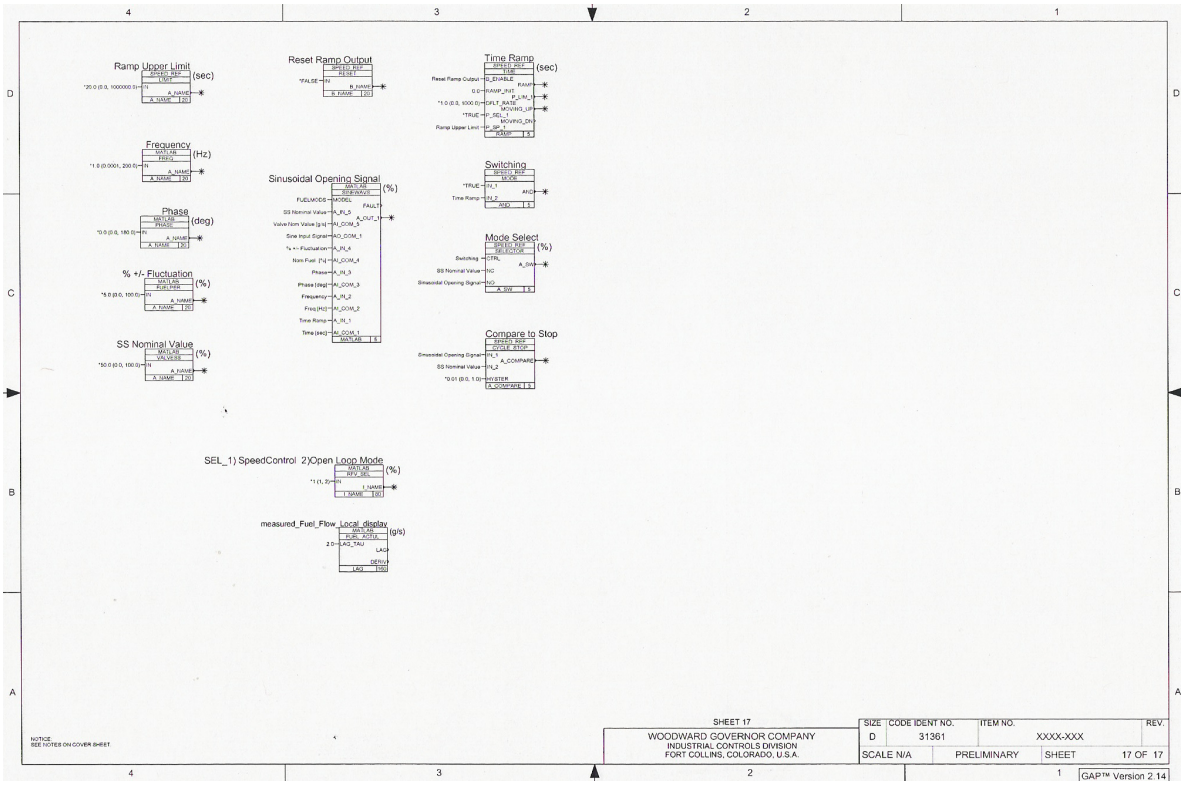
Ramp Upper Limit
(sec)
Reset Ramp Output
Time Ramp
(sec)
Frequency
(Hz)
Switching
Phase
(deg)
Sinusoidal Opening Signal
(%)
% +/- Fluctuation
(%)
Mode Select
(%)
SS Nominal Value
(%)
Compare to Stop
SEL_1) SpeedControl 2)Open Loop Mode
(%)
measured_Fuel_Flow_Local_display
(g/s)
SHEET 17
WOODWARD GOVERNOR COMPANY
INDUSTRIAL CONTROLS DIVISION
FORT COLLINS, COLORADO, U.S.A.
SIZE D
CODE IDENT NO. 31361
ITEM NO. XXXX-XXX
REV.
SCALE N/A
PRELIMINARY
SHEET 17 OF 17
NOTICE
SEE NOTES ON COVER SHEET.
GAP™ Version 2.14

Appendix G

HYPER Test Plan and Check List
August 25 2006

Purpose: The purpose of the startup test is to bring the turbine up to the operational steady state nominal speed of 40,500rpm, with all valves closed at 45kW electrical load.

The purpose of the operational test is to determine the magnitude range of the fuel flow valve when the valve is fluctuated sinusoidally. This test is intended to be a scoping study in preparation for the frequency response test that follows. The fuel valve is to be fluctuated at given amplitude and frequency, for two separate chosen frequencies.

The test will ramp up the speed to the nominal value of 40,500rpm under speed control, and switch to open loop mode. At this point, the fuel valve is to be fluctuated sinusoidally, starting with a magnitude of +/-10.15% of the nominal fuel flow, corresponding to 13.5g/s i.e. 40,500rpm, and a frequency of 0.017Hz i.e. 60s period. This magnitude limit is set to avoid the lower speed limit restriction set at 38,475rpm. The magnitude percentage will be slowly increased in 1% steps, until a speed interlock warning flashes or any other interlock is activated. This test will be repeated for a frequency of 1.667Hz i.e. 0.6s period. For each case, the signal will remain at a given frequency for up to 3 periods of oscillation, before the next frequency is tested.

All Hyper states will be recorded.

Start Procedure of Startup Test (060825)

☐ ☐ **DR** Pre-Operational inspection **COMPLETE**.
☐ ☐ **DR** GAP and Watchwindows **OPEN**. Note GAP version:

☐ ☐ **AT** APACS and Atlas Clocks **SYNCHONIZED**.
☐ ☐ **AT** Live Engineering Data Spreadsheet **INITIALIZED**.

☐ ☐ **DR** Natural Gas Totalizer **RESET**.
☐ ☐ **DR** HV-414, HV-408 and HV-430 **CLOSED**.

☐ ☐ **AT** Set Gas Valve FV-432 Mode to **Auto Ramp** **(Ramp initiated at 9000rpm)**
☐ ☐ **AT** Set **All OTHER GAP Gains** to **DEFAULT** settings

☐ ☐ **DR** Set Hot Air By-Pass **FV-380** Mode to **1: Manual, 0% Open**
☐ ☐ **DR** Set Bleed Air **FV-162** Mode to **2: Manual, 100% Closed**
☐ ☐ **DR** Set Cold Air By-Pass **FV-170** Mode to **1: Manual, 0% Open**
☐ ☐ **DR** Blower **ON** (Alt-Tab)

☐ ☐ **DR** APACS Log **START**
☐ ☐ **AT** Data Log **START**

☐ ☐ **DR** HV-600 **OPEN** (Alt-Tab)

☐ ☐ **AT** System Purge **ON**
☐ ☐ **DR** FE-380 positive flow ≥ 0.10kg/s **CHECK**

☐ ☐ **DR** HV-408 and HV-430 **REQUEST OPEN**

☐ ☐ **DR** Purge Complete **CHECK**
☐ ☐ **DR** HS-460C Burner Ignition Automated at 9,000rpm **CHECK**
☐ ☐ **DR** If purge complete over 9,000rpm, HS-460A Manual Ignition **ON**
☐ ☐ **DR** TE-333 shows flame **CHECK**
☐ ☐ **DR** ST-502 > 35,000rpm, I-4 enabled **CHECK**
☐ ☐ **DR** ST-502 > 41,000rpm, HV-600 **CLOSED**
☐ ☐ **DR** Blower **OFF**

Procedure of Operational Test (060825)

☐ ☐ **AT** At 40,500rpm, verify the default rate of Time Ramp Block to be 1, **CHECK**

☐ ☐ **AT** Verify that Phase Block has input 0, %NomFuel has input 10.15% and NomFuelFlow is at 13g/s. **CHECK**

☐ ☐ **AT** Input frequency of 0.017Hz i.e. 60s period, in Frequency Block, and input multiple of 60 second times in the Ramp Upper Limit Box i.e. 1*60, 2*60, 3*60 to discretion

☐ ☐ **AT** Enable the Activate Signal Block by selecting IN to be **TRUE**

☐ ☐ **DR** Observe that the speed response and TIT temperature do not exceed operational limits

☐ ☐ **AT** Increase the %NomFuel Block by 1% and observe speed response. Repeat increasing until an interlock warning displays

☐ ☐ **AT** Disable the Activate Signal Block by selecting IN to be **FALSE**

☐ ☐ **AT** Verify that TIT and Shaft speed are stabilized at their nominal value

☐ ☐ **AT** Input frequency of 1.667Hz i.e. 0.6 s period, in the Frequency Block, and input multiple of 0.6 second times in the Ramp Upper Limit Box at discretion

☐ ☐ **AT** Enable the Activate Signal Block by selecting IN to be **TRUE**

☐ ☐ **DR** Observe that the speed response and TIT temperature do not exceed operational limits

☐ ☐ **AT** Increase the %NomFuel Block by 1% and observe speed response. Repeat increasing until an interlock warning displays

☐ ☐ **AT** Disable the Activate Signal Block by selecting IN to be **FALSE**

☐ ☐ **AT** Verify that TIT and Shaft speed are stabilized at their nominal value

System Shutdown

☐ ☐ **DR** Select GAP Speed Sheet- Set Gas Valve Mode to Automated fuel shutdown ramp.

☐ ☐ **DR** At stall or 28,000rpm, Fuel **OFF (Control #1)**

☐ ☐ **AT** Data Log **STOP, RETRIEVE, RENAME and SAVE.**

HYPER Test Plan and Check List
November 7, 2006

Purpose: The purpose of the startup test is to bring the turbine up to the operational steady state nominal speed of 40,500rpm, with all valves closed at 45kW electrical load.

The purpose of the operational test is to determine the magnitude range of all the bypass valves and the load bank when these are fluctuated sinusoidally. This test is intended to be a scoping study in preparation for the frequency response test that follows. The cold, hot and bleed air bypass valves as well as the load bank are to be fluctuated at given amplitude and frequency, for two separate chosen frequencies.

The test will ramp up the speed to the nominal value of 40,500rpm under speed control, and switch to open loop mode once the bypass valve position or load bank nominal value is set. At this point, each valve is to be fluctuated separately in a sinusoidal fashion, from the valve's 40% opened position for the CA and HA valves. The fluctuation for the load bank is to be around the offset of 45kW i.e. the operational midrange of the available load. Sinusoidal fluctuation of the BA is to have an offset of the midrange between minimum and maximum safe values as observed from valve characterization tests. This offset is found to be 14% opened with a maximum allowable fluctuation of +/- 4%. Each individual CA and HA bypass valve will be fluctuated with amplitudes of +/-5% of its above mentioned designated nominal values, increased by 5% steps until the lower speed limit restriction of 38,475rpm is reached or any other interlock is activated. The load bank will be fluctuated at +/-5kW with an increment of 1kW steps i.e. 50kW~11.1%, 55kW~22.2% of 45kW. The frequencies of oscillation under study are 0.05Hz and 0.004Hz. For each case, the signal will remain at a given frequency for up to 5 periods of oscillation, before the next frequency is tested.

All Hyper states will be recorded.

Start Procedure of Startup Test (061107)

☐ ☐ **DR** Pre-Operational inspection **COMPLETE**.
☐ ☐ **DR** GAP and Watchwindows **OPEN**. Note GAP version:

☐ ☐ **AT** APACS and Atlas Clocks **SYNCHONIZED**.
☐ ☐ **AT** Live Engineering Data Spreadsheet **INITIALIZED**.

☐ ☐ **DR** Natural Gas Totalizer **RESET**.
☐ ☐ **DR** HV-414, HV-408 and HV-430 **CLOSED**.

☐ ☐ **AT** Set Gas Valve FV-432 Mode to **Auto Ramp** **(Ramp initiated at 9000rpm)**
☐ ☐ **AT** Set **All OTHER GAP Gains** to **DEFAULT** settings

☐ ☐ **DR** Set Hot Air By-Pass **FV-380** Mode to **1: Manual, 0% Open**
☐ ☐ **DR** Set Bleed Air **FV-162** Mode to **2: Manual, 100% Closed**
☐ ☐ **DR** Set Cold Air By-Pass **FV-170** Mode to **1: Manual, 0% Open**

☐ ☐ **AT** Verify that the Fuel Valve Control, CA Control Selector, and HA Control Selector blocks SEL input is at 1.

☐ ☐ **DR** Blower **ON** (Alt-Tab)

☐ ☐ **DR** APACS Log **START**
☐ ☐ **AT** Data Log **START**

☐ ☐ **DR** HV-600 **OPEN** (Alt-Tab)

☐ ☐ **AT** System Purge **ON**
☐ ☐ **DR** FE-380 positive flow ≥ 0.10kg/s **CHECK**

☐ ☐ **DR** HV-408 and HV-430 **REQUEST OPEN**

☐ ☐ **DR** Purge Complete **CHECK**
☐ ☐ **DR** HS-460C Burner Ignition Automated at 9,000rpm **CHECK**
☐ ☐ **DR** If purge complete over 9,000rpm, HS-460A Manual Ignition **ON**
☐ ☐ **DR** TE-333 shows flame **CHECK**
☐ ☐ **DR** ST-502 > 35,000rpm, I-4 enabled **CHECK**
☐ ☐ **DR** ST-502 > 41,000rpm, HV-600 **CLOSED**

☐ ☐ **DR** Blower **OFF**

Preheat System Piping and Vessels

☐ ☐ **DT** Load Bank Cooling Fan (HS-530) **ON**
☐ ☐ **DT** Interlock 14 **ENABLED**
☐ ☐ **DT** Load Bank in Manual Mode **CHECK**
☐ ☐ **DT** Set Bleed Air By-Pass **FV-162** Mode to **2: Manual, 85% Closed**
☐ ☐ **DT** Increase load to 45kW
☐ ☐ **DT** ST-502 at approximately 40,500rpm **CHECK**
☐ ☐ **DT** Wait until TE-344 is at about 1000F **CHECK**
☐ ☐ **DT** Select Bleed Air By-Pass **FV-162** Mode to **2: Manual, 100% Closed**

☐ ☐ **AT** Data Log **STOP, RETRIEVE, RENAME, SAVE and START NEW LOG**

Stop Time:
Start Time:

☐ ☐ **DT** Wait until TE-344 is constant for 30s (+/-0.1C) **CHECK**
☐ ☐ **DT** If stall indicated, implement stall recovery

Procedure of Operational Test: CA Scoping (061107)

☐ ☐ **AT** At 40,500rpm, under speed control input 40% in the SS Valve Opening block

☐ ☐ **AT** At 40,500rpm, under speed control change the CA Control Selector SEL input from 1 to 2. Check that the Fuel Valve Control block and the HA Control Selector block SEL are both at 1. **CHECK**
☐ ☐ **AT** At 40,500rpm, switch to Open Loop Mode by inputting the Measured Fuel Flow on the Demanded Valve Position. **CHECK**
☐ ☐ **AT** Once speed is stabilized to 40,500rpm, verify the default rate of Time Ramp Block to be 1, **CHECK**
☐ ☐ **AT** Verify that Phase Block has input 0, SS Valve Opening has input 40% and % +/- Bypass Valve Opening is at 5%. **CHECK**
☐ ☐ **AT** Input frequency of 0.05Hz i.e. 20s period, in Frequency Block, and input multiple of 20 second times in the Ramp Upper Limit Box i.e. 5*20=100 second duration for 5 oscillations
☐ ☐ **AT** Enable the Switching block by selecting IN_1 to be **TRUE**

☐ ☐ **AT** Start the fluctuations by selecting TRUE in the Reset Ramp Output block. **CHECK**

☐ ☐ **DR** Observe that the speed response and TIT temperature do not exceed operational limits

☐ ☐ **AT** When Time Ramp reaches the final time, set IN_1 of Switching block to FALSE, input 0 in the Ramp Upper Limit block, and increase the DFLT rate of Time Ramp as desired. **CHECK**

☐ ☐ **AT** When Time Ramp stops, select Reset Ramp Output to FALSE, input 1 in the DFLT rate of Time Ramp and set new test time i.e. multiples of 20 seconds. **CHECK**

☐ ☐ **AT** Increase the %+/- Bypass Valve Opening input by 5%, **CHECK**

☐ ☐ **AT** Repeat last 10 steps until operational limits are exceeded either on speed or TIT temperature.

☐ ☐ **AT** Repeat last 11 steps for a frequency of 0.004Hz.

☐ ☐ **AT** Switch back to speed control, **CHECK**

☐ ☐ **AT** Input 1 in the CA Control Selector block, **CHECK**

Procedure of Operational Test: HA Scoping (061107)

☐ ☐ **AT** At 40,500rpm, under speed control input 40% in the SS Valve Opening block

☐ ☐ **AT** At 40,500rpm, under speed control change the HA Control Selector SEL input from 1 to 2. Check that the Fuel Valve Control block and the CA Control Selector block SEL are both at 1. **CHECK**

☐ ☐ **AT** At 40,500rpm, switch to Open Loop Mode by inputting the Measured Fuel Flow on the Demanded Valve Position. **CHECK**

☐ ☐ **AT** Once speed is stabilized to 40,500rpm, verify the default rate of Time Ramp Block to be 1, **CHECK**

☐ ☐ **AT** Verify that Phase Block has input 0, SS Valve Opening has input 40% and % +/- Bypass Valve Opening is at 5%. **CHECK**

☐ ☐ **AT** Input frequency of 0.05Hz i.e. 20s period, in Frequency Block, and input multiple of 20 second times in the Ramp Upper Limit Box i.e. 5*20=100 second duration for 5 oscillations

☐ ☐ **AT** Enable the Switching block by selecting IN_1 to be **TRUE**

☐ ☐ **AT** Start the fluctuations by selecting TRUE in the Reset Ramp Output block. **CHECK**

☐ ☐ **DR** Observe that the speed response and TIT temperature do not exceed operational limits

☐ ☐ **AT** When Time Ramp reaches the final time, set IN_1 of Switching block to FALSE, input 0 in the Ramp Upper Limit block, and increase the DFLT rate of Time Ramp as desired. **CHECK**

☐ ☐ **AT** When Time Ramp stops, select Reset Ramp Output to FALSE, input 1 in the DFLT rate of Time Ramp and set new test time i.e. multiples of 20 seconds. **CHECK**

☐ ☐ **AT** Increase the %+/- Bypass Valve Opening input by 5%, **CHECK**

☐ ☐ **AT** Repeat last 10 steps until operational limits are exceeded either on speed or TIT temperature.

☐ ☐ **AT** Repeat last 11 steps for a frequency of 0.004Hz.

☐ ☐ **AT** Switch back to speed control, **CHECK**

☐ ☐ **AT** Input 1 in the HA Control Selector block, **CHECK**

Procedure of Operational Test: BA Scoping (061107)

☐ ☐ **AT** At 40,500rpm, under speed control input 14% in the SS Valve Opening block

☐ ☐ **AT** Under Apacs Vision/Atlas button, select ATLAS, **CHECK**

☐ ☐ **AT** At 40,500rpm, under speed control, change the SEL_FV162 SEL input to 1. Check that the Fuel Valve Control block, the CA Control Selector and the HA Control Selector blocks SEL are both at 1. **CHECK**

☐ ☐ **AT** At 40,500rpm, switch to Open Loop Mode by inputting the Measured Fuel Flow on the Demanded Valve Position. **CHECK**

☐ ☐ **AT** Once speed is stabilized to 40,500rpm, verify the default rate of Time Ramp Block to be 1, **CHECK**

☐ ☐ **AT** Verify that Phase Block has input 0, SS Valve Opening has input 14% and % +/- Bypass Valve Opening is at 4%. **CHECK**

☐ ☐ **AT** Input frequency of 0.05Hz i.e. 20s period, in Frequency Block, and input multiple of 20 second times in the Ramp Upper Limit Box i.e. 5*20=100 second duration for 5 oscillations

☐ ☐ **AT** Enable the Switching block by selecting IN_1 to be **TRUE**

☐ ☐ **AT** Start the fluctuations by selecting TRUE in the Reset Ramp Output block. **CHECK**

☐ ☐ **DR** Observe that the speed response and TIT temperature do not exceed operational limits

☐ ☐ **AT** When Time Ramp reaches the final time, set IN_1 of Switching block to FALSE, input 0 in the Ramp Upper Limit block, and increase the DFLT rate of Time Ramp as desired. **CHECK**

☐ ☐ **AT** When Time Ramp stops, select Reset Ramp Output to FALSE, input 1 in the DFLT rate of Time Ramp and set new test time i.e. multiples of 20 seconds. **CHECK**

☐ ☐ **AT** Increase the %+/- Bypass Valve Opening input by 1%, **CHECK**

☐ ☐ **AT** Repeat last 10 steps until operational limits are exceeded either on speed or TIT temperature.

☐ ☐ **AT** Repeat last 11 steps for a frequency of 0.004Hz.

☐ ☐ **AT** Switch back to speed control, **CHECK**

☐ ☐ **AT** Input 2 in the SEL_FV162 block, **CHECK**

☐ ☐ **AT** Under Apacs Vision/Atlas button, select VISION, **CHECK**

Procedure of Operational Test: Load Bank Scoping (061107)

☐ ☐ **AT** At 40,500rpm, under speed control switch the Apacs Vision/Atlas button to VISION, **CHECK**

☐ ☐ **AT** At 40,500rpm, under speed control input 45% in the SS Valve Opening block

☐ ☐ **AT** At 40,500rpm, under speed control, change the SEL_FV162 SEL input to 1. Check that the Fuel Valve Control block, the CA Control Selector and the HA Control Selector blocks SEL are both at 1. **CHECK**

☐ ☐ **AT** At 40,500rpm, switch to Open Loop Mode by inputting the Measured Fuel Flow on the Demanded Valve Position. **CHECK**

☐ ☐ **AT** Once speed is stabilized to 40,500rpm, verify the default rate of Time Ramp Block to be 1, **CHECK**

☐ ☐ **AT** Verify that Phase Block has input 0, SS Valve Opening has input 50% and % +/- Bypass Valve Opening is at 5%. **CHECK**

☐ ☐ **AT** Input frequency of 0.05Hz i.e. 20s period, in Frequency Block, and input multiple of 20 second times in the Ramp Upper Limit Box i.e. 5*20=100 second duration for 5 oscillations

☐ ☐ **AT** Enable the Switching block by selecting IN_1 to be **TRUE**

☐ ☐ **AT** Start the fluctuations by selecting TRUE in the Reset Ramp Output block. **CHECK**

☐ ☐ **DR** Observe that the speed response and TIT temperature do not exceed operational limits

☐ ☐ **AT** When Time Ramp reaches the final time, set IN_1 of Switching block to FALSE, input 0 in the Ramp Upper Limit block, and increase the DFLT rate of Time Ramp as desired. **CHECK**

☐ ☐ **AT** When Time Ramp stops, select Reset Ramp Output to FALSE, input 1 in the DFLT rate of Time Ramp and set new test time i.e. multiples of 20 seconds. **CHECK**

☐ ☐ **AT** Increase the %+/- Bypass Valve Opening input by 5%, **CHECK**

☐ ☐ **AT** Repeat last 10 steps until operational limits are exceeded either on speed or TIT temperature.

☐ ☐ **AT** Repeat last 11 steps for a frequency of 0.004Hz.

☐ ☐ **AT** Switch back to speed control, **CHECK**

☐ ☐ **AT** Input 2 in the SEL_FV162 block, **CHECK**

System Shutdown

☐ ☐ **DR** Select GAP Speed Sheet- Set Gas Valve Mode to Automated fuel shutdown ramp.

☐ ☐ **DR** At stall or 28,000rpm, Fuel **OFF (Control #1)**

☐ ☐ **AT** Data Log **STOP, RETRIEVE, RENAME and SAVE.**

HYPER Test Plan and Check List
December 27, 2006

Purpose: The purpose of the startup test is to bring the turbine up to the operational steady state nominal speed of 40,500rpm, with all valves closed at 45kW electrical load.

The purpose of the operational test is to determine system structure by means of frequency response data. The fuel valve is to be fluctuated at given amplitude and frequency, over a range of frequencies covering three orders in magnitude. System delay and order are obtained from magnitude and phase plots covering the frequency range i.e. with the use of a Bode Plot. Transfer functions for states at the inlet of the air plenum are derived as a function of valve flow. This test will validate the analytical transfer function for the above mentioned variables, provide steady state error detection, give a stability margin criteria for the fuel valve input, estimate system bandwidth, identify any nonminimum phase system behavior, pinpoint unstable frequencies, and serve as an element of the piecewise transfer function in the development of an overall transfer function matrix covering all system inputs and outputs of interest. Further loop shaping techniques and state space representation can be applied to this matrix.

The test will ramp up the speed to the nominal value of 40,500rpm under speed control, and switch to open loop mode once the system is under steady state with all temperatures and pressures within nominal operating values. At this point, the fuel valve is to be fluctuated sinusoidally at a magnitude of +/- 10% of the nominal valve position % demand value. This is to avoid the lower speed limit restriction set at 38,475rpm. The signal is to start with a period of 1 seconds i.e. 1Hz, and decrease to 0.1Hz down to 0.01Hz down to 0.001Hz. A frequency input will consist of 10 samples between decades i.e. 10 frequency inputs from 1Hz-0.1Hz, 10 frequency inputs from 0.1Hz-0.01Hz, and 10 frequency inputs from 0.01Hz-0.001Hz. In terms of input periods for ten periods of oscillation for the highest decade, the waiting time for each data window will increase as follows: 10, 11.11, 12.5, 14.29, 16.67, 20, 25, 33.3, 50, and 100 seconds. The signal will remain at a given frequency for up to 10 periods of oscillation, for the first two decades, before dropping to 5 periods of oscillation for the last decade having the slowest frequencies tested. The total test duration is approximately 9.5 hours, including system startup time, system shutdown time, and elapsed time between frequency samples for the states to reach their steady state nominal values.

All Hyper states will be recorded.

Start Procedure of Startup Test (061227)

☐ ☐ **DR** Pre-Operational inspection **COMPLETE**.
☐ ☐ **DR** GAP and Watchwindows **OPEN**. Note GAP version: HyperAlexBodeAllBypass

☐ ☐ **AT** APACS and Atlas Clocks **SYNCHONIZED**.
☐ ☐ **AT** Live Engineering Data Spreadsheet **INITIALIZED**.

☐ ☐ **DR** Natural Gas Totalizer **RESET**.
☐ ☐ **DR** HV-414, HV-408 and HV-430 **CLOSED**.

☐ ☐ **AT** Set Gas Valve FV-432 Mode to **Auto Ramp** **(Ramp initiated at 9000rpm)**
☐ ☐ **AT** Set **All OTHER GAP Gains** to **DEFAULT** settings: EGT@625

☐ ☐ **DR** Set Hot Air By-Pass **FV-380** Mode to **1: Manual, 0% Open**
☐ ☐ **DR** Set Bleed Air **FV-162** Mode to **2: Manual, 100% Closed**
☐ ☐ **DR** Set Cold Air By-Pass **FV-170** Mode to **1: Manual, 0% Open**

☐ ☐ **AT** Verify that the Fuel Valve Control, CA Control Selector, BA/Load Selector and HA Control Selector blocks SEL input is at 1. **CHECK**

☐ ☐ **DR** Blower **ON** (Alt-Tab)

☐ ☐ **DR** APACS Log **START**
☐ ☐ **AT** Data Log **START**

☐ ☐ **DR** HV-600 **OPEN** (Alt-Tab)

☐ ☐ **AT** System Purge **ON**
☐ ☐ **DR** FE-380 positive flow ≥ 0.10kg/s **CHECK**

☐ ☐ **DR** HV-408 and HV-430 **REQUEST OPEN**

☐ ☐ **DR** Purge Complete **CHECK**
☐ ☐ **DR** HS-460C Burner Ignition Automated at 9,000rpm **CHECK**
☐ ☐ **DR** If purge complete over 9,000rpm, HS-460A Manual Ignition **ON**
☐ ☐ **DR** TE-333 shows flame **CHECK**
☐ ☐ **DR** ST-502 > 35,000rpm, I-4 enabled **CHECK**

☐ ☐ **DR** ST-502 > 41,000rpm, HV-600 **CLOSED**
☐ ☐ **DR** Blower **OFF**

Preheat System Piping and Vessels

☐ ☐ **DT** Load Bank Cooling Fan (HS-530) **ON**
☐ ☐ **DT** Interlock 14 **ENABLED**
☐ ☐ **DT** Load Bank in Manual Mode **CHECK**
☐ ☐ **DT** Set Bleed Air By-Pass **FV-162** Mode to **2: Manual, 85% Closed**
☐ ☐ **DT** Increase load to 45kW
☐ ☐ **DT** ST-502 at approximately 40,500rpm **CHECK**
☐ ☐ **DT** Wait until TE-344 is at about 1300F **CHECK**
☐ ☐ **DT** Select Bleed Air By-Pass **FV-162** Mode to **2: Manual, 100% Closed**

☐ ☐ **AT** Data Log **STOP, RETRIEVE, RENAME, SAVE and START NEW LOG**

Stop Time:
Start Time:

☐ ☐ **DT** Wait until TE-344 is constant for 30s (+/-0.1C) **CHECK**
☐ ☐ **DT** If stall indicated, implement stall recovery

Procedure of Operational Test: Fuel (061227)

☐ ☐ **AT** Check that the Fuel Valve Control, the BA/Load Selector, the CA Control Selector and the HA Control Selector blocks SEL are at 1. **CHECK**

☐ ☐ **AT** At 40,500rpm, under speed control, input the % fuel demand in the SS Nominal Value block. **CHECK**

☐ ☐ **AT** At 40,500rpm, switch to Open Loop by changing the Fuel Valve Control Selector SEL input from 1 to 2. **CHECK**

☐ ☐ **AT** Once speed is stabilized to 40,500rpm, verify the default rate of Time Ramp Block to be 1, **CHECK**

☐ ☐ **AT** Verify that Phase Block has input 0, SS Nominal Value has the % fuel demand, and % +/- Fluctuation is at 10%. **CHECK**

☐ ☐ **AT** Input first frequency of 1Hz i.e. 1s period, in Frequency Block, and input multiple of 1 second times in the Ramp Upper Limit Box i.e. 10*1=10 second duration for 10 oscillations

☐ ☐ **AT** Enable the Switching block by selecting IN_1 to be **TRUE**

☐ ☐ **AT** Start the fluctuations by selecting TRUE in the Reset Ramp Output block. **CHECK**

☐ ☐ **DR** Observe that the speed response and TIT temperature do not exceed operational limits

☐ ☐ **AT** When Time Ramp reaches the final time, set IN_1 of Switching block to FALSE, input 0 in the Ramp Upper Limit block, and increase the DFLT rate of Time Ramp as desired. **CHECK**

☐ ☐ **AT** When Time Ramp stops, select Reset Ramp Output to FALSE, input 1 in the DFLT rate of Time Ramp and set new test time from the attached frequency table, **CHECK**

☐ ☐ **AT** Change the frequency input in the Frequency Block to the next value listed in the table, **CHECK**

☐ ☐ **AT** Repeat last 10 steps for all the frequencies listed in the attached table until operational limits are exceeded either on speed or TIT temperature.

☐ ☐ **AT** Switch back to speed control, **CHECK**

System Shutdown

☐ ☐ **DT** Unload Generator. **CHECK**

☐ ☐ **AT** Open CA to 20% for 2 min. **CHECK**

☐ ☐ **DT** Load Bank Cooling Fan **OFF**. **CHECK**

☐ ☐ **DR** Select GAP Speed Sheet- Set Gas Valve Mode to Automated fuel shutdown ramp.

☐ ☐ **DR** At stall or 28,000rpm, Fuel **OFF (Control #1)**

☐ ☐ AT Data Log STOP, RETRIEVE, RENAME and SAVE.

HYPER Test Plan and Check List
November 21, 2006

Purpose: The purpose of the startup test is to bring the turbine up to the operational steady state nominal speed of 40,500rpm, with all valves closed at 45kW electrical load.

The purpose of the operational test is to determine system structure by means of frequency response data. The load bank is to be fluctuated at given amplitude and frequency, over a range of frequencies covering three orders in magnitude. System delay and order are obtained from magnitude and phase plots covering the frequency range i.e. with the use of a Bode Plot. Transfer functions for states at the inlet of the air plenum are derived as a function of input load fluctuations. This test will validate the analytical transfer function for the above mentioned variables, provide steady state error detection, give a stability margin criteria for the fuel valve input, estimate system bandwidth, identify any nonminimum phase system behavior, pinpoint unstable frequencies, and serve as an element of the piecewise transfer function in the development of an overall transfer function matrix covering all system inputs and outputs of interest. Further loop shaping techniques and state space representation can be applied to this matrix.

The test will ramp up the speed to the nominal value of 40,500rpm under speed control, and switch to open loop mode once the load bank has been set to 45kW and the system is under steady state with all temperatures and pressures within nominal operating values. At this point, the load bank is to be fluctuated sinusoidally at a magnitude of +/-11.11% of 45kW corresponding to +/-5kW. This is to avoid the lower speed limit restriction set at 38,475rpm. The signal is to start with a period of 1 seconds i.e. 1Hz, and decrease to 0.1Hz down to 0.01Hz down to 0.001Hz. A frequency input will consist of 10 samples between decades i.e. 10 frequency inputs from 1Hz-0.1Hz, 10 frequency inputs from 0.1Hz-0.01Hz, and 10 frequency inputs from 0.01Hz-0.001Hz. In terms of input periods for ten periods of oscillation for the highest decade, the waiting time for each data window will increase as follows: 10, 11.11, 12.5, 14.29, 16.67, 20, 25, 33.3, 50, and 100 seconds. The signal will remain at a given frequency for up to 10 periods of oscillation, for the first two decades, before dropping to 5 periods of oscillation for the last decade having the slowest frequencies tested. The total test duration is approximately 9.5 hours, including system startup time, system shutdown time, and elapsed time between frequency samples for the states to reach their steady state nominal values.

All Hyper states will be recorded.

Start Procedure of Startup Test (061121)

☐ ☐ **DR** Pre-Operational inspection **COMPLETE**.
☐ ☐ **DR** GAP and Watchwindows **OPEN**. Note GAP version: HyperAlexBodeAllBypass

☐ ☐ **AT** APACS and Atlas Clocks **SYNCHONIZED**.
☐ ☐ **AT** Live Engineering Data Spreadsheet **INITIALIZED**.

☐ ☐ **DR** Natural Gas Totalizer **RESET**.
☐ ☐ **DR** HV-414, HV-408 and HV-430 **CLOSED**.

☐ ☐ **AT** Set Gas Valve FV-432 Mode to **Auto Ramp** **(Ramp initiated at 9000rpm)**
☐ ☐ **AT** Set **All OTHER GAP Gains** to **DEFAULT** settings

☐ ☐ **DR** Set Hot Air By-Pass **FV-380** Mode to **1: Manual, 0% Open**
☐ ☐ **DR** Set Bleed Air **FV-162** Mode to **2: Manual, 100% Closed**
☐ ☐ **DR** Set Cold Air By-Pass **FV-170** Mode to **1: Manual, 0% Open**

☐ ☐ **AT** Verify that the Fuel Valve Control, CA Control Selector, and HA Control Selector blocks SEL input is at 1.

☐ ☐ **DR** Blower **ON** (Alt-Tab)

☐ ☐ **DR** APACS Log **START**
☐ ☐ **AT** Data Log **START**

☐ ☐ **DR** HV-600 **OPEN** (Alt-Tab)

☐ ☐ **AT** System Purge **ON**
☐ ☐ **DR** FE-380 positive flow ≥ 0.10kg/s **CHECK**

☐ ☐ **DR** HV-408 and HV-430 **REQUEST OPEN**

☐ ☐ **DR** Purge Complete **CHECK**
☐ ☐ **DR** HS-460C Burner Ignition Automated at 9,000rpm **CHECK**
☐ ☐ **DR** If purge complete over 9,000rpm, HS-460A Manual Ignition **ON**
☐ ☐ **DR** TE-333 shows flame **CHECK**
☐ ☐ **DR** ST-502 > 35,000rpm, I-4 enabled **CHECK**

☐ ☐ **DR** ST-502 > 41,000rpm, HV-600 **CLOSED**
☐ ☐ **DR** Blower **OFF**

Preheat System Piping and Vessels

☐ ☐ **DT** Load Bank Cooling Fan (HS-530) **ON**
☐ ☐ **DT** Interlock 14 **ENABLED**
☐ ☐ **DT** Load Bank in Manual Mode **CHECK**
☐ ☐ **DT** Set Bleed Air By-Pass **FV-162** Mode to **2: Manual, 85% Closed**
☐ ☐ **DT** Increase load to 45kW
☐ ☐ **DT** ST-502 at approximately 40,500rpm **CHECK**
☐ ☐ **DT** Wait until TE-344 is at about 1000F **CHECK**
☐ ☐ **DT** Select Bleed Air By-Pass **FV-162** Mode to **2: Manual, 100% Closed**

☐ ☐ **AT** Data Log **STOP, RETRIEVE, RENAME, SAVE and START NEW LOG**

Stop Time:
Start Time:

☐ ☐ **DT** Wait until TE-344 is constant for 30s (+/-0.1C) **CHECK**
☐ ☐ **DT** If stall indicated, implement stall recovery

Procedure of Operational Test: Load Bank Scoping (061121)

☐ ☐ **DT** At 40,500rpm, under speed control check that the Apacs Vision/Atlas button is set to Vision, **CHECK**

☐ ☐ **AT** At 40,500rpm, under speed control input 45%~45kW in the SS Nominal Value block

☐ ☐ **DT** Change the load bank control window in Apacs to AUTO, **CHECK**

☐ ☐ **AT** At 40,500rpm, under speed control, change the SEL_FV162 SEL input to 1. **CHECK**

☐ ☐ **AT** Check that the Fuel Valve Control block, the CA Control Selector, the BA/Load Selector and the HA Control Selector blocks SEL are at 1. **CHECK**

☐ ☐ **AT** Wait until TE-344 comes to steady state. **CHECK**

☐ ☐ **AT** At 40,500rpm, in Sheet 5, BA/Load Selector Block, input 2 in SEL. **CHECK**

☐ ☐ **AT** In Sheet 17, input 2 in SEL entry of RFV_SEL block to be in Open Loop. **CHECK**

☐ ☐ **AT** Once speed is stabilized to 40,500rpm, verify the default rate of Time Ramp Block to be 1, **CHECK**

☐ ☐ **AT** Verify that Phase Block has input 0, SS Nominal Value has input 45% and % +/- Fluctuation is at 11.11%~5kW. **CHECK**

☐ ☐ **AT** Input frequency of 1Hz i.e. 1s period, in Frequency Block, and input multiple of 1 second times in the Ramp Upper Limit Box i.e. 10*1=10 second duration for 10 oscillations

☐ ☐ **AT** Enable the Switching block by selecting IN_1 to be **TRUE**

☐ ☐ **AT** Start the fluctuations by selecting TRUE in the Reset Ramp Output block. **CHECK**

☐ ☐ **DR** Observe that the speed response and TIT temperature do not exceed operational limits

☐ ☐ **AT** When Time Ramp reaches the final time, set IN_1 of Switching block to FALSE, input 0 in the Ramp Upper Limit block, and increase the DFLT rate of Time Ramp as desired. **CHECK**

☐ ☐ **AT** When Time Ramp stops, select Reset Ramp Output to FALSE, input 1 in the DFLT rate of Time Ramp and set new test time from attached table. **CHECK**

☐ ☐ **AT** Change the frequency input of the Frequency Block to new value from the attached table, **CHECK**

☐ ☐ **AT** Repeat last 10 steps until operational limits are exceeded either on speed or TIT temperature.

☐ ☐ **AT** Switch back to speed control, **CHECK**

☐ ☐ **AT** Set load bank control window back to MANUAL, **CHECK**

☐ ☐ **AT** Input 2 in the SEL_FV162 block, **CHECK**

System Shutdown

☐ ☐ **DT** Unload Generator. **CHECK**

☐ ☐ **DT** Open CA to 20% for 2 min. **CHECK**

☐ ☐ **DR** Select GAP Speed Sheet- Set Gas Valve Mode to Automated fuel shutdown ramp.

☐ ☐ **DR** At stall or 28,000rpm, Fuel **OFF (Control #1)**

☐ ☐ **AT** Data Log **STOP, RETRIEVE, RENAME and SAVE.**

HYPER Test Plan and Check List
December 28, 2006

Purpose: The purpose of the startup test is to bring the turbine up to the operational steady state nominal speed of 40,500rpm, with all valves closed at 35kW electrical load.

The purpose of the operational test is to determine system structure by means of frequency response data. The bleed air BA bypass valve is to be fluctuated at given amplitude and frequency, over a range of frequencies covering three orders in magnitude. System delay and order are obtained from magnitude and phase plots covering the frequency range i.e. with the use of a Bode Plot. Transfer functions for states at the inlet of the air plenum are derived as a function of BA bypass mass flow. This test will validate the analytical transfer function for the above mentioned variables, provide steady state error detection, give a stability margin criteria for the valve input, estimate system bandwidth, identify any nonminimum phase system behavior, pinpoint unstable frequencies, and serve as an element of the piecewise transfer function in the development of an overall transfer function matrix covering all system inputs and outputs of interest. Further loop shaping techniques and state space representation can be applied to this matrix.

The test will ramp up the speed to the nominal value of 40,500rpm under speed control, and switch to open loop mode once the BA valve has been set to 88% closed and the system is under steady state with all temperatures and pressures within nominal operating values. At this point, the BA bypass valve is to be fluctuated sinusoidally at a magnitude of +/-2.27% ~ +/-2% valve, of the nominal valve position corresponding to 88% closed. This is to avoid the lower speed limit restriction set at 38,475rpm. The signal is to start with a period of 1 seconds i.e. 1Hz, and decrease to 0.1Hz down to 0.01Hz down to 0.001Hz. A frequency input will consist of 10 samples between decades i.e. 10 frequency inputs from 1Hz-0.1Hz, 10 frequency inputs from 0.1Hz-0.01Hz, and 10 frequency inputs from 0.01Hz-0.001Hz. In terms of input periods for ten periods of oscillation for the highest decade, the waiting time for each data window will increase as follows: 10, 11.11, 12.5, 14.29, 16.67, 20, 25, 33.3, 50, and 100 seconds. The signal will remain at a given frequency for up to 10 periods of oscillation, for the first two decades, before dropping to 5 periods of oscillation for the last decade having the slowest frequencies tested. The total test duration is approximately 9.5 hours, including system startup time, system shutdown time, and elapsed time between frequency samples for the states to reach their steady state nominal values.

All Hyper states will be recorded.

Start Procedure of Startup Test (061228)

☐ ☐ **DR** Pre-Operational inspection **COMPLETE**.

☐ ☐ **DR** GAP and Watchwindows **OPEN**. Note GAP version: HyperAlexBodeAllBypass

☐ ☐ **AT** APACS and Atlas Clocks **SYNCHONIZED**.
☐ ☐ **AT** Live Engineering Data Spreadsheet **INITIALIZED**.

☐ ☐ **DR** Natural Gas Totalizer **RESET**.
☐ ☐ **DR** HV-414, HV-408 and HV-430 **CLOSED**.

☐ ☐ **AT** Set Gas Valve FV-432 Mode to **Auto Ramp (Ramp initiated at 9000rpm)**
☐ ☐ **AT** Set **All OTHER GAP Gains** to **DEFAULT** settings

☐ ☐ **DR** Set Hot Air By-Pass **FV-380** Mode to **1: Manual, 0% Open**
☐ ☐ **DR** Set Bleed Air **FV-162** Mode to **2: Manual, 100% Closed**
☐ ☐ **DR** Set Cold Air By-Pass **FV-170** Mode to **1: Manual, 0% Open**

☐ ☐ **AT** Verify that the Fuel Valve Control, CA Control Selector, and HA Control Selector blocks SEL input is at 1.

☐ ☐ **DR** Blower **ON** (Alt-Tab)

☐ ☐ **DR** APACS Log **START**
☐ ☐ **AT** Data Log **START**

☐ ☐ **DR** HV-600 **OPEN** (Alt-Tab)

☐ ☐ **AT** System Purge **ON**
☐ ☐ **DR** FE-380 positive flow ≥ 0.10kg/s **CHECK**

☐ ☐ **DR** HV-408 and HV-430 **REQUEST OPEN**

☐ ☐ **DR** Purge Complete **CHECK**
☐ ☐ **DR** HS-460C Burner Ignition Automated at 9,000rpm **CHECK**
☐ ☐ **DR** If purge complete over 9,000rpm, HS-460A Manual Ignition **ON**
☐ ☐ **DR** TE-333 shows flame **CHECK**
☐ ☐ **DR** ST-502 > 35,000rpm, I-4 enabled **CHECK**

☐ ☐ **DR** ST-502 > 41,000rpm, HV-600 **CLOSED**
☐ ☐ **DR** Blower **OFF**

Preheat System Piping and Vessels

☐ ☐ **DT** Load Bank Cooling Fan (HS-530) **ON**
☐ ☐ **DT** Interlock 14 **ENABLED**
☐ ☐ **DT** Load Bank in Manual Mode **CHECK**
☐ ☐ **DT** Set Bleed Air By-Pass **FV-162** Mode to **2: Manual, 85% Closed**
☐ ☐ **DT** Increase load to 45kW
☐ ☐ **DT** ST-502 at approximately 40,500rpm **CHECK**
☐ ☐ **DT** Wait until TE-344 is at about 1300F **CHECK**
☐ ☐ **DT** Select Bleed Air By-Pass **FV-162** Mode to **2: Manual, 88% Closed**
☐ ☐ **DT** Decrease load to 35kW

☐ ☐ **DT** Wait until TE-344 is constant for 30s (+/-0.1C) **CHECK**

☐ ☐ **AT** At 40,500rpm, under speed control input 88% closed in the SS Nominal Value block

☐ ☐ **AT** Check that the Fuel Valve Control block, the CA Control Selector, the BA/Load Selector and the HA Control Selector blocks SEL are both at 1. **CHECK**

☐ ☐ **AT** Data Log **STOP, RETRIEVE, RENAME, SAVE and START NEW LOG**

Stop Time:
Start Time:

☐ ☐ **DT** If stall indicated, implement stall recovery

Procedure of Operational Test: BA (061228)

☐ ☐ **AT** Under the Apacs Vision/Atlas button, select ATLAS, **CHECK**

☐ ☐ **AT** At 40,500rpm, enter the % fuel demand in Fuel Valve Control Block IN_3. **CHECK**

☐ ☐ **AT** Switch to Open Loop by selecting Fuel Valve Control Block SEL input to 3. **CHECK**

☐ ☐ **AT** Once speed is stabilized to 40,500rpm, verify the default rate of Time Ramp Block to be 1, **CHECK**

☐ ☐ **AT** Verify that Phase Block has input 0, SS Nominal Value has input 88% and % +/- Fluctuation is at 2.27% ~ 2% valve. **CHECK**

☐ ☐ **AT** Input frequency of 1Hz i.e. 1s period, in Frequency Block, and input multiple of 1 second times in the Ramp Upper Limit Box i.e. 10*1=10 second duration for 10 oscillations

☐ ☐ **AT** Enable the Switching block by selecting IN_1 to be **TRUE**

☐ ☐ **AT** Start the fluctuations by selecting TRUE in the Reset Ramp Output block. **CHECK**

☐ ☐ **DR** Observe that the speed response and TIT temperature do not exceed operational limits

☐ ☐ **AT** When Time Ramp reaches the final time, set IN_1 of Switching block to FALSE, input 0 in the Ramp Upper Limit block, and increase the DFLT rate of Time Ramp as desired. **CHECK**

☐ ☐ **AT** When Time Ramp stops, select Reset Ramp Output to FALSE, input 1 in the DFLT rate of Time Ramp and set new test time as listed on the attached table, **CHECK**

☐ ☐ **AT** Input new frequency in the Frequency Block from given table, **CHECK**

☐ ☐ **AT** Repeat last 10 steps until operational limits are exceeded either on speed or TIT temperature.

☐ ☐ **AT** Switch back to speed control, **CHECK**

☐ ☐ **AT** Under the Apacs Vision/Atlas button, select VISION, **CHECK**

System Shutdown

☐ ☐ **DT** Unload Generator. **CHECK**

☐ ☐ **DT** Turn off fan. **CHECK**

☐ ☐ **AT** Open CA to 20% for 2 min. **CHECK**

☐ ☐ **DR** Select GAP Speed Sheet- Set Gas Valve Mode to Automated fuel shutdown ramp.

☐ ☐ **DR** At stall or 28,000rpm, Fuel **OFF (Control #1)**

☐ ☐ **AT** Data Log **STOP, RETRIEVE, RENAME and SAVE.**

HYPER Test Plan and Check List
December 14, 2006

Purpose: The purpose of the startup test is to bring the turbine up to the operational steady state nominal speed of 40,500rpm, with all valves closed at 45kW electrical load.

The purpose of the operational test is to determine system structure by means of frequency response data. The cold air CA bypass valve is to be fluctuated at given amplitude and frequency, over a range of frequencies covering three orders in magnitude. System delay and order are obtained from magnitude and phase plots covering the frequency range i.e. with the use of a Bode Plot. Transfer functions for states at the inlet of the air plenum are derived as a function of valve flow. This test will validate the analytical transfer function for the above mentioned variables, provide steady state error detection, give a stability margin criteria for the fuel valve input, estimate system bandwidth, identify any nonminimum phase system behavior, pinpoint unstable frequencies, and serve as an element of the piecewise transfer function in the development of an overall transfer function matrix covering all system inputs and outputs of interest. Further loop shaping techniques and state space representation can be applied to this matrix.

The test will ramp up the speed to the nominal value of 40,500rpm under speed control, and switch to open loop mode once the CA valve has been set to 40% opened and the system is under steady state with all temperatures and pressures within nominal operating values. At this point, the CA bypass valve is to be fluctuated sinusoidally at a magnitude of +/-25% (+/-10% valve) of the nominal valve position corresponding to 40%. This is to avoid the lower speed limit restriction set at 38,475rpm. The signal is to start with a period of 1 seconds i.e. 1Hz, and decrease to 0.1Hz down to 0.01Hz down to 0.001Hz. A frequency input will consist of 10 samples between decades i.e. 10 frequency inputs from 1Hz-0.1Hz, 10 frequency inputs from 0.1Hz-0.01Hz, and 10 frequency inputs from 0.01Hz-0.001Hz. In terms of input periods for ten periods of oscillation for the highest decade, the waiting time for each data window will increase as follows: 10, 11.11, 12.5, 14.29, 16.67, 20, 25, 33.3, 50, and 100 seconds. The signal will remain at a given frequency for up to 10 periods of oscillation, for the first two decades, before dropping to 5 periods of oscillation for the last decade having the slowest frequencies tested. The total test duration is approximately 9.5 hours, including system startup time, system shutdown time, and elapsed time between frequency samples for the states to reach their steady state nominal values.

All Hyper states will be recorded.

Start Procedure of Startup Test (061214)

☐ ☐ **DR** Pre-Operational inspection **COMPLETE**.
☐ ☐ **DR** GAP and Watchwindows **OPEN**. Note GAP version: HyperAlexBodeAllBypass

☐ ☐ **AT** APACS and Atlas Clocks **SYNCHONIZED**.
☐ ☐ **AT** Live Engineering Data Spreadsheet **INITIALIZED**.

☐ ☐ **DR** Natural Gas Totalizer **RESET**.
☐ ☐ **DR** HV-414, HV-408 and HV-430 **CLOSED**.

☐ ☐ **AT** Set Gas Valve FV-432 Mode to **Auto Ramp** **(Ramp initiated at 9000rpm)**
☐ ☐ **AT** Set **All OTHER GAP Gains** to **DEFAULT** settings

☐ ☐ **DR** Set Hot Air By-Pass **FV-380** Mode to **1: Manual, 0% Open**
☐ ☐ **DR** Set Bleed Air **FV-162** Mode to **2: Manual, 100% Closed**
☐ ☐ **DR** Set Cold Air By-Pass **FV-170** Mode to **1: Manual, 0% Open**

☐ ☐ **AT** Verify that the Fuel Valve Control, CA Control Selector, and HA Control Selector blocks SEL input is at 1.

☐ ☐ **DR** Blower **ON** (Alt-Tab)

☐ ☐ **DR** APACS Log **START**
☐ ☐ **AT** Data Log **START**

☐ ☐ **DR** HV-600 **OPEN** (Alt-Tab)

☐ ☐ **AT** System Purge **ON**
☐ ☐ **DR** FE-380 positive flow ≥ 0.10kg/s **CHECK**

☐ ☐ **DR** HV-408 and HV-430 **REQUEST OPEN**

☐ ☐ **DR** Purge Complete **CHECK**
☐ ☐ **DR** HS-460C Burner Ignition Automated at 9,000rpm **CHECK**
☐ ☐ **DR** If purge complete over 9,000rpm, HS-460A Manual Ignition **ON**
☐ ☐ **DR** TE-333 shows flame **CHECK**
☐ ☐ **DR** ST-502 > 35,000rpm, I-4 enabled **CHECK**

☐ ☐ **DR** ST-502 > 41,000rpm, HV-600 **CLOSED**
☐ ☐ **DR** Blower **OFF**

Preheat System Piping and Vessels

☐ ☐ **DT** Load Bank Cooling Fan (HS-530) **ON**
☐ ☐ **DT** Interlock 14 **ENABLED**
☐ ☐ **DT** Load Bank in Manual Mode **CHECK**
☐ ☐ **DT** Set Bleed Air By-Pass **FV-162** Mode to **2: Manual, 85% Closed**
☐ ☐ **DT** Increase load to 45kW
☐ ☐ **DT** ST-502 at approximately 40,500rpm **CHECK**
☐ ☐ **DT** Wait until TE-344 is at about 1000F **CHECK**
☐ ☐ **DT** Select Bleed Air By-Pass **FV-162** Mode to **2: Manual, 100% Closed**

☐ ☐ **AT** Data Log **STOP, RETRIEVE, RENAME, SAVE and START NEW LOG**

Stop Time:
Start Time:

☐ ☐ **DT** Wait until TE-344 is constant for 30s (+/-0.1C) **CHECK**
☐ ☐ **DT** If stall indicated, implement stall recovery

Procedure of Operational Test: CA (061214)

☐ ☐ **AT** Check that the Fuel Valve Control, the BA/Load Selector, the CA Control Selector and the HA Control Selector blocks SEL are at 1. **CHECK**

☐ ☐ **AT** At 40,500rpm, under speed control input 40% in the SS Nominal Value block

☐ ☐ **AT** At 40,500rpm, under speed control change the CA Control Selector SEL input from 1 to 2. **CHECK**

☐ ☐ **DT** Wait until TE-344 comes to steady state. **CHECK**

☐ ☐ **AT** Under speed control, observe the % fuel valve demand in Sheet 12. **CHECK**

☐ ☐ **AT** Input the observed % demand in IN_3 of the Fuel Valve Control Block, and switch to Open Loop by selecting 3 in SEL. **CHECK**

☐ ☐ **AT** Once speed is stabilized to 40,500rpm, verify the default rate of Time Ramp Block to be 1, **CHECK**

☐ ☐ **AT** Verify that Phase Block has input 0, SS Nominal Value has input 40% and % +/- Fluctuation is at 25% ~10% valve. **CHECK**

☐ ☐ **AT** Input first frequency of 1Hz i.e. 1s period, in Frequency Block, and input multiple of 1 second times in the Ramp Upper Limit Box i.e. 10*1=10 second duration for 10 oscillations

☐ ☐ **AT** Enable the Switching block by selecting IN_1 to be **TRUE**

☐ ☐ **AT** Start the fluctuations by selecting TRUE in the Reset Ramp Output block. **CHECK**

☐ ☐ **DR** Observe that the speed response and TIT temperature do not exceed operational limits

☐ ☐ **AT** When Time Ramp reaches the final time, set IN_1 of Switching block to FALSE, input 0 in the Ramp Upper Limit block, and increase the DFLT rate of Time Ramp as desired. **CHECK**

☐ ☐ **AT** When Time Ramp stops, select Reset Ramp Output to FALSE, input 1 in the DFLT rate of Time Ramp and set new test time from the attached frequency table, **CHECK**

☐ ☐ **AT** Change the frequency input in the Frequency Block to the next value listed in the table, **CHECK**

☐ ☐ **AT** Repeat last 10 steps for all the frequencies listed in the attached table until operational limits are exceeded either on speed or TIT temperature.

☐ ☐ **AT** Switch back to speed control, **CHECK**

☐ ☐ **AT** Input 1 in the CA Control Selector block, **CHECK**

System Shutdown

☐ ☐ **DT** Unload Generator. **CHECK**

☐ ☐ **AT** Open CA to 20% for 2 min. **CHECK**

☐ ☐ **DT** Load Bank Cooling Fan **OFF**. **CHECK**

☐ ☐ **DR** Select GAP Speed Sheet- Set Gas Valve Mode to Automated fuel shutdown ramp.

☐ ☐ **DR** At stall or 28,000rpm, Fuel **OFF (Control #1)**

☐ ☐ **AT** Data Log **STOP, RETRIEVE, RENAME and SAVE.**

HYPER Test Plan and Check List
December 21, 2006

Purpose: The purpose of the startup test is to bring the turbine up to the operational steady state nominal speed of 40,500rpm, with all valves closed at 45kW electrical load.

The purpose of the operational test is to determine system structure by means of frequency response data. The hot air HA bypass valve is to be fluctuated at given amplitude and frequency, over a range of frequencies covering three orders in magnitude. System delay and order are obtained from magnitude and phase plots covering the frequency range i.e. with the use of a Bode Plot. Transfer functions for states at the inlet of the air plenum are derived as a function of valve flow. This test will validate the analytical transfer function for the above mentioned variables, provide steady state error detection, give a stability margin criteria for the fuel valve input, estimate system bandwidth, identify any nonminimum phase system behavior, pinpoint unstable frequencies, and serve as an element of the piecewise transfer function in the development of an overall transfer function matrix covering all system inputs and outputs of interest. Further loop shaping techniques and state space representation can be applied to this matrix.

The test will ramp up the speed to the nominal value of 40,500rpm under speed control, and switch to open loop mode once the HA valve has been set to 40% opened and the system is under steady state with all temperatures and pressures within nominal operating values. At this point, the HA bypass valve is to be fluctuated sinusoidally at a magnitude of +/-25% (+/-10% valve) of the nominal valve position corresponding to 40%. This is to avoid the lower speed limit restriction set at 38,475rpm. The signal is to start with a period of 1 second i.e. 1Hz, and decrease to 0.1Hz down to 0.01Hz down to 0.001Hz. A frequency input will consist of 10 samples between decades i.e. 10 frequency inputs from 1Hz-0.1Hz, 10 frequency inputs from 0.1Hz-0.01Hz, and 10 frequency inputs from 0.01Hz-0.001Hz. In terms of input periods for ten periods of oscillation for the highest decade, the waiting time for each data window will increase as follows: 10, 11.11, 12.5, 14.29, 16.67, 20, 25, 33.3, 50, and 100 seconds. The signal will remain at a given frequency for up to 10 periods of oscillation, for the first two decades, before dropping to 5 periods of oscillation for the last decade having the slowest frequencies tested. The total test duration is approximately 9.5 hours, including system startup time, system shutdown time, and elapsed time between frequency samples for the states to reach their steady state nominal values.

All Hyper states will be recorded.

Start Procedure of Startup Test (061221)

☐ ☐ **DR** Pre-Operational inspection **COMPLETE**.

☐ ☐ **DR** GAP and Watchwindows **OPEN**. Note GAP version: HyperAlexBodeAllBypass

☐ ☐ **AT** APACS and Atlas Clocks **SYNCHONIZED**.
☐ ☐ **AT** Live Engineering Data Spreadsheet **INITIALIZED**.

☐ ☐ **DR** Natural Gas Totalizer **RESET**.
☐ ☐ **DR** HV-414, HV-408 and HV-430 **CLOSED**.

☐ ☐ **AT** Set Gas Valve FV-432 Mode to **Auto Ramp** **(Ramp initiated at 9000rpm)**

☐ ☐ **AT** Set **All OTHER GAP Gains** to **DEFAULT** settings

☐ ☐ **DR** Set Hot Air By-Pass **FV-380** Mode to **1: Manual, 10% Open**
☐ ☐ **DR** Set Bleed Air **FV-162** Mode to **2: Manual, 100% Closed**
☐ ☐ **DR** Set Cold Air By-Pass **FV-170** Mode to **1: Manual, 0% Open**

☐ ☐ **AT** Verify that the Fuel Valve Control, CA Control Selector, and HA Control Selector blocks SEL input is at 1.

☐ ☐ **DR** Blower **ON** (Alt-Tab)

☐ ☐ **DR** APACS Log **START**
☐ ☐ **AT** Data Log **START**

☐ ☐ **DR** HV-600 **OPEN** (Alt-Tab)

☐ ☐ **AT** System Purge **ON**
☐ ☐ **DR** FE-380 positive flow ≥ 0.10kg/s **CHECK**

☐ ☐ **DR** HV-408 and HV-430 **REQUEST OPEN**

☐ ☐ **DR** Purge Complete **CHECK**
☐ ☐ **DR** HS-460C Burner Ignition Automated at 9,000rpm **CHECK**
☐ ☐ **DR** If purge complete over 9,000rpm, HS-460A Manual Ignition **ON**
☐ ☐ **DR** TE-333 shows flame **CHECK**

☐ ☐ **DR** ST-502 > 35,000rpm, I-4 enabled **CHECK**
☐ ☐ **DR** ST-502 > 41,000rpm, HV-600 **CLOSED**
☐ ☐ **DR** Blower **OFF**

Preheat System Piping and Vessels

☐ ☐ **DT** Load Bank Cooling Fan (HS-530) **ON**
☐ ☐ **DT** Interlock 14 **ENABLED**
☐ ☐ **DT** Load Bank in Manual Mode **CHECK**
☐ ☐ **DT** Set Bleed Air By-Pass **FV-162** Mode to **2: Manual, 85% Closed**
☐ ☐ **DT** Increase load to 45kW
☐ ☐ **DT** ST-502 at approximately 40,500rpm **CHECK**
☐ ☐ **DT** Wait until TE-344 is at about 1000F **CHECK**
☐ ☐ **DT** Select Bleed Air By-Pass **FV-162** Mode to **2: Manual, 100% Closed**

☐ ☐ **AT** Data Log **STOP, RETRIEVE, RENAME, SAVE and START NEW LOG**

Stop Time:
Start Time:

☐ ☐ **DT** Wait until TE-344 is constant for 30s (+/-0.1C) **CHECK**
☐ ☐ **DT** If stall indicated, implement stall recovery

Procedure of Operational Test: HA (061221)

☐ ☐ **AT** Check that the Fuel Valve Control, the BA/Load Selector, the CA Control Selector and the HA Control Selector blocks SEL are at 1. **CHECK**

☐ ☐ **AT** At 40,500rpm, under speed control input 40% in the SS Nominal Value block

☐ ☐ **AT** At 40,500rpm, under speed control change the HA Control Selector SEL input from 1 to 2. **CHECK**

☐ ☐ **DT** Wait until TE-344 comes to steady state. **CHECK**

☐ ☐ **AT** Under speed control, observe the % fuel valve demand in Sheet 12. **CHECK**

☐ ☐ **AT** Input the observed % demand in IN_3 of the Fuel Valve Control Block, and switch to Open Loop by selecting 3 in SEL. **CHECK**

☐ ☐ **AT** Once speed is stabilized to 40,500rpm, verify the default rate of Time Ramp Block to be 1, **CHECK**

☐ ☐ **AT** Verify that Phase Block has input 0, SS Nominal Value has input 40% and % +/- Fluctuation is at 25% ~10% valve. **CHECK**

☐ ☐ **AT** Input first frequency of 1Hz i.e. 1s period, in Frequency Block, and input multiple of 1 second times in the Ramp Upper Limit Box i.e. 10*1=10 second duration for 10 oscillations

☐ ☐ **AT** Enable the Switching block by selecting IN_1 to be **TRUE**

☐ ☐ **AT** Start the fluctuations by selecting TRUE in the Reset Ramp Output block. **CHECK**

☐ ☐ **DR** Observe that the speed response and TIT temperature do not exceed operational limits

☐ ☐ **AT** When Time Ramp reaches the final time, set IN_1 of Switching block to FALSE, input 0 in the Ramp Upper Limit block, and increase the DFLT rate of Time Ramp as desired. **CHECK**

☐ ☐ **AT** When Time Ramp stops, select Reset Ramp Output to FALSE, input 1 in the DFLT rate of Time Ramp and set new test time from the attached frequency table, **CHECK**

☐ ☐ **AT** Change the frequency input in the Frequency Block to the next value listed in the table, **CHECK**

☐ ☐ **AT** Repeat last 10 steps for all the frequencies listed in the attached table until operational limits are exceeded either on speed or TIT temperature.

☐ ☐ **AT** Switch back to speed control, **CHECK**

☐ ☐ **AT** On Sheet 10, input 0% in the Manual FV380 block. **CHECK**

☐ ☐ **AT** Input 1 in the HA Control Selector block, **CHECK**

System Shutdown

☐ ☐ **DT** Unload Generator. **CHECK**

☐ ☐ **AT** Open CA to 20% for 2 min. **CHECK**

☐ ☐ **DT** Load Bank Cooling Fan **OFF**. **CHECK**

☐ ☐ **DR** Select GAP Speed Sheet- Set Gas Valve Mode to Automated fuel shutdown ramp.

☐ ☐ **DR** At stall or 28,000rpm, Fuel **OFF (Control #1)**

☐ ☐ **AT** Data Log **STOP, RETRIEVE, RENAME and SAVE.**

Appendix H

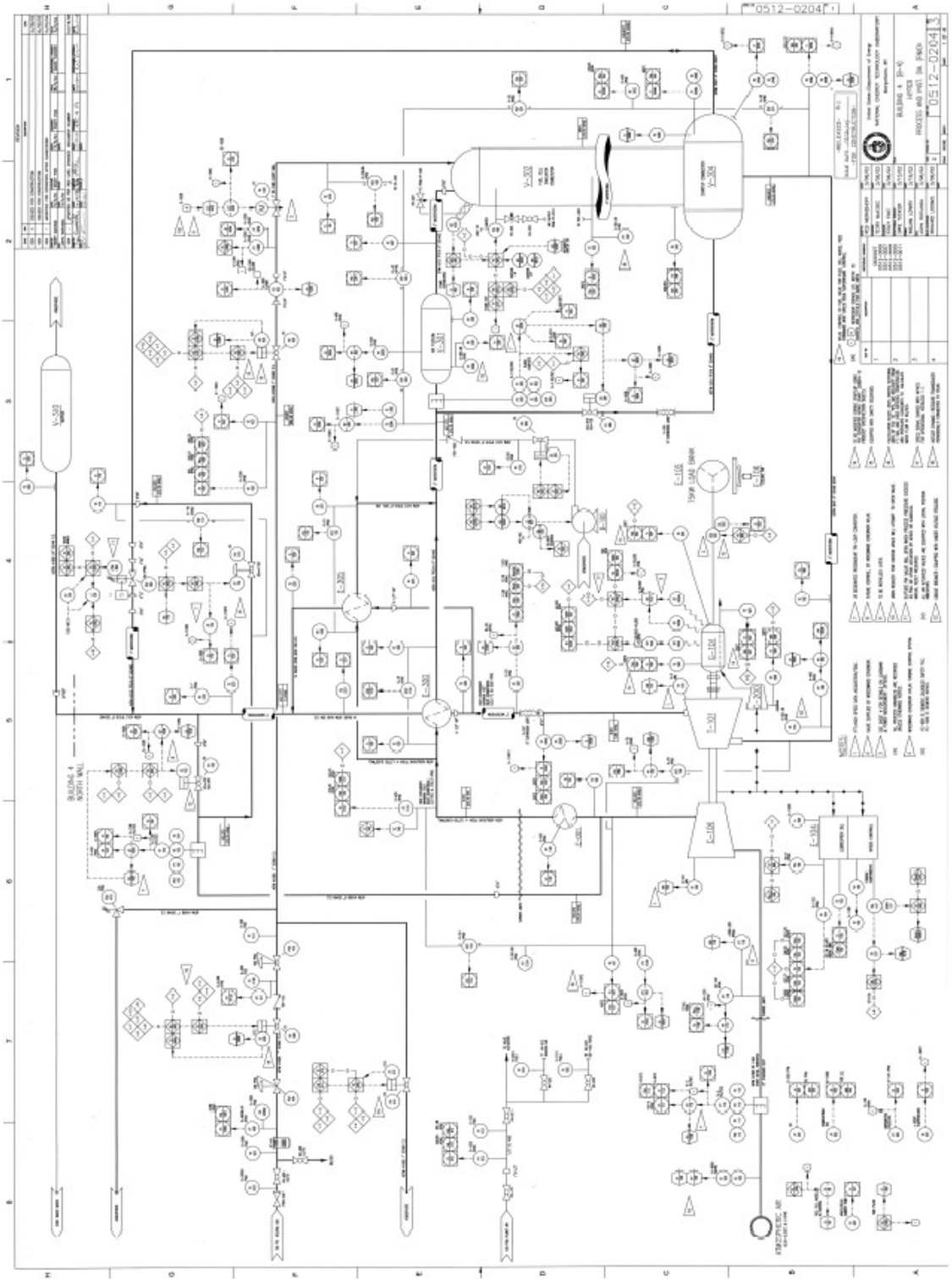

HyPer Process and Instrumentation Diagram

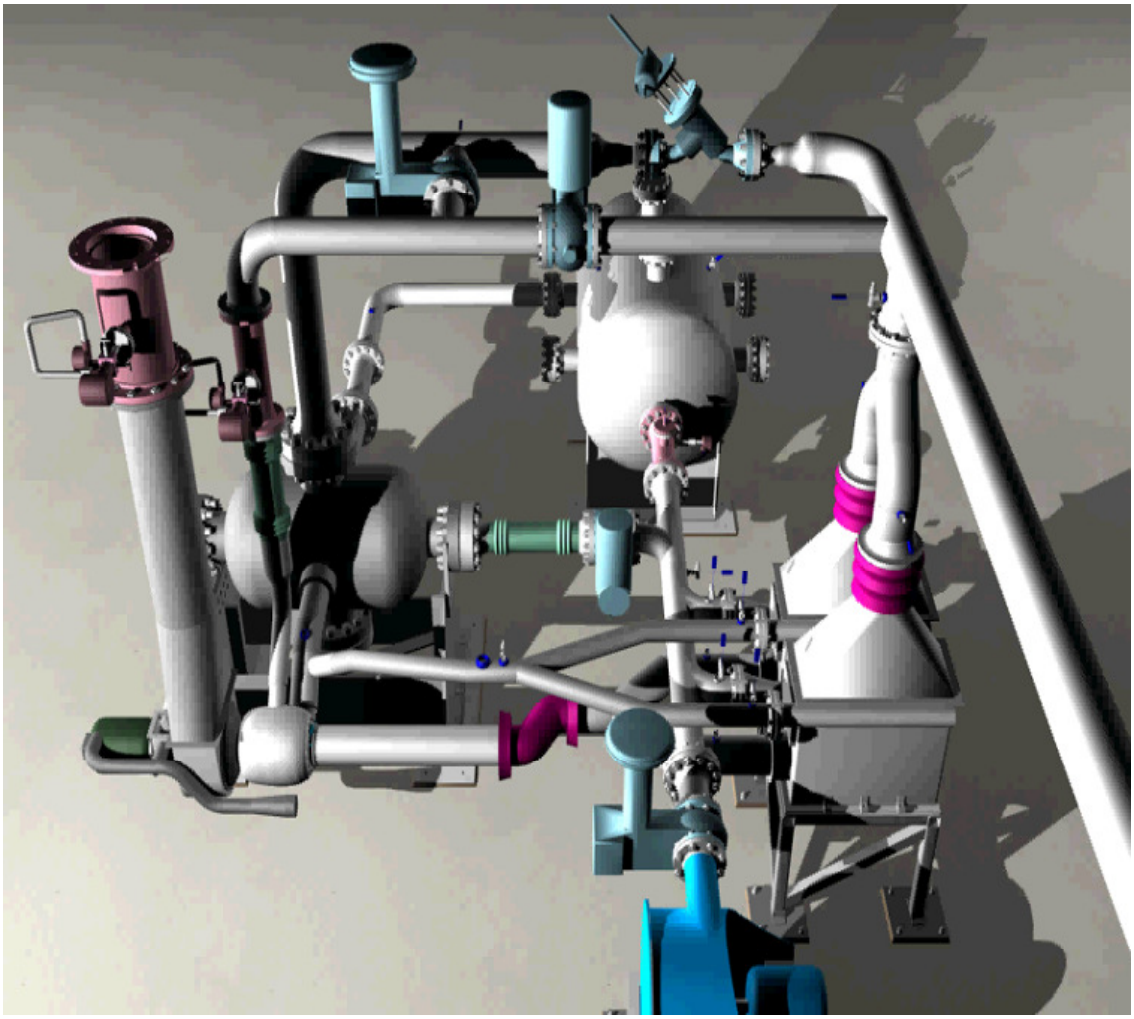

AutoCAD Rendering of the “Hyper” Facility

Appendix I

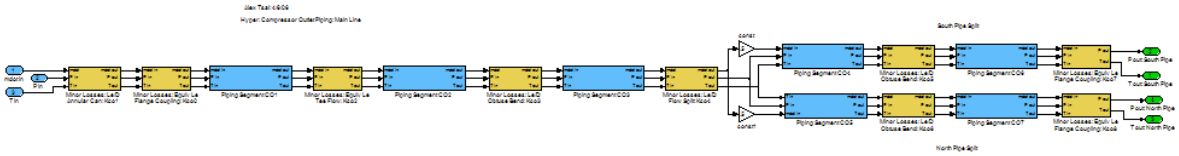

Compressor Exit to Heat Exchangers Pipe

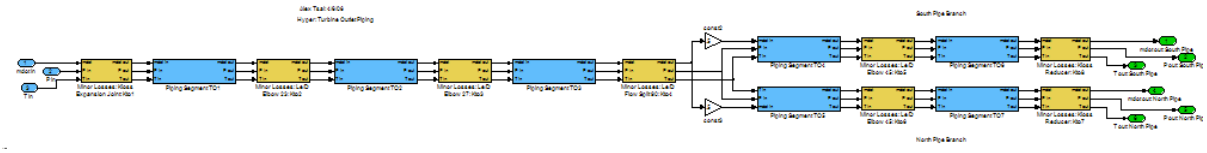

Turbine Exit to Heat Exchangers Pipe

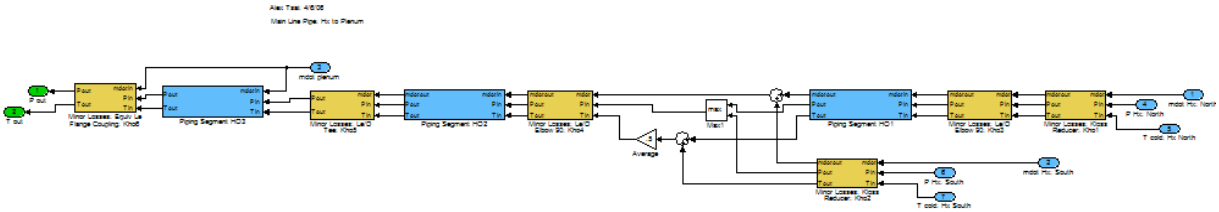

Heat Exchangers to Air Plenum Pipe

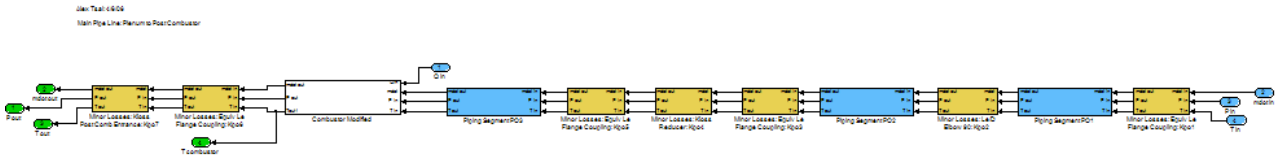

Air Plenum Exit to Post Combustor Pipe

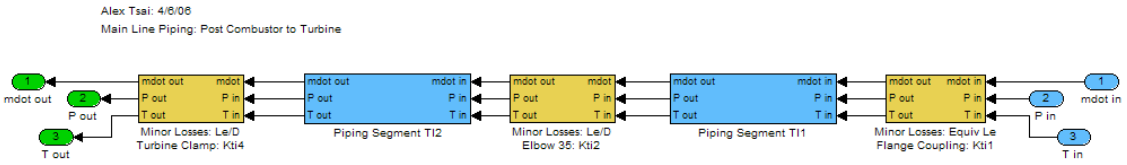

Post-Combustor to Turbine Inlet Pipe

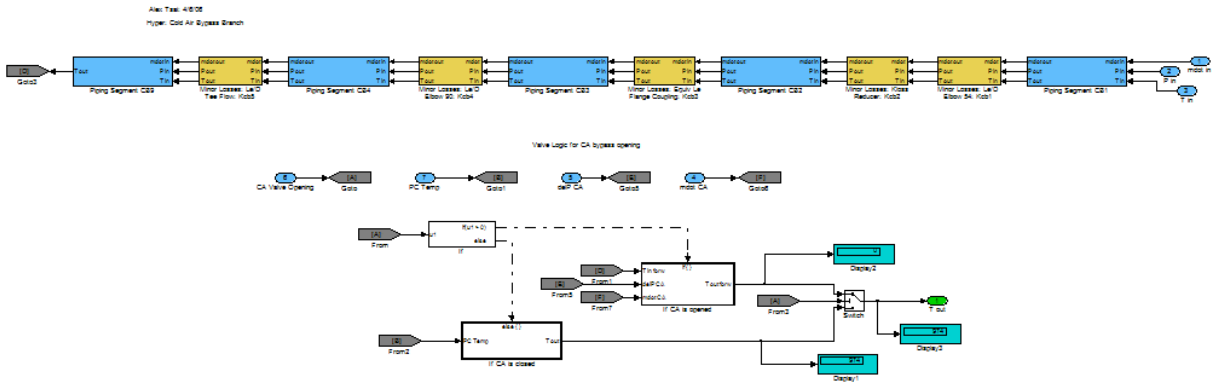

Cold Air Bypass Pipe and Logic

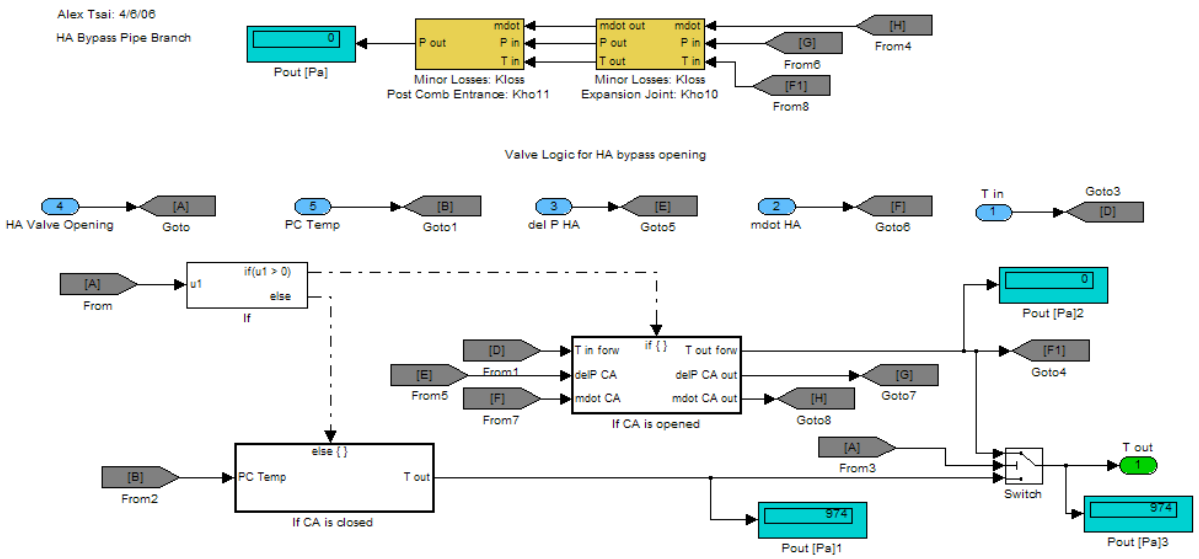

Hot Air Bypass Pipe and Logic